



**HAL**  
open science

# Molecules at surfaces : formation, reactivity, assembly of (bio)molecules on external and internal surfaces of nanosized/nanostructured materials

Ola El Samrout

## ► To cite this version:

Ola El Samrout. Molecules at surfaces : formation, reactivity, assembly of (bio)molecules on external and internal surfaces of nanosized/nanostructured materials. Material chemistry. Sorbonne Université; Università degli studi (Turin, Italie), 2023. English. NNT : 2023SORUS085 . tel-04138067

**HAL Id: tel-04138067**

**<https://theses.hal.science/tel-04138067v1>**

Submitted on 22 Jun 2023

**HAL** is a multi-disciplinary open access archive for the deposit and dissemination of scientific research documents, whether they are published or not. The documents may come from teaching and research institutions in France or abroad, or from public or private research centers.

L'archive ouverte pluridisciplinaire **HAL**, est destinée au dépôt et à la diffusion de documents scientifiques de niveau recherche, publiés ou non, émanant des établissements d'enseignement et de recherche français ou étrangers, des laboratoires publics ou privés.

# Sorbonne Université

Ecole doctorale de Physique et Chimie des matériaux

*Laboratoire de Réactivité de Surface*

# University of Turin

PhD School of Pharmaceutical and Biomolecular Sciences

*Department of Chemistry*

## **Molecules at surfaces: formation, reactivity, assembly of (bio)molecules on external and internal surfaces of nanosized/nanostructured materials**

Par Ola El Samrout

Doctoral Thesis

Supervised by Prof. Jean-François LAMBERT and Prof. Gloria BERLIER

Presented and defended publicly on February 6, 2023

In front of a committee composed of :

Mrs. Barbara Onida	Associate Professor (Politecnico di Torino)	Rapporteur
Mr. Lorenzo Stievano	Professor (Université de Montpellier)	Rapporteur
Mrs. Enrica Gianotti	Associate Professor (Università del Piemonte Orientale)	Examiner
Mrs. Louwanda Lakiss	Research Engineer (University of Caen)	Examiner
Mrs. Maguy Jaber	Professor (University of Sorbonne)	Examiner
Mr. Piero Ugliengo	Professor (University of Turin)	President
Mrs. Gloria Berlier	Professor (University of Turin)	Supervisor
Mr. Jean-François Lambert	Professor (University of Sorbonne)	Supervisor



# Acknowledgment

When I came to write my acknowledgments, I realized how heavy but fruitful these past three years were. I did not only promote my scientific maturity but also, I became more mature in life.

Besides the long COVID confinement that was stressful for everyone, especially in the case of being far from family, losing my supervisor Prof. Gianmario Martra suddenly at the beginning of my second PhD year was a big shock that no words could describe. It was an impediment that put me in the deepest abyss. With tears in my eyes, I would like to express my endless gratitude to him as he offered me the chance to apply for a PhD candidacy and pave the way for me to delve into the realm of research about prebiotic chemistry with his huge passion, continuous support and deep scientific skills. I will be forever indebted to him for promoting and nourishing my intellectual maturity. I have never imagined that I will reach the end of my PhD journey without having him here with us, reading, discussing, and reviewing my work for long and long hours as he used to do and finishing our endless meetings with the same encouraging sentence: “tu sei brava, molto brava”. I wish you are now proud of all the work achieved so far as I am proud for having the chance of meeting you, learn from your enormous scientific background that you have transmitted part of it to me. I will never forget you; I am still referring to some of your handwritten notes on my lab copybook to get inspired...I miss you...

It would be impossible to overcome such impediment without the enormous support of my supervisors Prof. Jean-François Lambert from the Sorbonne University and Prof. Gloria Berlier from the University of Torino who have greatly invested in this thesis. Their continuous motivation, guidance and valuable advices were really essential for the completion of this work while bringing out the best in me. I would like to seize the opportunity to deeply thank Prof. Jean-François, the backbone of this work, for his continuous support and for creating through his outstanding scientific conversations an enriching environment which was conducive to an ever-rising drive for research and learning. He truly played the role of a catalytic support in accelerating my thesis work and providing me with interesting scientific knowledge about the world of origin of life. He will always be my reference who embodies hard work, success, and resolution.

In parallel, I also owe my deepest gratitude to Prof. Gloria Berlier who offered to take care of me and my research work after the departure of Prof. Martra. Her support encompassed all

aspects: moral, emotional, and educational. She made me embrace positivity with her exceptional smile she wears and made me strongly believe that nothing can abate me from reaching my goals. In addition, she was always available with a lot of patience whenever I needed help, and was constantly engaged in the exploitation of the work results and she assisted me at every point in the writing. The ideas we shared were very fruitful for shaping up my research. She guided me on the right path and will always be a great inspiration for me.

Without my supervisors, I would not have been as independent and responsible as I am today. We formed a great team which resulted in a huge amount of work achieved and well-shaped into three research articles.

It is a pleasure to thank Prof. Lorenzo Stievano and Prof. Barbara Onida for accepting to read my manuscript and give their objective and constructive opinions about this work. I am honored by their presence with Prof. Enrica Gianotti, Prof. Piero Ugliengo, Prof. Maguy Jaber, and Dr. Louwanda Lakiss as jury members to evaluate my work.

Here I would greatly recognize the availability of Prof. Piero Ugliengo at all times we asked him for some meetings for fruitful scientific discussions and for sharing his deep knowledge and huge experience with us.

My colleagues and friends, especially Pavlo, Marco, Eya, Rosengela, Erica, Chiara, Guille, Louis, Alice, Leila, Yara, Hagop and Oscar have played a pivotal role as they were by my side throughout these three years. Your support and encouragement were worth than I can express.

Words fail to convey my appreciation to my husband, my support system, and my favorite person who has always encouraged and believed in me. With his unconditional love and support, he made me embark on my thesis journey in the lightest possible way and converted my stressors into laughters. He has truly made what is impossible possible. He was always providing me with a warm shoulder to lean on whenever I needed support. Thank you for always being here for me.

I will also seize the great opportunity to express my endless gratitude to my parents and my siblings for their unconditional support. I owe them my achievements and success; without them all this work would not have been done. They were always there to encourage and comfort me when necessary. Thank you for always giving me the strength to carry on.

To all of them, Thank you, Merci, Grazie....

# Table of content

<b>Acknowledgment</b> .....	<b>1</b>
<b>Table of content</b> .....	<b>3</b>
<b>List of abbreviations</b> .....	<b>5</b>
<b>General introduction</b> .....	<b>6</b>
<b>I. Chapter I: Literature review</b> .....	<b>9</b>
I.1. Catalytic methods for direct amide bond synthesis .....	10
I.1.1. Biocatalysts .....	12
I.1.2. Boron-based catalysts .....	12
I.1.3. Metal-based catalysts .....	13
I.2. Applications of amide bond formation .....	13
I.2.1. Industrial medicinal chemistry .....	14
I.2.2. Prebiotic chemistry .....	15
I.3. Amide/peptide bond formation on mineral surfaces.....	19
I.3.1. Challenges in the synthesis of peptides from amino acids .....	19
I.3.2. Role of the mineral surfaces in the polymerization reaction .....	21
I.4. The world of silica .....	23
I.4.1. Structure and features of silica samples .....	25
I.4.2. Synthesis of silica samples.....	29
I.4.3. Amino acid polymerization on amorphous silica surface.....	32
I.5. Thesis objectives and methodology .....	33
<b>II. Chapter II: Technical part</b> .....	<b>36</b>
II.1. Characterization techniques.....	37
II.1.1. Spectroscopies .....	37
II.1.2. Thermal techniques.....	45
II.1.3. Physicochemical techniques .....	46
II.1.4. Analytical techniques .....	49
II.2. Experimental protocols.....	51
II.2.1. Pre-treatment of silica materials .....	51
II.2.2. Monomers adsorption from the gas phase .....	52
II.2.3. Monomers adsorption from liquid phase.....	54
<b>III. Chapter III: Emergence of order in origins-of-life scenarios on mineral surfaces: polyglycine chains on silica</b> .....	<b>55</b>
III.1. Introduction .....	57
III.2. Experimental Section .....	59
III.2.1. Materials .....	59
III.2.2. Pre-treatment of the silica materials .....	60
III.2.3. Glycine adsorption procedure from the gas phase .....	61
III.2.4. Analysis of the products extracted by washing and of the washed samples .....	61
III.2.5. Infrared (IR) spectroscopy .....	62
III.2.6. High-resolution mass spectrometry (HR-MS) analysis .....	62
III.2.7. X-ray Diffraction (XRD).....	63
III.2.8. Thermal gravimetric Analysis (TGA) .....	63
III.3. Results And Discussion.....	63
III.3.1 Adsorption and reaction of formic acid on the silica surface at 160 °C.....	64
III.3.2. Gly deposition and polymerization on silica surfaces in CVD conditions .....	67
III.3.3. Self-assembly and secondary structures of poly-Gly .....	73
III.3.4. Effect of hydration/dehydration cycles on grafted poly-Gly .....	77

III.4. Conclusion.....	80
<b>IV. Chapter IV: Polypeptide chain growth mechanisms and secondary structure formation in glycine gas-phase deposition on silica surfaces .....</b>	<b>82</b>
IV.1. Introduction.....	84
IV.2. Experimental Section .....	87
IV.2.1. Materials.....	87
IV.2.2. Dehydration of the silica surface .....	87
IV.2.3. Gly adsorption from the gas phase under temperature fluctuations (CVD with TF).....	87
IV.2.4. Hydration fluctuations (HF) cycles procedure, and H/D isotopic exchange .....	88
IV.2.6. Description of the samples .....	89
IV.2.7. Infrared (IR) spectroscopy .....	89
IV.2.8. X-ray diffraction (XRD) .....	90
IV.2.9. High-resolution mass spectrometry (HR-MS).....	90
IV.3. Results And Discussion .....	91
IV.3.1. Difference in the polymerization reaction between a system subjected to temperature fluctuations and another one subjected to both temperature and humidity fluctuations .....	92
IV.3.2. Structural dynamics of the peptide chains revealed by H/D exchange.....	99
IV.3.3. Effect of HF and WD cycles on Gly deposition for extended durations. ....	104
IV.4. Conclusion .....	110
<b>V. Chapter V: Cyclic or linear? Parameters determining the outcome of glycine polymerization in silica surface prebiotic scenarios.....</b>	<b>112</b>
V.1. Introduction .....	114
V.2. Experimental section .....	116
V.2.1. Materials .....	116
V.2.2. Thermal Treatment of silicas.....	116
V.2.3. Gly adsorption on silica supports from the gas phase .....	116
V.2.4. Gly adsorption on silica supports from the liquid phase.....	117
V.2.5. Infrared (IR) spectroscopy.....	118
V.2.6. Attenuated total reflection infrared (ATR-IR) spectroscopy .....	118
V.2.7. Raman Spectroscopy .....	119
V.2.8. Specific surface area measurements.....	119
V.2.9. X-ray diffraction (XRD).....	119
V.2.10. Thermogravimetric analysis (TGA) .....	119
V.3. Results and Discussion.....	120
V.3.1. Gly deposited on silica from the vapor phase .....	120
V.3.2. Gly deposited on silica from the liquid phase .....	133
V.4. Conclusion.....	144
<b>General conclusion and perspectives.....</b>	<b>147</b>
<b>References .....</b>	<b>151</b>
<b>Appendix 1: Emergence of order in origins-of-life scenarios on mineral surfaces: polyglycine chains on silica.....</b>	<b>174</b>
<b>Appendix 2: Polypeptide chain growth mechanisms and secondary structure formation in glycine gas-phase deposition on silica surfaces .....</b>	<b>183</b>
<b>Appendix 3: Cyclic or linear? Parameters determining the outcome of glycine polymerization in silica surface prebiotic scenarios.....</b>	<b>187</b>
<b>List of figures .....</b>	<b>196</b>
<b>List of tables.....</b>	<b>199</b>
<b>Journal Publications .....</b>	<b>200</b>

## List of abbreviations

AAs	Amino acids
APIs	Active Pharmaceutical Ingredients
ATR	Attenuated Total Reflection
BET	Brunauer-Emmet-Teller
bt	beam temperature
CD	Circular Dichroism
CVD	Chemical Vapor Deposition
DKP	Diketopiperazine
DTA	Differential Thermal Analysis
DTG	Differential Thermal Gravimetry
DTGS	Deuterated Triglycine Sulphate
ESI	Electrospray Ionization
FA	Formic Acid
FTIR	Fourier Transform Infrared
FWHM	Full Width at Half Maxima
Gly	Glycine
HF	Humidity Fluctuations
HR-MS	High-Resolution Mass Spectrometry
ICDD	International Center for Diffraction Data
IWI	Incipient Wetness Impregnation
MCT	Mercury Cadmium Telluride
NFS	Nearly-free Silanol
NMR	Nuclear Magnetic Resonance
RNA	Ribonucleic Acid
rt	room temperature
SMA	Surface Mixed Anhydride
SSA	Specific Surface Area
TF	Temperature Fluctuations
TGA	Thermogravimetric Analysis
WD	Wetting Drying
XRD	X-ray Diffraction

## General introduction

The interactions of molecules with surfaces play a significant role in many fields such as heterogeneous catalysis, biomedical applications, etc. Among the huge variety of molecular events that involve the interactions with surfaces, the catalytic formation of CO-NH bonds (amides and peptides) through the condensation of unactivated reagents in mild-conditions, when adsorbed on nanomaterials, is garnering interest, owing to its high importance in fine chemistry. This reactivity may also explain the formation of (bio)macromolecules such as oligopeptides from amino acids in prebiotic conditions, a phenomenon that constituted a crucial step in the development of the complexity in the origins of life.

The selection of silica as a catalyst for the amide bond formation and its extension to polymerization is of potential interest due to its high availability, low cost, and ubiquitousness in the crust throughout Earth's history.

However, the polymerization reaction of amino acids on silica, and especially on amorphous silicas, is still poorly understood. Studies strive to understand the mechanism and kinetics of the reaction, the role of adsorption sites, and the parameters that govern the type of products obtained under different environmental conditions.

In this thesis work, we will investigate the key surface sites for the polymerization reaction from unactivated amino acids on amorphous silica, the mechanism of adsorption, polymerization, as well as self-assembly of the peptide chains. We will also study how the surface of silica, the presence of water, and the environmental conditions employed affect the product of the polymerization reaction.

This research work was conducted in a joint PhD- or "cotutelle" thesis- between the Department of Chemistry at the University of Torino and the Laboratoire de Réactivité de Surface (LRS) at Sorbonne University.



The manuscript is divided into five main chapters. Chapter I provides a general overview of the amide bond formation reaction, the methods for its implementation, its applications and extension to form peptides which are key players in the complexity of origins of life. A detailed explanation is provided on the world of silica (types, features, structures, ways of synthesis, and applications). Then, the state of the art of biomolecules/silica systems prepared by adsorption and oligomerization of unactivated amino acids is elaborated to identify the challenges still faced on this topic.

Chapter II contains the technical part of the thesis work. It provides a description of the principles of all the characterization techniques employed in this research followed by an explanation of the procedures used to carry out the measurements on the tested samples. This chapter also provides a general overview of the derived results from each technique. The experimental procedures of thermal treatments of the samples, and the different ways of adsorption of amino acids on silica from gas and liquid phases are also described. Note however that this chapter will not illustrate the conditions of preparation for further samples used to study specific tasks; that will be explained in the respective following chapters where they are developed.

Chapter III intends to study the role and type of the crucial surface sites for the polymerization reaction on amorphous silica. This chapter starts with a brief bibliographic reminder on the progress done so far in literature, then presents the preparation of the samples studied for this task and the characterization techniques employed. It then focuses on the elaboration of a detailed mechanism for the adsorption and polymerization reaction of gas-phase glycine on silica and a description of their self-assembling behavior upon contact with water vapor.

Chapter IV focuses on the thermal condensation of gas-phase glycine in fluctuating silica environments, as a model of prebiotic environments. Firstly, this chapter provides concise reminders on the difference between various prebiotic environments and highlights the

importance of the biomolecules-silica-water interface for the complexity of the origins of life. Then, the preparation of the samples tested for this task is exposed in detail before presenting the results of the characterization techniques used to study the efficiency and kinetics of the polymerization reaction based on the environmental conditions adopted. In addition, the secondary structures and the structural dynamics of the peptide chains are also elaborated. A mechanism is suggested for the prolongation of the peptides upon further monomers feeding with particular attention given to the resistance of the self-assembled chains upon an extended polymerization reaction.

Chapter V broadens the scope of the systems used in the previous two chapters. This chapter starts with an overview of some research works that studied the polymerization of amino acids on silica surfaces and ended up with different outcomes regarding the nature of the reaction product. We describe the systematic variation of the support surface, thermal pretreatment, and procedure of glycine deposition (from the gas phase, or from an aqueous solution). Then, the main results concerning the parameters that govern the formation of linear peptides as opposed to cyclic dimer (DKP) on silica are discussed.

This manuscript ends with a summary of the main conclusions reached during this research work in addition to suggested perspectives for future works.

# I. Chapter I: Literature review



Amide bond formation is considered to be among the most important reactions in organic chemistry since the amide linkages represent the key chemical connections of proteins, which are one of the fundamental components of living matter. Moreover, these linkages are the basis of widely used (bio)synthetic polymers as well as pharmaceutical active compounds. However, the reaction is still riddled with inherent limits related to its wastefulness and expense, which require continuous improvements in the chemical approaches for amide formation to be developed and optimized.<sup>1</sup> In this chapter, some of the various chemical routes and applications of amide bond formation are presented. We are particularly interested in the amide/peptide bond formation for peptide synthesis on mineral surfaces and especially on silica surface which is of high interest in the prebiotic chemistry and pharmaceutical fields. Here we will summarize the advancements achieved and challenges still encountered for this reaction on silica surface. This chapter ends with an outline of the objectives and methodology of the present thesis.

## **I.1. Catalytic methods for direct amide bond synthesis**

Amide bond formation involves the condensation between a carboxylic acid and an amine group resulting in the release of one equivalent of water. This reaction is challenging due to the competing acid-base reaction upon mixing a carboxylic acid with an amine. In 2007, the American Chemical Society Green Chemistry Institute voted “amide formation avoiding poor atom economy reagents” as the top challenge for organic chemistry.<sup>2</sup> In fact, chemical routes used for amide bond synthesis are among the most widespread reactions in organic chemistry, yet they are often highly inefficient. The conventional chemical route followed in the industry for the synthesis of amide bond is through the addition of coupling reagents, base, and solvent for the activation of the carboxylic acid. This is followed by a nucleophilic attack by the free amine to give a new amide bond (Figure I-1).<sup>3-5</sup> This traditional way relies on the use of an

activating agent; it may occur in mild reaction conditions and result in good yields but requires stoichiometric amount of activating reagents: consequently, it generates one equivalent of waste per product molecule formed, resulting in an overall low atom economy. Beside the toxicity and the high cost of the coupling agent used, the process adopted for waste removal is also expensive. In the absence of such coupling reagent, the reaction of the carboxylic acid and the amine simply results in the formation of a carboxylate-ammonium salt, rather than a product involving an amide bond. In particular, in the presence of water (and thus of course in aqueous solutions), an internal proton transfer results in the formation of zwitterionic amino acids. The thermodynamics of the amide bond formation reaction is unfavorable in water because it is accompanied by the liberation of one water molecule.

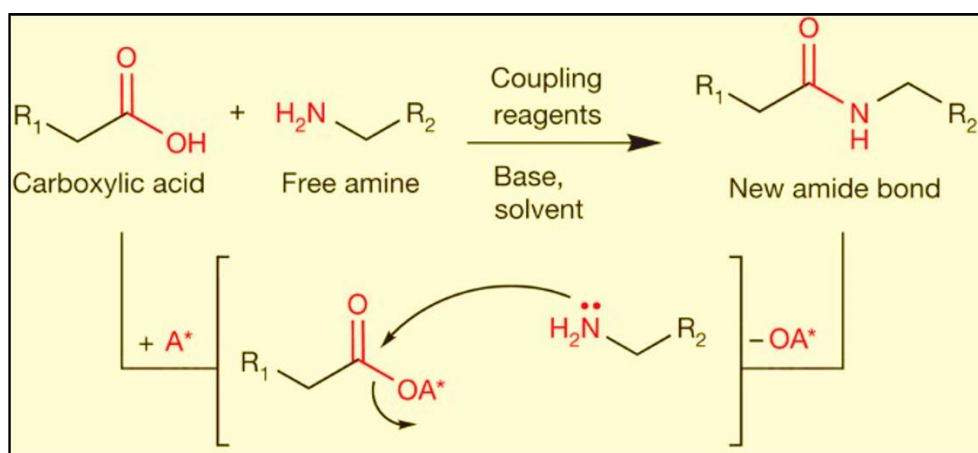


**Figure I-1:** Schematic representation of a conventional pathway for amide bond formation using coupling reagents where A\* represents an activating agent and R<sub>1</sub> and R<sub>2</sub> are organic moieties.<sup>1</sup>

Therefore, the development of clean, catalytic, and low-cost synthetic routes with a good atom economy for amide bond formation has been highly pursued.<sup>2</sup> Among the different new methods involving the use of non-activated carboxylic acid and amine proposed in the literature,<sup>6,7</sup> some are reported in the following parts. We will focus on the use of two main types of catalysts: enzymes or biocatalysts, and Lewis acids including boron-based and metal-

based catalysts. Of course catalysts do not modify the reaction thermodynamics and amide formation will only be favored in conditions of low water activity.

### **I.1.1. Biocatalysts**

Biocatalysts or enzymes represent nature's own catalysts involved in a huge variety of reactions including amide bond formation. Enzymes are usually characterized by a high selectivity toward crucial biological processes at ambient temperature, which makes them desirable for synthetic processes.<sup>7</sup> Lipases represent the most common enzyme class adopted for the synthetic formation of amide bond from carboxylic acids and amines.<sup>8,9</sup> However, enzyme-based catalysts adopted in amide bond formation present several limitations. One of the drawbacks is that the range of substrates is often limited when using a biocatalyst, in addition to a long reaction time in the order of days.<sup>7</sup>

### **I.1.2. Boron-based catalysts**

Boron-based compounds have been used as catalysts in the direct amidation of unactivated carboxylic acid and amine since the 1960's.<sup>10</sup> Boronic acids and their derivatives, characterized by their extremely low cost, are successful candidates as catalysts for amide bond synthesis,<sup>11-14</sup> including industrial processes at large scale.<sup>15</sup> This type of catalysts show a high stability in the presence of water along with a fairly broad substrate scope. Besides their high yields, boron-based catalysts can be recycled without loss of activity. However, the main drawback is their lack of catalytic activity when using more challenging substrates such as amino acids to form peptides which is to date limited to dimerization. Moreover, while the catalyst itself is stable towards water, water removal remains crucial to drive the reaction forward, which might cause trouble when dealing with large-scale applications. One additional drawback is that boron-based catalysts usually require the use of elevated temperatures which can directly result in racemization and limited substrate scope.<sup>6,7</sup>

### **I.1.3. Metal-based catalysts**

Although underexplored for a long time, the use of metal-based catalysts for the direct amidation of carboxylic acids and amines has attracted a great attention in the last years; both homogenous and heterogenous catalysts protocols are available.

On the one hand, the (limited) literature on homogenous metal-based catalysts<sup>16–20</sup> has shown that transition metals represent the most attractive class of catalysts to be used under homogenous conditions. Generally, using homogeneous metal-based catalysts requires high to fairly high temperature conditions which can affect some substrates. When using homogeneous catalysts, removal of water during the reaction is necessary to reach high conversion.

On the other hand, following a heterogenous catalyst approach has shown more benefits compared to the homogeneous one. Heterogeneous catalysts in the form of noble metal nanoparticles,<sup>18</sup> or common oxides such as SiO<sub>2</sub>, TiO<sub>2</sub>, and ZnO, exhibit promising efficiency toward amide bond formation reaction.<sup>21–24</sup> Heterogenous catalysts have been used in a large number of experiments dealing with the investigation of the origins of life, and studying peptide formation from amino acids as an application for amide bond formation.<sup>25</sup> In particular oxides, readily available and at low cost, effectively catalyze the amide bond formation reaction without the production of toxic by-products. These materials of good atom economy show a large substrate scope. Moreover, using heterogenous catalysts for amide bond synthesis makes possible the separation of the catalysts from the reaction medium which is not the case when using homogeneous ones. In addition, these catalysts show an excellent recyclability with a negligible decrease in activity after many cycles of reaction.<sup>7</sup>

## **I.2. Applications of amide bond formation**

Amide functionality represents one of the most fundamental chemical building blocks found in nature, such as in peptides. They also represents key chemical connections in widely

used agrochemicals, and industrial materials such as synthetic polymers, detergents, and lubricants.<sup>1</sup> Over the last decades, amide bond synthesis has gained a position of importance in industrial medicinal chemistry as well as in prebiotic chemistry.

### **I.2.1. Industrial medicinal chemistry**

In the pharmaceutical industry, amide bond formation is crucial and represents one of the most frequently performed reaction, especially for the synthesis of drug candidates.<sup>26,27</sup> Amide linkages have constituted the main structural pattern for best-selling active pharmaceuticals ingredients (APIs) and major marketed drugs (Figure I-2). For example, Atorvastatin, the top-selling drug worldwide since 2003, used in order to block the production of cholesterol, contains an amide bond. This is also the case for Paracetamol that treats fever and moderate pain. In addition, amide bond is the main structural group for Amoxicillin, an antibiotic medication adopted to treat a significant number of bacterial infections; as well as for Methotrexate, a chemotherapy agent and immune-system suppressant used to treat cancer and other autoimmune diseases.<sup>3,28</sup> Most of the synthetic approaches of amide bond formation included in these products suffer from a poor atom economy when dealing with large scale operations, due to synthetic routes that rely on the use of coupling reagents, organic solvents, and large amount of reagents.<sup>3</sup> Big concerns have been raised in the last decades to find green, inexpensive, and non-toxic alternatives for amide bond formation for large scale production to dramatically reduce waste generation.<sup>26</sup> Indeed, the development of catalytic processes for amide bond formation has started to be implemented on large scale, including the use of boron-based catalysts,<sup>29,30</sup> enzymes,<sup>7</sup> and homogeneous-based catalysts such the use of ruthenium complexes.<sup>31</sup> Moreover, heterogenous-based catalysts that employ titanium compounds,<sup>32-35</sup> alumina,<sup>36</sup> silica,<sup>21,24,37</sup> etc. could also be very promising alternatives to displace the traditional, toxic, and expensive stoichiometric approaches in the pharmaceutical field.<sup>38,39</sup>



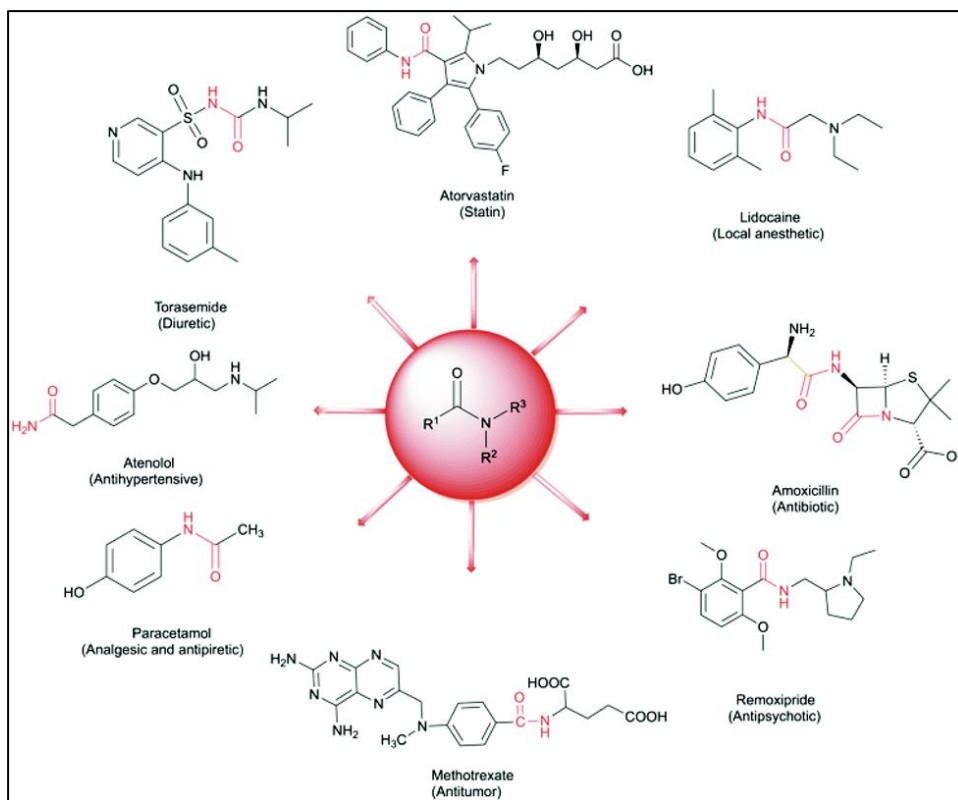


**Figure I-2:** Examples of drugs involving an amide bond linkage.<sup>28</sup>

### I.2.2. Prebiotic chemistry

The first applications for amide bond formation are the syntheses of small molecules, but the extension of these applications to include the formation of peptides or biopolymers, the key players in the origin of life, from small building blocks like amino acids is highly valuable.<sup>40–44</sup> The formation of peptides almost certainly takes place in two general steps: an initial formation of amino acids or related monomeric building blocks, followed by their ligation or polymerization through amide bonds to form peptides.

#### Origin of amino acids

Before highlighting the critical importance of peptides in the quest of origin of life, it is important to consider first the mechanism by which amino acids could have been produced.  $\alpha$ -amino acids, the building blocks of peptides and proteins, consist of amino ( $-\text{NH}_2$ ) and carboxyl

(-COOH) groups together with a side chain specific to each amino acid.<sup>44</sup> The Miller-Urey experiments carried out in the 1950s are the first and widely considered as the most important attempts at abiotic amino acids synthesis under simulated Early Earth conditions.<sup>45</sup>

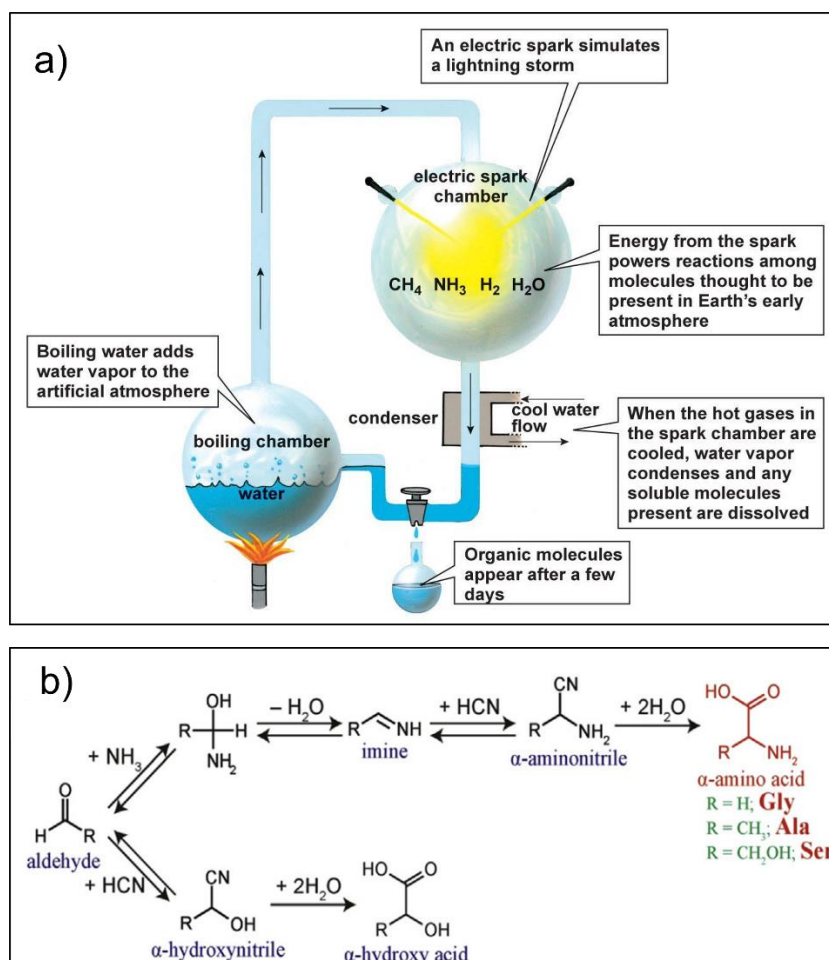


**Figure I-3:** a) Schematic drawing of the spark-discharge apparatus used in the Miller-Urey experiments; b) schematic representation of the Strecker reaction mechanism for abiotic synthesis of amino acids (and hydroxy acids).<sup>44</sup>

The experiment (Figure I-3, a) consists in the activation with an electric discharge of a highly reducing gas mixture of  $\text{CH}_4$ ,  $\text{NH}_3$ , and  $\text{H}_2$ , supposedly representative of the primitive atmosphere. These conditions resulted in the generation of amino acids in rather high yields (up to 4.7% of the initial carbon) including Gly, Ala, and Asp along with other organic molecules.<sup>45,46</sup> The results obtained have supported the theory of “Prebiotic Soup” suggested by Oparin.<sup>47</sup> The extracts from the Miller-Urey experiments were re-analyzed recently<sup>48–50</sup> and

the outcomes revealed the detection of 23 amino acids, i.e., more than the five ones originally reported. Subsequently, other experiments were performed to synthesize amino acids through procedures involving various types of energy sources such as UV,<sup>51,52</sup> X-ray,<sup>53,54</sup> and proton irradiation.<sup>55,56</sup> In addition to the terrestrial synthesis of amino acids, more than 80 different amino acids, including at least eight proteinogenic ones, have been found in meteorites.<sup>57</sup> Moreover, Gly has been also observed in interstellar gas clouds.<sup>58,59</sup> Its presence has been confirmed in the Stardust's Wild 2<sup>60,61</sup> and Rosetta's 67P<sup>62</sup> comets as well as in several CC meteorites.<sup>63–65</sup>

The Strecker reaction (Figure I-3, b) has been a key mechanism for the abiotic formation of amino acids as it is able to generate both amino acids and hydroxy acids on the prebiotic earth.<sup>66</sup> It involves a first gas phase production of HCN and aldehyde with a subsequent formation of  $\alpha$ -aminonitriles through the condensation of the formed molecules with NH<sub>3</sub>. This is followed by a hydrolysis of the nitrile group to a carboxyl one, yielding  $\alpha$ -amino acids.<sup>41</sup>

### **Peptides: central players for the origin of life**

The polymerization of amino acids to peptides requires the formation of amide bonds between these small building blocks accompanied by the removal of water molecules from the amino and carboxyl groups of the reaction partners. According to the literature, carrying this reaction on heterogenous systems involving mineral surfaces (possibly together with metal cations) acting as catalysts and drying platforms, represents an efficient pathway that has probably occurred on the Primitive Earth.<sup>25,67–72</sup> In fact, polymers represent the most important molecules in biochemistry: they represent a qualitative step in the transition from non-living matter to life. Besides their uses to store and transmit heredity information (nucleic acids), biopolymers also have an important functional role as they are the root cause of phenotypic behaviors at the molecular and cellular levels (proteins). Several reviews<sup>41,73–78</sup> have suggested that the origin of life must have involved cooperative interactions among the different classes

of biomolecules (Figure I-4) including proteins, nucleic acids, carbohydrates, lipids, etc. with proteins being the hubs of interactions. Understanding the origin of proteins could lead to important insights in biology and prebiotic chemistry and solve some of the longstanding problems in the origin of life. Among the different chemical processes that involve peptides and could have contributed to early chemical evolution,<sup>40</sup> several studies have highlighted the crucial role of proteins in origin of life that extends to RNA world. The ribosome structure itself includes evidence of coevolution between RNA and proteins.<sup>79,80</sup> In fact, proteins are involved in every step of RNA synthesis, processing, and functions.

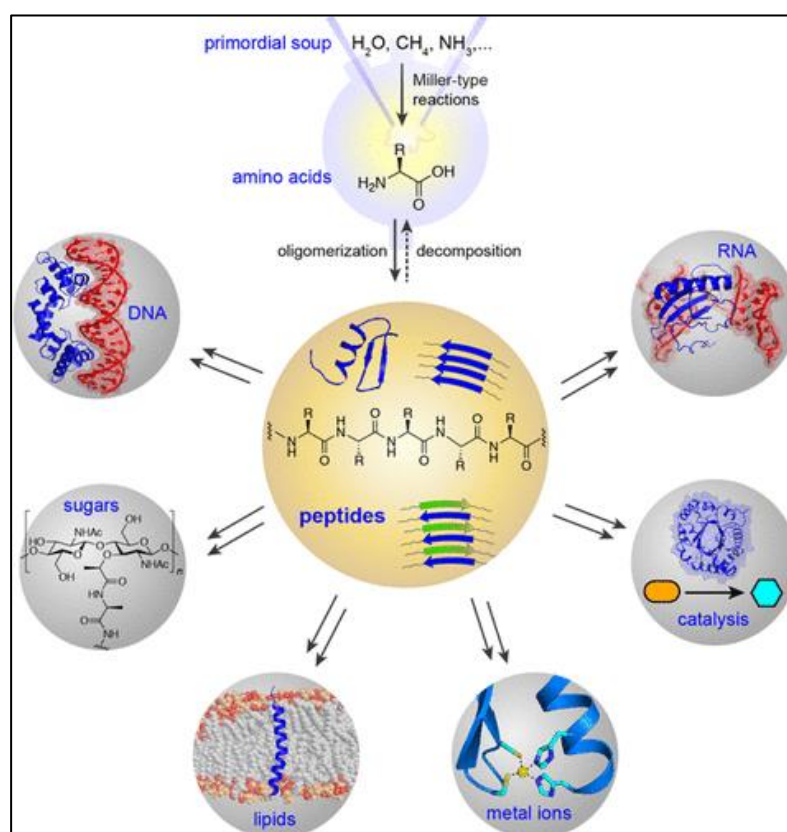


**Figure I-4:** Schematic representation showing the central role of peptides in molecular interactions and functions in extant life. Similar interactions could have occurred between prebiotic peptides and other molecules.<sup>40</sup>

## **Self-assembly of peptides**

Peptides self-assembly provides a crucial pathway for the emergence of functions in prebiotic chemical evolution.<sup>81-83</sup> In fact, the self-assembly behavior is one of the characteristics of peptides, a phenomenon observed even with short peptides.

Short peptide self-assemblies of different stability could be coupled with various remarkable physical properties and functions. For instance, spider silks are mainly composed of highly repetitive sequences of Gly and Ala amino acids that assemble into amorphous and crystalline phases to provide the silk its overall tensile properties.<sup>84</sup> Moreover, simple peptides can also self-assemble to act as membranes<sup>85,86</sup> or to drive the formation of coacervate droplets; both phenomena can compartmentalize organic molecules,<sup>87</sup> compartmentalization being one of the defining features of life. In addition, peptide assembly can result in the generation of catalytic properties.<sup>83</sup> Such diverse functions exhibited by self-assembled peptides result in selective advantages for molecular networks involving peptides.

### **I.3. Amide/peptide bond formation on mineral surfaces**

#### **I.3.1. Challenges in the synthesis of peptides from amino acids**

The extension of the amide bond formation reaction to include the formation of peptides would be highly valuable. The polymerization of amino acids to form peptides (Figure I-5) is in fact a condensation reaction that involves the removal of water molecules. As a consequence, peptide synthesis in water is a thermodynamically unfavorable process (in addition to being kinetically slow). This means that its standard Gibbs free energy of reaction is significantly

positive and therefore its equilibrium constant  $K$  is very low.<sup>88,89</sup>

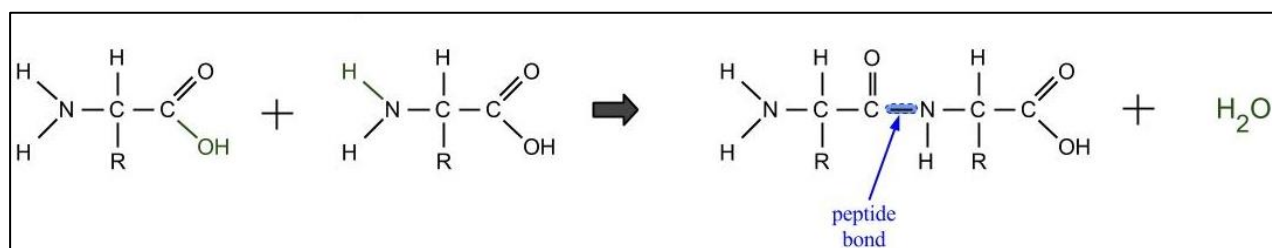


**Figure I-5:** Scheme representing the condensation reaction of peptide bond formation between two amino acids

For instance, the dimerization of Gly, the simplest amino acid, carried out in water at room temperature and neutral pH to form dipeptide (GlyGly) has a standard Gibbs energy of + 14.84 kJ·mol<sup>-1</sup> with an equilibrium constant  $K$  of  $2.51 \times 10^{-3}$ .<sup>90</sup> This value implies that less than 0.01% of Gly is converted into GlyGly unless the initial concentration of Gly is extremely high (> 100 mM). Similar results were presented in another research work dealing with the polymerization of amino acids.<sup>75</sup> Therefore, conducting a polymerization of amino acids in aqueous solution will only yield ridiculously small amounts of polypeptides. For instance, considering an average value for the free enthalpy for peptide bonds formation of +10.45 kJ·mol<sup>-1</sup>, it is found that the equilibrium concentration is  $2.6 \times 10^{-30}$  and  $1.49 \times 10^{-38}$  mol·L<sup>-1</sup> in the same solution for a 14-mer and 18-mer respectively, which is about one molecule per 100 km<sup>3</sup> of highly concentrated primordial soup for this solution.<sup>91</sup>

Several solutions were proposed in literature in order to overcome this difficulty including salt-induced peptide formation,<sup>92-94</sup> hydrothermal synthesis,<sup>95</sup> impact polymerization,<sup>96,97</sup> polymerization by coupling to metaphosphate hydrolysis,<sup>98</sup> and polymerization in the adsorbed phase involving heterogeneous systems that include mineral surfaces and metal cations.<sup>68-71,99,100</sup> However, it has been argued that the occurrences of these suggested mechanisms, except the last one, on the primitive earth were unlikely or had at most only a marginal probability to take place in specific locations.<sup>44</sup> Therefore, our concern will be focused specifically on the

adsorption and polymerization of amino acids on surfaces resembling the mineral ones as they were likely present on the early earth surface, mostly silicates, oxides, and sulfides. Adsorption of amino acids on reduced metal surfaces will also be excluded despite the availability of significant information on the topic since reduced metals do not represent likely candidates for prebiotic chemistry and their reactivity is quite different from the one of oxide surfaces.<sup>101</sup>

### **I.3.2. Role of the mineral surfaces in the polymerization reaction**

Over 50 years ago, Bernal<sup>102</sup> suggested that mineral surfaces have played a crucial role in the chemical evolution of life, acting as promising locations for the transition from chemical geochemistry to biochemistry.<sup>103</sup> Bernal argued that increasing the local amino acid concentration by adsorption would automatically favor the polymerization in the adsorbed phase. However, this would experimentally require an impossibly high concentration of amino acids in the adsorbed phase. Thus, another explanation was obviously required. In 1991, de Duve and Miller<sup>104</sup> proposed, based on a theoretical analysis that in order for a dimer to be formed on the surface, its free energy of adsorption should be more negative than that of the two monomers reactants and subsequently, as the peptide chain becomes longer, it would strongly and irreversibly adsorb on the surface. This was confirmed by Hill et al.<sup>105</sup> regarding the increase in the free energy of adsorption as a function of the oligomers length. Experimentally, Gerstner<sup>106</sup> observed that the Gibbs energy of each additional monomer unit bonded to the surface remains approximately constant, so that the global Gibbs adsorption energy would indeed increase linearly as a function of polymer length.

It is only 60 years after Bernal's hypothesis that the proposition of the polymerization of amino acids through increasing K in the adsorbed phase was experimentally tested by the work of Marshall-Bowman et al. in 2010<sup>107</sup> where they tried to compare the Gly equilibrium polymerization in aqueous solution using different minerals with the same reaction in a homogeneous solution. They deduced that there is no significant difference of K, invalidating

the hypothesis of a polymerization favored by preferential polymer/surface interaction. And yet in the meantime successful polymerization of amino acids had been demonstrated on several mineral oxide surfaces,<sup>108-110</sup> including silica.<sup>99,111-113</sup> It should be noted that all successful instances involved the use of a drying step, often in a series of wetting-and-drying (WD) cycles.

In fact, the thermodynamics of the surface-induced amino acids polymerization can be simply explained through the role of water based on Le Châtelier's principle that states that the removal of a reaction product automatically drives the reaction in the forward direction. In other words, eliminating water by drying will drive the amino acids condensation equilibrium to the right and favor the polymerization of peptides, and that can easily be done when amino acids are supported on silica.<sup>114</sup>

Then, if the thermodynamic challenge of the polymerization reaction can be simply solved by going through a drying step, does the mineral surface remain indispensable for the reaction? Is the adsorption of amino acids on minerals important for origin of life?<sup>115</sup>

In fact, several research works have shown that bulk amino acids can polymerize without the presence of any mineral.<sup>116,117</sup> However, in the absence of any mineral surface, such reactions takes place at significantly higher temperatures than when monomers are deposited on the surface (i.e. 240 °C for bulk Gly instead of 150 °C for Gly deposited on silica). Bulk polymerization is therefore less interesting from a prebiotic chemistry point of view, as the high temperatures can cause a severe degradation of biomolecules. Thus, mineral surfaces do play an important role: they have a catalytic effect as they increase the reaction rate at a given temperature; they indeed play the role that is now devolved to enzymes in living cells. In order to ensure an efficient catalysis, a good catalyst must interact strongly enough with the reagents in order to activate them but not too strongly in order to prevent them from being trapped in the formation of stoichiometric compound. This highlights the importance of studying the biomolecules/surface interaction that will be undertaken in this thesis work.



The most relevant situation for prebiotic chemistry is probably when biomolecules are adsorbed from aqueous solutions.<sup>118-125</sup> However, results obtained by adsorbing amino acids from the gas phase can also be very significant, either at a fundamental level for elucidating the influence of particular adsorption modes, or for confirming the reaction pathway of the adsorbed amino acids when the water activity is decreased through drying (such as through the exposure to the sun under prebiotic conditions).<sup>25,88,112,126-128</sup> More complicated procedures could also be studied by adopting fluctuating environments<sup>108</sup> involving successive wetting and drying (WD) cycles which can serve to simulate in the lab natural prebiotic variations of the experimental conditions that may have occurred on the prebiotic earth such as daily fluctuations of temperatures and seasonal fluctuations of humidity (by rain or exposure to tides). All these different environmental conditions for polymerization reaction will be tested in this thesis while studying the biomolecules/surface interactions.

#### **I.4. The world of silica**

Biomolecules/silica interactions have garnered much interest in research works<sup>129,130</sup> due to many reasons. First, silica represents the most abundant component of the Earth's crust, of which oxygen and silicon represent 45.5 and 27.2% respectively, and that manifests in the occurrence of a large variety of silica and silicate materials.<sup>131</sup> Nowadays, the interactions between these materials and living matter is pervasive.

Silica already represented an ubiquitous mineral in the crust when our planet was devoid of life. Figure I-6 represents the timeline of early Earth involving the key steps for life evolution starting from initial sterile conditions, through the early Hadean era characterized by a high meteorite bombardment, to the rise of atmospheric oxygen during the Proterozoic era. Between these two events, a large impact between 4.53 and 4.45 created the Moon. Subsequently the first reducing atmosphere was created by outgassing of the mantle. Variations in oxygen

fugacity resulted in the formation of a significant amount of CO in the high temperature atmosphere while the cooling of the atmosphere lead to the stabilization of the CH<sub>4</sub> and engendered H<sub>2</sub>O to condense and form the first ocean at c.a. 4.4 Ga. As a consequence of these events, silica started to accumulate in a worldwide alkaline ocean where silicate polymerization was pervasive, causing silica-organic interactions in the Hadean.<sup>132</sup> The silica input that increased in the early oceans<sup>133</sup> resulted in a global silicification of the early Archean seafloor as evidenced by the presence of abundant cherts and underlying strongly silicified volcanic rocks in Archean rocks such as the Barberton Greenstone Belt,<sup>134,135</sup> the Pilbara Granitoid Greenstone Belt,<sup>135,136</sup> and other exposure areas of Archean seafloor.<sup>137</sup>

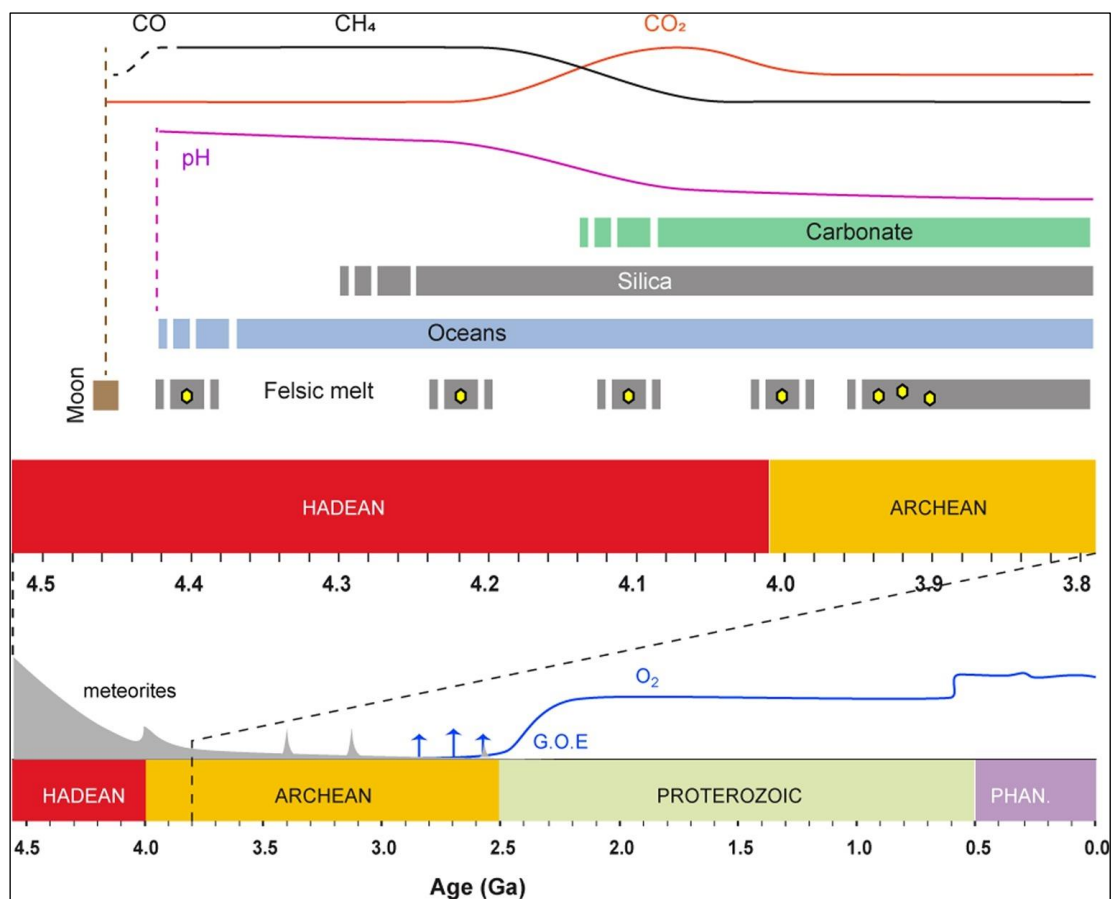


**Figure I-6:** Timeline of the early Earth, showing key steps for the evolution of life, from initial sterile conditions during high meteorite bombardment in the early Hadean to the rise of atmospheric oxygen during the Neoproterozoic (G.O.E., Great Oxidation Event).<sup>132</sup>

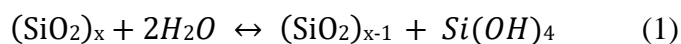
In addition, silica surfaces play a central role in various applications related to biomolecules interactions<sup>138</sup> such as in chromatography<sup>139</sup> used in pharmaceutical industry, in the analysis of pesticides, contaminants, drug residues in food and drinks, etc. Moreover, studying the interaction between biomolecules and silica is also beneficial to understand how artificial implants based on bioglasses constituted mainly of silica merge with bone tissue of the body.<sup>140</sup> Silica has also been adopted in the drug delivery field as it can be designed to encapsulate a specific drug which can be then released in situ through silica matrix degradation in order to enhance therapeutic effects and decrease toxicological side effects.<sup>141</sup> Interestingly, amorphous silica particles characterized by a high biocompatibility with cellular systems (contrary to the crystalline ones) have been considered good candidates for drug delivery systems.<sup>142</sup> High-surface amorphous silica has also proved to represent a good test material for prebiotic condensation studies which will be the main focus in this thesis.<sup>25,114,120,143,144</sup>

#### **I.4.1. Structure and features of silica samples**

Silica, in all its different forms and fields of application, has become one of the most studied material in the fields of chemistry, material science, physics, biomaterials, and engineering.<sup>129</sup> Silica, of chemical formula  $\text{SiO}_2$ , is a solid compound of high melting point (c.a. 1700 °C) with a density between 2 and 3  $\text{g}\cdot\text{cm}^{-3}$ . It is mostly found on Earth's crust as crystalline quartz. In the structure of most crystalline polymorphs<sup>1</sup>, a silicon atom is bound to four oxygen atoms, and each oxygen is bound to two silicon atoms, in such a way that the  $\text{SiO}_4$  tetrahedra are organized into periodic rings via siloxane bonds that bridge between two silicon centers<sup>145</sup> (see Figure I-7, a). Silica is subjected, within the biosphere, to continuous cycles of hydration and dehydration via reversible hydrolysis and condensations reactions as described in equation (1):

---

<sup>1</sup> With the exception of stishovite, which is only formed at very high pressures



Such weathering process engenders soluble silicic acid species  $\text{Si}(\text{OH})_4$  which form, upon dehydration, amorphous silica composed of 2- to 8-membered siloxane rings, usually in the form of nanoparticles. We will not dwell on the many crystalline silica polymorphs (including zeolites), but the high pliability of the Si-O-Si angle is the reason behind the large variety of all-silica materials.

The silica surface represents the region of contact and interaction with molecules from the “outside world” such as biomolecules; understanding it at the atomic level is of great interest.<sup>130</sup>

Both amorphous and crystalline silica surfaces are composed of siloxane bonds (Si-O-Si) present also in the bulk, and silanol groups that result from lattice termination in a water-rich medium – which is almost always the case on the surface of the Earth. Alternatively, they may be considered as the result of incomplete condensation of silicic acid units during the polymerization involved for silica synthesis.

Different types of silanol groups having different acidities (pKa values) and including isolated, geminal, vicinal, and H-bonded silanol groups are present on silica surface<sup>146</sup> (Figure I-7, b). Thus, the amorphous silica surface can exhibit different patterns of hydrogen bonding, charge, and hydrophobicity. Isolated Si-OH groups (labeled as  $\text{Q}^3$ ), sometimes also called terminal silanols, may be defined as those whose distance to their closest SiOH neighbors is higher than 6 Å so that they cannot be involved in any H-bond interactions. Isolated silanol groups may however establish H-bond interactions with biomolecules as both H-bond donors and acceptors. Pairs of silanols on tetrahedra sharing a common oxygen vertex and distant by 4-6 Å are called vicinal and are usually involved in weak H-bond interactions. Strongly H-bonded silanols correspond to silanol pairs that are separated by a distance between 2.5 and 2.8 Å.

In addition, geminal silanols represent two OH groups linked to the same surface silicon atom (labeled as  $\text{Q}^2$ ) to give  $\text{Si}(\text{OH})_2$ .

Surface radicals (Figure I-7, c and d) may also be present. The concentration of siloxane rings, silanols and radicals both on the silica surface and within the bulk depends on the synthetic conditions followed as well as the thermal and environmental exposure. Heating a highly hydrated silica surface at relatively high temperature results in the progressive condensation of surface silanol pairs involved in H-bond interactions to form siloxane rings  $(\text{SiO})_n$  of distinct nuclearity  $n$ , based on the condensed pair of H-bonded silanol groups.

Conversely, strained siloxane rings  $(\text{SiO})_{n=2,3}$  of 2- or 3- membered rings may undergo cleavage by water molecules present in the surrounding environments:<sup>147</sup> water molecules can break the Si-O-Si bridge to form a pair of H-bonded SiOH or vicinal pair which increases the number of silanol groups on the surface while decreasing the fraction of isolated ones (Figure I-7, e).

Studying the parameters that affect the formation, condensation, or cleavage of the functional groups of silica is of high importance since the hydrophilic/hydrophobic character of silica toward biomolecules is directly related to the density of siloxane and silanol groups. On a surface rich in SiOH groups (4-5 SiOH/nm<sup>2</sup>), molecules are adsorbed through H-bonding to groups of neighboring silanol sites, while on a surface less rich in SiOH (1-2 SiOH/nm<sup>2</sup>) which contains more siloxane rings due to dehydration, the hydrophobic character is dominating, driving the molecules to be adsorbed through dispersive interactions (or weak interactions with siloxane rings) rather than H-bonds with silanol groups.<sup>148,149</sup>

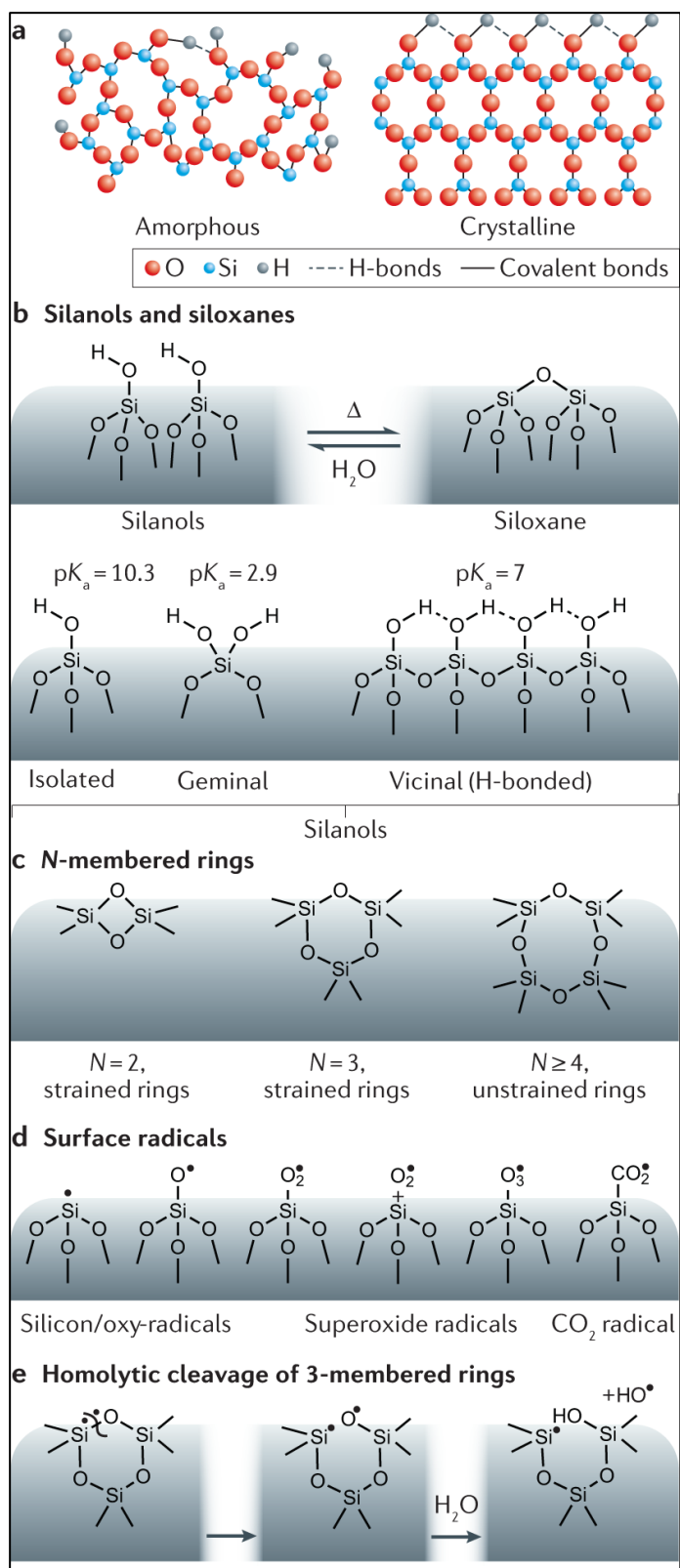


**Figure I-7:** Schematic representations of the framework and surface chemistry of amorphous and crystalline silica.<sup>130</sup>

## I.4.2. Synthesis of silica samples

Understanding the different ways to synthesize silica samples is key to unravel the complexity and variability of silica behaviors. Figure I-8 summarizes the timeline of the development of the syntheses of silica samples, some of which are detailed in the following sub-parts.

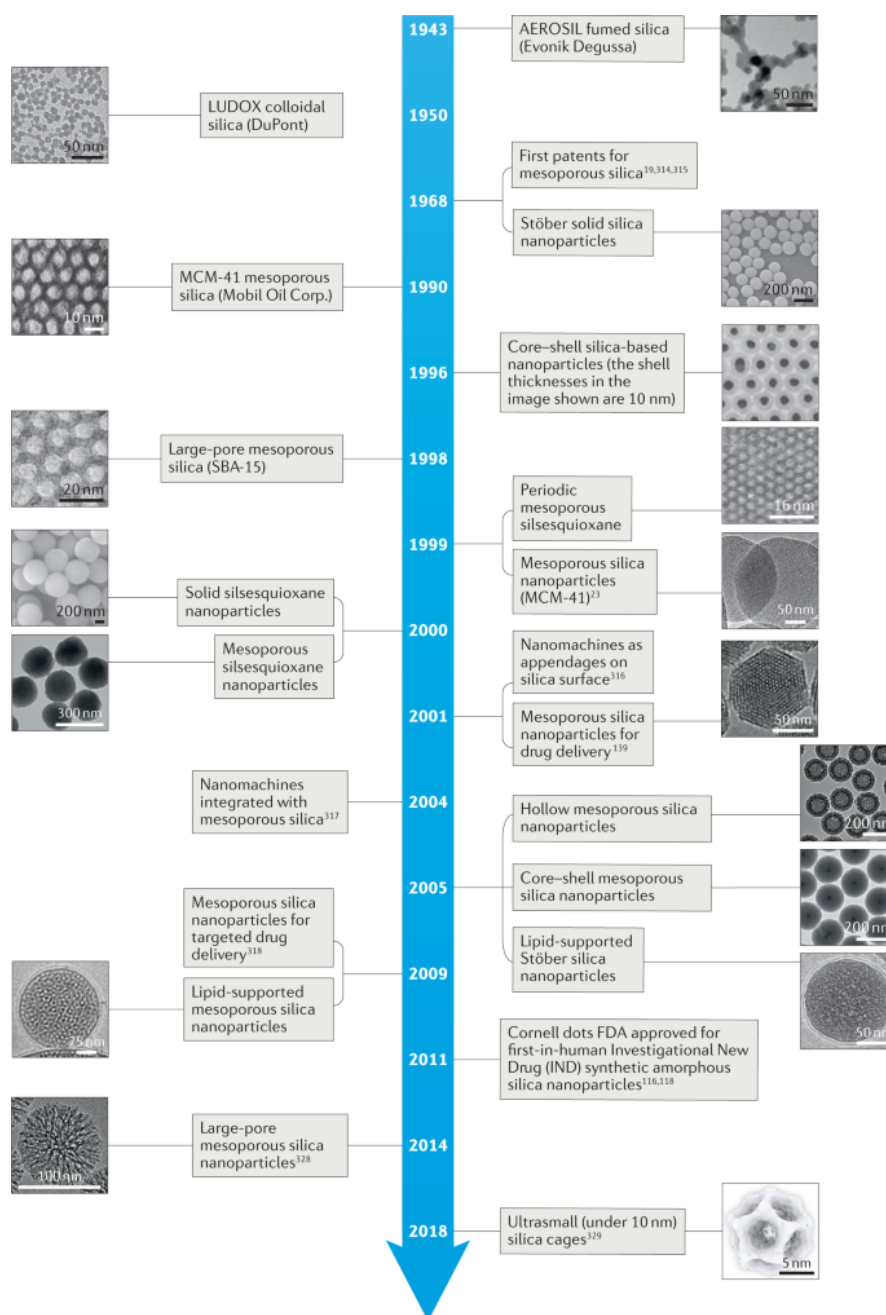


**Figure I-8:** Timeline of the development of the synthesis of amorphous nanoparticles.<sup>130</sup>

a) Fumed-silica synthesis:

In order to find an alternative for carbon black used in tire industry, Harry Kloepfer discovered in the 1930s the fumed silica (known as Cab-O-sil in the USA or Aerosil in Europe) by adopting a synthesis via flame pyrolysis of  $\text{SiCl}_4$  according to equation (2):<sup>150</sup>

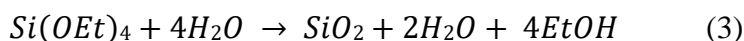


The process of flame pyrolysis consists of a heating at very high temperature in the range of 1200-1400 °C followed by a rapid thermal quenching. This involves the vaporization and hydrolysis of  $\text{SiCl}_4$  through in situ water production to form  $\text{Si}(\text{OH})_4$  that then polymerizes into  $\text{SiO}_2$  seeds. The latter start to grow into highly condensed and dense primary particles having a diameter of 5-50 nm. After that, they start to aggregate to form string-of-pearl-like morphologies of fractal dimensions.<sup>151</sup> The synthesis environment of the overall reaction that may contain up to 30 mol%  $\text{H}_2\text{O}$  results in a partial hydration of the prepared silica with a concentration of 2-3  $\text{SiOH}$  groups/nm<sup>2</sup>.<sup>152</sup> This is the type of silica that has been investigated in this thesis.

Doped fumed silica can also be formed through a simultaneous vaporization of metal halides (i.e.  $\text{AlCl}_3$ ,  $\text{TiCl}_4$ , etc.) with  $\text{SiCl}_4$  during the flame-pyrolysis process (Figure I-9, a).

b) Colloidal silica synthesis:

Colloidal silica including precipitated, Stöber, and mesoporous silica are used as adhesive, fillers, thickening and reinforcing agents, food additives, imaging agents, drug delivery vectors, etc.<sup>146,153-156</sup> They are typically prepared under basic conditions (pH 7-10) by a nucleation and growth mechanisms through the attack of a nucleophilic deprotonated silanol on a neutral silicate species. Monosized Stöber silica nanoparticles can be synthesized through hydrolysis of tetraethoxysilane in basic solutions of water and alcohol according to equation (3):





Stöber silica nanoparticles of diameters ranging from tens of nanometer to tens of microns with tunable surface areas ( $30\text{-}500\text{ m}^2\cdot\text{g}^{-1}$ ) can be formed by varying the concentration of water and ammonia in ethanol<sup>157</sup> (Figure I-9, b).

c) Mesoporous silica synthesis:

Besides fumed and Stöber silica, much effort has been devoted to synthesize highly porous and ordered silica with uniform pores larger than 2 nm in order to allow host-guest chemistry with large molecules and polymers. In 1992, Kresge et al.<sup>158</sup> discovered the first periodic mesoporous silica. It was shown that this type of silica can be prepared through self-assembly of cylindrical surfactant micelles and a silica precursor like tetraethyl orthosilicate (TEOS) which condenses to silica in the available space between the micelles, replicating their organization to form an ordered nanocomposite. Mesoporous silica is then obtained by the removal of the surfactant template<sup>159</sup> (Figure I-9, c). One example of these highly porous silicas that present pores with amorphous silica walls are the molecular sieves named M41S of very high specific surface areas ( $700\text{ m}^2\cdot\text{g}^{-1}$ ) and pore volumes. The pores are ordered in an hexagonal phase named MCM-41.

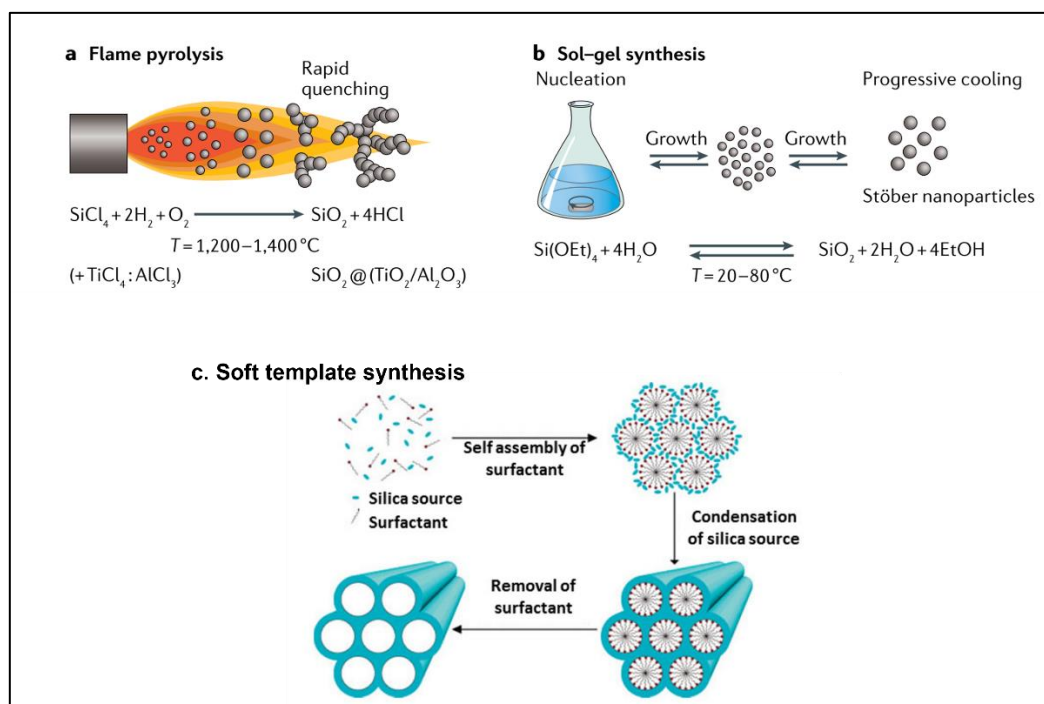


**Figure I-9:** Schematic representation of different synthesis routes for amorphous silica: a) flame pyrolysis, b) sol-gel synthesis,<sup>130</sup> and c) soft template synthesis.<sup>159</sup>

### **I.4.3. Amino acid polymerization on amorphous silica surface**

Polymerization of unactivated amino acids on amorphous silica surface to form peptides remains till today a difficult task as it still suffers from a lack of knowledge regarding the mechanism of the reaction, its kinetics, and the adsorption sites that are involved during polymerization. A number of investigations have been performed to study amide bond formation on silica both experimentally and theoretically.<sup>88</sup> Limiting ourselves to systems consisting in a single amino acid on amorphous silica, several teams have attempted to elucidate the amide bond formation using mainly NMR and IR spectroscopy techniques. One can mention here the work of Lopes et al.<sup>143</sup> and Kitadai et al.<sup>72</sup> about glycine, Guo et al.<sup>23,160</sup> about alanine, and lysine,<sup>161</sup> as well as Swanson et al.<sup>162</sup> related to histidine, and Rai et al.<sup>163</sup> focusing on leucine on silica, etc. In addition to the laboratory works, the application of computational modelling to biomolecules adsorption on silica was extensively reviewed in 2013.<sup>129</sup> Important insights have been provided by modelling Gly on silica by Ugliengo et al.<sup>24,164–170</sup> and Costa et al.<sup>171–173</sup>. Other workers have also studied the adsorption state of different amino acids on silica.<sup>174</sup> And more recently, Abadian et al.<sup>175</sup> have combined macroscopic (TGA, XRD) and spectroscopic (IR, NMR) techniques with molecular modelling by DFT to study the adsorption of leucine on amorphous silica.

Despite this large number of research works about amide bond formation, no full understanding of the mechanism and the products of the polymerization reaction has yet been reached, in part due to the fact that different amino acids are investigated by different scientific groups using different deposition and activation procedure, which makes the comparison of the results difficult.

In fact, the main results could be divided into two categories. On the one hand, several spectroscopic studies carried out by Lambert and co-workers<sup>89,114,120,143,176,177</sup> reveal that Gly

adsorbs on amorphous silica from an aqueous solution as a zwitterion which upon activation at 160 °C reacts to give the undesired cyclic dimer also known as diketopiperazine (DKP).

In contrast, in situ IR measurements of Martra et al.<sup>25</sup> who carried out the adsorption of Gly from the gas phase on amorphous silica, indicate that long oligomers are formed from a successive feeding of Gly vapor at the same temperature. The formation of linear oligomers on silica was also observed before by other research works using IR spectroscopy.<sup>67,99</sup>

Certainly, the outcomes obtained from these two different research groups are not inconsistent but they highlight the fact that different results may follow when adopting different adsorption procedures. This shows the importance of deeply studying the amino acid/silica interaction, the crucial adsorption sites, the mechanism, the parameters of adsorption and activation, etc. which will be the main task undertaken in this thesis work.

## **I.5. Thesis objectives and methodology**

Based on this review on amide bond synthesis and its extension to form peptides on oxide surfaces, and the recent advances obtained when carrying out this reaction on amorphous silica surface, understanding the reaction mechanism, kinetics, and the parameters that determine the product type has not been reached due to the complexity of the surface of amorphous silica. Studies have demonstrated that different conditions during the adsorption can heavily influence the product type and the efficiency of the reaction. Studying the surface chemistry of amorphous silica during the polymerization reaction could represent a central key to understand the biomolecules/silica interactions important for prebiotic chemistry and material science. Needless to say, glycine having both terrestrial (among the products of Miller experiments) and extraterrestrial origins (found in many comets and meteorites) enjoys a central position among all other amino acids in prebiotic chemistry. This simple amino acid has been

considered a reference molecule in a large number of experimental and theoretical investigations for the matter of biomolecules/silica (mineral) interactions.

In this context, the objective of this thesis is to take advantage of the extant knowledge from theoretical and experimental studies about amino acid adsorption on amorphous silica described above to go further in the elaboration of the role of silica and the parameters that affect the efficiency of the polymerization reaction. The results we have obtained have been summarized in three research papers that are reproduced here. Their purpose is:

1. In chapter 3: To elucidate the reactivity of Gly from the vapor phase on amorphous silica under controlled atmosphere with and without a prior activation of the surface with a carboxylic molecule. The target is to investigate the type of adsorption sites crucial for monomers activation and polymerization, to propose a mechanism for oligopeptide chains prolongation and to understand their behavior upon contact with water vapor.
2. In chapter 4: To study the polymerization reaction in fluctuating silica environments under both temperature and hydration changes. The target is to study the effect of these conditions on the efficiency of the reaction and to propose a mechanism of the prolongation of peptide in wetting/drying cycles. Furthermore, we have also investigated the secondary structure as well as the structural dynamics of the peptides for an extended duration of polymerization.
3. In chapter 5: To investigate the parameters that govern the formation of linear peptides or of the cyclic dimer DKP on silica surfaces upon Gly adsorption from both gas and liquid phases. The aim is to determine the role of special surface features of amorphous silica in obtaining linear peptides over a cyclic product when adopting the Gly adsorption from the gas phase. Furthermore, to elucidate the role of water molecules and specific surface area of silica when adsorption from liquid phase is adopted.

To achieve our purpose, different characterization techniques were employed to characterize in detail the biomolecules/silica systems. They will be presented in chapter 2 where the equipment and the experimental conditions for the characterization techniques, in addition to the procedures of amino acid adsorption from gas and liquid phases as well as hydration and washing are elaborated.

## II. Chapter II: Technical part



## II.1. Characterization techniques

The aim of the present chapter is to provide a rigorous explanation of the different characterization techniques employed in this thesis work to analyze the different silica and biomolecules/silica systems. After explaining each technique used, the procedures followed to treat the silica samples as well as to adsorb glycine from both gas and liquid phases will be elaborated. The methods and procedures adopted to prepare additional samples to study specific tasks will be explained in the respective chapters where these materials are analyzed.

### II.1.1. Spectroscopies

#### II.1.1.1. Fourier transform infrared spectroscopy

##### Principle of the technique:

Fourier transform infrared (FTIR) spectroscopy is a vibrational spectroscopy technique that can provide information about characteristic molecular vibrations from which interesting structural information about materials can be deduced. It is considered a universal and powerful technique that can be used to analyze solids, liquids, gas, powders, and polymers and give useful information about organic and inorganic compounds. FTIR spectroscopy is a fast, non-destructive, and relatively non-expensive technique and requires little or no sample preparation. It provides a huge amount of information from the peak intensities, positions, widths, and shapes in the spectrum of a sample.<sup>178</sup> The infrared (IR) range can be divided into three main regions: the near-infrared (14000-4000  $\text{cm}^{-1}$ ) where overtone and combination modes of molecular vibrations are observed; the mid-infrared (4000-400  $\text{cm}^{-1}$ ) which is the most frequently used region for chemical analysis where the fundamental vibrations and the associated rotational-vibrational structures are seen; and the far-infrared region (400-10  $\text{cm}^{-1}$ ) that is useful for molecules containing heavy atoms such as inorganic and metal-organic compounds.<sup>179</sup>

All molecules have a set of frequencies at which they vibrate according to vibrational modes that are classified into three types: stretching, bending, and torsional modes.<sup>180</sup> In order for a vibration mode to be active in the infrared, it should produce a change in the dipole moment of the molecule. In that case, when the frequency of the radiation matches the vibrational frequency of the molecule, the radiation can be adsorbed. Consequently, the IR spectrum provides all the frequency information about the IR radiation adsorbed or transmitted, which are very characteristic as they are directly related to the structure of the molecule.<sup>181</sup>

Concerning the basics of the instrumentation of this technique (Figure II-1), the radiation containing all the IR spectrum frequencies originates from a thermal source called the IR source. It enters the so-called Michelson Interferometer where the IR beam is split into two by the means of a beam-splitter, a half-transparent window: the two beams travel different distances and then merge into one. Because of the interferometer, the obtained beam is a pulsating beam that mimics the pattern of frequencies in the IR beam. Once it exits from the interferometer, the obtained beam goes to the sample which adsorbs some of the frequencies before reaching the detector. An interferogram called also time-domain spectrum is first recorded, then a mathematical transformation called the Fourier Transform (FT) is applied to convert the interferogram into a frequency-domain spectrum. The latter is then compared to a reference spectrum called background to obtain the absorbance or transmittance spectrum used for chemical analysis.<sup>178,179</sup>

Two types of detectors can be used: Deuterated Triglycine Sulphate (DTGS) and Mercury Cadmium Telluride (MCT). The comparison between these two detectors is presented in Table II-1. The use of such detectors results in an increase in the benefits acquired when using FTIR technique. It also ensures a maximum use of the radiation along with a fast spectral averaging which results in an enhancement in the signal to noise ratio. In addition, the



wavenumber scale of FTIR instrument is reliably fixed by the wavelength of the controlling laser used.

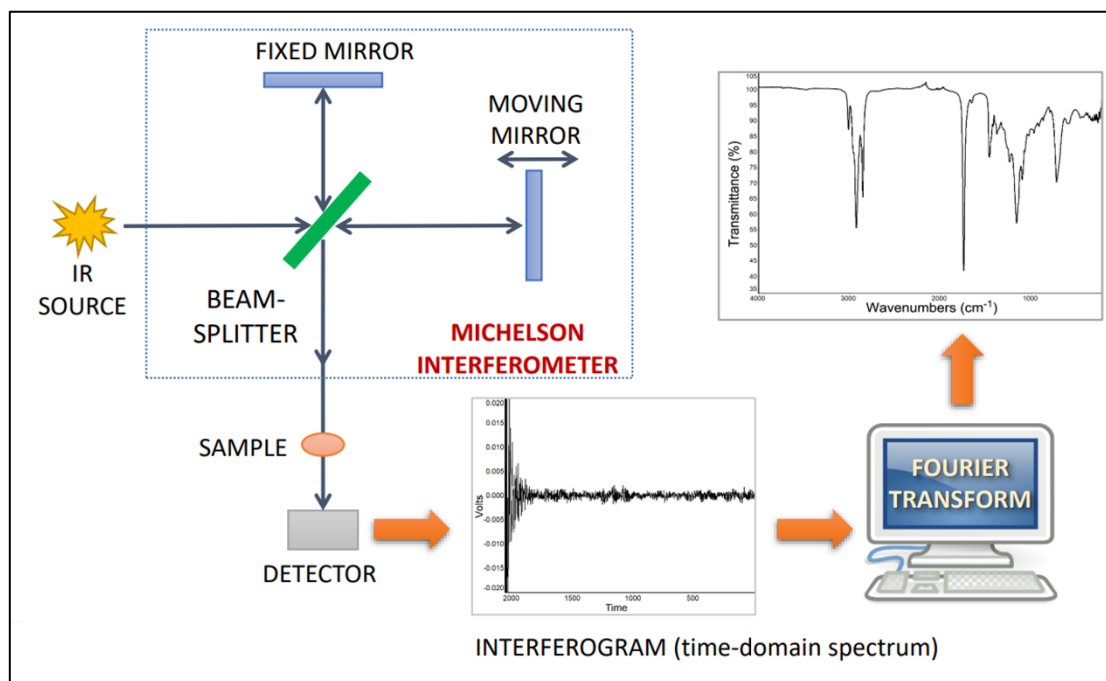


**Figure II-1:** Diagram representative of the principle of FTIR instrument.

Parameters	DTGS	MCT
Wavenumber region	12000 - 350 $\text{cm}^{-1}$	11700 – 700 $\text{cm}^{-1}$
Sensitivity	Less sensitive	Up to 10 times more sensitive than DTGS
Signal to noise ratio	Satisfactory	Good
Cooling requirements	No	Yes (at liquid nitrogen temperature)
Time of measurements	Slow	3 to 4 times faster than DTGS
Price	Inexpensive	Several times higher than DTGS
Usage	Ordinary FTIR spectrometers	High-end FTIR spectrometers

**Table II-1:** Table showing the comparison between DTGS and MCT detectors for FTIR spectroscopy.

### Procedure:

IR spectra for the samples prepared in this thesis work were recorded using two different IR spectroscopy instruments:

A Bruker Vector 22 instrument with a DTGS detector, using a resolution of  $4\text{ cm}^{-1}$  and accumulating 64 scans was used for a set of experiments carried out at the Department of Chemistry at University of Torino. The self-supporting pellets of the samples were placed in a traditional IR cell with  $\text{CaF}_2$  windows and equipped with a valve to be connected to a vacuum line (residual pressure  $< 1.0 \times 10^{-5}$  mbar) where the experiments of adsorption/desorption were carried out in situ.

In addition, a Bruker Vertex 80 spectrometer equipped with MCT detector under a RapidScan mode using a resolution of  $4\text{ cm}^{-1}$  and accumulating 250 scans to have a good signal to noise ratio was used for another set of experiments at the LRS at Sorbonne University. The samples in self-supporting pellets form were placed between two transparent calcium fluoride  $\text{CaF}_2$  windows sealed with a paraffine film.

In order to obtain a wider spectral window, KBr-IR spectra for the silica samples were also recorded in the transmission mode using Bruker Vertex 80 (MCT detector, resolution of  $4\text{ cm}^{-1}$  with the accumulation of 250 scans). The spectra were measured in potassium bromide KBr pellets with a concentration of the sample in the pellet of a few percent by weight. The absorption of a pellet of pure KBr was used as a background.

The data collected were normalized to the intensity of the signals in the  $2100\text{-}1700\text{ cm}^{-1}$  range due to a combination and overtone of vibration modes of bulk materials in order to render differences in intensity independent of differences in the thickness of the pellets.

### Nature of the IR information:

Infrared (IR) spectroscopy was the major technique adopted in this thesis work for in situ characterization of the growing peptides chains throughout glycine deposition as well as

peptides folding. IR is highly sensitive, compared to other spectroscopic methods, to the H-bonding state and conformation of the different peptide groups. It has proven to be a useful and powerful technique in the study of protein structures, providing not only qualitative information on the presence of functional groups in organic compounds but also a quantitative estimation of the protein secondary structures yielding important structural and dynamical information of the peptides.<sup>182</sup>

#### II.1.1.2. Attenuated total reflection infrared spectroscopy

##### Principle of the technique:

Attenuated total reflection infrared (ATR-IR) spectroscopy is a non-destructive technique used to get a qualitative analysis of samples with little or no sample preparation. ATR is easily miniaturized as it can provide high-quality spectra of samples with a diameter less than a millimeter. This technique is based on a total internal reflection phenomenon. The sample is placed in contact with an ATR crystal, where an IR radiation is directed through the ATR crystal to the surface of the sample at a certain angle  $\theta$  so that the light is totally reflected (Figure II-2).<sup>183</sup> In order to have a total internal reflection, the incident radiation angle  $\theta$  must exceed the value of the critical angle  $\theta_c$  defined as follows:  $\sin \theta_c = \frac{n_2}{n_1}$  where,  $n_1$  and  $n_2$  represent the refractive index of the ATR crystal and the sample respectively.

Consequently, for the total reflection to occur, the refractive index of the crystal must be higher than that of the sample. Therefore, high refractive index materials of good hardness are selected for the ATR crystal such as diamond, zinc selenide, and germanium.<sup>180,183</sup> Upon internal reflection, a part of the incident IR beam, called the evanescent wave, penetrates the sample to a depth ( $d_p$ ) of few micrometers and is partially adsorbed by the sample. Due to the interaction between the sample and the penetrated beam, a selective attenuation of the radiation results

where the beam loses energy at the wavenumbers where the sample adsorbs infrared radiation. This leads to the generation of the infrared spectrum for the sample.<sup>184</sup>

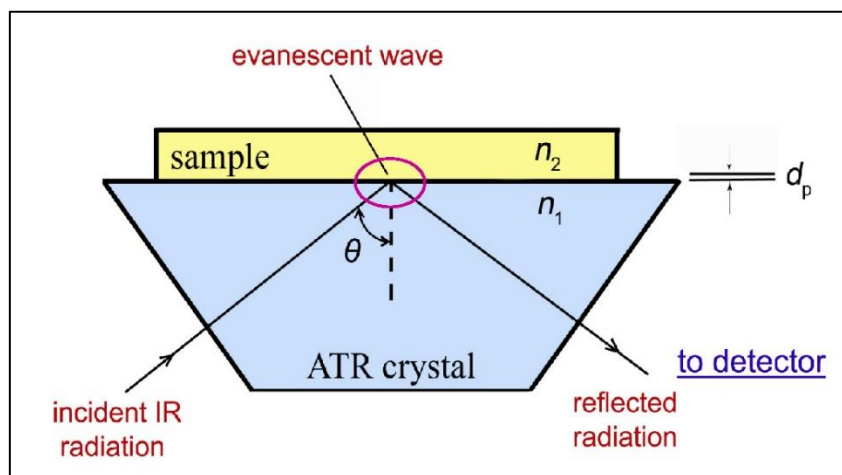


**Figure II-2:** Schematic representation of total internal reflection in ATR-IR system.<sup>183</sup>

#### Procedure:

ATR-IR spectra for silica samples were recorded using Bruker Vertex 80 spectrometer equipped with a mono-reflection diamond Bruker, A225/Q-DLST ATR device. The refractive index of the diamond is 2.4. Measurements were carried out with a RapidScan mode using a DTGS detector with a mirror speed of 20 kHz. The spectral window recorded was from 4000-200  $\text{cm}^{-1}$  using a resolution of 2  $\text{cm}^{-1}$  while accumulating 200 scans for a better signal to noise ratio.

#### Nature of the ATR information:

In this work, ATR is used to analyze different silica samples as it allows to obtain information on the nanostructure of the material, by analysis of characteristic behaviors of its building units  $\text{SiO}_4$  through the asymmetric stretching of longitudinal optic  $\nu_{\text{as(LO)}}$ , asymmetric stretching of transverse optic  $\nu_{\text{as(TO)}}$ , symmetric stretching (LO+TO)  $\nu_s$ , and bending  $\delta$  motions of the Si-O-Si bonds, in addition to the Si-(OH) stretching, and which exhibit different main

bands at around 1188, ~1100, ~800, ~450, and ~966  $\text{cm}^{-1}$  respectively in an ATR-IR spectrum.<sup>185</sup>

### II.1.1.3. Raman spectroscopy

#### Principle of the technique:

The Raman spectroscopy measurements consist in illuminating the sample with a monochromatic laser beam which results in a scattered light upon interaction with the sample molecules. After interacting with the sample, the incident light scatters in all direction. The majority of the scattered light still has the same frequency of the incident one, and this is known as Rayleigh scattering. However, a small amount of the scattered light acquires a distinct frequency from that of the excitation source, this results in the construction of the Raman spectrum because this shift in energy results from the interactions between the incident electromagnetic waves and the vibrational energy levels of the molecules in the sample. When the incident frequency is higher than the one of the scattered light, one speaks of “Stokes lines” whereas when the frequency of the scattered light is higher, “anti-Stokes” lines are seen (Figure II-3). The Raman spectrum of the sample is constructed by plotting the intensity of the shifted light versus its frequency difference from the incident light, and each band corresponds to a specific vibrational frequency of a bond within the molecule. A lot of information can be provided from a Raman spectrum about the quantity of the components present deduced from the intensity of the spectrum, the stress and strain states inferred from the peak shift, etc.<sup>186,187</sup>

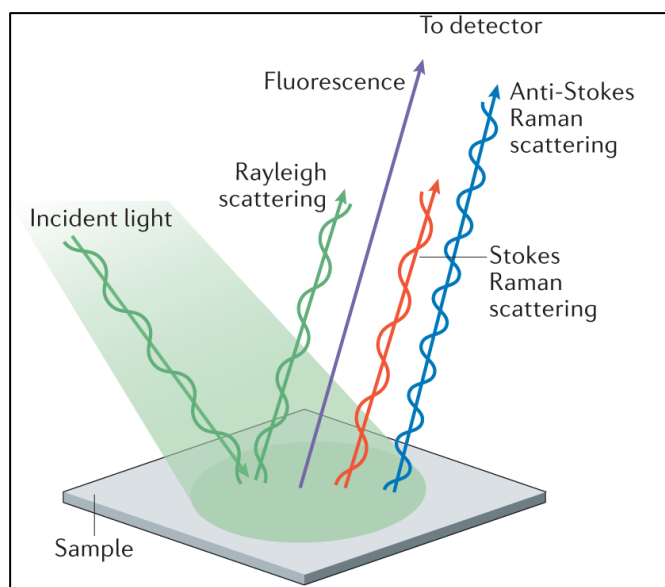


**Figure II-3:** Schematic representation of the Raman Spectroscopy scattering<sup>186</sup>

Procedure:

A Kaiser microscope optical system (RXN1) equipped with a charge-coupled detector was used to measure Raman spectra for silica surfaces (in pristine form or thermally treated at different temperatures) at room temperature. The laser beam working at 785 nm was focused by adjusting the microscope to an objective of 50X long working distance (8 mm) lens. The spectral window was in the range of 3200-150  $\text{cm}^{-1}$ , obtained with an incident laser power of 10 mW, resolution of 4  $\text{cm}^{-1}$ , 10 seconds acquisition time while accumulating 30 scans for each spectrum.

Nature of the Raman information:

Raman spectroscopy is used in this thesis work to study the difference in structural properties of various silica surfaces. Different features of the silica surface related to silanol groups and siloxane rings can be detected through the different specific Raman spectral bands. The evolution of the silanol groups can be estimated from the band present in the 960-990  $\text{cm}^{-1}$  range related to the Si-(OH) stretching. The breathing vibration modes of the 4- and 3-membered rings, designated as D1 and D2, are represented by their characteristic bands at 495

and  $607\text{ cm}^{-1}$  respectively. The bending motions of the oxygen atoms of the Si-O-Si angle in the network, a key band in the understanding of silica structure, is represented by the R-band peaked at around  $440\text{ cm}^{-1}$ .<sup>188,189</sup>

## **II.1.2. Thermal techniques**

### II.1.2.1. Thermogravimetric technique

#### Principle of the technique:

Thermogravimetric analysis consists in recording weight changes of a solid sample submitted to a (generally linear) temperature ramp. It is often coupled with differential thermal analysis (DTA) that records the exothermic and endothermic heat flows corresponding to the thermal events.

#### Procedure:

Thermogravimetric analysis was carried out using a TA instrument with a STD Q600 analyser. TGAs were performed with a heating rate of  $1\text{ }^{\circ}\text{C}/\text{min}$  under dry air flow ( $100\text{ mL}/\text{min}$ ). The samples of (poly)Gly/silica analyzed by TGA are used in form of crushed pellets. Quantification of adsorbed peptides was evaluated by correcting the weight loss between  $130$  and  $400^{\circ}\text{C}$  for the corresponding value for the blank sample.

#### Nature of TG information:

TGA is used in this thesis to calculate the number of silanol groups on the surface of pristine silica or calcined at different temperatures. This is performed by heating blank silica samples from room temperature to  $800$  or  $1000\text{ }^{\circ}\text{C}$ ; the number of silanol groups is deduced from the weight loss of water stemming from silanols condensation. In addition, (poly)Gly/silica systems were also analyzed by TGA. Three main events were observed to take place: desorption of physisorbed water which occurs on silica for  $T < 100\text{ }^{\circ}\text{C}$ , amide bond formation with the elimination of water, and oxidative decomposition of the organic compounds

from the surface. Since this decomposition is quantitative, the integration of the differential thermal gravimetry (DTG) profiles provides an estimate of the amount of peptides formed on the surface during polymerization.

### **II.1.3. Physicochemical techniques**

#### **II.1.3.1. N<sub>2</sub> physisorption (gas-volumetric analysis)**

##### Principle of the technique:

N<sub>2</sub> physisorption is a non-destructive technique used to obtain information on the surface area, pore volume, and pore diameter of a solid material. It consists of a gas-solid adsorption phenomenon that involves intermolecular (Van der Waals) forces. The measurements are conducted on a volumetric basis at constant temperature (77 K) and are preceded by vacuum outgassing to remove all physisorbed species from the surface of the sample. This is followed by Nitrogen N<sub>2</sub> gas introduction in successive amounts and the system is allowed to reach equilibrium pressure following which the adsorbed amount is measured. The corresponding isotherm of the material is then depicted point by point where each point is determined by measuring the volume of nitrogen gas adsorbed or desorbed.

##### Procedure:

N<sub>2</sub> adsorption/desorption isotherms of silica samples were recorded using Belsorp-max (BEL JAPAN) apparatus. 70 to 80 mg of the sample were enclosed in a specific glass tube and degassed under vacuum at 250 °C for 2 h (residual pressure 10<sup>-4</sup> mbar) on a BelprepII-vac unit. The adsorption isotherms were then obtained by introducing stepwise known volume of N<sub>2</sub> into the cell then evacuating the cell progressively.



### Nature of information from N<sub>2</sub> physisorption:

The values of the surface areas of pristine or calcined silica samples were calculated automatically from the instrument software following the Brunauer-Emmet-Teller (BET) method by applying the following conventional linear equation:

$$\frac{\frac{P}{P_0}}{n \times \left(1 - \frac{P}{P_0}\right)} = \frac{1}{n_m \times C} + \frac{C - 1}{n_m \times C} \times \frac{P}{P_0}$$

where,

- $P/P_0$  is the reduced pressure (total pressure over the saturating vapor pressure of the adsorbate) deduced from the isotherm curve (x-axis);
- $n$  is the volume of gas adsorbed (expressed at standard temperature and pressure) deduced from the isotherm curve (y-axis);
- $n_m$  is the specific monolayer capacity;
- $C$  is the BET constant which is exponentially related to the energy of monolayer adsorption.

Subsequently, the BET surface area is calculated based on the following equation:

$$a_{S(BET)} = \frac{n_m \times N_A \times \sigma_m}{m}$$

where,

- $a_{S(BET)}$  is the BET specific surface area of the adsorbent of mass  $m$  (g),
- $n_m$  is the volume adsorbed at monolayer coverage (ml),
- $N_A$  is the Avogadro's number ( $6.023 \times 10^{23}$  molecules·mol<sup>-1</sup>),
- $\sigma_m$  is the molecular cross sectional area taken by the adsorbate molecule in the complete monolayer ( $\sigma_m$  (N<sub>2</sub>): 0.162 nm<sup>2</sup>).<sup>190</sup>

### II.1.3.2. X-ray diffraction

### Principle of the technique:

X-ray Diffraction (XRD) is a non-destructive technique used to investigate crystalline phases. An incident X-ray beam is directed toward the solid material, which diffracts part of it; the intensity of the diffracted X-ray is recorded as a function of the diffracting angle. Diffraction takes place when the angle between the incident X-ray and a crystallographic plane (reticular plane) is identical to the one between this plane and the diffracted X-ray (Figure II-4). More specifically, Bragg's law<sup>191</sup> states that constructive interference, and thus the observation of a diffracted beam, will be observed when the following equation is satisfied:  $2d \sin \theta = n\lambda$ ; where  $d$  is the distance between two planes of the same crystallographic family ( $\text{\AA}$ ) with indices  $hkl$ ;  $\theta$  is the half of the diffraction angle;  $n$  is the order of diffraction (equal to 1); and  $\lambda$  is the wavelength of the radiation.

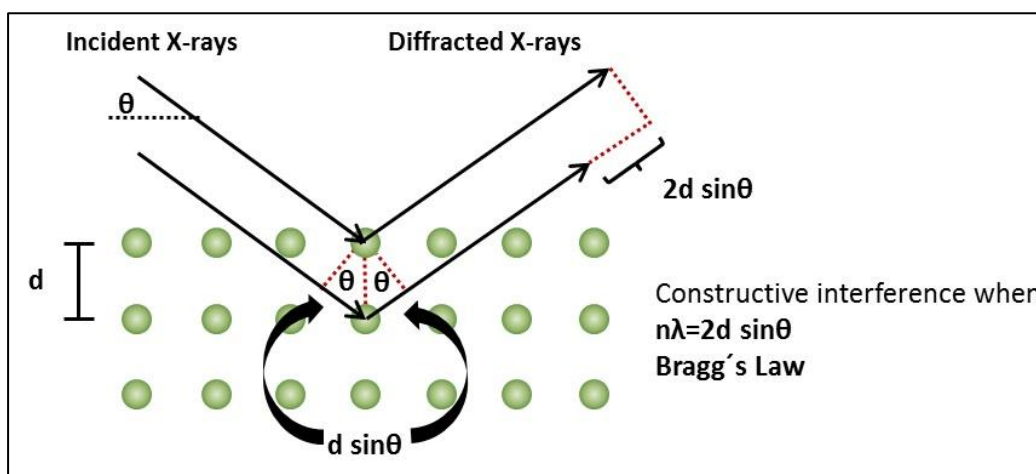


**Figure II-4:** Schematic representation for X-ray Diffraction (XRD)

### Procedure:

The samples in this thesis work were characterized by X-ray powder diffraction patterns recorded on a PANalytical X'Pert diffractometer using a Cu  $K\alpha$  ( $\lambda = 1.5405 \text{ \AA}$ ) radiation source and working at 30 mA and 40 kV. The diffractograms were recorded for  $2\theta$  angles ranging from 10 to  $45^\circ$ , with a step size of  $0.01^\circ$  and a dwell time of 1 s per step.

### Nature of XRD information:

The silica supports we used are amorphous and thus do not diffract X-Rays. However, when dealing with the adsorption of amino acids on silica surface, some systems may show the existence of a bulk crystalline phase along with adsorbed amino acids. This bulk phase formation takes place when the adsorption sites on the surface of the support become saturated. XRD technique is used in this thesis for the identification of the saturation point which can be detected through the formation of Bragg peaks on the smoothed background of amorphous silica. The appearance of such peaks on a diffractogram indicates the formation of a crystalline amino acid phase. The nature of the crystalline phases is determined through a comparison between the XRD patterns of the solid material analyzed and the diffraction patterns of the standard powder XRD files available in the International Center for Diffraction Data (ICDD).

## **II.1.4. Analytical techniques**

### II.1.4.1. Mass spectrometry

#### Principle of the technique:

Mass spectrometry (MS) is an analytical technique employed for qualitative and quantitative chemical analysis. It consists in the measurement of the mass-charge ratio ( $m/z$ ) of any analyte of organic or inorganic nature which has been previously ionized. The  $m/z$  ratio is a dimensionless number and represents the relative mass  $m$  of an ion on the unified atomic scale divided by the charge number  $z$ .<sup>192</sup> High-resolution mass spectrometry (HR-MS) technique is coupled with an analyzer such as the Orbitrap type. The mass analyzer has the shape of a spindle and it involves a central electrode and two surrounding semi-electrodes. A high-voltage DC is gradually applied to the central electrode, which results in the generation of a special geometry electrostatic field in the Orbitrap. Due to the central electric field, the ions inside the Orbitrap start a circular orbital motion around the central electrode. Simultaneously, the ions follow the

horizontal and vertical directions along the central electrode. The external electrode limits the orbital change of the ions and identifies the induced electromotive force generated by the ions' oscillation. A differential amplifier detects the signal which is then converted to the oscillating frequency of each ion by the FT converter. After that, an ultra-high resolution  $m/z$  is calculated (Figure II-5).<sup>193</sup>

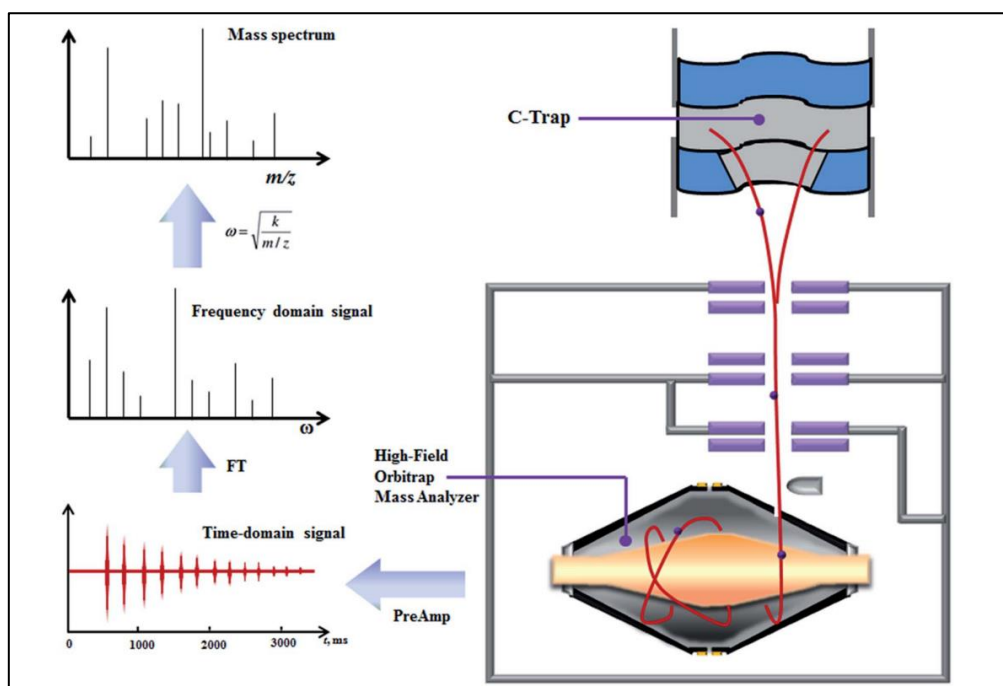


**Figure II-5:** Schematic representation of the structure and the signal converter manner for Orbitrap mass analyzer.<sup>193</sup>

### Procedure:

Analyses by high-resolution mass spectrometry were performed using an LTQ Orbitrap mass spectrometer (Thermo Scientific) equipped with an atmospheric pressure interface and an electrospray ionization (ESI) source. The source voltage was set to 4.48 kV. The heated capillary temperature was maintained at 265 °C. The tuning parameters adopted for the ESI source were as follow: capillary voltage 0.02 V, tube lens 24.77 V; for ions optics: multipole zero offset – 4.28 V, lens zero voltage – 4.36 V, multipole zero offset – 4.28 V, lens 1 voltage – 13.69, gate lens voltage -8.84 V, multipole 1 offset -18.69 V, and front lens voltage -5.09 V.

The mass accuracy of recorded ions (vs. calculated) was  $\pm 1$  mmu (without internal calibration). The samples, added to 100  $\mu$ L of a 0.1 M HCOOH aqueous solution, were delivered directly to mass spectrometer via Hamilton microliter syringe at a constant flow (10  $\mu$ L/ min).

#### Nature of MS information:

The supernatants obtained from the washing of the prepared samples in this thesis were subjected to MS analysis, as complementary information to the FTIR technique in order to detect the number of monomers and type of components present in the resulting solutions. This provides useful insights about the product of the polymerization reaction as it is possible to deduce the length of the peptide chains, detect the presence of the cyclic dimer DKP or even identify remaining monomers.

## **II.2. Experimental protocols**

### **II.2.1. Pre-treatment of silica materials**

Here we provide a general presentation of sample preparation procedures that will be further elaborated in the following chapters. Silica samples were subjected to thermal treatments carried out in a muffle furnace. SiO<sub>2</sub> powder was pressed in the form of self-supporting pellets before being introduced in the furnace at room temperature (rt) with a ramp of 30 min up to 450 °C and kept at this temperature for 2.5 h. The temperature was then cooled down to rt.

A higher temperature treatment was also carried on where another set of pellets previously treated at 450 °C was then ramped for 30 min up to 700 °C, kept at this temperature for 2.5 h, and then left to cool down to rt. Only in one case (Aerosil380), silica was subjected to an even higher temperature (850 °C). To do so, a pellet of silica pre-treated at 450, and 700 °C was further ramped for 30 min to 850 °C, kept again for 2.5 h at this temperature and left in the furnace until the temperature cooled down at rt.

Prior to any FTIR measurements, silica samples were outgassed at room temperature or at 160 °C in order to remove physisorbed water molecules from the surface. This is done either under vacuum using a pyrex vacuum cell or under argon flow using a U-shaped cell.

### **II.2.2. Monomers adsorption from the gas phase**

The adsorption of Gly from the vapor phase on silica using the chemical vapor deposition method (CVD) was done using two different types of cells: a vacuum cell and a U-shaped cell under argon flow.

In the first case, a vacuum cell was used composed of two main parts: one was dedicated for the thermal treatment and the other was an IR-transparent part equipped with CaF<sub>2</sub> windows. The pressed SiO<sub>2</sub> sample was put in a gold frame as a holder. First, the silica pellet was placed in the thermal treatment part of the cell connected to a vacuum line, where a tubular furnace was adjusted around the corresponding part of the cell for treatment at 160 °C. The temperature was measured by means of a thermocouple placed in contact with the external surface of the cell (Figure II-6, A).

Once the temperature was cooled down, the gold frame holding the pellet was moved to the transparent part in the bottom, for IR spectroscopic measurements in situ (Figure II-6, B).

After outgassing, the silica pellet was moved again to the thermal treatment part where it was placed next to a Gly pellet and heated up to 160 °C in static vacuum for 2.5 hrs where Gly started to sublime and adsorb on the silica pellet. During this process, the valve connecting the cell to the vacuum line was closed and the cell was kept in contact with a liquid-nitrogen trap in order to remove the generated water formed during Gly condensation reaction (Figure II-6, C).

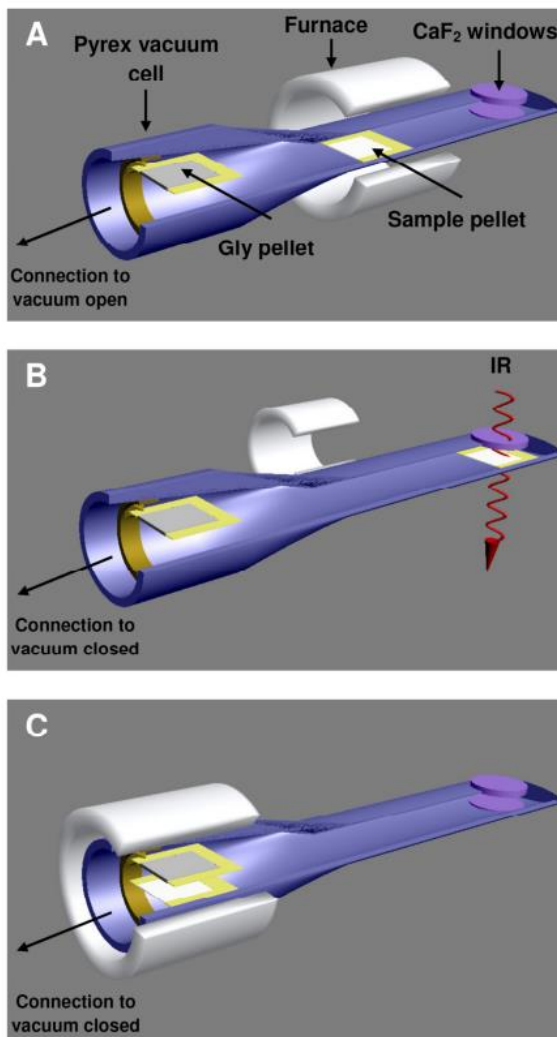


**Figure II-6:** Gly adsorption from vapor phase using the vacuum cell on silica surface.<sup>25</sup>

For CVD under argon flow, 200 mg of silica support were introduced in a U-shaped cell and placed on its sintered glass bed, while 30 mg of Gly were placed upstream, in the U-shaped part of the cell. The system was first subjected to an outgas at rt for 2 h under a 100 ml/min argon flow to remove physisorbed water before the start of the reaction. The cell was then placed in a tubular oven controlled by a temperature programmer. A linear temperature ramp of 1 °C/min was applied up to 160 °C and this temperature was kept for 20 h under argon flow, then the sample was left to cool down to rt (Figure II-7).

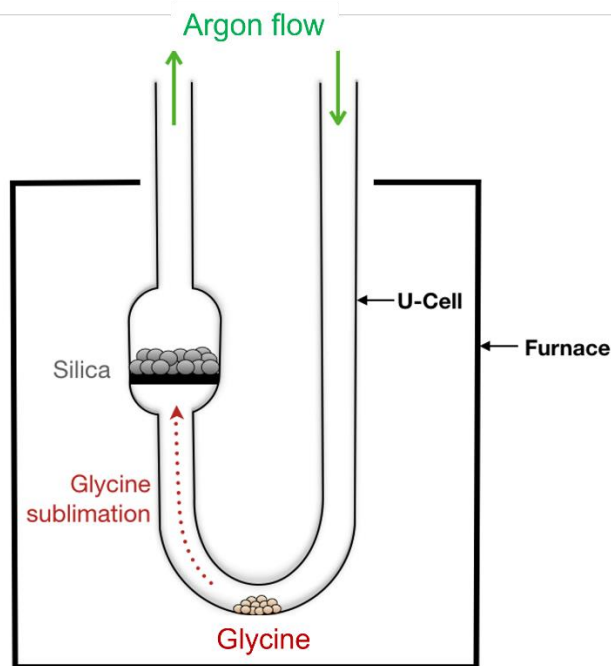


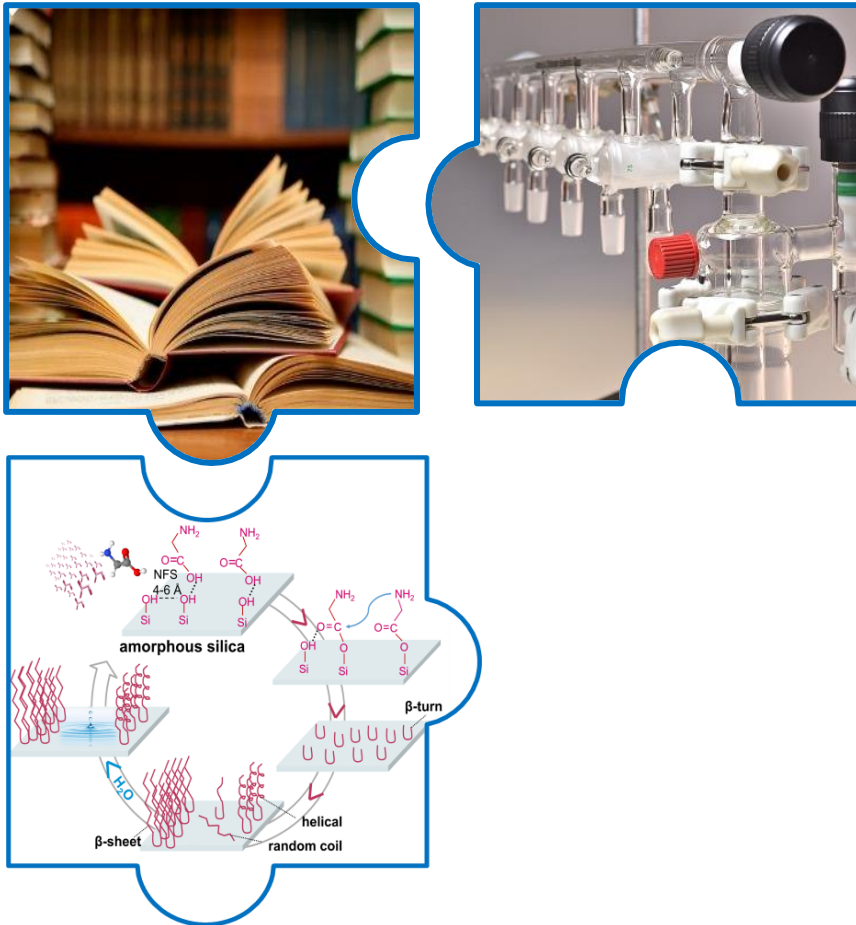
**Figure II-7:** Gly adsorption from vapor phase using the U-shaped cell on silica surface.

### II.2.3. Monomers adsorption from liquid phase

Gly monomers were deposited on silica surfaces from water solutions using the incipient wetness impregnation (IWI) procedure, derived from the field of supported catalysis synthesis. Briefly, the required amount of Gly monomers were dissolved in ultrapure water and the resulting Gly solution was added to the silica support respecting a ratio of 10 ml of Gly solution for 1 g of silica. This resulted in a homogeneous slurry without a separate liquid phase, which was left to dry under a slow nitrogen flow at rt overnight. The Gly/silica system was then dried under vacuum then introduced in U-shaped cell (shown above in Figure II-7) for outgas at rt for 10 h under a 100 ml/min argon flow. Subsequently, the U-shaped cell, still under the same argon flow, was placed in a tubular oven coupled with a temperature programmer for thermal activation of the system. A controlled linear temperature ramp of 1 °C/min was applied to reach a final value of 160 °C where a plateau was maintained for 30 min. The temperature was then cooled down to rt and the resulting sample was stored in a desiccator for future characterization by different techniques.



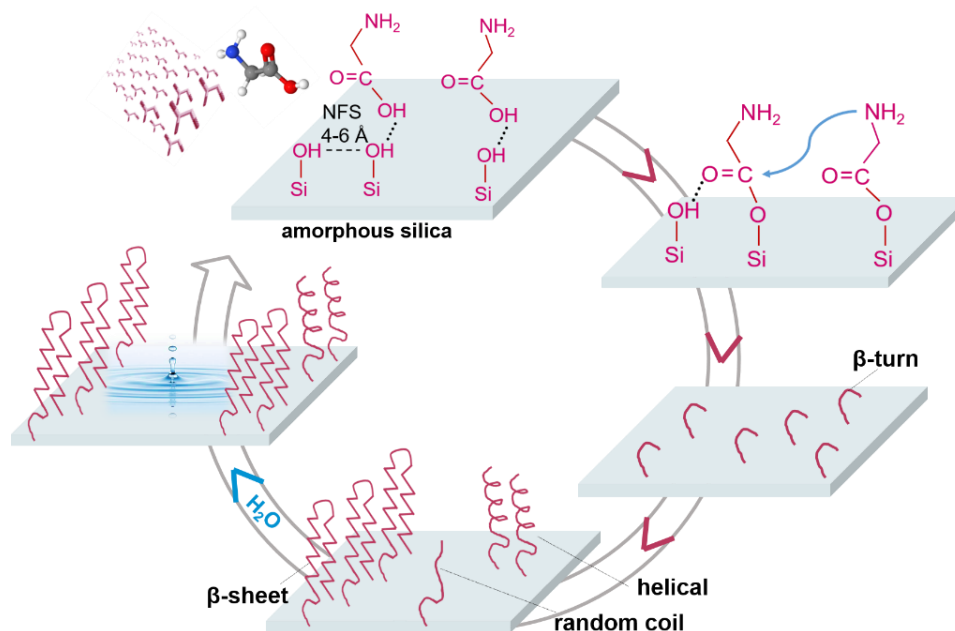
### III. Chapter III: Emergence of order in origins-of-life scenarios on mineral surfaces: polyglycine chains on silica



***The work presented in this chapter is published as a peer-reviewed article in Langmuir, 2022***

*El Samrout, O., Fabbiani, M., Berlier, G., Lambert, J. F., & Martra, G. (2022). Emergence of Order in Origin-of-Life Scenarios on Mineral Surfaces: Polyglycine Chains on Silica. Langmuir 2022, 38, 50, 15516–15525*

The polymerization of amino acids to peptides on oxide surfaces has attracted interest, owing to its high importance in bio-technology, prebiotic chemistry and origin of life theories. However, its mechanism is still poorly understood. We tried to elucidate the reactivity of glycine (Gly) from the vapor phase on the surface of amorphous silica under controlled atmosphere at 160 °C. IR spectroscopy reveals that Gly functionalizes the silica surface through the formation of ester species which represent, together with the weakly interacting silanols, crucial elements for monomers activation and polymerization. Once activated,  $\beta$ -turns start to form as initiators for the growth of long linear polypeptides (poly-Gly) chains and which elongate into ordered structures containing both  $\beta$ -sheet and helical conformations. The work also points on the role of water vapor in the formation of further self-assembled  $\beta$ -sheet structures that are highly resistant to hydrolysis.



### III.1. Introduction

The polymerization of amino acids (AAs) to peptides has attracted significant attention for a long time due to its importance in various fields ranging from biological applications<sup>194,195</sup>, and green syntheses development<sup>40,196</sup>, to the study of the origin of life.<sup>40,88</sup> A number of studies have suggested methods for polymerization in the absence of activating agents, such as the use of multiple wetting and drying cycles<sup>117,197,198</sup> on bulk AAs. Peptide bonds formation can also be accomplished by gently heating unactivated amino acids at relatively low temperatures at the interface of inorganic oxide materials such as silica, or titania<sup>23,25,144,199</sup>, a scenario that is considered of high interest in prebiotic chemistry. In his seminal work, Bernal<sup>102</sup> proposed a key role for mineral surfaces in promoting peptide bond formation. In fact, their effect is twofold. Thermodynamically, they make polymerization favorable by allowing conditions of low water activity and kinetically, they exhibit catalytic effects, by increasing the reaction rate at a given temperature.<sup>88,107</sup> The surface-catalyzed peptide bonds formation is also of high relevance in several fields such as bio/nanotechnology, drug delivery and biomineralization.

Among all inorganic materials, silica is one of the most important and abundant minerals on Earth's crust, likely present in the primordial Earth. According to literature<sup>132</sup>, most of the oldest rocks on Earth during Archean and Precambrian are cherts (silica) or are silicified. This suggests a high mobilization of silica even in the Hadean, where alkaline silica-rich seas and lakes most likely occur. The bare silica surface is characterized by two main chemical functionalities: silanol (Si-OH) groups and siloxane (Si-O-Si) bridges, whose distribution, nature and density depend on the preparation method and thermal treatment, and are directly responsible for the hydrophilic/hydrophobic character of the surface and its physico-chemical behavior towards (bio)molecules.<sup>148,149</sup> According to the literature, silica is highly suitable as a platform for oligomerization.<sup>129</sup> However, the mechanism of peptide formation on silica is still poorly understood. One convenient way to study the mechanism of this reaction is to carry it

out at the gas (amino acid vapor) /solid (silica surface) interface by chemical vapor deposition (CVD), where the influence of water may be minimized. In this setting, infrared spectroscopy under controlled atmosphere may be used as a characterization method. It is a powerful technique that provides useful and detailed information on the chemical transformation of the amino acids during the reaction. In contrast, amino acids reactions are more difficult in the presence of water that can initiate competing reactions in the system under study.<sup>99</sup> Adsorbing amino acid from gas phase may be relevant for astrochemical scenarios; interestingly, the possible occurrence of polymerization reactions on the surface of space dust grains is suggested by the recent discovery of a protein analog (hemolithin, involving chains of Gly and hydroxy-Gly residues) of extraterrestrial origin inside a meteorite.<sup>200</sup>

For years, glycine (Gly), the simplest amino acid, which can be formed in high quantities from gas-phase reactions and Miller-Urey-type experiments representing potential abiotic syntheses in diverse environments<sup>201</sup>, has been used as a reference molecule to study AA/silica systems without the additional complexity introduced by the lateral substituent. This has led to a fruitful interplay between experimental<sup>172,202</sup> and computational works<sup>164,167,203</sup> dealing with amino acids polymerization on mineral surfaces. Furthermore, recent studies suggested that Gly may have been formed in pre-solar environments and/or inside meteorite parent bodies, which has made it extensively studied in astrochemistry as it could provide insights into the processes that took place prior, during and following the formation of the Solar System.<sup>201</sup>

One recent study published by Chien et al.<sup>204</sup> highlighted the ester-mediated peptide formation as an efficient pathway for the formation of amino-acid enriched oligomers. Regarding the interaction of amino acids vapors with silica, early research<sup>99</sup> suggested that ester linkages that may be formed during adsorption, also known as surface mixed anhydrides (SMA), play the role of “activated intermediates” in the oligomerization of amino acids.<sup>119</sup>

Surface esters were originally thought to form through the esterification of the surface silanols by a carboxylic acid to form chemisorbed species on the surface.<sup>205</sup> However, Rimola et al.<sup>169</sup> established, in their computational work, that only highly strained two or three-membered rings on the silica surface ((Si-O)<sub>2</sub> and/or (Si-O)<sub>3</sub>) should be reactive toward a carboxylic moiety. Other surface groups that could play an important role in amino acids oligomerization on a silica surface are silanol pairs. Rimola et al. suggested recently<sup>24</sup> that the amide bond formation reaction specifically occurs at specific weakly interacting Si-OH pairs, separated by a distance between 4 and 6 Å and known as nearly-free silanols (NFS).

In the present work, we aim (i) to study experimentally the surface modifications during the adsorption and reaction of a carboxylic moiety on a silica surface to form ester species; (ii) to investigate the role of ester species and NFS groups in the formation of linear poly-Gly produced by a continuous feeding of Gly from the vapor phase and (iii) to assess how the presence of these active sites on the surface affects the secondary structure and mobility of poly-Gly on amorphous silica.

## **III.2. Experimental Section**

### **III.2.1. Materials**

The commercial highly pure pyrogenic silica powder AEROSIL OX 50 (AOX50) (provided by Evonik, SiO<sub>2</sub> content ≥ 99.8 wt %) with a specific surface area (SSA) of 50 m<sup>2</sup>.g<sup>-1</sup> was used in the present work. Glycine (99 %) from Sigma-Aldrich was used as received. Formic acid (FA) and deuterated water D<sub>2</sub>O (99.90 atom % D) were high-purity products obtained from Sigma-Aldrich. The vapors of these chemicals as well as those of Milli-Q water (Millipore system) were admitted onto the sample in the IR vacuum cell after several freeze-pump-thaw cycles.

### III.2.2. Pre-treatment of the silica materials

Amorphous AOX50 silica has been selected for this work because according to Raman spectroscopy measurements reported in literature,<sup>206</sup> it contains a significant number of strained rings that could constitute reactive sites for the peptide formation reaction. In addition, its specific surface area of  $50 \text{ m}^2 \cdot \text{g}^{-1}$  is high enough to obtain clearly detectable IR signals of surface species.<sup>24</sup> Moreover, the used amorphous silica has been used in several works dealing with the abiotic polymerization of amino acids<sup>89,120</sup> and had been previously demonstrated to cause the formation of linear oligopeptides from amino acids.<sup>25</sup>

A conventional IR cell for in situ measurements in transmission mode, was used. This cell was equipped with a valve to connect it to vacuum lines (residual pressure  $1 \times 10^{-5}$  mbar), and composed of two main parts: one was dedicated to the thermal treatment and the other was an IR-transparent part with  $\text{CaF}_2$  windows for IR spectroscopic measurements. The temperature was measured by means of a thermocouple placed in contact with the external surface of the cell.

Silica AOX50 powder was pressed in the form of three self-supporting pellets denoted as  $\text{AX}_{(\text{rt})}$ , AX, F-AX. The pressed  $\text{SiO}_2$  sample was put in a gold frame as a holder. The first two samples,  $\text{AX}_{(\text{rt})}$  and AX, were just outgassed in the IR cell connected to a conventional vacuum line, respectively at room temperature (rt) or at  $160 \text{ }^\circ\text{C}$  for 2 h (the latter treatment should allow to attain a complete surface dehydration before the start of glycine adsorption and polymerization reaction). These two  $\text{SiO}_2$  pellets were prepared for comparison with the formic acid-treated sample, designated as F-AX.

To prepare the F-AX sample, a silica pellet was first outgassed at  $160 \text{ }^\circ\text{C}$  for 2 h in the IR cell to attain a high dehydration level and to remove surface species such as  $\text{H}_2\text{O}$ , carbonates, etc. FA vapor (48 mbar) was admitted on the sample which was then directly heated at  $160 \text{ }^\circ\text{C}$  for 2 h in the closed IR cell. Subsequently, the pellet was again outgassed in the IR cell at beam

temperature (bt) (ca. 50 °C) overnight. After that, water vapor (20 mbar) was admitted on the sample for 20 min before being outgassed for 30 min at bt then for 2 h at 160 °C. This sequence of FA adsorption, heating at 160 °C, outgassing at bt, water contact then outgassing, was repeated for 3 successive runs. After each successive step, an IR spectrum was measured in-situ.

### **III.2.3. Glycine adsorption procedure from the gas phase**

For Gly sublimation and adsorption in situ in the IR cell, we used a similar method to Martra et al. based on chemical vapor deposition (CVD).<sup>25</sup> In summary, after outgassing, the silica sample ( $AX_{(rt)}$ , AX, or F-AX) was moved to the thermal treatment part for the start of the sublimation reaction where it was placed next to a Gly pellet and heated up to 160 °C in static vacuum for 2.5 h so that Gly started to sublime and adsorb on the silica pellet. During this process, the valve connecting the cell to the vacuum line was closed and the cell was kept in contact with a liquid-nitrogen trap in order to remove water formed during Gly condensation reaction. After 2.5 h, the temperature was decreased to rt and the pellet was moved to the IR-transparent part for IR measurements. The (contact with Gly vapor/IR spectra recording) sequence was repeated until reaching 20 h of sublimation in total (steps of 2.5 h). The samples obtained after Gly adsorption were referred to as  $G/AX_{(rt)}$ ,  $G/AX$ , and  $G/F-AX$ .

The sublimation procedure was followed by: (i) exposure to H<sub>2</sub>O vapor for 20 min with a subsequent outgas for 30 min at bt, (ii) H/D exchange by exposure to D<sub>2</sub>O vapor with a subsequent outgas for 30 min at bt. The D<sub>2</sub>O adsorption/desorption cycle was repeated until invariance of the IR spectra was observed.

### **III.2.4. Analysis of the products extracted by washing and of the washed samples**

After the experiments of contact with Gly vapor followed by exposure to H<sub>2</sub>O vapor and H/D exchange were performed on the three different samples ( $AX_{(rt)}$ , AX, F-AX), the pellets

were removed from the IR cell and each of them was ground manually in an agate mortar before suspending it in 0.5 ml of Milli-Q water. The three suspensions were shaken for 10 min by a Vortex mixer then centrifuged at 10,000 rpm for 10 min. For each sample, the supernatant was recovered and the solid was extracted four more times using the same volume of water. The first two aliquots of the aqueous solutions were mixed and analyzed by high-resolution mass spectrometry.

As regards the solid phase, the washed sample of G/F-AX was dried under a flow of nitrogen then pelletized and put in an IR cell for subsequent measurements in order to observe any organic matter remaining on the surface. First, the sample was outgassed at bt before the admission of D<sub>2</sub>O vapor in the vacuum line for several adsorption/desorption cycles until invariance of IR spectra.

### **III.2.5. Infrared (IR) spectroscopy**

Throughout the treatment procedure, the pellets were monitored by means of in situ IR spectroscopy. The spectra were collected with a Bruker VECTOR22 instrument (resolution 4 cm<sup>-1</sup>, DTGS detector) at bt (~ 50 °C) by accumulating 64 scans to obtain a good signal to noise ratio. The spectra were reported in the absorbance mode after scattering correction.

Integrated areas of the amide I band were calculated with the OPUS software (Bruker Optics GmbH) using the Levenberg-Marquardt algorithm. The peak fitting was performed using Gaussian and Lorentzian function.

### **III.2.6. High-resolution mass spectrometry (HR-MS) analysis**

The washing solutions obtained were analyzed by high-resolution mass spectrometry using an LTQ Orbitrap mass spectrometer (Thermo Scientific) equipped with an atmospheric pressure interface and an electrospray ionization (ESI) source. The source voltage was set to 4.48 kV. The heated capillary temperature was maintained at 265 °C. The tuning parameters



adopted for the ESI source were as follow: capillary voltage 0.02 V, tube lens 24.77 V; for ions optics: multipole zero offset – 4.28 V, lens zero voltage – 4.36 V, multipole zero offset – 4.28 V, lens 1 voltage – 13.69, gate lens voltage -8.84 V, multipole 1 offset -18.69 V, and front lens voltage -5.09 V. The mass accuracy of recorded ions (vs. calculated) was  $\pm 1$  mmu (without internal calibration). The samples, added to 100  $\mu$ L of a 0.1 M HCOOH aqueous solution, were delivered directly to mass spectrometer via Hamilton microliter syringe at a constant flow (10  $\mu$ L/ min).

### **III.2.7. X-ray Diffraction (XRD)**

The samples were characterized by X-ray powder diffraction patterns recorded on a PANalytical X'Pert diffractometer using a Cu K $\alpha$  ( $\lambda = 1.5405$  Å) radiation source and working at 30 mA and 40 kV. The diffractograms were recorded for  $2\theta$  angles ranging from 10 to 45°, with a step size of 0.01° and a dwell time of 1 s per step.

### **III.2.8. Thermal gravimetric Analysis (TGA)**

Thermogravimetric analysis (TGA) of crushed pellets was carried out using a TA instrument with a STD Q600 analyser. TGAs were performed with a heating rate of 1 °C/min under dry air flow (100 mL/min). Quantification of adsorbed peptides was evaluated by correcting the weight loss between 130 and 400°C for the corresponding value for the blank sample.

## **III.3. Results And Discussion**

Amorphous AEROSIL OX 50 SiO<sub>2</sub> powder has been used as it was selected in several previous studies dealing with amide/peptide bond formation.<sup>24,25</sup> In these studies, Gly sublimation temperature was optimized at 160 °C, and therefore this temperature was selected to pre-treat the silica sample under vacuum (this silica sample is hereafter labeled as AX after

this treatment) and in the presence of formic acid (labeled as F-AX; IR spectra recorded after the pre-treatment of silica samples are shown in Figure A1- 1 in the Appendix 1.

In situ IR spectroscopy under controlled atmosphere was used to follow the surface modifications during the adsorption and reaction of formic acid (FA) on silica and during the successive steps of Gly deposition (adsorption and polymerization) on the two pre-treated silica samples (hereafter noted as G/AX and G/F-AX).

### **III.3.1 Adsorption and reaction of formic acid on the silica surface at 160 °C**

FA, the simplest carboxylic acid, was adsorbed from vapor phase on the silica surface pre-treated at 160 °C (AX). FA vapor (48 mbar) was dosed at rt on AX which was then heated at 160 °C for 2 h, still in the presence of the acid, and finally outgassed overnight (residual pressure  $10^{-4}$  mbar) at infrared beam temperature (bt).

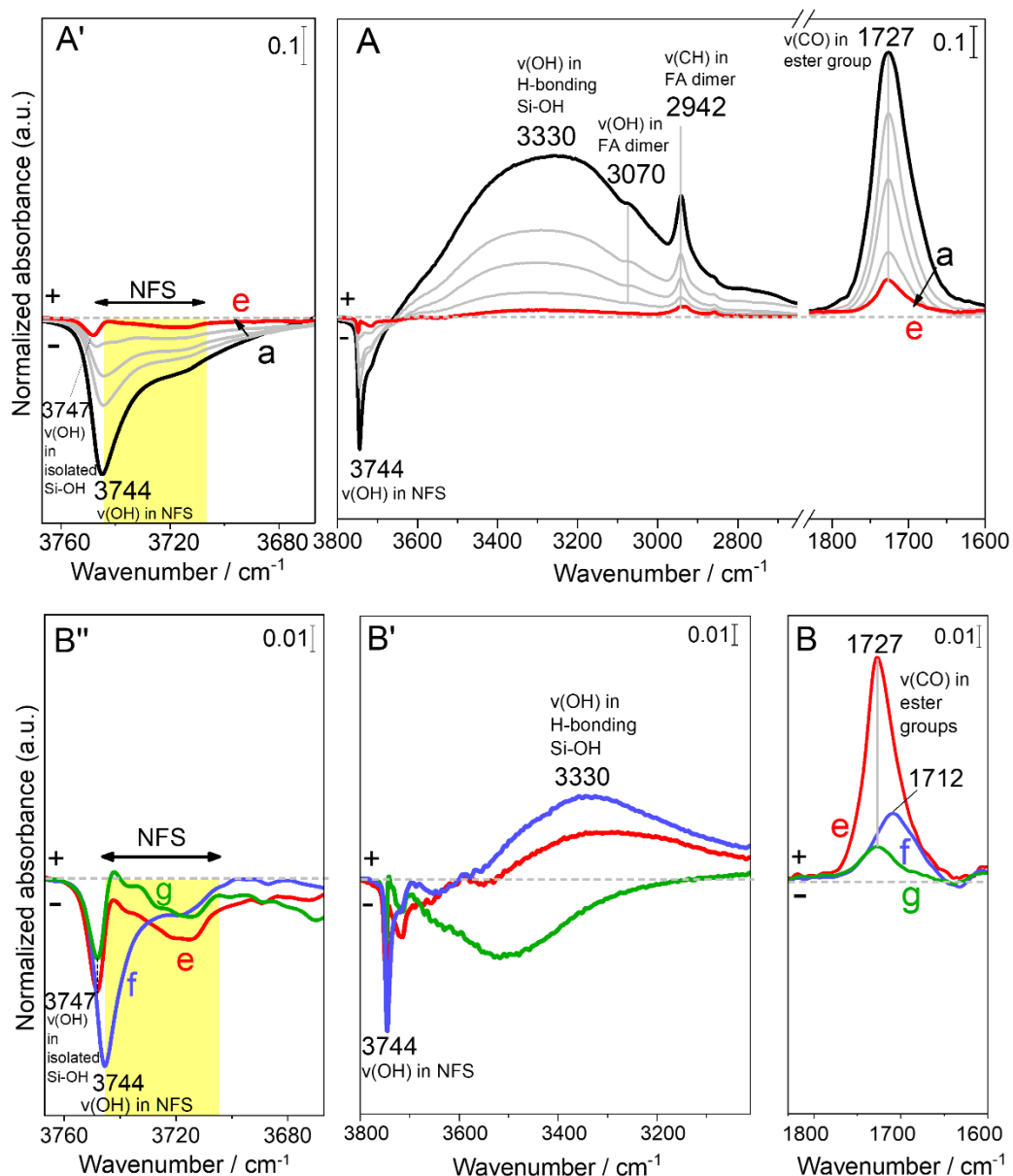


**Figure III-1:** IR spectra of F-AX for the first run: (a) after treatment in FA vapor (48 mbar) at 160 °C for 2 h; (a - e) after outgassing overnight at bt until invariance of spectra; (f) after contact with water vapor (20 mbar) for 30 min followed by outgassing at bt; (g) after outgassing at 160 °C for 2 h. The spectrum of bare SiO<sub>2</sub> after outgassing at 160 °C for 2 h (AX) is subtracted as a baseline. In panels B, B' and B'', the intensities are enhanced for the sake of clarity.

Figure III-1 shows the difference spectra during the outgassing of the first adsorption cycle (curves a to e) of the sample F-AX. At low wavenumbers, the infrared profiles show the progressive decrease in intensity of the band at 1727 cm<sup>-1</sup> attributed to the  $\nu_{CO}$  of FA. At high wavenumbers, a signal at 2942 cm<sup>-1</sup> and a shoulder at 3070 cm<sup>-1</sup> are assigned to the  $\nu_{CH}$  and  $\nu_{OH}$

of the same molecule. The  $\nu_{\text{CH}}$  and  $\nu_{\text{OH}}$  bands are close to their position in FA dimers according to the literature, while the  $\nu_{\text{CO}}$  is significantly redshifted.<sup>207</sup> After prolonged outgassing (curve e), the  $\nu_{\text{CO}}$  signal is conserved, in contrast to what was previously reported for FA adsorbed at rt (i.e., without thermal treatment) on the same silica surface.<sup>24</sup> Its redshift as compared to the vapor phase forms (about  $15\text{ cm}^{-1}$  with respect to the dimer,  $39\text{ cm}^{-1}$  with respect to the monomer)<sup>207</sup> suggests the occurrence of a strong interaction with the silica surface. The overall behavior of the infrared signals upon outgassing is compatible with the fact that the treatment at  $160\text{ }^{\circ}\text{C}$  has favored the formation of strongly bonded surface ester species  $\text{Si}_{\text{surf}}\text{-O-C(=O)-H}$ , as observed in the case of acetic acid.<sup>205</sup> In addition no evidence of the formation of formate was detected on the surface,<sup>132</sup> excluding a strong electrostatic interaction.

In the  $\nu_{\text{OH}}$  region, the silanol pattern is affected by the presence of FA molecules on the surface. During outgassing (curves a to e), the progressive decrease of the broad positive band centered at  $3330\text{ cm}^{-1}$  (curve a), attributed to H-bonded silanols, is accompanied by the recovery of the negative profile peaking at  $3744\text{ cm}^{-1}$ , where weakly interacting silanols are found.

Even after long outgassing (Figure III-1 A', curve e), some of the intensity of the band of weakly interacting silanols is not fully restored. Noticeable residual intensities are left in the region of isolated ( $3747\text{ cm}^{-1}$ ) and nearly free silanols ( $3744 - 3742\text{ cm}^{-1}$ ).<sup>208</sup> This suggests that resilient ester species (with  $\nu_{\text{CO}}$  around  $1727\text{ cm}^{-1}$ ) were formed through a reaction with this type of silanols.

At the end of the adsorption/desorption cycle, water vapor (20 mbar) is contacted with the sample and outgassed at bt prior to a final outgas at  $160\text{ }^{\circ}\text{C}$  for 2 h, the spectra at the end of each outgas being shown in Figure III-1 B, B'.

After contact with water vapor and rt outgassing (curve f),  $\nu_{\text{CO}}$  undergoes an important decrease in intensity, leaving a signal at  $1712\text{ cm}^{-1}$  of residual adsorbed FA molecules. Contact with water probably promotes the hydrolysis of a large fraction of the surface ester species, but

since outgassing is performed at bt, the FA molecules remain H-bonded with a  $\nu_{\text{CO}}$  at  $1712\text{ cm}^{-1}$ ; they are probably H-bonded to NFS groups (strong negative signal at  $3744\text{ cm}^{-1}$ , positive signal for corresponding H-bonded silanols at  $3300\text{ cm}^{-1}$ ).

After the final outgassing at  $160\text{ }^{\circ}\text{C}$  (curve g), only the underlying signal of the non-hydrolyzed ester species is left (apparently those that were formed on terminal silanols), while the NFS previously H-bonded to FA are restored. This high temperature outgassing removes the residual FA molecules leaving only some leftover surface esters at  $1727\text{ cm}^{-1}$ . The preferential recovery of the NFS (Figure III-1 B') indicates that indeed on these species, FA is able to react and be hydrolyzed depending on the chemical environment it is interacting with.

The described sequence of FA adsorption, heating at  $160\text{ }^{\circ}\text{C}$ , outgassing at bt, water contact then outgassing, was repeated for 3 successive runs in the hope to increase the amount of surface esters (corresponding IR spectra in the  $\nu_{\text{CO}}$  region reported in Figure A1- 2, Appendix 1).

### **III.3.2. Gly deposition and polymerization on silica surfaces in CVD conditions**

Gly vapor was then adsorbed at  $160\text{ }^{\circ}\text{C}$  for 20 h by CVD on AX and F-AX following the procedure adopted by Martra et al.<sup>25</sup>. Figure III-2 shows the IR spectra recorded after 20 h CVD (with steps of 2.5 h) for both samples, named G/AX and G/F-AX.

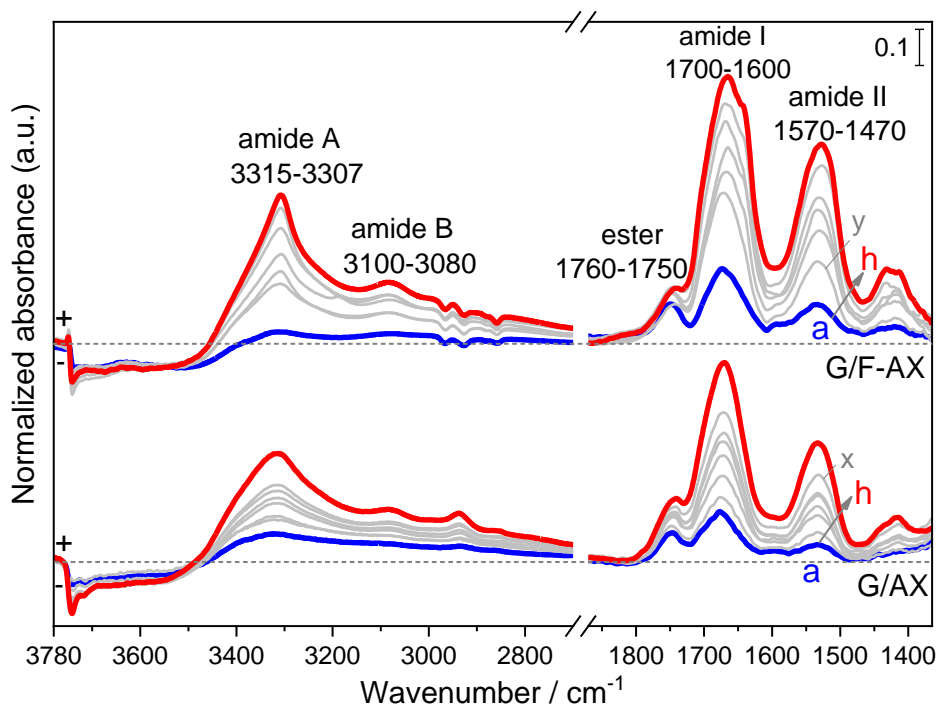


**Figure III-2:** IR difference spectra resulting from Gly sublimation by CVD at 160 °C measured from 2.5 h (a) to 20 h (h) (gray curves show intermediate sublimation steps of 2.5 h) on the two samples: G/AX and G/F-AX. The corresponding spectra of the materials obtained before the start of CVD process are subtracted as baselines.

At low frequency, the infrared profiles of both samples show a progressive increase in intensity of the bands formed in the 1700-1600 and 1570-1470  $\text{cm}^{-1}$  ranges (curves a to h), identified as amide I and amide II respectively.<sup>209</sup> These bands exhibit higher intensities for G/F-AX for each step until 20 h CVD (curve h for each sample). The presence of the amide II band is characteristic of the formation of linear peptides rather than of cyclic products.<sup>25</sup> In addition, the appearance of a band in the 1760-1750  $\text{cm}^{-1}$  range, indicates the formation of surface ester groups involving Gly molecules  $[\text{Si}_{\text{surf}}-\text{O}-\text{C}(=\text{O})-\text{CH}_2-\text{NH}-\text{R}]$ .<sup>25,99,169</sup> Their behavior will be further discussed in the comments to Figure III-5.

At high frequency, the infrared profiles for both samples display bands in the 3315-3307 and 3080-3100  $\text{cm}^{-1}$  ranges which correspond to  $\nu_{\text{NH}}$  in poly-Gly species, designated as amide A and B respectively. They progressively increase in intensity and narrow in shape with

increasing contact times, and are more intense and narrower for G/F-AX than for G/AX after 20 h CVD. This is an indication of the formation of peptides with more ordered self-assembled structures on G/F-AX.<sup>25</sup> The XRD pattern of the final samples (G/AX and G/F-AX, Figure A1-3 in Appendix 1) indicates that after 20 h CVD, no crystalline glycine (or crystalline peptides) is present in the sample: we are exclusively dealing with adsorbed species.

The relative amount of peptides may be evaluated from the integrated area of the amide I band (Figure A1-4 in Appendix 1). For all three samples (G/F-AX, G/AX, and G/AX<sub>(rt)</sub>), the temporal evolution of peptide bands can be roughly fitted with straight lines with non-zero intercepts. This would be compatible with the fast initial formation of small linear chains that elongate with a constant growth rate. On G/F-AX, peptides are significantly more abundant than on G/AX for the same time of Gly sublimation, with G/AX<sub>(rt)</sub> showing the smallest amounts. Thus, the FA modified sample is the most efficient platform for peptide formation and growth.

Quantifying the absolute amount of surface peptides from IR is more difficult. Yet, TGA data (Figure A1-5 in Appendix 1) on the final pellet (taking into account the desorption efficiency, *vide infra*) indicate that the maximum amount of peptides after 20 h CVD is about 3.25% by weight with respect to the silica support. This value would translate to a density of Gly residues of 6.9 per nm<sup>2</sup>. In Figure A1-3, this value was used as a basis to provide a y-axis graduated in units of Gly residues density, supposing that the extinction coefficient of polyGly species remained constant.

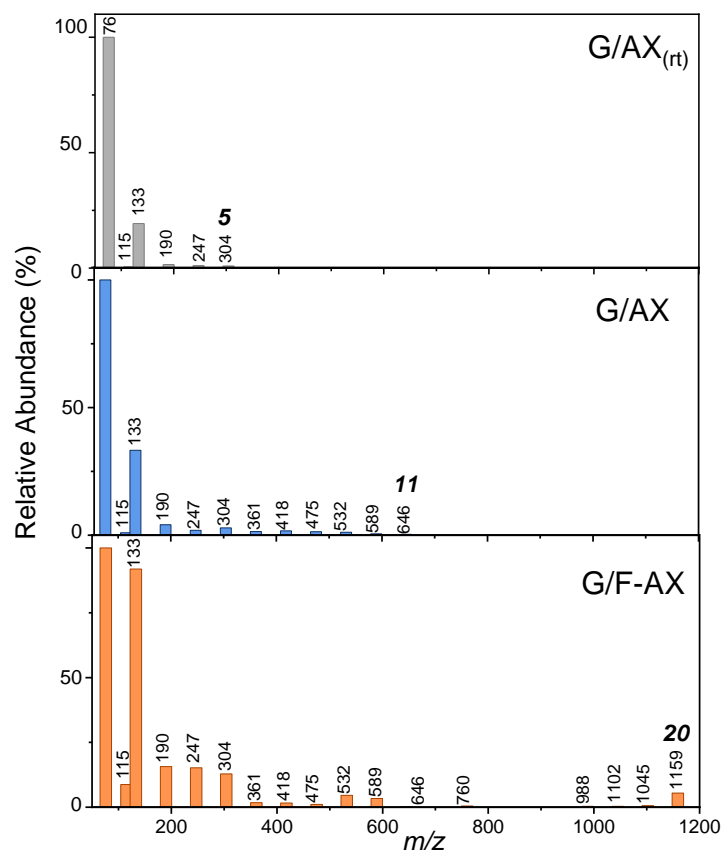


**Figure III-3:** HR-MS spectra of the solutions resulting from washing (with pure water) of the samples produced by adsorbing Gly from the vapor phase onto the three samples: G/AX<sub>(rt)</sub>, G/AX, and G/F-AX.

Numbers on the black bars are the  $m/z$  values of singly protonated species derived from  $(\text{-Gly})_n$  peptides. The number of monomers present in the peptides detected on the samples is indicated in italics above the corresponding signal.

High Resolution Mass spectrometry (HR-MS) analysis of the peptides desorbed from silica surface by washing with ultrapure water (Figure III-3) reveals the formation of longer poly-Gly chains containing at least 20 ( $m/z = 1159$  for  $(\text{Gly})_{20}\text{H}^+$ ) monomers for G/F-AX compared to oligomers up to 11 ( $m/z = 646$ ) monomers units formed on G/AX, coherent with what was reported by Martra et al.<sup>25</sup> for a similar sample, and only 5 ( $m/z = 304$ ) monomers for G/AX<sub>(rt)</sub>. Thus, the longer (desorbed and solubilized) chains are observed for samples that showed the more organized peptides based on the amide A and B bands. It must be underlined that washing with water only allows solubilization of ca. 24% of the formed peptides (see later), indicating that a considerable fraction of the Gly polymerization products are strongly bonded



to the surface, likely through the surface ester group in  $[\text{Si}_{\text{surf}}-\text{O}-\text{C}(=\text{O})-\text{CH}_2-\text{NH}-\text{R}]$  (band at  $1760\text{-}1750\text{ cm}^{-1}$ ). Thus, not much can be deduced from the high intensity of the Gly monomer and Gly-Gly dimer signals: these species may just be the easiest to desorb. The weak signal of the cyclic dimer ( $m/z = 115$ ) with respect to the linear dimer is worth mentioning, however. It confirms that, contrary to what is often observed after aqueous phase deposition, the cyclic dimers are not a predominant product.

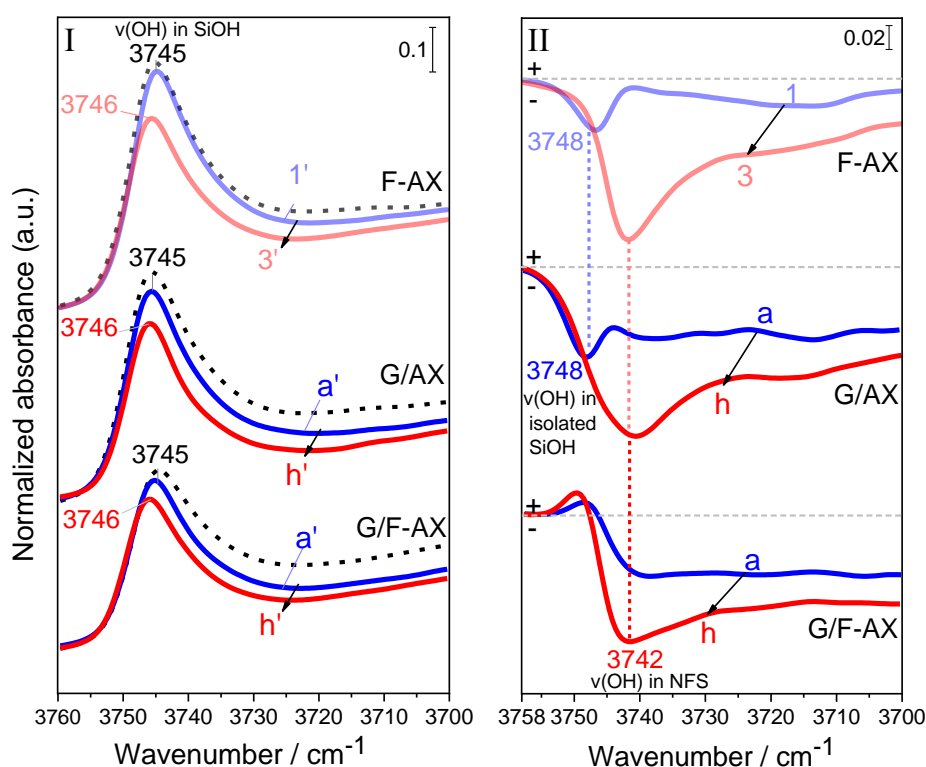


**Figure III-4:** Enlarged sections in the  $3760 - 3700\text{ cm}^{-1}$  range of IR spectra measured on: F-AX, G/AX, and G/F-AX.

Panel (I) shows the direct IR spectra of Si-OH populations present on the surface after the first and last step of contact with (1' and 3') FA or (a' and h') Gly. The dotted spectra refer to the corresponding material before any reactant contact (AX for the first two sets and F-AX for the last one).

Panel (II) shows the corresponding difference IR spectra, obtained using the corresponding spectra before contact with the desired reactant (dotted curves in panel I) as baselines.

When focusing on the silanols region (Figure III-4), it appears that the first silanols to disappear upon contact of a pristine surface with either FA (F-AX) or Gly (G/AX) were the

isolated terminal silanols, as witnessed by a negative signal at  $3748\text{ cm}^{-1}$ . Later on, the NFS are also affected (negative signal at  $3742\text{ cm}^{-1}$ ). In contrast, when Gly was deposited on the FA pretreated sample (G/F-AX), only the NFS groups were affected even at the start of the deposition. This could be expected since in this sample, isolated terminal silanols are apparently already esterified with FA, even after hydrolysis and outgassing (cf. discussion of Figure III-1). Thus, the behavior of G/AX is different from that of G/F-AX in the first deposition steps, but the two become similar at later CVD steps.

A similar behavior between the last CVD steps in G/AX and the first steps in G/F-AX is also evident in the evolution of the amide A, amide I and amide II bands (compare curve x and curve y in Figure III-2). This suggests that the reaction of the carboxylic group of Gly on AX at  $160\text{ }^{\circ}\text{C}$  modifies the silica surface in the same way as the carboxylic group of FA does. In other words, Gly dosed on silica by CVD does not only act as a reactant for polymerization, but also as a surface modifier in forming surface esters.

A more in-depth analysis of the behavior of G/F-AX during Gly polymerization (Figure III-5, panel I) allows to observe a negative correlation between the evolution of NFS groups (negative peak at  $3742\text{ cm}^{-1}$ ) and that of the ester groups (positive peak at  $1750\text{-}1760\text{ cm}^{-1}$ ) throughout the 20 h CVD, while the peptide bands (amide I and II) are progressively increasing. To better appreciate the trend, we plotted the double difference spectra between successive CVD steps (Figure III-5, panel II). In all these spectra, a negative NFS signal corresponds to a positive ester one, and vice versa. This suggests that NFS are specifically converted to esters, and conversely that the destruction of esters may regenerate NFS (and isolated silanols especially in the first CVD steps).

### III.3.3. Self-assembly and secondary structures of poly-Gly

Further information about the growth and evolution of polypeptides on the silica surface can be obtained by a closer analysis of the amide I band for G/F-AX, whose position strongly depends on the secondary structure of the peptides. After the first 2.5 h CVD (curve a, Figure III-5, Panel I), the amide I band is symmetrical and peaks at  $1671\text{ cm}^{-1}$ . This falls in the typical range of  $\beta$ -turns conformations ( $1680\text{-}1665\text{ cm}^{-1}$ ) and definitely outside the ranges of helices ( $1657\text{-}1649\text{ cm}^{-1}$ ),  $\beta$ -sheets ( $1694\text{-}1681$ ;  $1641\text{-}1623\text{ cm}^{-1}$  ranges) and even of disordered structures ( $1642\text{-}1647\text{ cm}^{-1}$ ).<sup>210-213</sup> Starting from the following 2.5 h CVD step (curve b, Figure III-5, Panel I), a significant increase in the intensity of amide I and II bands is detected, suggesting that poly-Gly chains progressively become long enough to exhibit structure as the reaction proceeds. The evolution of their secondary structures along 20 h CVD is detected from the change in shape of the amide I band in the double difference spectra (Figure III-5, Panel II); the components of this band may be identified from the computation of the second derivative of the spectra (Figure A1- 6). From 5 h till 20 h CVD, poly-Gly chains containing  $\beta$ -sheets and helices are formed in different quantities besides  $\beta$ -turns conformations. Some non-ordered structures are also formed during some intermediate CVD steps, on the basis of a minimum at  $1642\text{ cm}^{-1}$  in the corresponding second derivative (Figure A1- 6 in Appendix 1). In parallel, the narrowing of the  $\nu_{\text{NH}}$  band (“amide A” in Figure III-2) in the spectra of G/F-AX starting from 5 h CVD constitutes additional evidence of the formation of ordered structures.<sup>25</sup>

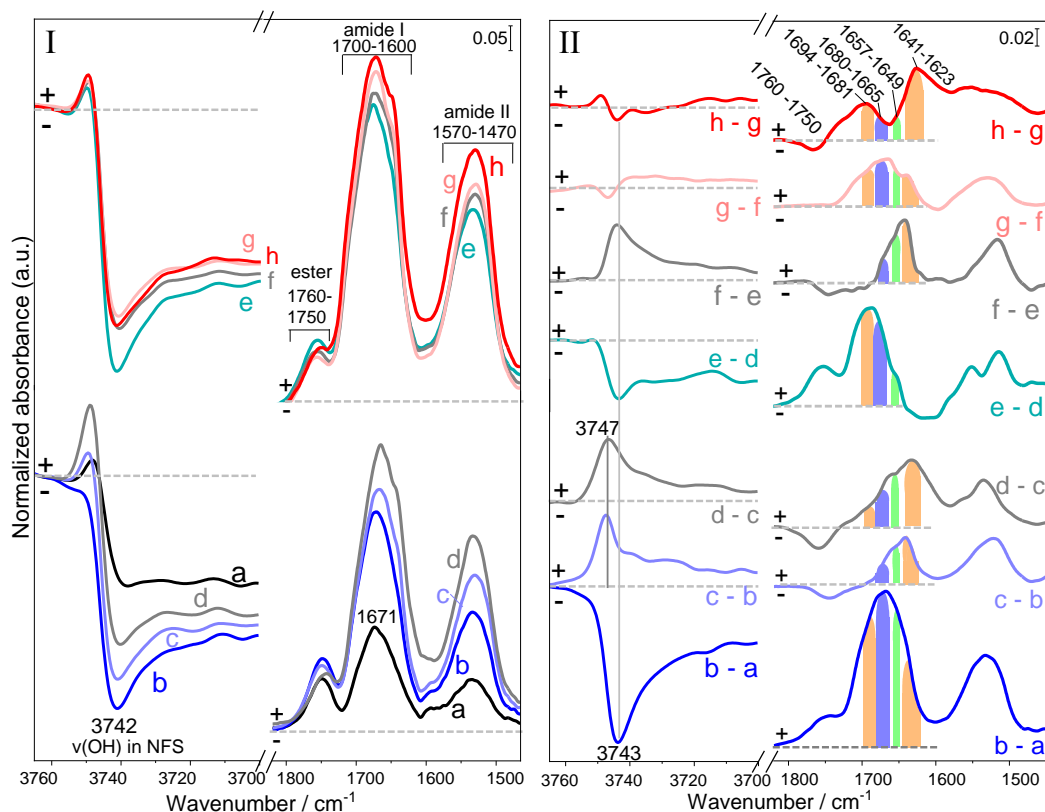


**Figure III-5:** Enlarged sections of IR spectra during Gly sublimation by CVD at 160 °C for 20 h (in 2.5 hr steps, from 2.5 h (a) to 20 h (h) sublimation) on G/F-AX: Panel (I) shows the 3760 – 3700  $\text{cm}^{-1}$  (containing Si-OH stretching vibrations) and the 1820 – 1450  $\text{cm}^{-1}$  ranges (containing the ester, amide I and amide II vibrations), using the spectrum before contact with Gly as baseline correction. Panel (II) shows the double difference IR spectra, in the 3760 – 3700  $\text{cm}^{-1}$  and in the 1820 – 1450  $\text{cm}^{-1}$  ranges (difference between each step and the previous one). The colored bars refer to the expected ranges for amide I in  $\beta$ -turns conformations (blue), helices (green) and  $\beta$ -sheets (orange).

During the first 5 h of CVD, the formation of a significant amount of  $\beta$ -turns is detected. They are probably grafted on the surface by ester groups (positive band in 1750-1760  $\text{cm}^{-1}$  range, Figure III-5, Panel II, curve b-a). Each of these ester species would be formed by reacting with one silanol of the NFS pair (negative band pointed at 3743  $\text{cm}^{-1}$ ) and probably stabilized by hydrogen bonding with the second silanol of the NFS (Figure III-6 A), although on G/AX additional adsorption on isolated silanols may occur. This may appear in contradiction with calculations by Rimola et al. showing that ester formation between Gly and silanol is

endergonic<sup>164</sup>; however, this reaction is a condensation implying water elimination, and in conditions of low water activity it may still be possible.

The  $\beta$ -turn configuration that predominates in the initial stage involves four Gly monomers and can be stabilized by its terminal -NH<sub>2</sub> group pointing towards the silica surface and thus allowing H-bond to silanols (Figure III-6 A).<sup>214</sup>

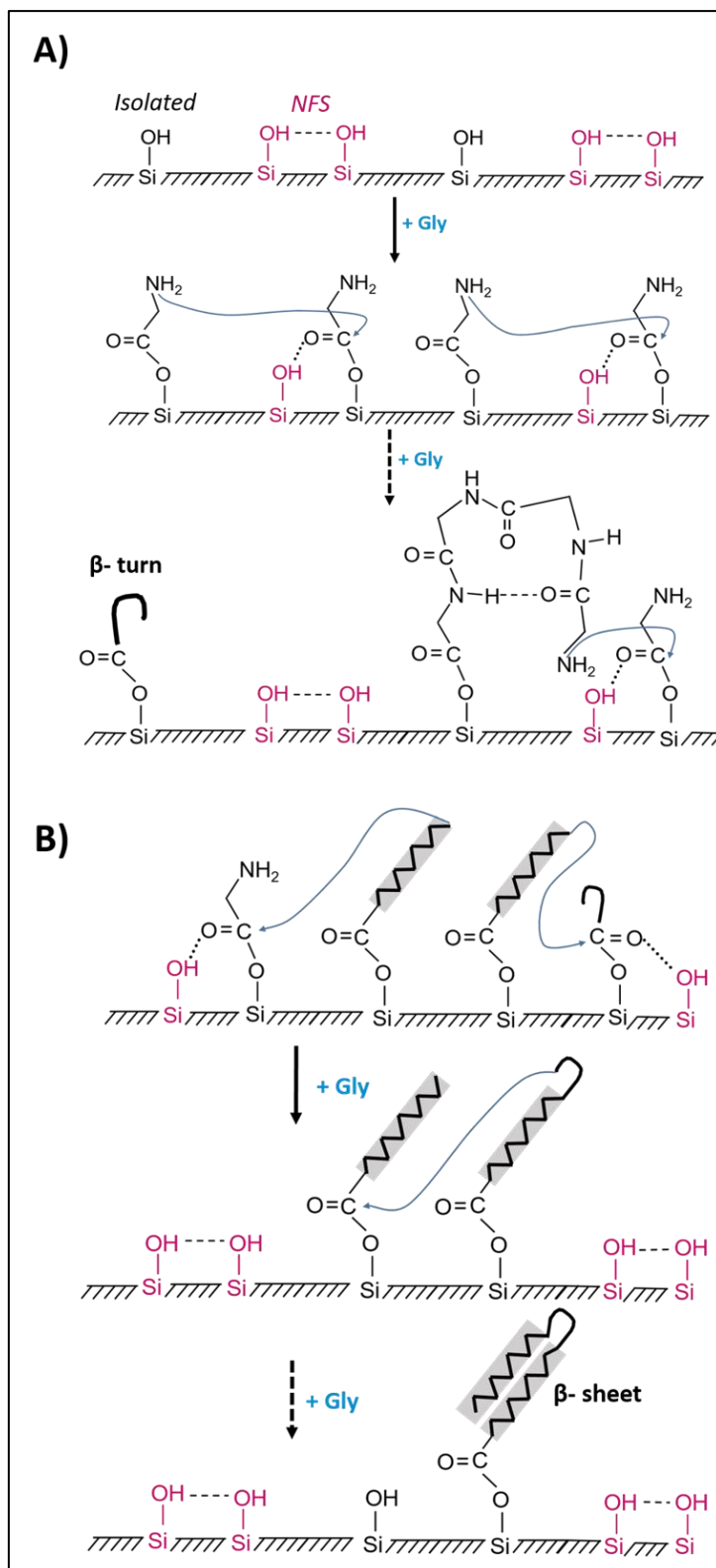


**Figure III-6:** Suggested scheme for (A)  $\beta$ -turn, (B) ligation and  $\beta$ -sheet structures formation.

As regards the mechanism of the peptide bond condensation, esterification of the Gly carboxylic terminus is expected to decrease the electron density on the ester carbon atom,

favoring a nucleophilic attack from the amine terminus of another Gly molecule, although the complete story probably also involves participation of neighboring H-bonded silanols (scheme 1A).<sup>169</sup> Another difficulty is that if the mechanism involved a Gly coming from the gas phase, it should result in desorption of the Gly residue, or of the polyglycine chain, that was initially bound to the surface as an ester.

We suggest that after a certain threshold of ester density on the surface, the grafted chains start to interact with each other (curves c-b, d-c, Figure III-5, Panel II); then, the terminal amino group of one surface-linked chain attacks the activated ester function of another poly-Gly chain (Figure III-6 B).<sup>67</sup> This results in the destruction of some esters and regeneration of the corresponding NFS and isolated silanols (negative band in 1750-1760  $\text{cm}^{-1}$  range and positive one at 3743 and 3747  $\text{cm}^{-1}$ , respectively). The substantial chain growth entailed by these condensations results in the formation of  $\beta$ -sheets conformations as major elements. After this process that might be called “ligation”, the regenerated NFS can form ester groups with gas-phase Gly again, then giving rise to new  $\beta$ -turn chains (curve e-d, Figure III-5, Panel II). At later stages (curves g-f and h-g, Figure III-5, Panel II), the surface is largely occupied by ordered structures that continue to elongate under continuous feeding of Gly monomers in keeping with the progressive increase in intensities of amide I and II until 20 h CVD (Figure III-5, Panel I).

Finally, one can wonder why FA pretreatment causes the surface to accumulate more poly-Gly chains. If, as we suggested, NFS groups play an important role in chain growth, it could mean that FA treatment creates more NFS. This could indeed be the case because FA could react with constrained siloxane rings, yielding after hydrolysis pairs of silanols that would be in the NFS range.<sup>169</sup>

#### **III.3.4. Effect of hydration/dehydration cycles on grafted poly-Gly**

Since Martra et al. have reported that poly-Gly rearrange on the TiO<sub>2</sub> surface to form self-assembled aggregates when contacted with water vapor,<sup>25</sup> G/F-AX (Figure III-7) and G/AX (Figure A1- 7) were exposed to water vapor (20 mbar) directly after the end of 20 h CVD to study the events that occur upon hydration. For G/F-AX, the IR profile collected after outgassing the excess of water vapor (Figure III-7, Panel I, curve b) shows a slight narrowing in the  $\nu_{\text{NH}}$  band of poly-Gly in the 3315-3307 cm<sup>-1</sup> range and the appearance of a component at 1640 cm<sup>-1</sup> in the region of the amide I band. The change in the  $\nu_{\text{NH}}$  band upon hydration is more significant on G/AX (Figure A1- 7) that initially (before exposure to water vapor) showed less ordered structures than G/FA-X.

Subsequently, D<sub>2</sub>O adsorption/desorption cycles were performed after water vapor admission. Significant changes are observed on the spectrum collected after outgassing D<sub>2</sub>O at bt (Figure III-7, Panel I, curve c). The amide I band at 1640 cm<sup>-1</sup> changes in shape and increases in intensity. This band has a small NH in-plane bending component, and shifts by a few cm<sup>-1</sup> upon deuteration:<sup>211</sup> a precise analysis is difficult in a situation where deuterated and non-deuterated NH probably coexist. A more obvious evolution occurs in the region of the amide II mode (mostly a combination of NH in-plane bending and CN stretching). The original band located at about 1528 cm<sup>-1</sup> is partly, but not entirely consumed, while a new band attributable to the amide II' mode of deuterated peptide linkages appears at 1466 cm<sup>-1</sup>. Moreover, in the  $\nu_{\text{NH}}$  region, only the narrow component at 3307 cm<sup>-1</sup> is left upon D<sub>2</sub>O vapor admission; the broader component at 3400 cm<sup>-1</sup> completely disappears. These observations strongly suggest that the amide links in the poly-Gly chains belong to two different populations, one that is susceptible to H/D exchange, and another one that is not, being inaccessible and/or stabilized by strong H-bonding. The second explanation sounds more likely since this population gives sharp bands characteristic of well-ordered structures. Both narrow bands in the amide I and in the  $\nu_{\text{NH}}$  regions that resist the H/D exchange are more intense in G/F-AX in comparison with G/AX.



This would reflect the higher amount of ordered poly-Gly formed on G/F-AX compared to G/AX. The second derivatives of the spectra (Figure III-7, Panel II, curve c) seem to indicate that random coils ( $1642\text{ cm}^{-1}$ ) are transformed into  $\beta$ -sheets ( $1617$ ,  $1636$ ,  $1684$ ,  $1694\text{ cm}^{-1}$ ) and helices ( $1650$ ,  $1657\text{ cm}^{-1}$ ) after H/D exchange while some  $\beta$ -turn initiators ( $1669$ ,  $1677\text{ cm}^{-1}$ ) are still present at the surface.

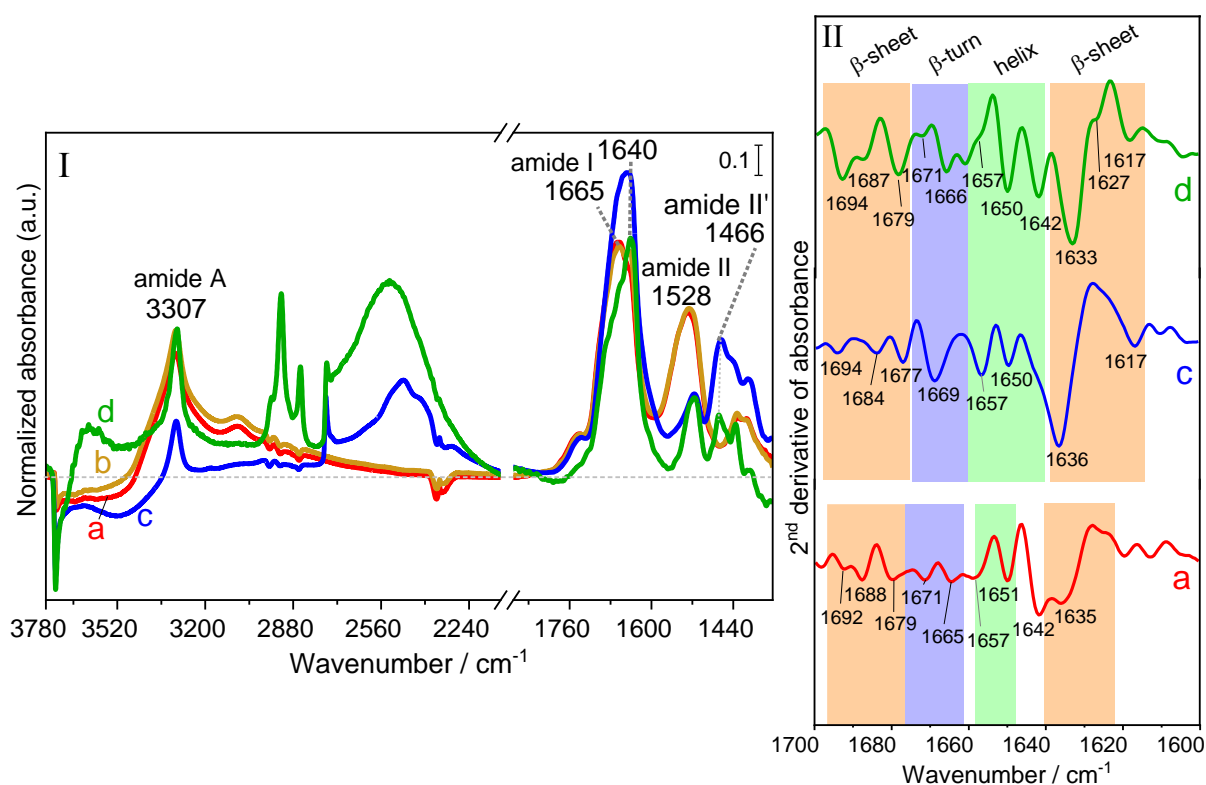


**Figure III-7:** Panel (I): IR spectra of G/F-AX submitted to successive treatments: (a) directly after Gly sublimation for 20 h, (b) after subsequent contact with water vapor (20 mbar) and outgassing for 30 min at bt, (c) after H/D exchange and then outgassing of  $\text{D}_2\text{O}$  for 30 min at bt and (d) after sample washing with ultrapure water followed by H/D exchange (then bt outgassing).

The spectrum of the material obtained before the start of the CVD process is subtracted as a baseline.

Panel (II) shows the second derivative of the IR spectra (a), (c) and (d) in the amide I region.

In order to assess the stability of the self-assembled aggregates formed on the surface, G/F-AX was washed with ultrapure water, then dried at rt and outgassed at bt before performing an H/D exchange. IR measurements (Figure III-7, Panel I, curve d) show that the  $\nu_{\text{NH}}$  band at

3307  $\text{cm}^{-1}$  becomes even narrower and is not affected by H/D exchange. Moreover, the peptides bands are still present with significant intensities, and the minima of the amide second derivative spectra (Figure III-6, Panel II, curve d) are compatible with the presence of  $\beta$ -sheets (1617, 1627, 1633, 1679, 1687, 1694  $\text{cm}^{-1}$ ) with some helices (1642, 1650, 1657  $\text{cm}^{-1}$ ) and  $\beta$ -turns (1666, 1671  $\text{cm}^{-1}$ ) conformations.<sup>211</sup> This confirms that the formed poly-Gly are in highly packed aggregates, anchored on the silica surface by ester bonds, which resist not only hydration and H/D exchange from the gas phase, but also washing in the presence of liquid water.<sup>215,216</sup>

The extraction yield of the washing procedure, used to analyze the products with HR-MS, has been evaluated by comparing the integrated areas of the IR spectra of the materials obtained after H/D exchange performed after adsorption of Gly and after subsequent washing with water (curves c and d, respectively), focusing on the 1570-1490  $\text{cm}^{-1}$  range, where the signals exclusively due to poly-Gly are present. For G/F-AX, the extraction yield has been estimated to be ca. 24%. In other words, 76% of the non-exchanged amide-containing molecules of the self-assembled structures resist washing and remain chemisorbed on the surface.

It is worth noting here that according to the literature, peptide chains with  $\beta$ -sheet structures are characterized by a high resistance to hydrolysis compared to helical and random-coil conformations. This long lifetime suggests the possibility of acting as stereo-selective templates for further peptide deposition in the emergence of primordial life.<sup>217</sup>

### **III.4. Conclusion**

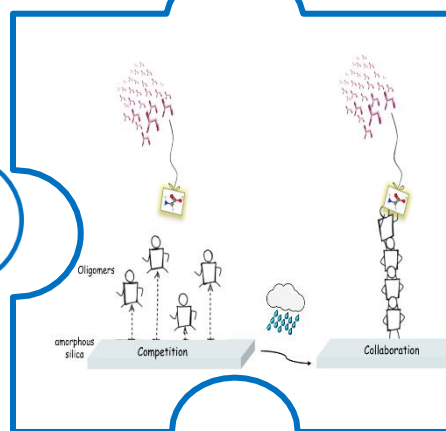
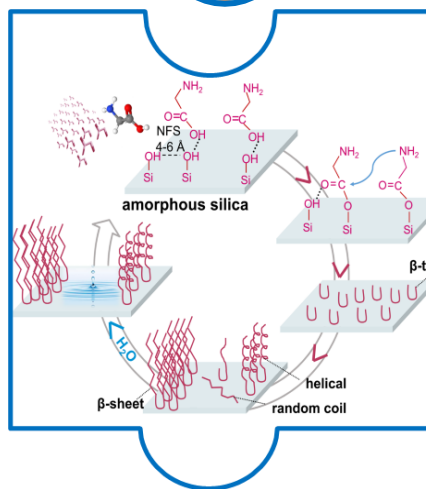
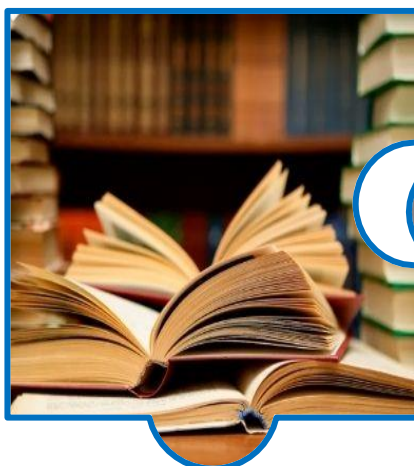
In comparison to previous studies, the novelty of the present work lies first in a deeper characterization of the successive steps of poly-Gly formation on silica surface. In CVD conditions, Gly seems able to bind covalently to the surface through the formation of ester

bonds at the expense of (probably) strained rings, isolated silanols and nearly-free silanol (NFS) pairs. Esterification of isolated silanols appears irreversible, while NFS seem able to interchange between esterified and free forms and thus to play a special role in surface reactivity. From these ester moieties, longer chains are formed, first in  $\beta$ -turns configurations, and later, through a process probably involving the ligation of neighboring chains, in longer and more ordered secondary structures including  $\beta$ -sheets. The density of chains can be increased by previous formic acid treatment.

The observation of secondary structures and their evolution through time are a second important observation with obvious interest for the rise in structural complexity at the origins of life. After a long enough reaction time with gas-phase Gly, a large part of the surface is occupied by highly organized poly-Gly chains that resist desorption and deuterium exchange.

An important question is why this system yields long linear polymers while many other studies have only reported the formation of the cyclic dimer diketopiperazine (DKP). This will be addressed in a forthcoming publication. As a general conclusion, the complexity of the phenomena observed proves the interest of bringing a surface science approach to the study of the origins of life.

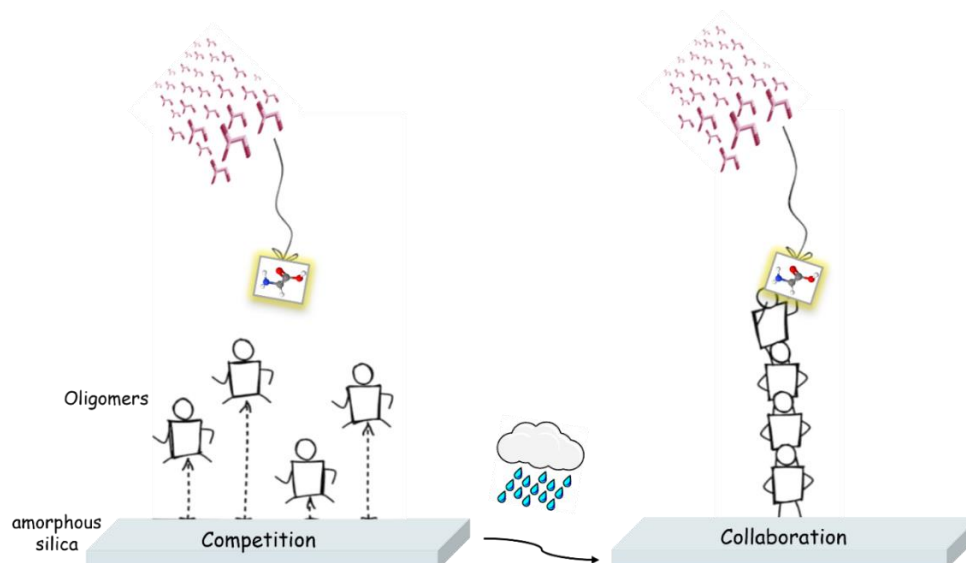
# IV. Chapter IV: Polypeptide chain growth mechanisms and secondary structure formation in glycine gas-phase deposition on silica surfaces



**The work presented in this chapter is published as a peer-reviewed article in the Journal of Physical Chemistry B, 2023.**

*El Samrout, O.; Berlier G.; Lambert J.F.; Martra G., Polypeptide chain growth mechanisms and secondary structure formation in glycine gas-phase deposition on silica surfaces. J. Phys. Chem. B 2023, 127, 3, 673–684*

Peptide formation by amino acids condensation represents a crucial reaction in the quest of the origins of life as well as in synthetic chemistry. However, it is still poorly understood in terms of efficiency, and reaction mechanism. In the present work, peptide formation has been investigated through thermal condensation of gas-phase glycine in fluctuating silica environments, as a model of prebiotic environments. In situ IR spectroscopy measurements under controlled atmosphere reveal that a humidity fluctuating system subjected to both temperature and water activity variations results in the formation of more abundant peptides compared to a dehydrated system subjected only to temperature fluctuations cycles. A model is proposed in which hydration steps result in the hydrolysis and redistribution of the oligomers formed during previous deposition in dry conditions. This results in the formation of self-assembled aggregates with well-defined secondary structures (especially  $\beta$ -sheets). Upon further monomers feeding, structural elements are conserved in newly-growing chains, with indications of templated polymerization. The structural dynamics of peptides were also evaluated. Rigid self-assembled structures with a high resistance to further wetting/drying cycles and inaccessibility to isotopic exchange were present in the humidity fluctuating system, compared to more flexible structures in the dehydrated system. The resistance and growth of self-assembled structures were also investigated for an extended duration of Gly deposition using isotope labeling.



## IV.1. Introduction

Among the different types of biomolecules reactions on mineral surfaces, amide/peptide bond formation through the condensation of amino acids is of high relevance due to its direct applications in various sectors ranging from bio/nanotechnology, and drug delivery<sup>194</sup>, to the quest of the origins of life<sup>88</sup>. A lot of research works have been devoted to study the mechanism, rate of amino acids polymerization reaction and the self-assembly of resulting peptides. In particular, in the field of prebiotic chemistry, systems consisting of a solid (mineral) surface, water and amino acid (AA) monomers were critically analyzed and evaluated for this reaction, including solid-gas, solid-liquid, solid-liquid-solid (mineral + aqueous solution + ice) and solid-liquid-gas, and so-called “fluctuating systems” undergoing wetting/drying (WD) cycles. However, the conclusions of these studies are most often purely empirical due to the lack of clear experimental data to support specific mechanisms for condensation and polymerization reactions. Each of these systems may be considered to represent the idealization of a particular prebiotic environment and in particular, the solid-gas system is representative of a dehydrated lagoon floor produced after the evaporation of the liquid phase.<sup>109</sup> One simplified experimental model to carry out the adsorption and polymerization of amino acids from the gas phase is by using chemical vapor deposition (CVD), a solvent-free method that can be conducted in mild reaction conditions without the use of activating agents<sup>25</sup>. The fluctuating solid-liquid-gas system with wetting-drying cycles simulates in the lab natural prebiotic variations of the experimental conditions that may have occurred on the prebiotic earth such as daily fluctuations of temperatures and seasonal fluctuations of humidity where hydration (flooding, tidal variation, rainstorms) and dehydration (evaporation, or exposure to the sun under prebiotic conditions) take place in a cyclic manner.<sup>88,108</sup>

It has been long ago suggested by Lahav et al.<sup>109</sup> that such fluctuating systems with both water content and temperature fluctuations should constitute the most favorable and

geologically relevant settings for prebiotic condensation reactions. The argument, which has been rephrased several times,<sup>218</sup> is that the drying phase drives the condensation reaction by removing water, a product of the condensation reaction, while the wet phase promotes the diffusion of reactants on the solid surface for a better reaction efficiency. Indeed, polymerization of various amino acids and their mixtures on several mineral phases subjected to WD cycles has been observed experimentally to yield oligopeptides up to at least the pentamers.<sup>110,219</sup> In particular, an experimental study dealing with the thermal condensation of Glycine (Gly) in fluctuating clay environments<sup>108</sup> showed that a system subjected to cyclic variations in both temperature and water content resulted in a higher yield of oligopeptides, as compared with one undergoing only temperature fluctuations (in this case, applied on wet systems).

Apart from peptides formation, the biomolecules-mineral-water interface is also important for prebiotic chemistry as it can promote the self-assembly of biomolecules, a possible step toward the formation of more complex structures. The study of self-assembling peptides has undergone a significant growth since the early 1990s due to their relevance in a large number of areas such as tissue engineering, biomedicine, synthetic biology and beyond.<sup>220,221</sup> Many studies have also demonstrated the self-assembly of peptide systems in the synthesis of nanomaterials. For instance, polyGly chains about 16 units long can form self-assembled aggregates containing both helical and  $\beta$ -sheet secondary structures on oxide surfaces including  $\text{TiO}_2$  and amorphous  $\text{SiO}_2$ , upon contact with water vapor after CVD deposition.<sup>25</sup> The natural abundance and low cost of silica stimulate current efforts to find catalytic routes for condensation and polymerization reaction on its surfaces.<sup>24,25</sup>

A previous paper has dealt with the initial steps of glycine polymerization on the silica surface upon deposition from the gas phase.<sup>222</sup> In the present work, we aim to study the effect of different environmental conditions on the extent and rate of the polymerization reaction and

especially on the self-assembly of three systems composed of amorphous silica (AX), a model of one of the most common mineral surfaces available on primitive Earth and other extraterrestrial bodies, glycine (Gly), the most prevalent amino acid in the earliest proteins, and water, the predominant solvent on the early Earth's surface. Namely, the three systems were subjected separately to: a) temperature fluctuations (TF) during chemical vapor deposition (CVD), b) both TF and humidity fluctuations (HF) cycles, and c) TF and HF cycles for an extended time of CVD (35 h) while using a silica surface subjected to conditions of high-water activity before the start of the polymerization. The types and relative concentrations of the secondary structures formed during the intermediate cycles of polymerization were assessed. Furthermore, the structural dynamics of the polypeptides were studied for the three systems, and related with the kinetics of H/D exchange.

Infrared (IR) spectroscopy was the major technique adopted in this work for in situ characterization of the growing peptides chains throughout glycine deposition. IR is highly sensitive, compared to other spectroscopic methods, to the H-bonding state and conformation of the different peptide groups. It has proven to be a useful and powerful technique in the study of protein structures, providing not only qualitative information on the presence of functional groups in organic compounds but also a quantitative estimation of the protein secondary structures yielding important structural and dynamical information of the peptides.<sup>182</sup>

While multinuclear solid-state NMR has been successfully used to amino acids transformations on silica,<sup>160,223</sup> it can only be applied after completion of the whole reaction, and it is difficult to avoid re-exposure to air. In the same way, circular dichroism (CD), also commonly used to study the secondary structures of proteins, requires a prior extraction of the peptides from the surface to study their secondary structures. IR spectroscopy on the other hand, does not require extensive sample preparation or extraction and can be applied without exposure to air.<sup>212</sup> Moreover, the use of isotope labeling during IR spectroscopy measurements on



biomolecules may help identify subtle conformational changes in the peptide secondary structures and probe specific local structures dynamics in the system, using deuterated water (D<sub>2</sub>O) instead of light water (H<sub>2</sub>O) or amino acids labeled with <sup>13</sup>C, <sup>15</sup>N, etc.<sup>224</sup>

## **IV.2. Experimental Section**

### **IV.2.1. Materials**

A pyrogenic amorphous silica Aerosil OX 50 (AX) (SiO<sub>2</sub> content  $\geq$  99.8 wt%, specific surface area 50 m<sup>2</sup>.g<sup>-1</sup>), provided by EVONIK was used. Natural abundance glycine as well as <sup>13</sup>C (99 atom% <sup>13</sup>C) and <sup>15</sup>N-enriched (98+ atom% <sup>15</sup>N) glycine were purchased from Sigma-Aldrich. Deuterated water D<sub>2</sub>O (99.90 atom % D), a high-purity product obtained from Sigma-Aldrich and Milli-Q water (Millipore system) were subjected to several freeze-pump-thaw cycles before admitting them in the IR cell through the vacuum line.

### **IV.2.2. Dehydration of the silica surface**

Silica pellets were outgassed in vacuum in the IR cell at room temperature (rt) or 160 °C (designated later as AX<sub>rt</sub> and AX<sub>160</sub> respectively) to remove the physisorbed water molecules and reach a good surface dehydration level.

### **IV.2.3. Gly adsorption from the gas phase under temperature fluctuations (CVD with TF)**

After dehydration of the silica surface under vacuum, glycine (Gly) sublimation and polymerization on the silica surface were carried out at 160 °C using the chemical vapor deposition (CVD) method described by Martra et al.<sup>25</sup>. Briefly, the pre-treated pellet of silica, held in a gold frame, was placed next to a pellet of Gly within a section of the IR cell acting as a reactor; a tubular furnace was placed around this part to heat it to 160 °C under a static vacuum. The temperature was measured and controlled using a thermocouple placed on the

external part of the cell during the reaction. The IR cell was connected to a liquid nitrogen trap to remove any water generated during the reaction from the system. For IR spectra collection, the temperature was cooled down to room temperature (rt) and the silica pellet was moved to the part of the cell equipped with CaF<sub>2</sub> windows.

The sublimation of Gly on the silica surface was performed in successive steps as following: (i) heating the experimental device (silica and Gly pellets) from room temperature to 160 °C for 2.5 h; (ii) cooling from 160 °C to room temperature (rt) for 14 h; (iii) repetition of the steps (i) and (ii) n times (n = number of temperature fluctuation cycles). After each cycle, the sample was subjected to in situ IR measurements to follow the chemical transformation of the amino acid on the surface.

#### **IV.2.4. Hydration fluctuations (HF) cycles procedure, and H/D isotopic exchange**

Before water vapor exposure, the sample, held in a gold frame in the IR cell, was outgassed under vacuum at rt until the residual pressure ( $< 10^{-3}$  mbar) was achieved. Water vapor under saturating pressure was then admitted at rt to the surface of the sample which was kept under water vapor while collecting in situ IR spectra until invariance of spectra (ca. 15 min). After that, the water vapor was removed by outgassing at rt until the invariance of spectra. For H/D isotopic exchange, the same procedure was followed using D<sub>2</sub>O vapor, for many cycles until invariance of in situ IR spectra.

#### **IV.2.5. Wetting/drying (WD) cycles with liquid water**

After the experiments involving Gly adsorption and H<sub>2</sub>O and D<sub>2</sub>O vapor exposures, the sample pellet was removed from the cell, manually ground in an agate mortar, then suspended in 0.5 ml of Milli-Q water. The suspension was shaken by a vortex mixer for 15 min, then centrifuged for 10 min at 10000 rpm. After removal of the supernatant, the solid was subjected to a second washing. The two aliquots of the aqueous solution obtained were mixed for analysis by high-resolution mass spectrometry.

The same procedure of wetting/drying cycles was applied to a bare silica before any Gly deposition.

After washing, the solid samples were dried under nitrogen flow then pelletized again and introduced in the IR cell for subsequent IR measurements after outgassing at rt under vacuum.

#### **IV.2.6. Description of the samples**

Three systems were prepared under different combinations of treatments as following:

- a)  $G_{TF}/AX_{160}$ : (i) dehydration of silica at 160 °C for 2 h under vacuum; (ii) 8 cycles of CVD with TF between rt and 160 °C (corresponding to a total time of 20 h Gly sublimation).

$G_{TF}/AX_{rt}$  was also prepared for the sake of comparison, using the same procedure but with a dehydration at rt instead of 160 °C before CVD.

- b)  $G_{TFHF}/AX_{160}$ : (i) dehydration of silica at 160 °C for 2 h under vacuum; (ii) 3 cycles of CVD with TF between rt and 160 °C; (iii) several cycles of HF; (iv) 5 cycles of CVD with TF between rt and 160 °C (corresponding to a total time of 20 h Gly sublimation).

In other words, this sample differed from  $G_{TF}/AX_{160}$  by the insertion of HF cycles between the 3<sup>rd</sup> and 4<sup>th</sup> steps of Gly CVD.

- c)  $G_{TFHF}/AX_{WD}$ : (i) WD cycles of the silica support; (ii) 8 cycles of CVD with TF between rt and 160 °C; (iii) several cycles of HF; (iv) several cycles of WD; (v) 6 cycles of CVD with TF between rt and 160 °C (corresponding to 35 h Gly sublimation in total).

All samples were subjected to HF cycles followed by H/D exchange at the end of the polymerization reaction.

#### **IV.2.7. Infrared (IR) spectroscopy**

IR spectra were recorded using a Bruker Vector 22 instrument with a DTGS detector at beam temperature (bt) (ca. 50 °C) in a spectral window of 400 - 4000  $\text{cm}^{-1}$  using a resolution

of  $4 \text{ cm}^{-1}$  and accumulating 64 scans to have a good signal to noise ratio. For the IR measurements, the powder of pristine silica (or of samples obtained after the thermal treatment) was pressed into self-supporting pellets and placed in a traditional IR cell with  $\text{CaF}_2$  windows, equipped with a valve to be connected to a vacuum line of a residual pressure of ca.  $1.0 \times 10^{-5}$  mbar where all experiments of adsorption/desorption were carried out in situ.

#### **IV.2.8. X-ray diffraction (XRD)**

X-ray powder diffraction patterns for the samples were recorded on a PANalytical X'Pert diffractometer using a  $\text{Cu K}\alpha$  ( $\lambda=1.5405 \text{ \AA}$ ) radiation source and working at 30 mA and 40 kV. The diffractograms were recorded with a scanning range set between  $10$  and  $45^\circ 2\theta$ , a step size of  $0.01^\circ 2\theta$ , and a dwell time of 1 s per step.

#### **IV.2.9. High-resolution mass spectrometry (HR-MS)**

The supernatant obtained from each washing suspension was removed and used for analysis by high-resolution mass spectrometry using an LTQ Orbitrap mass spectrometer (Thermo Scientific) equipped with an atmospheric pressure interface and an electrospray ionization (ESI) source in negative ion mode. The source voltage was set to 4.48 kV. The heated capillary temperature was maintained at 270 K. The mass accuracy of recorded ions (vs. calculated) was  $\pm 1 \text{ mmu}$  (without internal calibration). The samples were delivered directly to the mass spectrometer via a Hamilton microliter syringe at a constant flow ( $10 \mu\text{L}/\text{min}$ ). Data acquisition and processing were performed using the Xcalibur software.

#### **IV.2.10. Peak fitting**

The IR spectra were analyzed using OriginPro 2018 (OriginLab Corporation, Northampton, MA, USA). Non-linear fitting of the peaks in the spectral data was performed using a peak analyzer (adopting the Levenberg-Marquardt algorithm). Baseline corrections were executed using a second derivative (zeroes) method to find anchor points and determine

the baseline. Hidden peaks were specified using a second derivative method followed by smoothing with the 30- 40 points Savitsky–Golay function of a polynomial order of 2. The peak fitting was then carried out using the Gaussian function. (Equation (1));

$$y = y_0 + \frac{A e^{-\frac{4 \ln(2)(x-x_c)^2}{w^2}}}{w \sqrt{\frac{\pi}{4 \ln(2)}}} \quad (1)$$

where  $y_0$  = offset, A = area,  $x_c$  = center, W = Gaussian full width at half maxima (FWHM).

The baseline, peak center, and peak width parameters were fixed and released during fitting to help initializing the parameters. The iteration procedure was stopped when the best fit was reached (reduced  $\chi^2 < 1 \times 10^{-9}$ ). The secondary structures contents are reported as integrated areas of the corresponding fitted bands. Their percentage was evaluated by dividing the areas assigned to a specific secondary structure by the total area under the amide I band (most commonly used band to study the secondary structure of peptides, 1600-1700  $\text{cm}^{-1}$ ). The assignments of the various components were made using the ranges corresponding to structural elements as reported in Barth's review.<sup>225</sup> Note that the  $\beta$ -sheet structure gives rise to two components in separate ranges due to excitonic splitting, and that amide I deconvolution is facilitated in the case of polyglycine by the absence of absorption due to side chain groups.<sup>226</sup>

### IV.3. Results And Discussion

Amorphous silica of the AEROSIL type has been used in several works dealing with the abiotic polymerization of amino acids.<sup>25,120,227</sup> In our study, we selected the amorphous AEROSIL OX 50 (AX) silica, characterized by a specific surface area (SSA) of ca. 50  $\text{m}^2\cdot\text{g}^{-1}$ , high enough to get clearly detectable IR signals of the surface species, and which had been previously demonstrated to cause the formation of linear oligopeptides from amino acids.<sup>25</sup>

### **IV.3.1. Difference in the polymerization reaction between a system subjected to temperature fluctuations and another one subjected to both temperature and humidity fluctuations**

After dehydration of the silica at 160 °C under vacuum for 2 h, two samples were prepared with different procedures as explained in the experimental section: one subjected to temperature fluctuations (TF) during the adsorption of Gly monomers on the surface by CVD, and the other one to both TF and hydration fluctuations (HF) cycles. The samples are labeled as  $G_{TF}/AX_{160}$  and  $G_{TFHF}/AX_{160}$ , respectively.

The IR difference spectra of  $G_{TF}/AX_{160}$  and  $G_{TFHF}/AX_{160}$  samples during the successive cycles of the 20 h CVD are presented in Figure IV-1 A and B respectively.

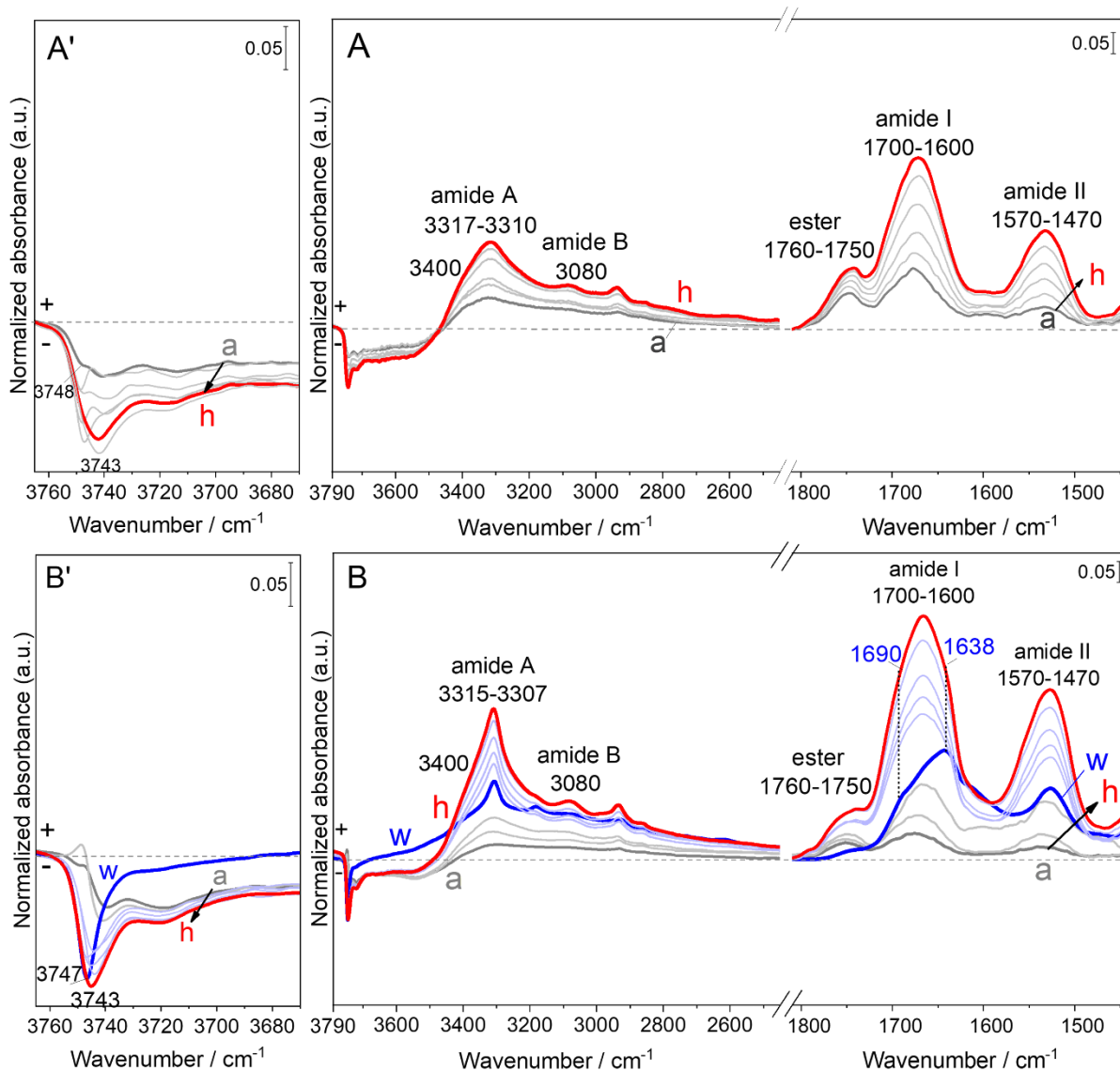


**Figure IV-1:** IR difference spectra resulting from Gly sublimation at 160 °C by CVD carried out from 2.5 h (a) to 20 h (h) on the two samples: A)  $G_{TF}/AX_{160}$ , Gly adsorbed on silica pre-treated at 160 °C, and B)  $G_{TFHF}/AX_{160}$ , Gly adsorbed on silica pre-treated at 160 °C and subjected to intermediate HF cycles during CVD.

In panels A' and B', the intensities in the silanols OH stretching region are enhanced for the sake of clarity. Gray curves show intermediate sublimation steps of 2.5 h. Light blue curves show intermediate CVD steps of 2.5 h following the HF cycle (bold blue curve (w)).

The corresponding spectrum of the material obtained before the start of CVD process ( $AX_{160}$ ) is subtracted as a baseline.

From the first CVD cycle, the amide I ( $1700-1600\text{ cm}^{-1}$ ) and amide II ( $1570-1470\text{ cm}^{-1}$ ) bands are observed, corresponding to  $\nu_{CO}/\delta_{NH}$  and  $\delta_{NH}/\nu_{CN}$  vibrations respectively. The high intensity ratio of amide II to amide I is an indication of the formation of linear peptide chains instead of

cyclic ones, while the band at 1760-1750  $\text{cm}^{-1}$  may be assigned to ester groups<sup>99</sup> formed between the peptide chains and surface silanols.<sup>222</sup> Each step of glycine CVD causes an increase of the ester groups (positive signal in the difference spectra of Figure IV-1A and B) together with a decrease of the nearly-free silanols (NFS) associated with the band at 3743  $\text{cm}^{-1}$ <sup>208</sup> (negative signal in the difference spectra of Figure IV-1A' and B'): both ester and NFS represent crucial elements for monomers activation and polymerization.<sup>222</sup> Further confirmation for the formation of linear peptides can be found in the amide A (3315-3307  $\text{cm}^{-1}$ ) and B (3080  $\text{cm}^{-1}$ ) bands that arise from the  $\nu_{\text{NH}}$  in the peptide units. In this sample, the amide A signal is broad and probably composite.

Both treatments illustrated in Figure IV-1 A and B start with three cycles of glycine CVD, and indeed the spectra up to that point are very similar, confirming the reproducibility of the experiment.

After the first three CVD cycles,  $\text{G}_{\text{TFHF}}/\text{AX}_{160}$  was subjected to HF cycles, resulting in spectrum (w) in Figure IV-1 B, recorded after outgassing under vacuum, which shows significant changes in the  $\nu_{\text{OH}}$  pattern and in the shape of the peptide bands. For the  $\nu_{\text{OH}}$  region (Figure IV-1B'), the admission/outgas of the water vapor results in modifications of the negative band in the silanol groups region, which indicates that the interaction of the silica surface with water vapor changed the Si-OH population. More specifically, NFS consumed during the first CVD steps are restored (the signal at 3743  $\text{cm}^{-1}$  becomes less negative), and isolated silanols are removed (sharp negative signal at 3747  $\text{cm}^{-1}$ ). Regarding the peptide bands, an important change in the shape and intensity of the amide I band is seen with the appearance of separate components at 1638 and 1690  $\text{cm}^{-1}$ , associated to the formation of  $\beta$ -sheet conformations<sup>228</sup> (more discussion on this matter in Figure IV-2). Moreover, a significant narrowing of the amide A band occurs along with a further increase in the intensity of the amide II band. This is coupled with a strong decrease in the intensity of the ester band, although it does not disappear completely (Figure



IV-2 B, b'). When glycine CVD resumes, the amide I and II bands for  $G_{\text{TFHF}}/\text{AX}_{160}$  exhibit an important, and abrupt increase with respect to the sample  $G_{\text{TF}}/\text{AX}_{160}$  (see Figure A2-1 in Appendix 2). Later on, the amide I intensity increases at the same rate in both samples. The narrow amide A component keeps growing during the subsequent steps for  $G_{\text{TFHF}}/\text{AX}_{160}$  while a broader component becomes apparent at higher wavenumbers (around  $3400\text{ cm}^{-1}$ ). While the band associated to the ester groups ( $1760\text{-}1750\text{ cm}^{-1}$ ), which represent the anchors of the peptide chains to the silica surface, undergoes a continuous increase in intensity along the 20 h CVD for  $G_{\text{TF}}/\text{AX}_{160}$  (Figure IV-2 A, a'), resuming CVD after the HF cycles ( $G_{\text{TFHF}}/\text{AX}_{160}$ ) abruptly restores it to a rather high intensity, after which only a negligible increase is observed (Figure IV-2 B, b').

All of these observations can be explained by the following scenario: glycine CVD causes both an increase in the length of already existing peptide chains by monomers condensation, and the appearance of new chains by ester formation with NFS centers.<sup>222</sup> Ester formation is normally slow because access of the Gly monomers to the surface is partly hindered by the growing peptide chains. When water vapor is admitted, some of the ester links are hydrolyzed and the corresponding peptide chains are detached from the surface. They become partly mobile and able to rearrange, forming regularly H-bonded aggregates with other chains. These highly self-organized aggregates are characterized by the narrow amide A band, and a specific signature in the amide I and II regions (see below). When glycine is readmitted, newly freed, NFS-rich regions on the surface quickly react with glycine monomers to form nucleating sites for additional chains, following which both aggregated and newly formed chains start growing again. More specifically, we believe that these two types of chains correspond to the two components in the amide A region: well-organized, regularly H-bonded chains to the narrow band at  $3300\text{ cm}^{-1}$  as already mentioned, and more disordered, weakly H-bonded chains to the

broader band around  $3400\text{ cm}^{-1}$ . This correlation of the amide A position with the H-bonding state is in line with previous observations<sup>229</sup> and theoretical calculations.<sup>230</sup>

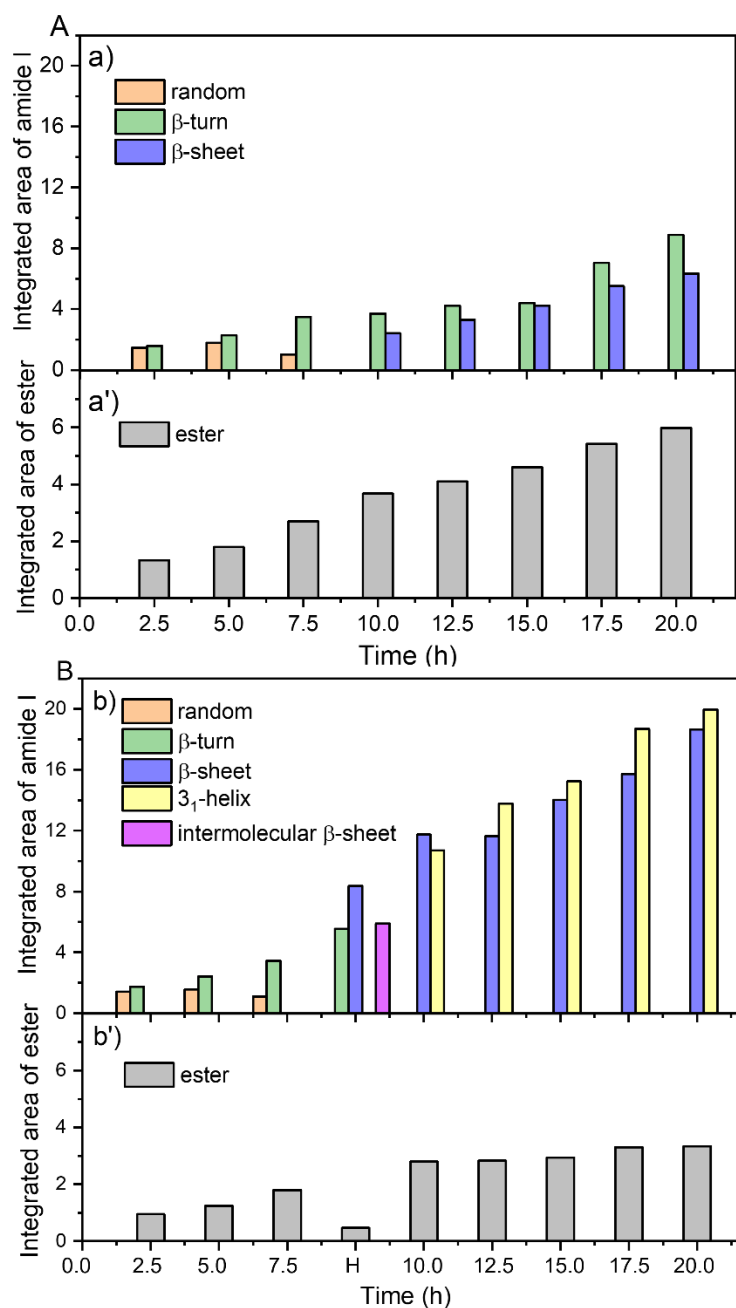


**Figure IV-2:** Evolution of (a) and (b) the absolute intensities of the different types of secondary structures and (a') and (b') integrated area of ester groups as a function of time during Gly deposition by CVD during the different cycles on the two samples: A) G<sub>TF</sub>/AX<sub>160</sub> and B) G<sub>TFHF</sub>/AX<sub>160</sub>.

The different integrated areas are obtained as a result of a peak fitting done on the ester ( $1760\text{-}1750\text{ cm}^{-1}$ ) and amide I ( $1700\text{-}1600\text{ cm}^{-1}$ ) bands.

The amide I band is very sensitive to the secondary structure of peptides and often used to identify it. Therefore, for each CVD cycle, we identified, separated and quantified its components using an enhanced peak fitting method based on the second derivative of the IR profiles. The absolute intensities of each secondary structural components are reported for both  $G_{TF}/AX_{160}$  and  $G_{TFHF}/AX_{160}$  in Figure IV-2 (A a and B b, respectively). The relative contents of the different secondary structures (see experimental part) have also been evaluated as percentage values for both samples. The integrated areas of the ester bands, already discussed above, are also reported as a function of the CVD time (Figure IV-2 A a' and 2 B b').

The quantitative analysis of the secondary structures shows the fast initial formation of random and  $\beta$ -turn conformations, representing about 45 and 55% respectively of the total amide I band after the first CVD cycle. For the following two CVD cycles (up to 7.5 h CVD), the amount of  $\beta$ -turn conformations increases progressively (up to 77%) at the expense of the random structures. For  $G_{TF}/AX_{160}$  (Figure IV-2 A a), a significant transition is observed after 10 h CVD, where the polyGly chains start forming more ordered structures, consisting of  $\beta$ -sheets, while random chains have disappeared. The relative proportions of  $\beta$ -sheets and  $\beta$ -turns vary little until the end of the 20 h CVD, where the proportion is 42% to 58%.

On  $G_{TFHF}/AX_{160}$ , the distribution of secondary structures is similar to  $G_{TF}/AX_{160}$  for the first three cycles of CVD (Figure IV-2 B b), confirming the reproducibility of the observations. The HF cycles applied after that promote the significant formation of ordered structures, including 42%  $\beta$ -sheet and 30% intermolecular  $\beta$ -sheet while random coils disappear and  $\beta$ -turn conformations fall down to only 28% of the total band area (Figure IV-2 B). This is the stage where the integrated area of the ester band exhibits a significant decrease.

The following five CVD cycles show a mixture of ordered structures containing both  $\beta$ -sheets and  $3_1$ -helices as polyglycine II (PG II)<sup>216,231-236</sup> in comparable amounts (49% to 51% at the end of the 20 h CVD). This is coherent with the fact that N-terminal domains are usually rich

in 3<sub>1</sub>-helices formed due to self-assembly of peptides that results from hydration with a subsequent hydrogen bond formation.<sup>212,237</sup>

One may wonder why 3<sub>1</sub>-helices are formed in high quantity after the water exposition step, while only  $\beta$ -sheets are encountered in the sample that did not undergo such a step. One possibility is that detached chains formed by hydrolysis may either agglomerate to existing  $\beta$ -sheets (whose absolute abundance indeed increases) through the formation of hydrogen bonds of N-H $\cdots$ O=C among neighboring chains, or rearrange independently of them to form 3<sub>1</sub>-helices, which would not strongly interact with the surface. When CVD resumes however, the amounts of both types of secondary structures grow constantly, indicating that they can both impart their structure to newly formed chains. These transformations are sketchily summarized in Figure IV-3.

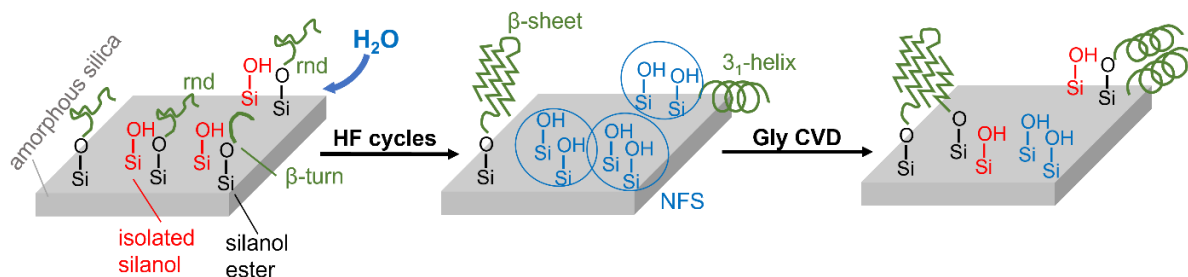


**Figure IV-3:** Suggested scheme for the polymerization of peptides on amorphous silica during Gly CVD with intermediate HF cycles.

It is important to underline that during this step, pre-formed polyglycine chains exert a twofold templating influence on the newly formed ones. First, as already stated, they define the type of secondary structure that the latter will adopt. Second, judging from the absolute values of the amide I components in Figure IV-2, the agglomeration of new Gly monomers is faster and reaches higher final amount in G<sub>TFHF</sub>/AX<sub>160</sub>, containing 3<sub>1</sub>-helices and  $\beta$ -sheets, than in G<sub>TF</sub>/AX<sub>160</sub>. Therefore, it seems likely that gas-phase Gly monomers have a higher probability of condensing with the growing end of the corresponding chains because they are pre-positioned by H-bonding, in a form of template-directed synthesis.<sup>238</sup> In the origins of life field,

template-directed polymerization has long been tested for growing RNA chains<sup>239</sup>, but it is more surprising to find it at work for polypeptide chains. Note that if this interpretation is correct, the promoting effect on polyGly chain growth at this stage would only be indirectly due to the silica surface, as opposed to the direct implication of surface groups observed at the beginning of CVD.<sup>222</sup>

### IV.3.2. Structural dynamics of the peptide chains revealed by H/D exchange

After Gly CVD for 20 h, both  $G_{TF}/AX_{160}$  and  $G_{TFHF}/AX_{160}$  were exposed to HF cycles followed by  $D_2O$  vapor exposure until invariance of in situ IR spectra. The admission/outgas of water vapor on both samples at this stage results in a significant change in the peptide bands of the IR signals (data not shown). These changes in amide A, amide I and amide II bands were more clearly evidenced after subsequent  $D_2O$  adsorption/desorption cycles until invariance of spectra (Figure IV-4, panel I, spectra A and B).

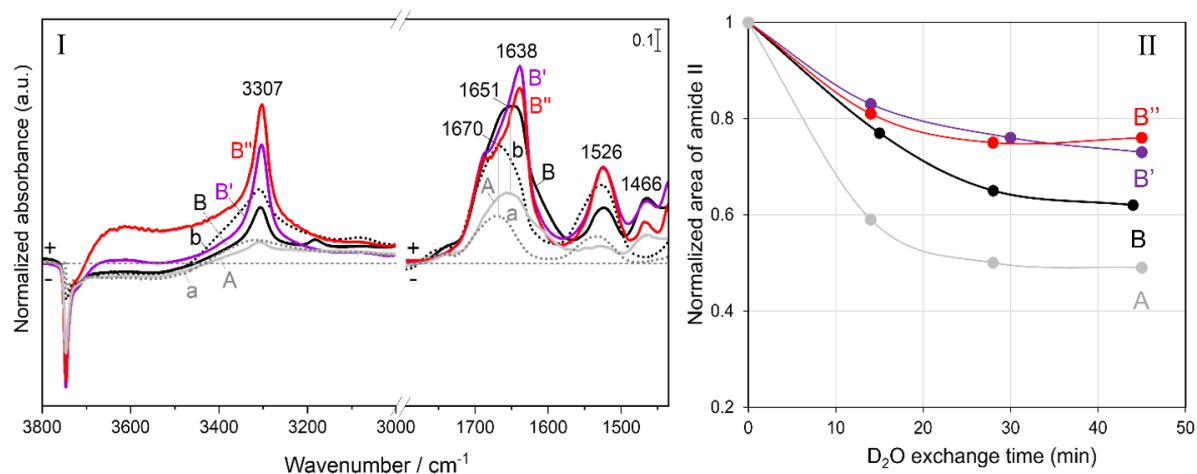


**Figure IV-4:** Panel (I) represents the IR difference spectra obtained (a and b) directly after Gly sublimation on silica for 20 h; (A and B) after subsequent H/D exchange and then outgassing of  $D_2O$  at rt until invariance of spectra, on the two samples:  $G_{TF}/AX_{160}$  and  $G_{TFHF}/AX_{160}$  respectively. For  $G_{TFHF}/AX_{160}$ , spectra obtained after a first washing with liquid water at rt (B') and a second washing with liquid water while heating at 70 °C (B'') on  $G_{TFHF}/AX_{160}$  are also displayed.

Panel (II) represents the evolution of the amide II band area during  $D_2O$  adsorption/desorption, after the end of the HF cycles (corresponding to time 0 for A and B) or after the end of the WD

cycles (at time 0 for B' and B''). In each case, band intensities have been normalized to a value of 1 at time = 0.

For both  $G_{TF}/AX_{160}$  and  $G_{TFHF}/AX_{160}$ , after 45 minutes of H/D exchange (curves A and B respectively), the amide II band exhibits a decrease in intensity while a new band appears at  $1466\text{ cm}^{-1}$  corresponding to the amide II vibration of the deuterated peptide linkages, sometimes called amide II' (this band is strongly displaced due to its significant NH bending component). It is noteworthy, however, that the original amide II linkages do not disappear completely, indicating that some protonated peptide links cannot be exchanged. This suggests that part of the peptide moieties is inaccessible to  $D_2O$  diffusion.

The IR profiles after H/D exchange also exhibit a narrow amide A band ( $3307\text{ cm}^{-1}$ ) as compared to the spectra (a and b) collected directly after Gly sublimation by CVD; in  $G_{TFHF}/AX_{160}$ , that clearly contained one narrow and one broad component, the broad component at  $3400\text{ cm}^{-1}$  has disappeared. In line of our previous assignments, this would mean that the weakly H-bonded structures can be exchanged by  $D_2O$ , while the strongly H-bonded ones resist exchange, as might have been intuitively expected. The deuterium-exchanged counterpart of the amide A band appears at around  $2760\text{ cm}^{-1}$ .

The amide I band (around  $1670\text{ cm}^{-1}$ ) is not expected to be strongly shifted by H/D exchange, but still it undergoes a change in shape and intensity with a shift of its maximum to  $1651\text{ cm}^{-1}$  as a result of a decoupling of vibrations due to the transformation of some N-H moieties in amide I to N-D ones.<sup>25</sup>

Both phenomena are more clearly marked for  $G_{TFHF}/AX_{160}$  (curve B, Figure IV-3, Panel I) as compared to  $G_{TF}/AX_{160}$  (curve A, Figure IV-4, Panel I) which reflects the higher amount of ordered self-assembled structures formed on the surface of the former. In order to study the resistance of these self-assembled structures on  $G_{TFHF}/AX_{160}$  to harsher treatments, the sample was subjected to a first set of several cycles of wetting/drying (WD) with liquid water at rt followed by a second set of several cycles of wetting with liquid water at  $70\text{ }^\circ\text{C}$ . The IR profiles

recorded after invariance of spectra at the end of each set (Figure IV-4, Panel I as curves B' and B'' respectively) show a further significant change in shape, increase in intensity and appearance of a sub-band at around 1638 cm<sup>-1</sup> for the amide I band. The latter is not due to adsorbed water because no strong absorbance is observed in the 3000-3500 cm<sup>-1</sup> region (O-H stretching), and it probably corresponds instead to the formation of more  $\beta$ -sheet structures.<sup>240</sup> Meanwhile, the narrow amide A band at 3307 cm<sup>-1</sup> increases in intensity while the amide II band shows resistance to deuteration (smaller ratio of the deuterated to the protonated species, as compared to the sample that had not been submitted to WD cycles). The latter feature may be explained by the fact that WD cycles induce the formation of a higher amount of ordered and tightly packed aggregates<sup>25</sup> that prevent the diffusion of the D<sub>2</sub>O molecules. These aggregates cannot be desorbed from the silica surface by washing with liquid water even at high temperature. Indeed, long oligoglycine peptides have a low water solubility<sup>216,241,242</sup>: they have more affinity for other polyglycine chains than for the aqueous phase.

In order to obtain more information on the structural dynamics (flexibility and degree of solvent accessibility of the formed peptides), the kinetics of H/D exchange in peptide links was followed by monitoring the residual intensity of the amide II band as a function of the sample exposure time to D<sub>2</sub>O during all the intermediate cycles of adsorption/desorption. The fraction of non-exchanged residues calculated following Eq. (2) is plotted as function of D<sub>2</sub>O exchange time in Figure IV-4, Panel II.<sup>243 244</sup>

$$\text{Fraction of non-exchanged residues} = \frac{\text{Amide II}_t}{\text{Amide II}_0} \quad (2)$$

where Amide II<sub>t</sub> and Amide II<sub>0</sub> represent the integrated area of amide II band at time t or time 0 of D<sub>2</sub>O exchange respectively.

The amide H/D exchange rate is faster in G<sub>TF</sub>/AX<sub>160</sub> (curve A) than in G<sub>TFHF</sub>/AX<sub>160</sub> (curve B). After the first 15 min of D<sub>2</sub>O adsorption/desorption cycles, around 41% of the amide groups of polyGly on G<sub>TF</sub>/AX<sub>160</sub> were deuterated, while only 23% were exchanged in G<sub>TFHF</sub>/AX<sub>160</sub>.

We also quantified the different types of secondary structures that evolved during the H/D exchange performed after 20 h CVD and hydration (Figure IV-5 A and B) and after WD cycles at rt (Figure IV-5, B') and at 70 °C (Figure IV-5, B''), since the kinetics of the amide H/D could be related to the rigidity of the peptide secondary structures.

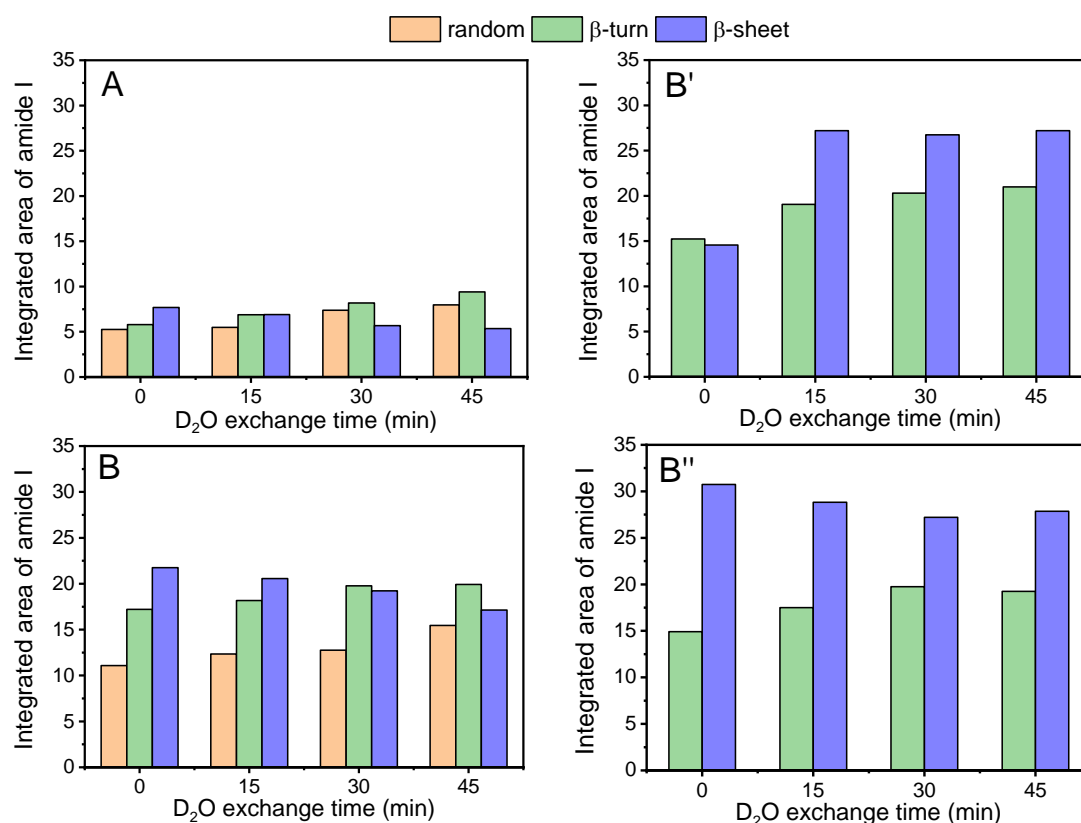


**Figure IV-5:** Evolution of the integrated area of the different types of secondary structures at the end of the HF cycles (time 0) and during subsequent D<sub>2</sub>O adsorption/desorption (time > 0) on the two samples:  $G_{TF}/AX_{160}$  (A), and  $G_{TFHF}/AX_{160}$  (B), and after washing of the latter with liquid water at rt (B') and at 70 °C (B'').

The different integrated areas are obtained from peak fitting in the amide I band range (1700-1600  $cm^{-1}$ ).

Quite unexpectedly, the final HF cycles caused the destruction of the  $3_1$ -helices that had been present after CVD in  $G_{TFHF}/AX_{160}$  (52% after 20 h CVD, Figure IV-2B), and were replaced by less organized structures:  $\beta$ -turns (32%) and random coils (20%; Figure IV-4B, time = 0). This is not unprecedented as proteins adsorbed on solid surfaces have been observed to lose their  $3_1$ -helices structural elements to random coils and turns upon exposure to water<sup>245</sup>. In  $G_{TF}/AX_{160}$ , the  $\beta$ -turns that represented the majority structure after CVD (58% after 20 h CVD, Figure IV-



2A) decreased to around 31%, probably transformed into random coils (28%; Figure IV- 4A, time = 0).

The remaining  $\beta$ -sheets represented 41% of the total secondary structures in  $G_{TF}/AX_{160}$  and 48% in  $G_{TFHF}/AX_{160}$  (Figure IV-5 A and B, time=0).

Altogether, after the HF cycles, the proportions of different secondary structure components were similar in  $G_{TF}/AX_{160}$  and  $G_{TFHF}/AX_{160}$ , although the global intensity of the amide bands was higher in the latter.

It might have been expected that the exchangeable fraction of peptide chains corresponds to the  $\beta$ -turn and random conformations since they present disordered, shorter and/or more flexible structures that should allow easier  $D_2O$  diffusion. At the end of the H/D exchange treatments, the exchanged percentage of peptide chains reached 52% for  $G_{TF}/AX_{160}$  and 38% on  $G_{TFHF}/AX_{160}$  (Figure IV-4, Panel II), as compared to 76% and 67% respectively for the  $\beta$ -turn + random coils (Figure IV-5 A and B, respectively at time = 45min). The trend is the same for the two observables, but the exchanged amounts remain smaller than the disordered configurations contents. Possibly, even some of the disordered structures are not quickly exchangeable, but precise quantification could also be complicated by differences in the extinction coefficients.

A further complication is that during  $D_2O$  exchange (Figure IV-5 A and B, time > 0), the amount of  $\beta$ -sheet slightly decreased while those of  $\beta$ -turns and random coils increased for both samples.  $D_2O$  vapor, like  $H_2O$  vapor in the HF cycles, seems to turn ordered into disordered structures, but the kinetics of this disordering is slow.

$G_{TFHF}/AX_{160}$  was submitted to WD cycles at rt, and while heating at 70 °C. A conspicuous effect of these washing treatments is the disappearance of the random coil components in the deconvolution of the amide I (Figure IV-5 B and B'). Most likely, these correspond to rather short, and therefore more soluble chains that may be eliminated by washing. The peptide chains

remaining on the surface are well-ordered, strongly H-bonded aggregates, consisting in a majority of  $\beta$ -sheets (around 60% of the integrated amide I area, Figure IV-5B' and B''), as was already apparent from the discussion of Figure IV-4, and therefore the amount of H/D exchange is limited (25% after 45 min; Figure IV-4, Panel II, curves B' and B'' respectively). In addition, the exchange kinetics is slower with respect to what is observed before WD cycles (Figure IV-4, Panel II, curves A and B).

### **IV.3.3. Effect of HF and WD cycles on Gly deposition for extended durations.**

In the following part, we study the deposition of glycine on strongly hydrated silica surfaces. It is known that the nature and local arrangements of the silica surface groups (silanols and siloxane rings) may induce either a hydrophobic or a hydrophilic behavior, respectively characterized by a heat of water adsorption lower or higher than the latent enthalpy of liquefaction ( $44 \text{ KJ.mol}^{-1}$ ).<sup>246</sup> In fact, it has been found that the surface density of silanol groups on the amorphous silica surface is simply related with the hydrophobic/hydrophilic character: a silica surface with  $4\text{-}5 \text{ Si-OH/nm}^2$  is hydrophilic since water molecules adsorb through strong H-bonding to silanol sites, while a surface with  $1\text{-}2 \text{ Si-OH/nm}^2$  is hydrophobic because most water molecules interact with the siloxane bridges.<sup>148,149,247</sup> Silica AX50 has a well-defined heat of water adsorption estimated to ca.  $40 \text{ KJ.mol}^{-1}$ , i.e., below the latent enthalpy of liquefaction<sup>248</sup>; thus, it may be considered as somewhat hydrophobic due to a relatively low concentration of silanol groups. This native silica, after outgassing at rt, is labeled as AX<sub>rt</sub>. In parallel, another sample was prepared where several WD cycles were applied to the silica support, also followed by an outgas under vacuum at rt (labeled hereafter as AX<sub>WD</sub>). The corresponding IR profile obtained, compared to that of AX<sub>rt</sub> in Figure A2- 2, showed a strong decrease of the band at  $3747 \text{ cm}^{-1}$  accompanied with a significant positive broad band centered at  $3450 \text{ cm}^{-1}$ , which indicates the transformation of the isolated silanols to H-bonded ones due

to their interaction with adsorbed water. This was coupled with the appearance of an intense narrow band peaked at  $3742\text{ cm}^{-1}$  that corresponds to the formation of nearly-free silanols (NFS). Indeed, several studies have demonstrated that the contact of silica with  $\text{H}_2\text{O}$  at room temperature can result in the fast opening of the highly strained siloxane bridges such as  $(\text{SiO})_2\text{-}_3$  to give two vicinal (weakly H-bonded) silanol sites.<sup>169,249,250</sup> Thus,  $\text{AX}_{\text{WD}}$  constituted an appropriate sample to study the effect of NFS on the polymerization reaction.

The IR profiles collected after successive steps of Gly sublimation for a total of 20 h CVD (Figure A2- 3, and Figure IV-6 a to h) show that  $\text{G}_{\text{TF}}/\text{AX}_{\text{WD}}$  exhibits higher intensities of the characteristic bands of linear peptides (amide I, amide II), as compared to  $\text{G}_{\text{TF}}/\text{AX}_{\text{r}}$ . The amide A band is also more intense, with two components at  $3400\text{ cm}^{-1}$  (originally predominant) and  $3300\text{ cm}^{-1}$  (developing later). Furthermore, a certain amount of zwitterionic Gly monomers are formed on the surface during polymerization as shown by the appearance of bands at  $1595$  and  $1413\text{ cm}^{-1}$  that may be assigned to  $\nu_{\text{as}}\text{COO}^-$  and  $\nu_{\text{s}}\text{COO}^-$  of Gly monomers respectively<sup>120</sup> – these bands were not present in the previously discussed samples that had been pretreated at  $160\text{ }^\circ\text{C}$ , and therefore the stabilization of zwitterionic glycine is probably correlated with the presence of adsorbed water.<sup>175</sup> In the silanols region (inset of Figure A2- 3), the NFS groups were selectively removed during Gly deposition on  $\text{G}_{\text{TF}}/\text{AX}_{\text{WD}}$  (negative band at  $3742\text{ cm}^{-1}$ ), while this removal is accompanied by the formation of new isolated silanols due to the condensation of some siloxane rings on  $\text{G}_{\text{TF}}/\text{AX}_{\text{r}}$  upon heating at  $160\text{ }^\circ\text{C}$  during CVD (positive band at  $3747\text{ cm}^{-1}$  for isolated silanols in parallel with a negative band at  $3742\text{ cm}^{-1}$  for NFS). This reflects that  $\text{G}_{\text{TF}}/\text{AX}_{\text{WD}}$ , with more NFS which constitute essential elements for monomers activation and polymerization<sup>222</sup>, represents a more efficient platform for the formation of polyGly chains.

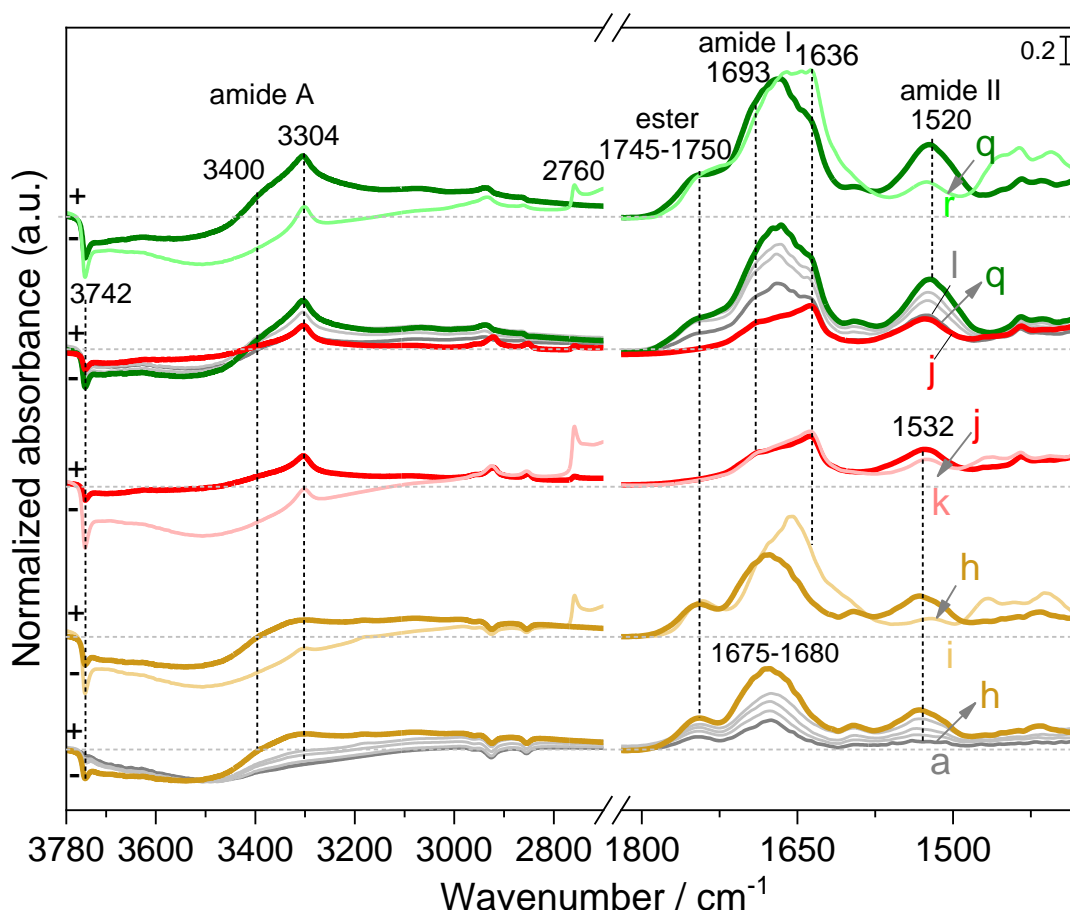


**Figure IV-6:** IR difference spectra on  $G_{TFHF}/AX_{WD}$  resulting from Gly sublimation at  $160\text{ }^{\circ}\text{C}$  by CVD with TF cycles measured from 2.5 h (a) to 20 h (h); (i) after  $D_2O$  adsorption/desorption cycles at bt until spectral invariance; (j) after wetting/drying cycles with liquid water and outgassing at rt; (k) after subsequent  $D_2O$  adsorption/desorption cycles at bt; a second set of  $^{15}\text{N}$ -Gly sublimation at  $160\text{ }^{\circ}\text{C}$  with TF cycles, by CVD measured from 2.5 h (l) to 15 h (q); (r) after  $D_2O$  adsorption/desorption at bt until spectral invariance. Gray curves show intermediate sublimation steps of 2.5 h. For all spectra, the spectrum of the silica support before the start of CVD process ( $AX_{WD}$ ) has been subtracted as a baseline.

After the first 20 h sublimation under TF cycles, the  $G_{TF}/AX_{WD}$  sample was subjected to HF cycles followed by H/D exchange until invariance of spectra. At this stage, the sample is designated as  $G_{TFHF}/AX_{WD}$ . The spectrum (Figure IV-6, curve i) shows a change in shape and intensity of the amide I along with a decrease in intensity of the amide II band that is however not completely suppressed by the H/D exchange, as well as a narrowing of the amide A band (disappearance of the broad component at  $3400\text{ cm}^{-1}$ ) together with the appearance of the D-exchanged counterpart at  $2760\text{ cm}^{-1}$ . These phenomena are similar to those observed previously

on  $G_{TF}/AX_{160}$  (Figure IV-4), which were rationalized by selective D exchange of the weakly H-bonded, disordered chains leaving the strongly H-bonded agglomerates in the protonated form.

Subsequently, the sample was subjected to WD cycles followed by an outgas at rt (Figure IV-6, curve j) and another H/D exchange until invariance of the spectrum (Figure IV-6, curve k). The IR profile at this stage shows a significant change in the shape of amide I which is now dominated by sub-bands centered at 1693 and 1636  $\text{cm}^{-1}$ , characteristic of  $\beta$ -sheets. The narrowing of the amide A band and the resistance of the amide II band to H/D exchange confirm that these  $\beta$ -sheet secondary structures are now preponderant. The XRD pattern recorded at this point (Figure A2- 4, curve a) shows that no crystalline Gly are present on the surface. In fact, the bands at 1595 and 1413  $\text{cm}^{-1}$  that we had assigned to monomeric glycine are no longer detectable at this stage (Figure IV-6, curve j), suggesting that most monomeric glycine has been desorbed by the WD treatment. The analysis by Mass Spectrometry of the supernatant collected after several washings of  $G_{TFHF}/AX_{WD}$  indeed reveals that only Gly monomers (98%) and Gly-Gly and DKP dimers (2%) were desorbed from the surface upon washing while the polyGly resist the WD cycles and remain on the surface.

To study whether these self-assembled aggregates and the silica support remain active to promote further polymerization and elongation of the polyGly chains, two further sets of Gly sublimation by CVD with TF cycles were applied for 15 h after the WD treatment on different  $G_{TFHF}/AX_{WD}$  pellets, using isotopically labeled glycine ( $^{15}\text{N}$  in Figure IV-6 or  $^{13}\text{C}$ -Gly in Figure A2- 5). Isotope labeling is a useful tool for vibrational spectroscopy analysis: it does not only facilitate bands assignment, but also makes it possible to probe specific local structures and dynamics, giving information on the mechanism of peptide aggregation and folding.<sup>182,243,251-253</sup> Substituting specific atoms in a molecule by isotopes of low natural abundance results in altering the vibrational frequencies of moieties that involve this atom, without changing their

chemical properties. The expected isotopic shift  $\Delta\nu$  is calculated using Eq. 3 where  $m_A$ ,  $m_B$ ,  $m_C$  and  $m_D$  are the reduced masses of atoms A, B, C, and D.<sup>182</sup>

$$\Delta\nu = \nu_{A-B} - \nu_{C-D} = \nu_{A-B} \left( 1 - \sqrt{\frac{m_A m_B (m_C + m_D)}{m_C m_D (m_A + m_B)}} \right) \quad (3)$$

Uniform <sup>15</sup>N labeling downshifts the amide II by around 14 cm<sup>-1</sup>, while the amide A band, which arises from the  $\nu_{NH}$  in the peptide units, is downshifted by ca. 8 cm<sup>-1</sup> and the amide I by only ca. 1 cm<sup>-1</sup>. Experimental observations for the amide I are in agreement with these weak displacements.<sup>211</sup>

The IR profiles of  $G_{TFHF}/AX_{WD}$  collected during the second set of Gly CVD (using <sup>15</sup>N-Gly with TF cycles; Figure IV-6, curves l to q) show a further increase in the intensity of amide I and amide II bands with a downshift of around 12 cm<sup>-1</sup> for the latter. This is in line with the progressive formation and prolongation of <sup>15</sup>N-labeled linear polyGly chains on the surface. The amide II band must be the sum of components corresponding to <sup>14</sup>N and <sup>15</sup>N-containing peptide regions, which are difficult to discriminate due to their small separation.

The amide A clearly shows the two components at 3300 and 3400 cm<sup>-1</sup>, both increasing in intensity along the deposition. The ester band exhibits an increase for the first 5 h CVD and then tends to a plateau. Since the ester band intensity is indicative of the number of covalent anchoring points for the polyglycine chains, it would mean that new anchored chains on the surface form only at the beginning of deposition, probably on the surface liberated by the WD treatment, while after 5 h, polymerization proceeds through the ligation of additional monomers to already existing chains. Further HF cycles followed by H/D exchange until invariance of spectra (Figure IV-5, curve r) reveal again a resistance to exchange of the polyGly chains in self-assembled structures on the surface (preservation of the narrow component of the amide A along with a resistance of a part of the amide II band and appearance of narrow sub-band at 1636 cm<sup>-1</sup> for amide I), while the disordered structures are fully deuterated (disappearance of the broad amide A component at 3400 cm<sup>-1</sup>).

A different isotopic enrichment experiment was carried out on a separately synthesized  $G_{\text{TFHF}}/A_{\text{XWD}}$  pellet, using glycine isotopically labeled with  $^{13}\text{C}$ , instead of  $^{15}\text{N}$ , for the second set of TF (after a first set of TF and HF cycles using  $^{12}\text{C}$  Gly, followed by WD). The main interest of this experiment is to discriminate between the sub-bands of the secondary structures already formed during the first set of TF cycles and remaining on the surface after washing (which therefore contain  $^{12}\text{C}$ ), and the ones of newly formed secondary structures during the second set, where  $^{13}\text{C}$  labeling downshifts the amide I band components by ca.  $38\text{ cm}^{-1}$ . Curve fitting of the IR spectra collected during the second set of CVD of  $^{13}\text{C}$ -Gly in TF cycles (Figure A2- 5, integrated areas as a function of time) reveals that after the WD cycles, the polyGly that remain chemisorbed on the surface contain 56%  $^{12}\text{C}$   $\beta$ -sheet and 44%  $^{12}\text{C}$   $\beta$ -turns. When proceeding with a second set of TF cycles, the first 2.5 h results in a transformation of the  $^{12}\text{C}$   $\beta$ -turn into  $^{12}\text{C}$   $\beta$ -sheet structures, which increase in concentration. In parallel, new  $^{13}\text{C}$  polyGly  $\beta$ -sheet structures are formed on the surface, at the exclusion of other secondary structures. Their concentration further increases with CVD time while the  $^{12}\text{C}$   $\beta$ -sheet content remains constant, as would be expected.

The integrated intensities of the ester bands are also plotted in Figure A2- 5. The  $^{12}\text{C}$  ester groups that had resisted WD cycles remain unaffected during the subsequent CVD steps: they constitute the anchors of the self-assembled structures that have not been removed by the WD treatments. However, another band develops immediately upon CVD resumption that can be assigned to newly anchored chains, containing Si-O- $^{13}\text{CO}$ - links. These new ester links form on regions of the surface previously liberated by the WD treatment, as outlined in Figure IV-3. This means that a significant part of the newly formed  $^{13}\text{C}$ -marked  $\beta$ -sheets belong to freshly-nucleated chains. Yet these do not pass through an intermediate, disordered state as in the first set of CVD steps. The surface density of  $^{12}\text{C}$   $\beta$ -sheet templates must be sufficient to impose immediate structuring of the additional chains.

## IV.4. Conclusion

Systems consisting of silica, glycine in the gas phase and water were subjected to cyclic variations in temperature and water activity to study the effect of various experimental scenarios on peptide elongation and structuring. A fluctuating system subjected to both temperature fluctuations (TF) and hydration fluctuation (HF) cycles represents a more favorable geochemical setting for the polymerization reaction as compared to a system subjected only to TF. The dehydration steps are necessary to thermodynamically drive the condensation-polymerization reaction between glycine monomers and pre-existing polyglycine chains. The role of the hydration steps is more complex. Exposure to water appears to hydrolyze some of the surface ester links that bind polyglycine chains to the silica surface, re-establishing the corresponding NFS (nearly-free silanols) anchoring sites. At the same time, the freed chains partly aggregate to pre-existing polyglycine nuclei with a  $\beta$ -sheet secondary structure, and partly form  $3_1$ -helices, probably weakly adsorbed. Further glycine deposition steps at low water activity causes the growth of these aggregates and the formation of new chains, with a higher amount of peptides and a higher level of structuring than in a sample not submitted to hydration. This may constitute an element of justification for the efficiency of often applied wetting-and-drying cycles. However, we are dealing with systems of much higher complexity than would be expected. The effect of water exposure will differ according to the state of the surface and growing chains, which depends on the succession of treatments applied: thus, if exposure to water happens before the beginning of CVD, it promotes the temporary stabilization of glycine monomers as zwitterions. We will deal in a later publication with the effect of initial surface state and different glycine deposition procedures on its reactivity.

The structural dynamics of the oligopeptide chains was also studied by H/D exchange and the application of washing steps. The  $\beta$ -sheets structural elements proved to be very resilient: they were inaccessible to deuterium exchange, and they were not desorbed and hardly perturbed

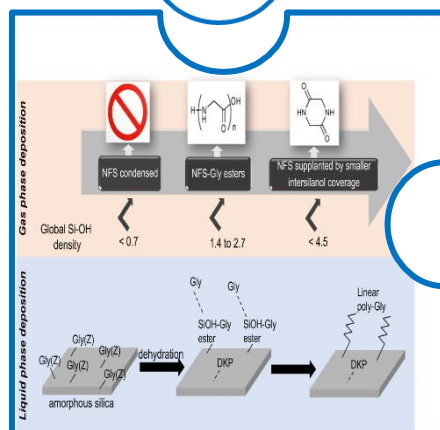
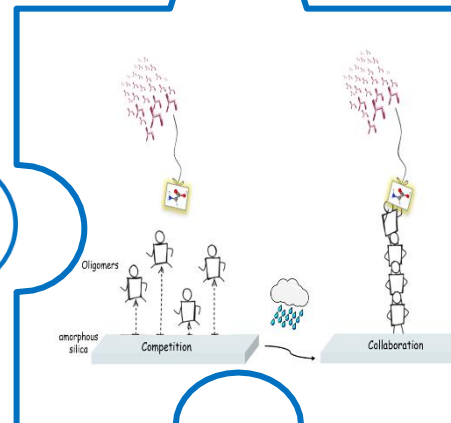
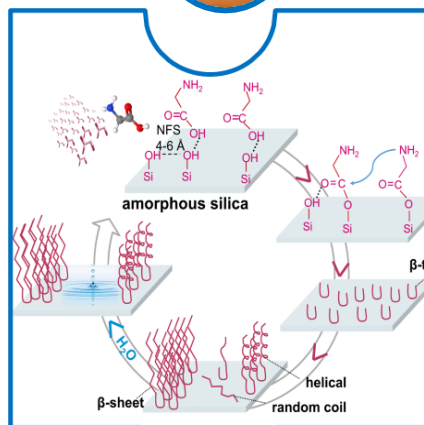
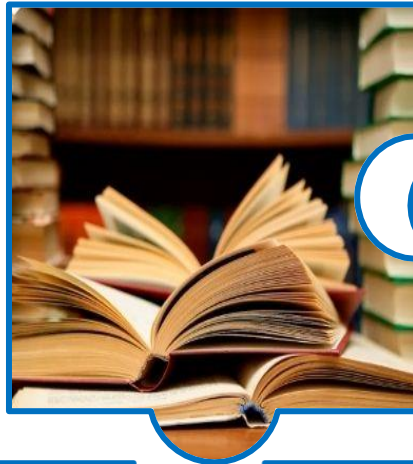


even by liquid water at high temperature, while other structural elements with weaker H-bonds could be exchanged by D<sub>2</sub>O in a few tens of minutes at room temperature. These conclusions were comforted by experiments with isotopically enriched glycine deposition. It is interesting to notice that the applied experimental approach is complementary to the mass spectrometry analysis of products detached from the surface of the catalysts, which often shows the formation of DKP, Gly monomers and dipeptide forms. The strong interaction of the poly(Gly) aggregates, coupled to their low solubility points to the importance of studying the surface bound interface environment and not rely only on measurements made in solution.

From the point of view of prebiotic chemistry, the systems investigated here go further than a polymerization of amino acids, which had been observed many times. Secondary structure elements that appear in current proteins represent a higher level of structuring, one that is indispensable for protein function. It is particularly intriguing that these systems showed some hints of templated peptide growth on  $\beta$ -sheets, i.e., the transmission of information from nuclei to growing chains.

It will be interesting in the future to study the formation of secondary peptide structures on silica surfaces from more complex and diverse monomers, although this will complicate the analysis of IR profiles.

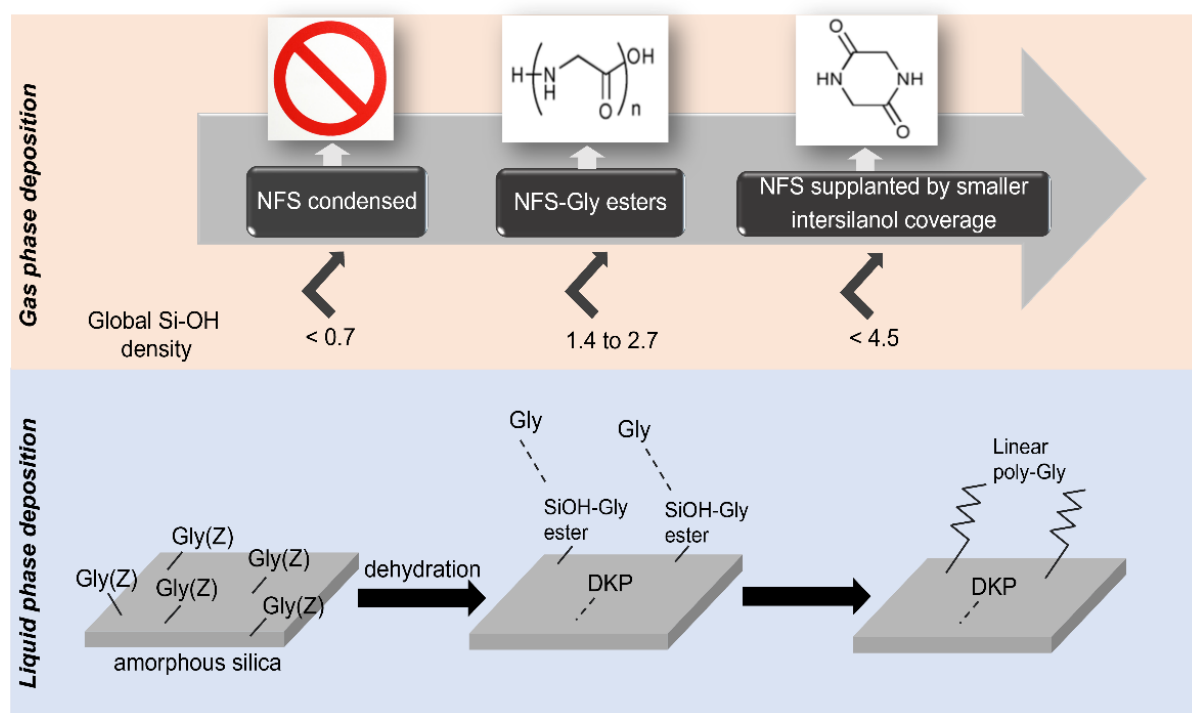
# V. Chapter V: Cyclic or linear? Parameters determining the outcome of glycine polymerization in silica surface prebiotic scenarios



***The work presented in this chapter is published as a peer-reviewed article to Chemistry - a European Journal, 2023.***

*El Samrout, O.; Mezzetti, A.; Berlier G.; Lambert J.F.; Cyclic or linear? Parameters determining the outcome of glycine polymerization in silica surface prebiotic scenarios,*  
<https://doi.org/10.1002/chem.202204010>

The parameters that determine the formation of linear peptides and cyclic dimers (diketopiperazine, DKP) on silica surfaces of different surface area, silanol and siloxane ring populations, controlled by thermal treatments, are investigated upon glycine deposition from gas and liquid phases. The formed products were characterized by infrared and Raman spectroscopies, X-ray diffraction and thermogravimetric analysis. The results reveal the importance of “nearly-free” silanols to form ester centers as primers for the formation of linear peptides over DKP, on surfaces with medium silanol density (1.4 to 2.7 nm<sup>-2</sup>). Quenched reactivity is seen on isolated silanols (density ≤ 0.7 nm<sup>-2</sup>), while silanols involved in hydrogen bonding (density of 4.5 nm<sup>-2</sup>) weakly interact with Gly resulting in its cyclization to DKP. Deposition of glycine from liquid phase may also form both DKP and linear polymers, depending on its loading and silica surface. These conclusions demonstrate the complexity of glycine surface chemistry in the polymerization reaction and highlight the interest of a surface science approach to evaluate geochemical prebiotic scenarios.



## V.1. Introduction

The interfacial process between biomolecules and mineral surfaces including silica-based materials is a subject of paramount interest due to its direct implication in promising fields such as bio-nanotechnology<sup>254</sup>, green chemistry<sup>196</sup>, biomedical sensors<sup>255</sup> and peptide-based pharmaceuticals.<sup>194</sup> It is also of high importance in the field of prebiotic chemistry where it has long been suggested that mineral surfaces play a key role in the peptide bond formation reaction through the condensation between two amino acids<sup>102</sup>, a critical step in the formation of the first biopolymers on the primitive Earth at the origin of life. To date, several experiments have been carried out to study the amino acid polymerization reactivity on various oxide surfaces, considered as adequate approximations to primordial Earth mineral surfaces. For instance, only a dimerization of glycine (Gly) to linear GlyGly and cyclic diketopiperazine (DKP) with yields higher than 10% was obtained upon heating Gly on TiO<sub>2</sub> at 120 °C for 1-35 days.<sup>256</sup> On alumina, GlyGly was produced along with minor amounts of DKP and triglycine after dry heating of Gly for seven days at 85 °C.<sup>257</sup> DKP has been the major product obtained upon dry heating of Gly on silica, after a selective adsorption procedure (on Aerosil A380)<sup>89,114,120</sup>, or a chemical vapor deposition (CVD) under vacuum at around 200 °C.<sup>111</sup> The cyclic dimer has been also the main product obtained when different amino acids (i.e. Leu, Val, Ala, etc.) other than Gly were deposited from an aqueous phase followed by a single step heating.<sup>258,259</sup> In contrast, only linear poly-Gly chains up to 11 mers were formed using CVD on an amorphous silica Aerosil 50 of a smaller specific surface area.<sup>25</sup>

The existence of diverging results suggests that the nature of the condensation products of amino acids polymerization (linear peptides or cyclic product) on the surface of oxides strongly depends on the reaction conditions, such as the reaction time, the reaction temperature, the deposition method of the adsorbate, the reactive surface sites on the particular type of silica used as a support and the glycine loading.<sup>88</sup> In order to unravel the effect of different factors,

we have chosen to address a specific (oxide) mineral-amino acid combination and to investigate their interaction while systematically varying the reaction conditions. Gly was chosen in this work because it is considered as a reference molecule in many theoretical<sup>169</sup> and experimental<sup>25,120</sup> studies dealing with peptide formation. Amorphous silica, a mineral of high natural abundance, low cost, prebiotic significance, and high importance in many potential nanotechnology applications<sup>155,260</sup>, has been considered as a good candidate to study the amino acid polymerization reaction. The surface of silica is characterized by two main surface functional groups, silanol groups and siloxane bridges. The amount of silanol groups directly depends on the type of the silica and the calcination/activation temperature of the surface, and it determines the hydrophilic/hydrophobic character of the material.<sup>261</sup> However, in contrast to ordered crystalline materials, the surface chemistry of amorphous silica is very hard to investigate. A detailed knowledge of the structure of amorphous silica and especially of its surface properties would provide a better understanding of the polymerization reactivity of amino acids.

In the present work, we performed experiments of Gly adsorption on amorphous fumed silica surfaces of different surface areas, and Gly deposition on the surfaces was carried out either from the gas (by Chemical Vapor Deposition, CVD) or from the liquid phase (by Incipient Wetness Impregnation, IWI). For gas phase deposition, the silica materials were thermally pre-treated at variable temperatures while for liquid phase deposition, different concentrations of Gly solutions were used. To elucidate the parameters that determine the nature of the condensation products (linear peptides or cyclic ones), several techniques including transmission Fourier transform infrared (FT-IR) spectroscopy, attenuated total reflection (ATR-IR) spectroscopy, Raman spectroscopy, thermogravimetric analysis (TGA), X-ray diffraction (XRD), and N<sub>2</sub> physisorption were employed. In particular, we attempt to clarify the role of the different functional groups of silica in the polymerization reaction.

## **V.2. Experimental section**

### **V.2.1. Materials**

Amorphous silicas Aerosil OX 50, Aerosil 200, and Aerosil 380 (designated as A50, A200, and A380) of nominal specific surface areas 50, 200 and 380  $\text{m}^2\cdot\text{g}^{-1}$  respectively, provided by Evonik (with  $\text{SiO}_2$  content  $\geq 99.8$  wt%), were used as supports. Glycine (Gly) (99%), purchased from Sigma-Aldrich was used as received. Ultrapure Milli-Q water was used for the preparation of the amino acid solution for the liquid phase deposition.

### **V.2.2. Thermal Treatment of silicas**

The silica samples were subjected to different thermal treatments carried out in a muffle furnace. The  $\text{SiO}_2$  powder was pressed in the form of a self-supporting pellet before being introduced in the furnace at room temperature (rt), heated with a 30 min ramp up to 450 °C and kept at this temperature for 2.5 h. The temperature was then lowered down to rt. Another set of pellets treated in this way was then ramped for 30 min from 450 °C up to 700 °C, kept at this temperature for 2.5 h, and then left in the furnace to cool down to rt. Only for A380, a fresh pellet previously pre-treated at 450 and 700 °C was further ramped for 30 min to 850 °C, kept again for 2.5 h at this temperature and left to cool down to rt. The supports obtained were labeled as  $A_{x(T)}$ , where x represents the specific surface area of the corresponding pristine silica and T refers to the temperature of the thermal treatment.

### **V.2.3. Gly adsorption on silica supports from the gas phase**

Gly deposition on the silica surfaces was performed using chemical vapor deposition (CVD) at 160 °C for 20 h. In summary, 200 mg of each silica support (in the pristine form or after thermal treatment), were introduced in a U-shaped cell and placed on its sintered glass bed, with 30 mg of Gly placed upstream in the cell. The system was first subjected to an outgas at rt for 2 h

under 100 ml/min argon flow to remove most of the physisorbed water before the start of the reaction. The cell was then placed in a tubular oven controlled by a temperature programmer. A linear temperature ramp of 1 °C/min was applied up to 160 °C and this temperature was kept for 20 h under argon flow, then the sample was left to cool down to rt. The samples obtained after Gly deposition from the gas phase are denoted as G/A<sub>x(T)</sub>.

For the sake of comparison, a set of pellets of A50 (rt, pre-treated at 450 and 700 °C) were subjected to Gly deposition from the gas phase, also using CVD but performed in an IR cell under vacuum using a method detailed by Martra et al.<sup>25,222</sup>

#### **V.2.4. Gly adsorption on silica supports from the liquid phase**

Gly monomers were deposited on silica surfaces from water solutions using the incipient wetness impregnation (IWI) procedure, derived from the field of supported catalysts synthesis. Briefly, the required amount of Gly monomers were dissolved in ultrapure water and the resulting Gly solution was added to the silica support respecting a ratio of 10 ml of Gly solution for 1 g of silica. This resulted in a homogeneous slurry without a separate liquid phase which was left to dry under nitrogen flow at rt overnight. For each type of silica surface, a series of samples with increasing Gly weight loadings from 0.5 to 5% was prepared. The different Gly/silica systems were dried under vacuum then introduced in a U-shaped cell for outgas at rt for 10 h under a 100 ml/min argon flow. Subsequently, the U-shaped cell, kept under the same argon flow, was placed in a tubular oven coupled with a temperature programmer for thermal activation of the system. A controlled linear temperature ramp of 1 °C/min was applied to reach a final value of 160 °C where a plateau was maintained for 30 min. The sample was then cooled down to rt and stored in a desiccator. Such samples are labeled as G<sub>y</sub>/A<sub>x</sub>, where y refers to the Gly weight loading and x represents the specific surface area of the pristine silica used.

### **V.2.5. Infrared (IR) spectroscopy**

IR spectra of the Gly-silica samples were recorded using a Bruker Vertex 80 spectrometer equipped with a MCT detector under a RapidScan mode using a resolution of  $4\text{ cm}^{-1}$  and accumulating 250 scans to have a good signal to noise ratio. The samples in the form of self-supporting pellets were placed between two IR-transparent calcium fluoride  $\text{CaF}_2$  windows sealed with a parafilm.

KBr-IR spectra for the silica samples (in pristine form or thermally treated at different temperatures) were also recorded in the transmission mode using Bruker Vertex 80 (MCT detector, resolution of  $4\text{ cm}^{-1}$  with the accumulation of 250 scans). The spectra were measured in potassium bromide KBr pellets with a sample concentration in the pellet of a few percent by weight. The absorption of a pellet of pure KBr was used as a background.

For the samples prepared using the IR cell under vacuum for Gly deposition in the gas phase, IR spectra were recorded using a Bruker Vector 22 instrument with a DTGS detector, using a resolution of  $4\text{ cm}^{-1}$  and accumulating 64 scans. The self-supporting pellets of the samples were placed in a traditional IR cell with  $\text{CaF}_2$  windows, equipped with a valve to be connected to a vacuum line (residual pressure  $< 1.0 \times 10^{-5}$  mbar) where the adsorption experiments were carried out in situ.

### **V.2.6. Attenuated total reflection infrared (ATR-IR) spectroscopy**

ATR-IR spectra for the silica samples (in pristine form or thermally treated at different temperatures) were recorded using a Bruker Vertex 80 spectrometer equipped with a mono-reflection diamond Bruker, A225/Q-DLST ATR device. The refractive index of the diamond is 2.4. Measurements were carried out with a RapidScan mode using a DTGS detector with a mirror speed of 20 kHz. The spectral window recorded was from  $4000\text{-}200\text{ cm}^{-1}$  using a resolution of  $2\text{ cm}^{-1}$  and accumulating 200 scans for a better signal to noise ratio.



### **V.2.7. Raman Spectroscopy**

Raman spectra were recorded at rt using a Kaiser microscope optical system (RXN1) equipped with a charge-coupled detector. The laser beam working at 785 nm was focused by adjusting the microscope to an objective of 50X long working distance (8 mm) lens. The spectral window was 3200-150  $\text{cm}^{-1}$ ; spectra were collected with an incident laser power of 10 mW, resolution of 4  $\text{cm}^{-1}$ , 10 seconds acquisition time, and accumulating 30 scans for each spectrum.

### **V.2.8. Specific surface area measurements**

Specific surface areas of the silica samples were determined from the  $\text{N}_2$  adsorption isotherms recorded at 77 K using Belsorp-max (BEL JAPAN) apparatus. Before measurements, the samples were degassed under vacuum at 250 °C for 2 h (residual pressure  $10^{-4}$  mbar) on a BelprepII-vac unit. Specific areas values were obtained using the BET equation.

### **V.2.9. X-ray diffraction (XRD)**

XRD patterns for the samples obtained after Gly deposition from gas and liquid phases were recorded on a PANalytical X'Pert powder diffractometer using a  $\text{Cu K}\alpha$  ( $\lambda=1.5405 \text{ \AA}$ ) radiation source generated at 30 mA and 40 kV. The diffractograms were recorded with a  $2\theta$  scanning range of 10 to 45°, a step size ( $2\theta$ ) of 0.01°, and a dwell time of 1 s per step.

### **V.2.10. Thermogravimetric analysis (TGA)**

Thermogravimetric analysis (TGA) of crushed pellets was carried out using a TA instrument with a STD Q600 analyzer. TGAs were performed with a heating rate of 1 °C/min under a 100 mL/min dry air flow. Quantification of adsorbed peptides was evaluated by correcting the weight loss between 130 and 400 °C for the corresponding value for the blank sample.

### V.3. Results and Discussion

Three types of fumed silica surfaces (Aerosil A50, A200, and A380) were used to study the product of the polymerization reaction of Gly when deposited from gas and liquid phases. In the former case, the silica supports were treated at 450, 700, and 850 °C before Gly deposition, in order to modulate their surface properties (silanol and siloxane concentration and nature) and correlate the surface structure to the changes in reactivity. For the Gly adsorption from the liquid phase, only pristine materials were used since it is expected that the exposure to liquid water would undo much of the thermal transformations by re-hydroxylating the surface.

#### V.3.1. Gly deposited on silica from the vapor phase

##### V.3.1.1. Silica supports

##### BET and TGA analysis

Specific surface areas of the silica supports measured by applying the BET method to N<sub>2</sub> physisorption isotherms are reported in Table V-1. The SSAs remain unchanged for A50 and A200 samples (and close to the nominal values) even after calcination at 700 °C. For A380, a decrease of 11% is seen after a thermal treatment at 700 °C. A more significant decrease of about 30% is recorded after a calcination at the higher temperature of 850 °C. This decrease probably results from sintering of the nanometric silica particles.<sup>262</sup>

sample	SSA <sub>BET</sub> (m <sup>2</sup> .g <sup>-1</sup> )		
	A50	A200	A380
pristine	47	197	387
calcined at 450 °C	52	195	371
calcined at 700 °C	52	195	343
calcined at 850 °C	---	---	270

**Table V-1:** Specific Surface Area (SSA<sub>BET</sub>) of silica samples (A50, A200, and A380) in the pristine form and after calcination in air at 450, 700 and 850 °C.

Thermogravimetric analysis (TGA) was employed as a one-step, fast, and simple method to estimate the OH density on the different silica supports<sup>263</sup> in the pristine form and

after the different thermal treatments. The number of silanol groups was estimated from the weight loss between 100 and 800 °C because, for silica, the weight loss occurring before 100 °C is associated to the desorption of the physisorbed water from the surface, while the weight loss between 100 and 800 °C is due to the irreversible condensation of surface silanol groups forming siloxane bonds.<sup>264</sup>

Since almost all silanols in Aerosil-type materials are located on the surface, their amount in a sample is given by the product of the surface area (cf. Table V-1) and the surface density. Table V-2 lists the silanol surface densities of all samples. It can be seen that the higher the surface area, the higher also the silanol density. This is understandable since the synthesis conditions that cause the most silanol condensation induce both the formation of larger particles by sintering (and thus a low surface area) and a transformation of silanols to siloxanes on the remaining exposed surface. According to Zhuravlev the density of 4.5 silanols per nm<sup>2</sup> observed on untreated Aerosil380 corresponds to a “fully hydroxylated silica surface”.<sup>265</sup>

For each support, there is a marked decrease in the silanol groups density upon calcination. On calcined A50, the total amount of silanols becomes too low to be quantified by this technique; A200 and A380 reach silanols densities as low as the untreated A50 after calcination, respectively at 450 and 700 °C.

Sample	Number of OH groups / nm <sup>2</sup>		
	A50	A200	A380
pristine	1.4-1.5	2.7	4.5
calcined at 450 °C	not measurable	1.6	2.0
calcined at 700 °C	not measurable	0.7	1.4

**Table V-2:** Number of silanol (OH) groups / nm<sup>2</sup> for silica samples (A50, A200, and A380) in the pristine form and after calcination in air at 450 and 700 °C, calculated using thermogravimetric analysis.

### Raman spectroscopic studies

Raman spectroscopy has been used to understand important structural properties of amorphous silicas at the molecular scale.<sup>188,189,206,266</sup> The Raman spectra of the different silica

supports (A50, A200, and A380) in pristine form and calcined at 450, 700 and 850 °C are reported in Figure V-1 (panels A, B, and C respectively). All spectra are normalized with respect to the 800 cm<sup>-1</sup> band, whose intensity and shape hardly change with thermal treatment as it corresponds to the LO and TO (longitudinal and transverse optic) network vibrations stemming from the  $\nu_{\text{sym}}$  (Si-O-Si).

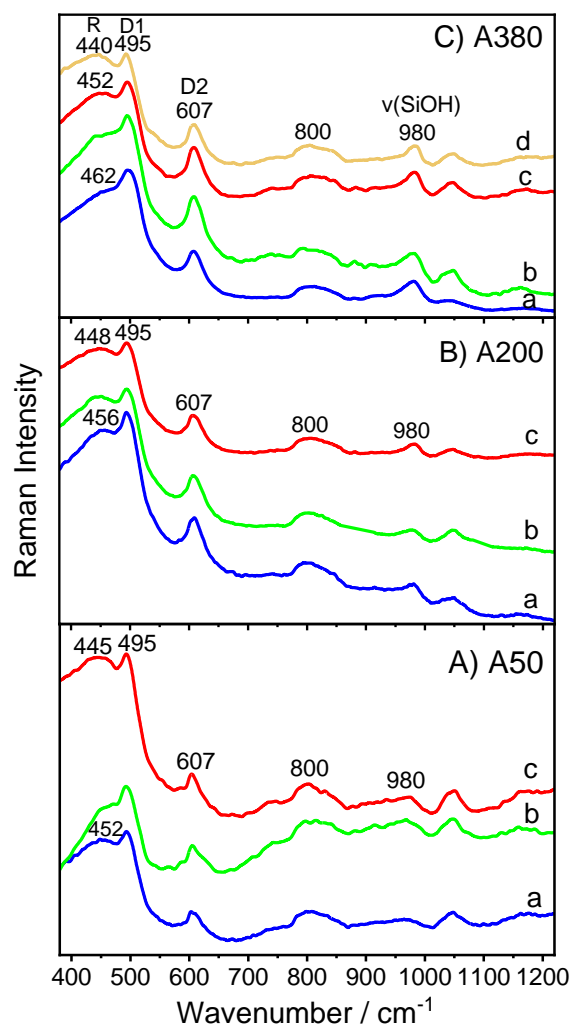


**Figure V-1:** Raman spectra recorded for A) A50, B) A200, and C) A380 silica samples; pre-treated each at different temperatures: (a) rt, (b) 450, (c) 700, and (d) 850 °C for 2.5 h. The spectra are normalized at 800 cm<sup>-1</sup>, a band characteristic of the silica network.

Different features of silica can be detected from the different spectral Raman bands. The evolution of the silanol groups is seen in the 960-990 cm<sup>-1</sup> range corresponding to the Si-(OH) stretching.<sup>267,268</sup> The change in the populations of 4- and 3-membered rings can be followed

from the characteristic bands of their breathing vibration modes, respectively located at 495 and 607  $\text{cm}^{-1}$  and designated as D1 and D2. The R-band, peaking at around 440  $\text{cm}^{-1}$  for bulk silica materials,<sup>188,189</sup> is assigned to the bending motions of the O-Si-O. It is sensitive to changes of the silica structure that are induced by small particle size. The R-band position has been reported to be related to the mean Si-O-Si angle.<sup>269</sup>

Comparing the silica materials in pristine form for each type (Figure V-1, curves a), the amplitude of the 980  $\text{cm}^{-1}$  band increases in the order A50 < A200 < A380, as expected from the silanol amounts deduced from the TG results. The R-band shifts to higher wavenumbers with the increase of the SSA of silica, as already observed by Alessi et al.<sup>188,266</sup> For a given silica, it shifts to lower wavenumbers as the sample is calcined to higher temperatures.

The change in the Raman spectrum upon calcination is most conspicuous for the silica of highest SSA (A380, Figure V-1, panel C). For a better quantification, the integrated areas of D1 and D2 as well as the peak position of the R-band were calculated by fitting the normalized Raman spectra using Gaussian function and are illustrated in Figure A3-1. In this case, after thermal treatment of the support at 450 °C, an increase in the intensity of D1 and D2 bands is seen, which implies the increase in the number of 4- and 3- membered rings in the system through condensation. When A380 is calcined at 700 °C (Figure V-1, Panel C, curve c), an opposite effect is observed as the D1 and D2 bands decrease significantly. Meanwhile, as the activation temperature increases, the R-band shifts significantly to lower wavenumber, its position becoming close to that of A50 or A200 calcined at 450 °C. Since the position of the R-band is related to the mean Si-O-Si bond angle, its shift to lower frequency can be interpreted as a higher mean inter-tetrahedral bond angle. As the distribution of the Si-O-Si bond angles is related to that of the ring sizes, this would correspond to a global shift of the ring size distribution toward larger rings.

When heating silica A380 at 850 °C for 2.5 h, the R-band further shifts to lower frequencies, while only negligible changes are observed in the D1 and D2 bands, or the 980 cm<sup>-1</sup> band (Figure V-1, panel C, curve d).

The overall behavior of A380 at temperatures higher than 450°C could be explained by the cementing of the silica nanoparticles through the formation of necks between the adjacent particles.<sup>262</sup> At the molecular level, silanol groups on originally separated nanoparticles would fuse together, causing the formation of new, rather large rings. Recall that at 850°C, a 30% decrease in the SSA was observed (Table V-1). This is probably due to a decrease in the interparticular porosity related to particle growth; but Raman spectroscopy suggests that this phenomenon starts before noticeable changes in the surface area can be detected.

A similar behavior is also seen on A200 (Figure A3-1, Appendix 3). The trend is less clear on A50, where the D1 and D2 bands were less intense to begin with.

### **ATR and transmission spectroscopic studies**

IR spectroscopy can provide complementary information with respect to Raman, due to the different selection rules of the two spectroscopies. In particular IR in the ATR mode has been used to study the structural and surface properties of silica.<sup>185</sup> ATR-IR measurements (Figure V-2) along with transmission measurements (Figure A3-2) on KBr-IR pellets were carried out on the silica supports in pristine form and after the thermal treatments.

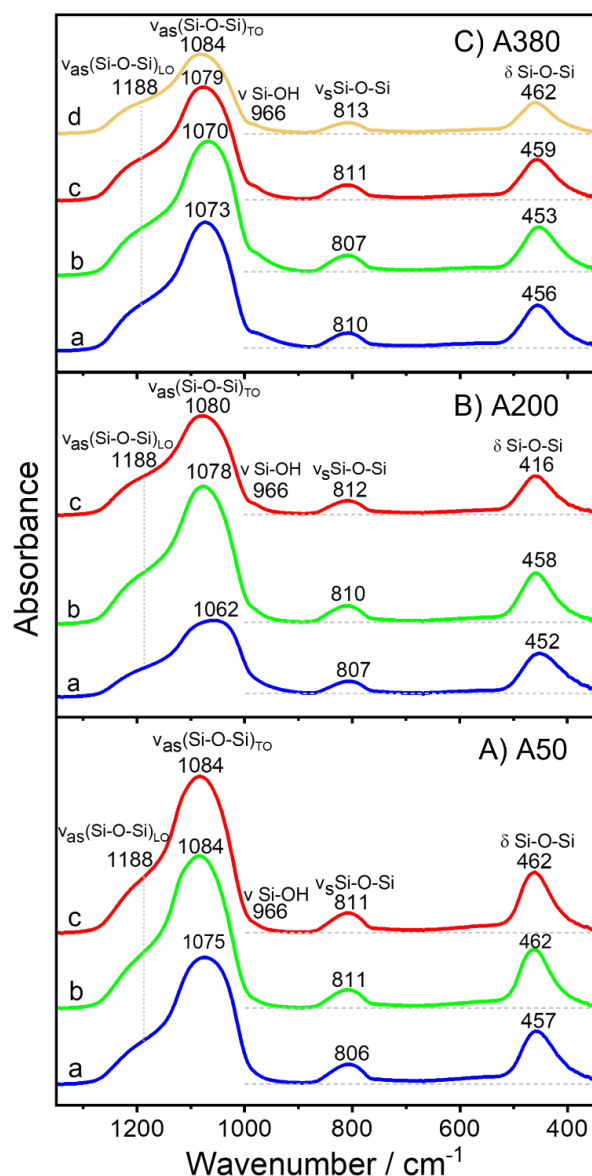


**Figure V-2:** ATR-IR spectra for A) A50, B) A200, and C) A380 silica samples, pre-treated at different temperatures: (a) rt, (b) 450, (c) 700, and (d) 850 °C for 2.5 h.

The spectra in Figure V-2 exhibit several characteristic bands at around 1188, ~1100, ~800, ~450  $\text{cm}^{-1}$  assigned to the LO and TO network vibrations stemming from the  $\nu_{\text{asym}}$  (Si-O-Si) ( $\nu_{\text{asym(LO)}}$  and  $\nu_{\text{asym(TO)}}$ ) LO and TO from symmetric stretching  $\nu_{\text{sym}}$ , and bending  $\delta$  motions respectively of the Si-O-Si bonds. Furthermore, an additional band can be observed at around 966  $\text{cm}^{-1}$  associated to the Si-(OH) stretching of silanol groups.<sup>185,267,268</sup>

The high polarity of Si-O bonds results in an intense absorption band in the 1300-1000  $\text{cm}^{-1}$  region from which can be derived the inter-tetrahedral Si-O-Si bond angle.<sup>270</sup> Many previous

studies<sup>271-274</sup> have extensively related mainly the TO adsorption band of  $\nu_{\text{asym}}(\text{Si-O-Si})$  and  $\delta(\text{Si-O-Si})$  to the bond angle of inter-tetrahedral Si-O-Si bonds. They have indicated that a shift to lower wavenumber is indicative of the formation of smaller rings. In our case, both  $\nu_{\text{asym}}(\text{Si-O-Si})$  and  $\delta(\text{Si-O-Si})$  bands exhibit a redshift along with a decrease in the band associated to  $\nu\text{Si-OH}$  upon thermal treatments for all the silica supports and especially for the A380 support, which is consistent with the results discussed for Raman spectroscopy (Figure V-1). This implies an increase in the mean Si-O-Si bond angle, and consequently the formation of bigger ring structures in the network.

### **V.3.1.2. Gly reactivity on silica**

#### **XRD analysis**

Three types of fumed silica surfaces (Aerosil A50, A200, and A380) were used to study Gly deposition from the gas phase. The XRD patterns of the samples (Figure A3-3) obtained after 20 h CVD show that no crystalline Gly (or crystalline peptide) is present on the surfaces: instead, only adsorbed species or chemically bonded<sup>222</sup> without crystalline periodicity are present in all silica-deposited samples.

#### **FTIR spectroscopic studies**

After 20 h Gly CVD sublimation under argon flow, all silica samples were subjected to FTIR measurements to discriminate among the condensation products obtained after the polymerization reaction. Difference IR spectra in Figure V-3 show that when silica A50 and A200 are initially in pristine form or calcined at 450 °C prior to CVD, both the amide I (1700-1610  $\text{cm}^{-1}$ ) and amide II (1570-1490  $\text{cm}^{-1}$ ) bands appear with significant intensities after 20 h Gly sublimation. These two bands are indeed intense in linear peptides, while the amide II band should be absent for symmetry reasons in the cyclic dimers.<sup>120</sup> This implies that linear peptides are formed on G/A50<sub>(rt)</sub>, G/A50<sub>(450)</sub> (Figure V-3, panel A, curves a and b respectively) and G/A200<sub>(rt)</sub>, G/A200<sub>(450)</sub> (Figure V-3, panel B, curves a and b respectively). Bands in the 1400-



1450  $\text{cm}^{-1}$  range are related to H-C-H bending modes, and are not informative about the nature of the formed products. On the other hand, the band in the 1750-1740  $\text{cm}^{-1}$  range has been firmly linked with the formation of ester groups between the peptide chains and the silanol groups on the surfaces. These observations are in line with previously observed behavior on the support A50.<sup>222,275</sup>

However, when the A50 and A200 silicas were calcined at 700 °C (G/A50<sub>(700)</sub> and G/A200<sub>(700)</sub>; Figure V-3, Panel A and B respectively, curves c), the amide I and amide II bands after 20 h CVD exhibited a significant decrease with respect to supports pretreated at lower temperatures and the band related to the surface esters disappeared. Thus, high-temperature pretreatment somehow “quenches” glycine polymerization reactivity on both samples.

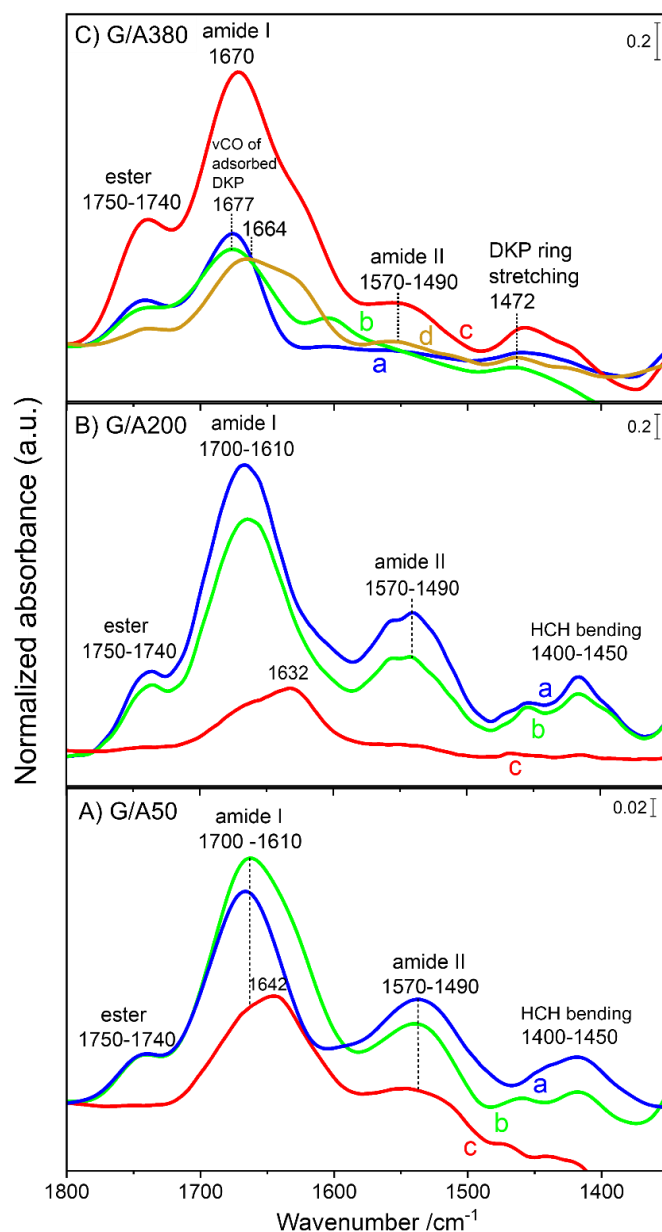


**Figure V-3:** Transmission IR difference spectra measured on self-supporting pellets resulting from Gly deposition by CVD under argon flow for 20 h at 160 °C for the following samples: (A) G/A50, (B) G/A200, and (C) G/A380; in each panel, supports were pre-treated at different temperatures: (a) room temperature (rt), (b) 450, (c) 700, and (d) 850 °C for 2.5 h.

On A50, the effect of pretreatment temperature on glycine polymerization kinetics were studied in more detail. Intermediate steps of 2.5 h Gly CVD were applied in a specific IR cell for in-situ measurements, as described in our previously published papers (Figure A3-4).<sup>222,275</sup> The results obtained in this setting are coherent with those obtained after ex situ thermal treatments and displayed in Figure V-3. In particular, amide I, amide II, amide A bands and surface esters

progressively increase during the 20 h CVD on A50, either untreated (Figure A3-4, panel A) or pre-calcined at 450 °C (Figure A3-4, panel B). For A50 pre-calcined at 700 °C (Figure A3-4, panel C), the amide bands are significantly smaller and appear more slowly: only traces are formed after 10 h CVD, even though a small ester band is already present. The DKP band is never observed. These observations in the 1400-1750 cm<sup>-1</sup> region, are correlated with those in the silanol stretching region (higher wavenumbers panels, A', B' and C'). Here, negative difference signals indicate that specific types of silanols are consumed during Gly CVD. On A50, untreated (Figure S4, panel A') or calcined at 450 °C (Figure A3-4, panel B'), these are specifically the “nearly-free silanol” (NFS) groups, i.e. pairs of silanols separated by a distance between 4 and 6 Å, and resonating in the 3744-3741 cm<sup>-1</sup> range.<sup>208</sup> It has been reported that calcination of silica A50 at 700 °C results in the condensation of the NFS groups so that only isolated silanol groups remain on the surface.<sup>24</sup> Indeed, Gly CVD on G/A50<sub>(700)</sub> does not cause a negative difference signal in the NFS region, but instead a sharp one at 3748 cm<sup>-1</sup>, a position characteristic of isolated silanols (Figure A3-4, panel C'). These NFS groups were already highlighted in our previous work<sup>222</sup> as being crucial partners for monomers activation for the polymerization reaction. The results of Figure A3-4 confirm and specify this hypothesis. Isolated silanols may serve as sites for Gly ester formation; but efficient polymerization from the latter necessitates the presence of NFS.

The relative amount of peptides may be evaluated from the integrated area of the amide I band (Figure A3-5 in Appendix 3). For all three samples (G/A50<sub>(rt)</sub>, G/A50<sub>(450)</sub>, and G/A50<sub>(700)</sub>, the temporal evolution of peptide bands for G/A50<sub>(rt)</sub> and G/A50<sub>(450)</sub> can be roughly fitted with straight lines. On G/A50<sub>(450)</sub>, peptides are significantly more abundant than on G/A50<sub>(rt)</sub> for the same time of Gly sublimation, with G/A50<sub>(700)</sub> showing the smallest amounts. Thus, the sample with a support A50 pretreated at 700 °C is the least efficient platform for peptide formation and growth.

For A380 silica-supported samples (Figure V-3, panel C), a totally different scenario was observed. When the A380 surface support was untreated or calcined at 450 °C prior to CVD, only an amide I band was observed, shifted to higher wavenumber (1677  $\text{cm}^{-1}$ ) as compared to polyglycine, with no amide II band (G/A380<sub>(rt)</sub> and G/A380<sub>(450)</sub> samples; Figure V-3, panel C, curves a and b respectively). There is however a band at around 1472  $\text{cm}^{-1}$ , that is not observed for the other silica supports. These features are characteristic of the cyclic dimer DKP (diketopiperazine), and in particular the band at 1472  $\text{cm}^{-1}$  is attributable to DKP ring stretching.<sup>276,277</sup> This implies that in these two cases, mostly DKP instead of linear peptides was formed on the surface. However, when A380 had been calcined at 700 °C, amide I (now at a lower wavenumber, around 1670  $\text{cm}^{-1}$ ) and amide II (1570-1490  $\text{cm}^{-1}$ ) bands were observed with an important growth in the ester band, indicating the formation of linear peptides on the surface along with a significant amount of DKP, detected through the band at 1472  $\text{cm}^{-1}$  (Figure V-3, panel C, curve c). In view of these results, A380 was further subjected to a pre-treatment at the very high temperature of 850 °C. The spectra of G/A380<sub>(850)</sub> after 20 h CVD (Figure V-3, panel c, curve d) shows the formation of amide I and amide II bands despite their decreased intensities compared to G/A380<sub>(700)</sub>: linear peptides form in this case as well.

### **Thermogravimetric analysis**

Thermogravimetric analysis has been used in previous studies dealing with amino acids oligomerization on silica supports<sup>23,223,278</sup> and especially for the Gly/SiO<sub>2</sub> system.<sup>120</sup> It constitutes an accurate tool to trace the transformation of amino acids to cyclic or linear peptides and to evaluate the amounts of adsorbed Gly and peptides on the surface. The derivative

thermogravimetric (DTG) patterns of G/A50, G/A200, and G/A380 measured after 20 h CVD on supports either untreated or calcined at 450 or 700 °C are displayed in Figure V-4.

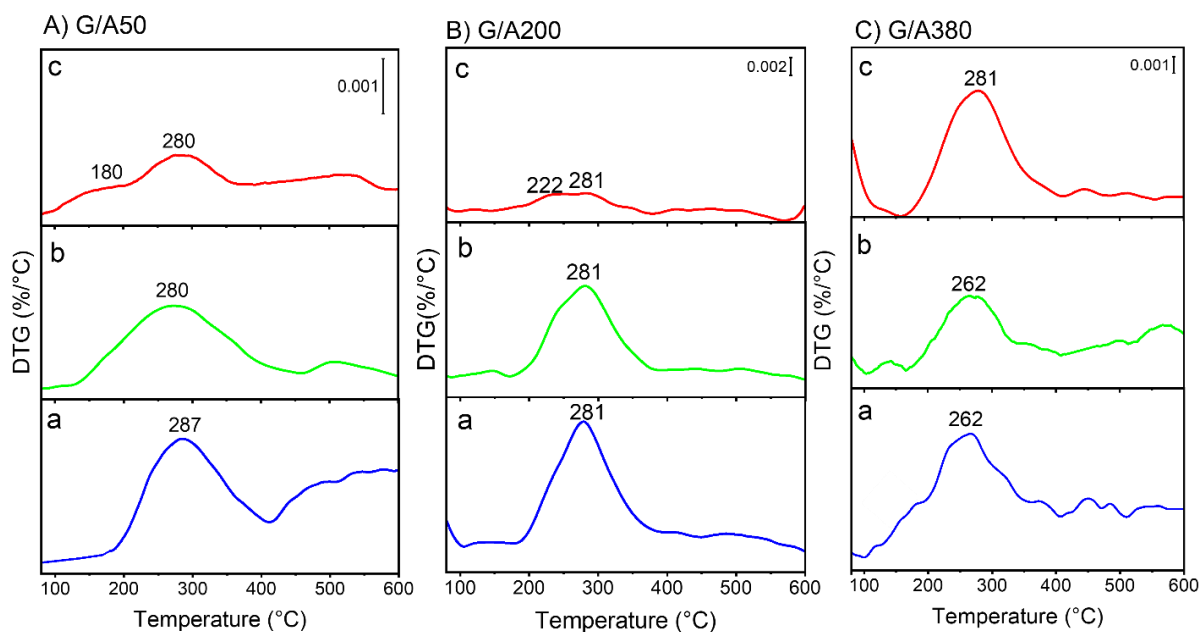


**Figure V-4:** Derivative thermograms (DTG) of samples obtained after Gly sublimation for 20 h by CVD at 160 °C under argon flow on silica: (A) G/A50, (B) G/A200, and (C) G/A380; which supports were pre-treated each at different temperatures: (a) rt, (b) 450, and (c) 700 °C for 2.5 hrs

In all cases, physisorbed water desorbs from the surface before 100 °C (not shown). For G/A50 and G/A200, in pristine form or calcined at 450 °C (Figure V-4, Panels A and B, curves a and b), a single thermal event is observed at 280-287 °C. Events in this range correspond to the oxidative degradation of the oligopeptides formed on the surface during the CVD.<sup>227</sup> No events are apparent in the 140-160 °C region where peptidic condensation with the loss of water molecules is normally observed.<sup>120,227</sup> This is in keeping with the nature of the CVD products inferred from the IR spectra: whether they consist in DKP or long linear peptides, no or very few free COOH or NH<sub>2</sub> termini are available for condensation anymore.

When A50 and A200 calcined at 700 °C were used as supports (Figure V-4, panels A and B, curves c), the peak at ca. 280 °C was barely distinguished along with another event of low intensity in the 180-222 °C range. The latter can perhaps be attributed to the desorption of

Gly monomers weakly bound to the surface. The integration of the bands for G/A50 and G/A200 samples reveals that the peptide loadings on G/A50<sub>(rt)</sub> and G/A50<sub>(450)</sub> are about 0.27 and 0.37% by weight of silica respectively while being 1.76 and 1.50% by weight on G/A200<sub>(rt)</sub> and G/A200<sub>(450)</sub>, with only traces estimated on G/A50<sub>(700)</sub> and G/A200<sub>(700)</sub>.

For G/A380, when the support used is in pristine form or calcined at 450 °C, one main peak was observed (Figure V-4, panel C a and b) at around 260 °C. This is related to the burning off of the resulting organic matter (consisting of DKP according to IR), at a temperature lower than the one observed in the case of linear peptides.<sup>120</sup> The deposited amounts of DKP constitute about 0.32 and 0.52% by weight for G/A380<sub>(rt)</sub> and G/A380<sub>(450)</sub> respectively. However, when the A380 support is calcined at 700 °C (Figure V-4, panel C c), a major event is seen at 281 °C corresponding to an amount of organic matter of 1.19% by weight. Thus, the TG becomes more similar to those of low temperature-treated G/A50 and G/A200. Recall that IR spectroscopy also indicated a similarity between these same samples, with some linear peptides formed in G/A380<sub>(700)</sub> (Figure V-3, panel C).

The amounts of adsorbed organic matter obtained by TGA are listed for all samples in Table V-3, expressed both as bulk loadings and in terms of surface density of Gly monomers. The main FTIR results are also recalled there.

Gly/SiO <sub>2</sub> sample	FTIR	TGA		
		Adsorbed organic matter		
		weight %	mmol Gly/g SiO <sub>2</sub>	Gly/nm <sup>2</sup> SiO <sub>2</sub>
G/A50(rt)	linear peptides	0.27	0.04	0.43
G/A50(450 °C)		0.37	0.05	0.59
G/A50(700 °C)	quenched reactivity	traces	...	...
G/A200(rt)	linear peptides	1.76	0.23	0.69
G/A200(450 °C)		1.5	0.20	0.60
G/A200(700 °C)	quenched reactivity	traces	...	...
G/A380(rt)	DKP	0.32	0.04	0.06
G/A380(450 °C)		0.52	0.07	0.11
G/A380(700 °C)	linear peptides	1.19	0.16	0.25

**Table V-3:** Main results obtained from the characterization techniques (FTIR, and TGA) for all the G/SiO<sub>2</sub> samples prepared by Gly deposition from the gas phase. XRD showed the absence of crystalline phases in all samples.

### V.3.2. Gly deposited on silica from the liquid phase

#### XRD analysis

When using the incipient wetness impregnation (IWI) deposition procedure, the weight loading of glycine may be imposed. Different weight loadings ranging from 0.5 (only for A50) to 5% were deposited on the three different silica samples A50, A200, and A380. After deposition, the samples were activated for 30 min at 160 °C under argon flow. The corresponding XRD patterns after activation are presented in Figure V-5 (panels A, B and C for A50, A200, and A380 support respectively). It is expected that the Gly monomers are able to adsorb on the silica surface only up to a maximum surface density known as the saturation coverage. Above the corresponding loading, any additional Gly monomers forced to deposit will precipitate on the surface as bulk Gly.

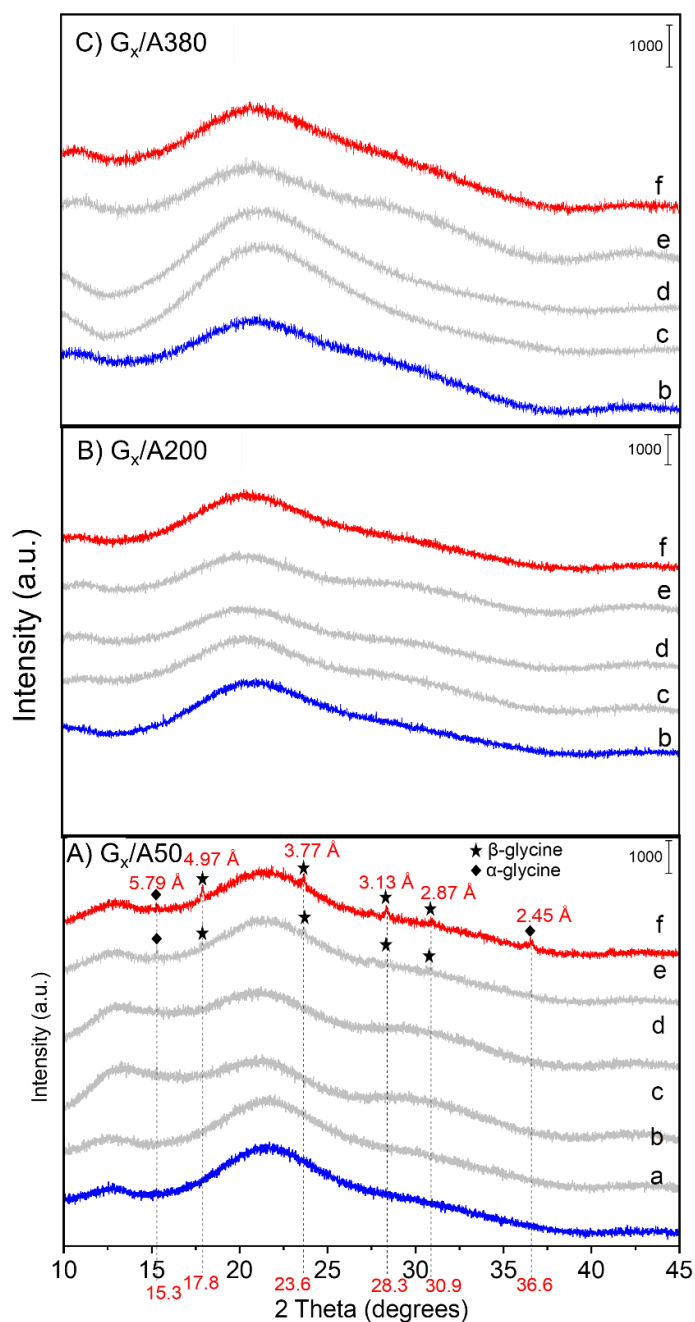


**Figure V-5:** XRD profiles measured after Gly deposition by incipient wetness impregnation followed by activation for 30 min at 160 °C under argon flow on silica: (A) G<sub>x</sub>/A50, (B) G<sub>x</sub>/A200, and (C) G<sub>x</sub>/A380; where x refers to different Gly monomers loadings: (a) 0.5, (b) 1, (c) 2, (d) 3, (e) 4, or (f) 5 wt%.

The XRD patterns of G<sub>x</sub>/A50 samples (Figure V-5, panel A) do not show any peaks of bulk Gly at low loadings ranging from 0.5 to 3 wt% whereas for 4 and 5 wt%, such peaks appear and grow with Gly loading. As a comparison, a physical (close-packed) monolayer of Gly (7.3 Gly/nm<sup>2</sup> based on an estimated area of the Gly molecule of 13.65 Å<sup>2279</sup> (molecules “lying flat”



on the A50 surface) would correspond roughly to 4.5 wt% (see Table A3-1 where the theoretical value of monolayer coverage may be compared with the surface densities of Gly/nm<sup>2</sup> for all G<sub>x</sub>/silica). Most of the XRD peaks observed (2θ equals 17.8, 23.6, 28.3, and 30.9°) may be assigned to bulk β-Gly whereas the ones at 15.3 and 36.6° are associated to α-Gly; this coexistence of the two phases in high-loading samples has been reported before.<sup>120</sup> The observation of bulk monomeric species is also coherent with the fact that bulk glycine does not polymerize at 160 °C, in contrast to silica-adsorbed glycine.<sup>227</sup> For both G<sub>x</sub>/A200 and G<sub>x</sub>/A380 and for all Gly loadings from 1 to 5 wt%, XRD patterns (Figure V-5, panel B and C respectively) only show the broad backgrounds of silica supports without any additional peaks. This implies that all Gly monomers are adsorbed on the surface at least up to 5 wt% without forming any observable crystallites. Indeed, for these samples the 5 wt% loading represents only a fraction of the estimated Gly physical monolayer (around 18 and 35% for A200 and A380, respectively).

### **FTIR spectroscopic studies**

The samples G<sub>x</sub>/A50, G<sub>x</sub>/A200, and G<sub>x</sub>/A380 obtained after Gly deposition by IWI followed by activation at 160 °C for 30 min were investigated by FTIR.

The IR difference spectra of G<sub>x</sub>/A50 (Figure V-6, panel A) show that at very low Gly loading of 0.5% by weight (curve a), the ester, amide I and amide II bands are formed indicating the formation of peptide bonds on the surface. However, when the Gly loading deposited on the surface increases (for 1 to 5%, panel A, curves b to f), the amide II band is not detected anymore, but instead the DKP ring stretching is observed at around 1473 cm<sup>-1</sup> indicating the formation of cyclic DKP as a major product on the surface. For curves e and f (panel A) corresponding to 4 and 5% Gly weight loading respectively, additional bands assigned to monomeric Gly appear, which is consistent with the XRD data showing Gly crystallites. These bands probably have a higher extinction coefficient than the amide ones, since they are already predominant in sample

$G_5/A_{50}$ , where monomeric Gly accounts for at most 30% of the total deposited glycine. They are located at 1422 and 1528  $\text{cm}^{-1}$ , and may be associated to  $\nu_s$  of  $\text{COO}^-$  and  $\delta_s$  of  $\text{NH}_3^+$  respectively. As regards the  $\nu_{as}$  of  $\text{COO}^-$  and  $\delta_{as}$  of  $\text{NH}_3^+$ , they are expected around 1593 and 1606  $\text{cm}^{-1}$  respectively, and may overlap with the  $\delta$  of  $\text{H}_2\text{O}$  adsorbed on silica surface which is located at approximately 1630  $\text{cm}^{-1}$ .<sup>280</sup>

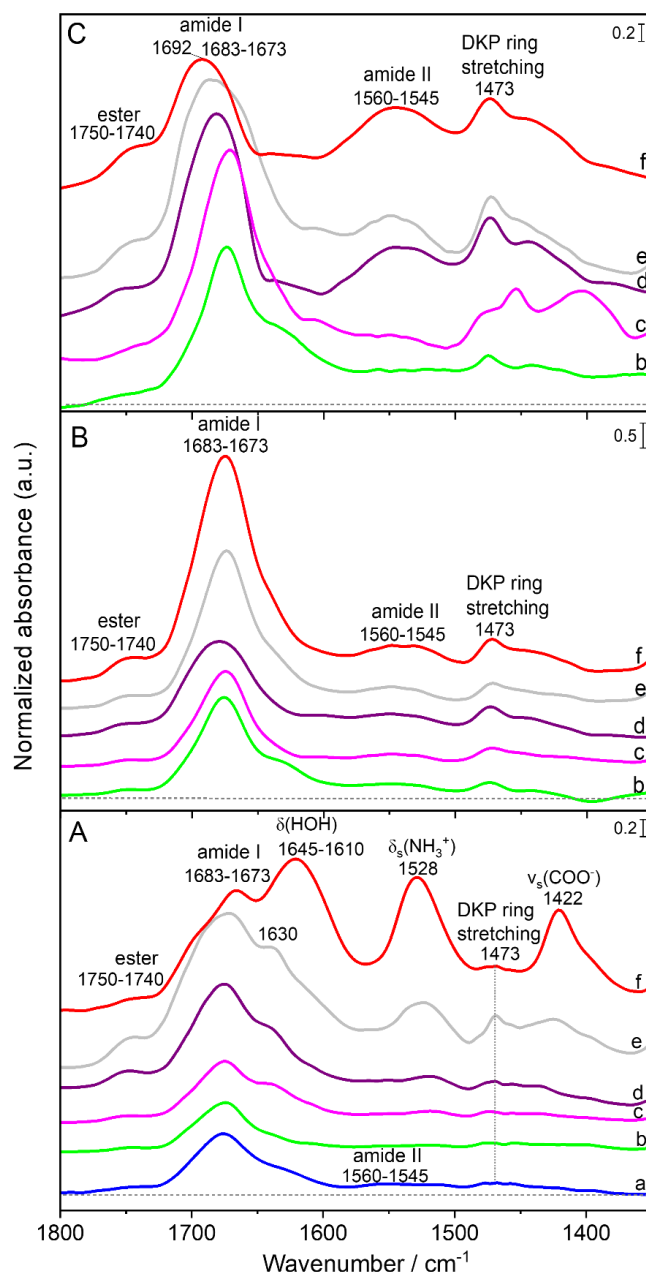


**Figure V-6:** Transmission IR difference spectra measured on self-supporting pellets after Gly deposition by incipient wetness impregnation followed by activation for 30 min at 160 °C under argon flow on silica: (A)  $G_x/A_{50}$ , (B)  $G_x/A_{200}$ , and (C)  $G_x/A_{380}$ ; where x refers to different Gly monomers loading: (a) 0.5, (b) 1, (c) 2, (d) 3, (e) 4, or (f) 5 wt%.

For G<sub>x</sub>/A200 samples (Figure V-6, panel B), the characteristic bands of DKP are predominant from the start, but the amide II band develops with increasing loadings – the ratio of the amide II to DKP breathing bands intensities increases regularly, except for the 3% loading. Thus, while DKP is always the main product, the probability of linear polymer formation increases with the Gly loading. The component around 1630 cm<sup>-1</sup> related to the water bending mode is apparently weaker with respect to A50.

For G<sub>x</sub>/A380 samples (Figure V-6, panel C), the samples with the lowest Gly weight loadings (1 and 2%, curves b and c) mostly show the amide I (1683-1673 cm<sup>-1</sup>), without a noticeable amide II component, and the DKP ring breathing bands (1473 cm<sup>-1</sup>): DKP is thus the major product. The component assigned to physisorbed water at 1630 cm<sup>-1</sup> is particularly evident on the low loading sample. As the Gly weight loading increases (3, 4, and 5%), the amide II band (1560-1545 cm<sup>-1</sup>) becomes conspicuous – this trend is clearer than in the case of G<sub>x</sub>/A200.

To summarize, when glycine is deposited from the aqueous phase (IWI procedure), DKP is the main product of thermal condensation on the low-surface A50 support, and also on the higher-surface A200 and A380 when the glycine loading is low, while linear polymers are only formed on high-surface supports with high glycine loadings. These findings stand in stark contrast with those obtained for deposition from the gas phase (CVD procedure), where linear polymers were observed on A50, and DKP predominated on A380.

### **Thermogravimetric analysis**

The DTG traces of two unactivated samples (G<sub>2%</sub>/A380 and G<sub>3%</sub>/A380) are presented in Appendix 3 (Figure A3-6 and Table A3-2). In agreement with previously published data, they exhibit a first, endothermal peak at 137-139 °C, previously shown to correspond to the elimination of water upon amide bond formation, and a second, exothermal event with a first maximum above 250 °C, corresponding to the oxidative degradation of the condensation

products. The total integrated values of the two events are in good agreement with the initially deposited glycine amounts, confirming that the thermal events are correctly attributed to Gly and the products of its transformation. However, the intensity ratio of the first to the second peak is higher than the value expected if the first one was exclusively due to amide condensation, especially for the G<sub>3%</sub>/A380 sample (38 against 24%). It has been previously observed that when deposited at high surface densities, part of the glycine sublimates instead of condensing.<sup>227</sup> Thus, even if the glycine loading after deposition and drying is known in the IWI procedure, it may be significantly decreased after thermal activation.

Considering now the DTGs of the samples activated at 160 °C (Figure V-7), it is expected of course that no thermal events at temperatures lower than this value should be present, and that is what we observed experimentally. Indeed, all G<sub>x</sub>/A200 and G<sub>x</sub>/A380 samples, as well as the low-loading G<sub>x</sub>/A50, only show exothermic events starting at 227 °C or higher, previously assigned to the decomposition of glycine polymers. In contrast, the highest-loading G<sub>x</sub>/A50 (4 and 5%) exhibit intense weight losses at 158 and 168 °C respectively, probably corresponding to the sublimation of glycine from the bulk crystallites present in these two samples: similar events have been observed previously for high-loading glycine deposited on Aerosil silica by IWI.<sup>120</sup> G<sub>5</sub>/A50 also shows a distinctive peak at 209 °C, perhaps corresponding to the peak at 221 °C in G<sub>4</sub>/A50; it may be due to amide condensation in the fraction of the bulk Gly crystallites that have not yet been sublimated.

The decomposition peaks above 200 °C have different fingerprints on A380 and A200, with a single peak at 250 °C in the first case and two components around 220 and 280 °C in the second case. This does not seem to reflect the nature of the polymers, which are similar in both cases according to IR, but perhaps the specifics of their interactions with the two surfaces.

Perhaps more surprising than the DTG profiles is the quantification of weight losses. While the integration of the DTG peaks for unactivated samples gave loadings that corresponded well to

the nominal values, the values found after thermal activation were considerably lower, even taking into account the decrease due to condensation water loss (see Fig. SI7). This means that a considerable proportion of the deposited glycine is lost on sublimation rather than polymerizing (up to 54% in the highest loading sample). This is in keeping with the remark made in the comments of Figure A3-6; furthermore, sublimation is confirmed by the observation of cloudy white deposits on the U-cell walls downstream from the sample in the thermal activation step.

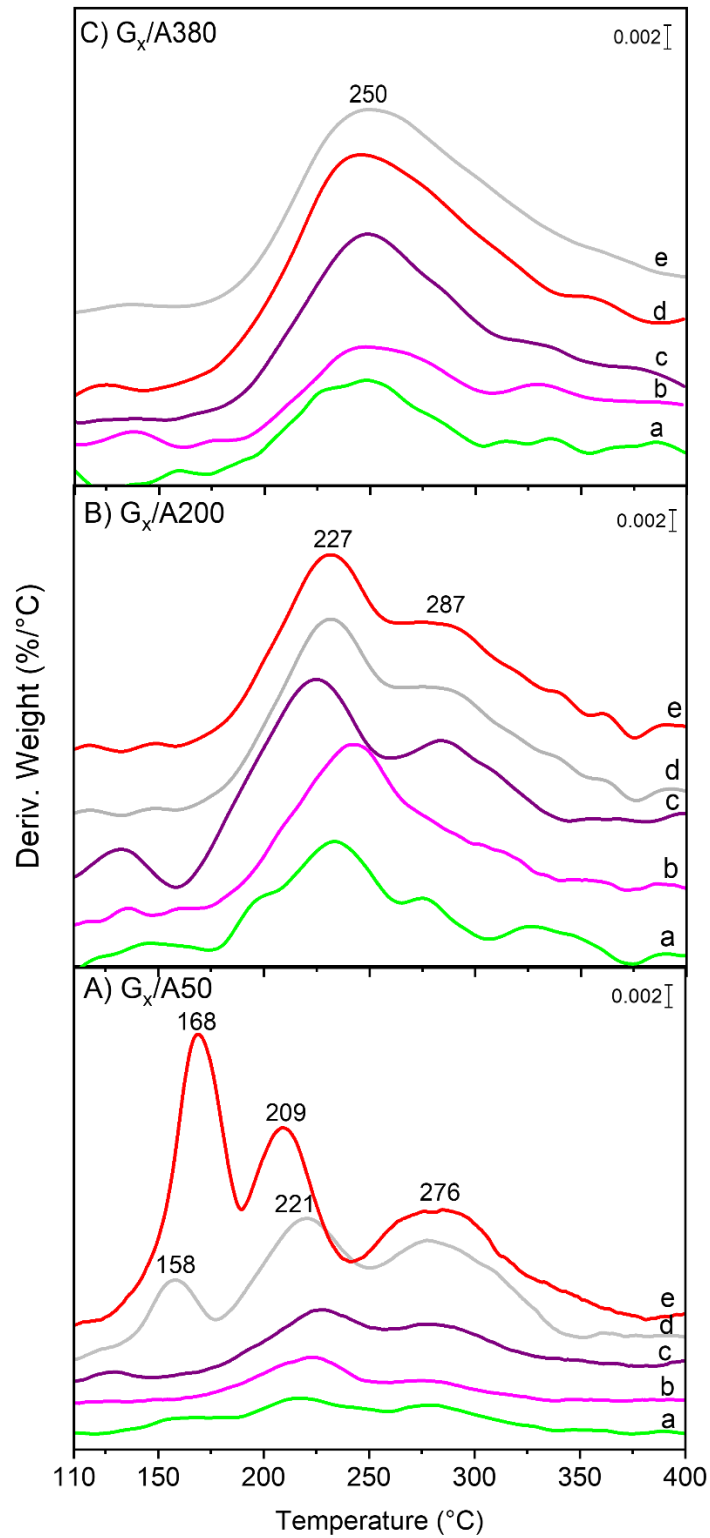


**Figure V-7:** Thermograms (DTG) of samples after Gly deposition by incipient wetness impregnation followed by activation for 30 min at 160 °C under argon flow on silica: (A) G<sub>x</sub>/A50, (B) G<sub>x</sub>/A200, and (C) G<sub>x</sub>/A380; where x refers to different Gly monomers loading: (a) 1, (b) 2, (c) 3, (d) 4, or (e) 5 wt%.

## General discussion

Thermally induced glycine polymerization on Aerosil-type silicas may result in the formation of linear polymers, cyclic polymers, or a mixture of both. The outcome of the polymerization cannot be simply related to experimental parameters. For instance, both types of polymers are found in CVD experiments with deposition of (canonic) glycine from the gas phase and in impregnation experiments, with deposition of (zwitterionic) glycine from the aqueous phase. The distribution is not simply correlated to the density of glycine on the surface either – which is not too surprising since, in the case of linear polymers, the amount of glycine retained depends not only on the chain density, but also on the chain length.

It is probably more promising to consider the possibility that linear polymers formation depends on the presence of particular sites that may exist on the silica surface in certain conditions. These would have to be special combinations of silanol groups and siloxane rings.

One candidate for such sites may be small, strained rings made of 2 to 4 ( $\text{SiO}_4$ ) tetrahedra.<sup>169</sup> We did observe 3-rings and 4-rings by Raman spectroscopy through the D1 and D2 features. Being all of the Aerosil type, our three silica supports did not differ markedly in the amount of 3- and 4-rings – if anything, they were less abundant in A50, that showed ample evidence for linear peptide growth. There was a significant effect of thermal pretreatment of the supports on the D1 and D2 bands. Low-temperature (450 °C) calcination caused an increase in these features, an expected consequence of the condensation of surface silanols.<sup>129</sup> However, calcination at higher temperatures unexpectedly caused them to decrease again. Figure A3-8 proposes a way in which the condensation of two strained rings might result in the formation of larger rings; if this process happens between strained rings in two different silica particles, it would cause necking, and explain the surface area decrease observed at the highest activation temperature.

At any rate, the amount of strained rings *per se* is not a good predictor of glycine polymerization reactivity: for instance, untreated A380 and A380 heated at 700 °C have about the same densities of 3- and 4-rings (Figure A3-1), but very different reactivities, as the first one forms mostly DKP, and the second one linear polymers (Table V-3).

In contrast, the global silanols density on the surface seems to be correlated with the transformations of glycine. In the CVD procedure, only two samples did not cause significant amide bond formation, namely G/A50(700 °C) and G/A200(700 °C). They were also the only two samples that did not exhibit the band at 1750-1740 cm<sup>-1</sup> that we assigned to silanol-glycine esters, and the ones with the lowest silanols density ( $\leq 0.7$  nm<sup>-2</sup>, cf. Table V-3). We can surmise that the dearth of silanol groups prevents the interaction of gas-phase glycine with the silica surface, as the molecule does not have any affinity for the siloxane moieties. In contrast, silanol densities in the 1.4 to 2.7 range seem favorable for linear peptide formation – samples with such densities include the pristine A50, which was used in our previous studies.<sup>25,222,275</sup> Gas-phase glycine can be grafted on these surfaces, forming ester groups, and rather long linear peptides grow from these over several tens of hours at 160 °C. Finally, on the sample with the highest density of silanols (A380<sub>(rt)</sub>, 4.5 nm<sup>-2</sup>), a large amount of DKP is formed (this is still observed on A380<sub>(450)</sub>, with 2 silanols nm<sup>-2</sup>). In our view, the simplest rationalization of these facts is as follows. A specific type of silanol groups is required to condense with the Gly molecules from the gas phase, providing the primers for growth of the oligopeptide chains. These groups exist in sufficient numbers on silica surfaces with intermediate silanol densities, which therefore constitute the best platforms for linear peptides growth. Surfaces with higher silanols densities contain in addition other types of silanols that do not form covalent bonds with glycine molecules. They can still activate them, perhaps by strong H-bonding, so that the adsorbed Gly will be activated for reaction with a second Gly coming from the gas phase. Once the Gly-Gly



dimer is obtained, it will immediately condense its two free termini to give the cyclic dimer, a reaction that is faster than the initial amide bond formation,<sup>227</sup> yielding the cyclic dimer DKP. A logical candidate for the crucial, specific surface groups would be the “nearly-free silanols” (NFS), i.e. groups of two silanols separated by a rather large distance (4 to 6 Å) allowing only a weak inter-silanol H-bond. We have demonstrated in a previous paper<sup>222</sup> that these groups play a special role in glycine polymerization. They can form ester groups with Gly, a property shared with isolated silanols; but they also seem to play a specific role in the catalysis of chain elongation, a property that isolated silanols do not share. A previous theoretical study had indeed shown that NFS could have specific properties for the catalysis of amide bond condensation.<sup>24</sup> It is difficult to precisely estimate the density of NFS as a function of the overall silanols density, since the distribution of silanols on the surface is not homogeneous. However, it is logical to think that it should go through a maximum for intermediate silanols coverage, and that at higher silanol densities they should be supplanted by pairs with smaller intersilanols coverage.

Considering now the results of deposition from the aqueous phase. Here the glycine molecules are initially in the form of zwitterions. When the amounts of glycine exceed the saturation coverage, which is close to a physical monolayer, part of the Gly will precipitate separately from the silica surface – this only concerns two samples, G<sub>4</sub>/A50 and G<sub>5</sub>/A50, that may be excluded from the discussion. For the others, by analogy with other amino acids such as leucine, we expect that a transition to the canonical form will only occur when most or all of the physisorbed water will be eliminated from the surface, at temperatures above 100 °C. At this stage, it seems that a fraction of the Gly does form ester bonds with the NFS (and isolated silanols), as witnessed by the ester bands observed in all IR spectra in Figure V-6. The remaining Gly molecules can undergo two different fates, either condensing with the grafted chains to give linear polymers, or with each other to give DKP. If these phenomena were

dependent on surface diffusion, it could have been expected that the higher the glycine surface density, the more likely the second fate is, because more concentrated Gly monomers would stand a better chance of meeting each other than of meeting fixed primers. However, exactly the opposite is observed: especially on A200 and A380, DKP predominates for the lowest loadings, while linear peptides are observed for the highest ones.

Therefore, the previous reasoning must contain a flawed assumption. It probably consists in positing that glycine condensation depends on surface diffusion. Diffusion on a dehydrated silica surface at 160 °C is probably slow – but diffusion through the gas phase is an alternate option. Neutral (canonical) Gly molecules formed above 100 °C have a lower adsorption capacity on the silica surface than the initially deposited Gly zwitterions. Therefore, a significant amount of the Gly deposited by IWI desorbs to the gas phase before 160 °C, as amply proved by Figure S7. This gas-phase Gly might then interact with the Gly ester primers on the surface (in an Eley-Rideal type catalytic mechanism), causing the growth of linear oligopeptide chains. This phenomenon would be more significant for the higher-loading Gly samples. In support of this mechanism, it may be noted that an amino acid condensation involving passage through the gas phase has been proposed before,<sup>227</sup> on the basis of a different reasoning.

#### **V.4. Conclusion**

Amino acids polymerization on silica has been well established for several decades, but previous studies have reported conflicting results as to its outcome, usually without an attempt at justification. In the present work, we have tried to unravel the different factors that determine the formation of cyclic dimers or of linear polymers by comparing several silica supports with different surface areas, varying the surface density of silanol groups by thermal pretreatments,

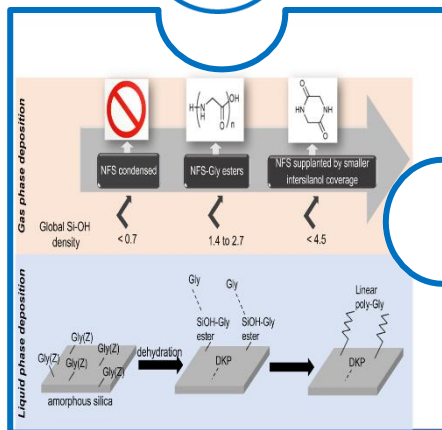
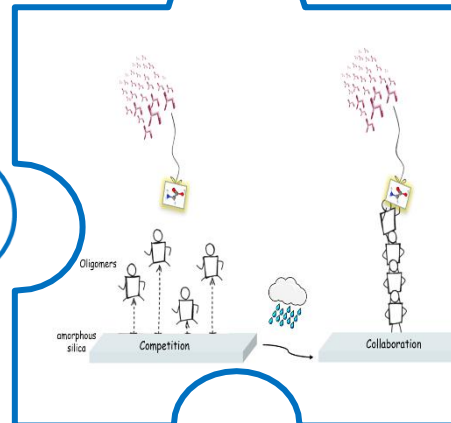
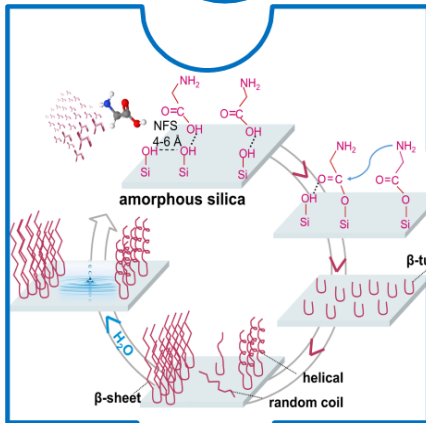
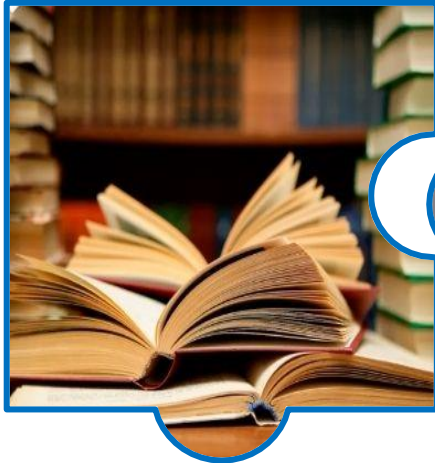
and applying a procedure of deposition from the aqueous phase in addition to the CVD procedure.

In most cases, glycine can form ester bonds with a limited number of silanols on the surface. A subset of these ester centers can act as primers for linear chain growth, as the grafting of one end of the growing chain prevents the otherwise entropically favored peptide cyclization. In agreement with our previous work, we hypothesized that this subset corresponds to the “nearly-free silanols” (NFS) separated a distance of 4 to 6 Å. As the surface silanols density increases, the amount of NFS goes through a maximum (at about 1.5 silanol.nm<sup>-2</sup> as global silanols density), and the corresponding samples are the most efficient platforms for linear polypeptide formation. Silica surfaces with much lower silanol densities are inactive; in contrast, surfaces richer in overall silanols contain different pairs that only interact with glycine through weak bonds, so that reaction with an additional Gly from the gas phase results in cyclization to DKP. Deposition of glycine from an aqueous solution followed by drying may also form both DKP and linear polymers, the latter being observed for high glycine loadings. Surprisingly, a significant amount of glycine desorbs to the gas phase when the samples are activated at 160 °C. Immediately after aqueous deposition, glycine is zwitterionic and may be adsorbed on silica with a rather high saturation coverage close to a physical monolayer; but after dehydration of the surface, it isomerizes to the canonical (neutral) form, which is only retained by the surface in smaller amounts, causing desorption. If enough glycine is desorbed in this way, it will react to the ester primers, forming linear peptide chains.

These results show the complexity of the surface chemistry of amino acids, even the simplest one, glycine. Starkly different outcomes are obtained depending on the glycine deposition procedure, the glycine loading or the thermal pretreatment of the support. Obviously, a correct evaluation of the potential of any prebiotic surface scenario necessitates a study of the systems using the concepts and the techniques of materials and surface science. In our case, the

elucidation of glycine surface chemistry was based on a combination of IR spectroscopy, Raman spectroscopy, thermogravimetric analysis, X-Ray Diffraction and N<sub>2</sub> physisorption. Solid-state NMR would also be an interesting addition to further studies.

# General conclusion and perspectives



Despite the big number of studies tackling the polymerization reaction from the condensation of unactivated amino acids on oxide surfaces and especially on silica, this reaction still faces obstructions regarding the mechanism, kinetics, selectivity and reaction efficiency. The problems encountered are mainly related to the lack of knowledge regarding the crucial surface sites for the reaction, the behavior of the biomolecules obtained under different environmental conditions, and the effect of water exposure at different stages of the reaction on the efficiency and type of the reaction product obtained.

During this PhD thesis, different experimental characterization techniques mainly in-situ IR spectroscopy, Raman spectroscopy, X-ray diffraction, thermogravimetric analysis, Mass spectrometry, and N<sub>2</sub> sorption were combined to investigate different amorphous silica surfaces along with various Gly/silica systems prepared either by Gly monomers deposition from gas or liquid phases.

First, we have successfully presented a suggested mechanism for the polymerization reaction through the condensation of unactivated Gly monomers after a deep characterization of the successive steps of the reaction including adsorption, initiation, and prolongation of the poly-Gly on silica. More importantly, we have shown the key surface sites crucial for such reaction on the silica surface: Gly monomers seem to be able to bind covalently to the surface through ester formation which play, along with a specific silanol arrangement, the nearly-free silanol (NFS) groups, a key role for monomers activation. Once activated,  $\beta$ -turn conformations start to form which then elongate into more complex secondary structures of mainly  $\beta$ -sheet of high resistance to hydrolysis, deuterium exchange and even desorption. The density of the self-assembled peptides obtained can be increased by a formic acid treatment of the silica surface prior to the reaction.

Second, an in depth study of the polymerization reaction under different environmental conditions was presented and we showed that a fluctuating system subjected to both

temperature and humidity fluctuations cycles is a more favorable geochemical setting for the polymerization reaction compared to a system subjected only to temperature fluctuations. A mechanism of the prolongation of poly-Gly under wetting-drying cycles was suggested where the results revealed that the dehydration steps are crucial to thermodynamically drive the condensation for the polymerization reaction while the hydration steps result in the hydrolysis, reorganization of the oligomers on the surface, and the re-establishment of the NFS anchoring sites. We demonstrated that the freed chains aggregate with pre-existing poly-Gly chains leading to the formation of a high amount of peptides with a high level of structuring. We justified by that the efficiency of applying wetting-drying cycles during the polymerization reaction. The structural dynamics on the oligopeptides were also evaluated and revealed that  $\beta$ -sheet conformations represent very resilient structures compared to the other structural elements. These results also suggest hints of a templated growth on  $\beta$ -sheet through a probable transmission of information from nuclei to growing chains.

Third, we tried to solve the apparent discrepancies found in the literature, about the formation of linear peptides or cyclic dimers upon glycine polymerization on silica. Thus, we studied in depth the parameters that determine the outcome of the polymerization of glycine mediated by the surface of silica samples of different surface areas and silanol densities by applying different thermal pretreatments. The Gly monomers deposition was done from both the gas phase using chemical vapour deposition and the liquid phase using incipient wetness impregnation followed by dehydration. The results evidenced the crucial role of the nearly-free silanols and ester groups as primers to promote the formation of linear peptides over DKP. A silica surface low on silanols shows a quenched reactivity toward peptide bond formation while a surface rich in different types of silanols that interact with Gly monomers via weak H-bonding promotes the cyclization of Gly monomers into DKP.

As for the perspectives, first, in parallel with the silica pre-treatment with formic acid prior to the polymerization reaction investigated in details in this work, pre-treatment of silica with succinic acid, on which I started very preliminary experiments, could be fruitful for getting more details on the possible reactivity of the amino group of Gly monomers for the adsorption and polymerization on silica surface. In addition, it would be interesting to improve the efficiency of the washing of oligomers/poly-Gly chemisorbed on the silica surface by adopting a washing procedure involving hydrofluoric (HF) acid, which could then allow a better estimation of the real length of the peptides formed by Mass Spectrometry. Furthermore, trying to perform the polymerization of Gly from gas phase on silica while using lower pressure for even longer times would be interesting from the point of view of adopting plausible conditions for the early Earth. Moreover, studying the formation of secondary peptide structures on silica surface in fluctuating environments but using more complex and diverse monomers than Gly, the reference amino acid, could also be interesting for future studies although it would complicate the IR analysis. It is also of great interest to study in more depth the conditions in which the cyclic dimer DKP behaves as a dead-end product or as a useful intermediate product for prolongation and whether this is related to the support employed or not. Note that some fruitful preliminary experiments were also performed regarding this idea, which suggested that DKP could be a useful product for further prolongation of oligomers on the surface.



## References

1. Pattabiraman, V. R. & Bode, J. W. Rethinking amide bond synthesis. *Nature* **480**, 471–479 (2011).
2. Constable, D. J. C. *et al.* Key green chemistry research areas—a perspective from pharmaceutical manufacturers. *Green Chem.* **9**, 411–42 (2007).
3. Valeur, E. & Bradley, M. Amide bond formation: Beyond the myth of coupling reagents. *Chem. Soc. Rev.* **38**, 606–631 (2009).
4. Han, S. Y. & Kim, Y. A. Recent development of peptide coupling reagents in organic synthesis. *Tetrahedron* **60**, 2447–2467 (2004).
5. El-Faham, A. & Albericio, F. Peptide coupling reagents, more than a letter soup. *Chem. Rev.* **111**, 6557–6602 (2011).
6. Sabatini, M. T., Boulton, L. T., Sneddon, H. F. & Sheppard, T. D. A green chemistry perspective on catalytic amide bond formation. *Nat. Catal.* **2**, 10–17 (2019).
7. Lundberg, H., Tinnis, F., Selander, N. & Adolfsson, H. Catalytic amide formation from non-activated carboxylic acids and amines. *Chem. Soc. Rev.* **43**, 2714–2742 (2014).
8. Čeřovský, V. & Kula, M. R. C-terminal peptide amidation catalyzed by orange flavedo peptide amidase. *Angew. Chemie - Int. Ed.* **37**, 1885–1887 (1998).
9. Čeřovský, V. & Kula, M.-R. Studies on peptide amidase-catalysed C-terminal peptide amidation in organic media with respect to its substrate specificity. *Biotechnol. Appl. Biochem.* **33**, 183 (2001).
10. Nelson, B. P. Notes 954. ITrisdialkylaminoboranes : New Reagents for the Synthesis. *Analysis* 5142–5144 (1953).
11. Ishihara, K., Ohara, S. & Yamamoto, H. 3,4,5-Trifluorobenzeneboronic acid as an extremely active amidation catalyst. *J. Org. Chem.* **61**, 4196–4197 (1996).
12. Sabatini, M. T., Boulton, L. T. & Sheppard, T. D. Borate esters: Simple catalysts for the sustainable synthesis of complex amides. *Sci. Adv.* **3**, 1–9 (2017).
13. Noda, H., Furutachi, M., Asada, Y., Shibasaki, M. & Kumagai, N. Unique physicochemical and catalytic properties dictated by the B3NO2 ring system. *Nat. Chem.* **9**, 571–577 (2017).

14. Wang, K., Lu, Y. & Ishihara, K. The: Ortho -substituent on 2,4-bis(trifluoromethyl)phenylboronic acid catalyzed dehydrative condensation between carboxylic acids and amines. *Chem. Commun.* **54**, 5410–5413 (2018).
15. Bannister, R. M., Brookes, M. H., Evans, G. R., Katz, R. B. & Tyrrell, N. D. A scaleable route to the pure enantiomers of verapamil. *Org. Process Res. Dev.* **4**, 467–472 (2000).
16. Krause, T., Baader, S., Erb, B. & Gooßen, L. J. Atom-economic catalytic amide synthesis from amines and carboxylic acids activated in situ with acetylenes. *Nat. Commun.* **7**, 1–7 (2016).
17. Lundberg, H. & Adolfsson, H. Hafnium-catalyzed direct amide formation at room temperature. *ACS Catal.* **5**, 3271–3277 (2015).
18. De Figueiredo, R. M., Suppo, J. S. & Campagne, J. M. Nonclassical Routes for Amide Bond Formation. *Chem. Rev.* **116**, 12029–12122 (2016).
19. Liu, H. *et al.* Potassium Thioacids Mediated Selective Amide and Peptide Constructions Enabled by Visible Light Photoredox Catalysis. *ACS Catal.* **6**, 1732–1736 (2016).
20. Allen, C. L. & Williams, J. M. J. Metal-catalysed approaches to amide bond formation. *Chem. Soc. Rev.* **40**, 3405–3415 (2011).
21. Comerford, J. W., Clark, J. H., MacQuarrie, D. J. & Breeden, S. W. Clean, reusable and low cost heterogeneous catalyst for amide synthesis. *Chem. Commun.* 2562–2564 (2009)
22. Hosseini-sarvari, M. & Sharghi, H. ZnO as a New Catalyst for N-Formylation of Amines under Solvent-Free Conditions ZnO under solvent-free conditions brings about highly and in excellent yields . The N-formylation reaction not only formamides . 7 Furthermore , formamides are very useful rea. *Tetrahedron* 6652–6654 (2006).
23. Guo, C., Jordan, J. S., Yarger, J. L. & Holland, G. P. Highly Efficient Fumed Silica Nanoparticles for Peptide Bond Formation: Converting Alanine to Alanine Anhydride. *ACS Appl. Mater. Interfaces* **9**, 17653–17661 (2017).
24. Rimola, A., Fabbiani, M., Sodupe, M., Ugliengo, P. & Martra, G. How Does Silica Catalyze the Amide Bond Formation under Dry Conditions? Role of Specific Surface Silanol Pairs. *ACS Catal.* **8**, 4558–4568 (2018).

25. Martra, G. *et al.* The formation and self-assembly of long prebiotic oligomers produced by the condensation of unactivated amino acids on oxide surfaces. *Angew. Chemie - Int. Ed.* **53**, 4671–4674 (2014).
26. Massolo, E., Pirola, M. & Benaglia, M. Amide Bond Formation Strategies: Latest Advances on a Dateless Transformation. *European J. Org. Chem.* **2020**, 4641–4651 (2020).
27. Brown, D. G. & Boström, J. Analysis of Past and Present Synthetic Methodologies on Medicinal Chemistry: Where Have All the New Reactions Gone? *J. Med. Chem.* **59**, 4443–4458 (2016).
28. Procopio, D. *et al.* Green solvents for the formation of amide linkages. *Org. Biomol. Chem.* **20**, 1137–1149 (2022).
29. Mylavarapu, R. K. *et al.* Boric acid catalyzed amidation in the synthesis of active pharmaceutical ingredients. *Org. Process Res. Dev.* **11**, 1065–1068 (2007).
30. Anderson, J., Davis, R., Fitzgerald, R. & Haberman, J. Selective phenol alkylation: An improved preparation of efaproxiral. *Synth. Commun.* **36**, 2129–2133 (2006).
31. Stephenson, J. P. *et al.* Direct Synthesis of Amides. *Science (80-. )*. **317**, 790–792 (2007).
32. Deiana, C. *et al.* Direct synthesis of amides from carboxylic acids and amines by using heterogeneous catalysts: Evidence of surface carboxylates as activated electrophilic species. *ChemCatChem* **5**, 2832–2834 (2013).
33. Shteinberg, L. Y., Kondratov, S. A., Shein, S. M. & Marshalova, V. V. Effect of water on the kinetics of the catalytic reaction between benzoic acid and aniline. *Kinet. Catal.* **48**, 632–635 (2007).
34. Hosseini-Sarvari, M., Sodagar, E. & Doroodmand, M. M. Nano sulfated titania as solid acid catalyst in direct synthesis of fatty acid amides. *J. Org. Chem.* **76**, 2853–2859 (2011).
35. Lundberg, H., Tinnis, F. & Adolfsson, H. Titanium(IV) isopropoxide as an efficient catalyst for direct amidation of nonactivated carboxylic acids. *Synlett* **23**, 2201–2204 (2012).
36. Ghosh, S. *et al.* Direct amide bond formation from carboxylic acids and amines using activated alumina balls as a new, convenient, clean, reusable and low cost

- heterogeneous catalyst. *Green Chem.* **14**, 3220–3229 (2012).
37. Comerford, J. W., Farmer, T. J., MacQuarrie, D. J., Breeden, S. W. & Clark, J. H. Mesoporous Structured Silica - An improved catalyst for direct amide synthesis and its application to continuous flow processing. *Arkivoc* **2012**, 282–293 (2012).
  38. Dunetz, J. R., Magano, J. & Weisenburger, G. A. Large-Scale Applications of Amide Coupling Reagents for the Synthesis of Pharmaceuticals. *Org. Process Res. Dev.* **20**, 140–177 (2016).
  39. Todorovic, M. & Perrin, D. M. Recent developments in catalytic amide bond formation. *Pept. Sci.* **112**, (2020).
  40. Frenkel-Pinter, M., Samanta, M., Ashkenasy, G. & Leman, L. J. Prebiotic Peptides: Molecular Hubs in the Origin of Life. *Chem. Rev.* **120**, 4707–4765 (2020).
  41. Ruiz-Mirazo, K., Briones, C. & De La Escosura, A. Prebiotic systems chemistry: New perspectives for the origins of life. *Chem. Rev.* **114**, 285–366 (2014).
  42. Pascal, R., Boiteau, L. & Commeyras, A. From the prebiotic synthesis of  $\alpha$ -amino acids towards a primitive translation apparatus for the synthesis of peptides. *Top. Curr. Chem.* **259**, 69–122 (2005).
  43. Danger, G., Plasson, R. & Pascal, R. Pathways for the formation and evolution of peptides in prebiotic environments. *Chem. Soc. Rev.* **41**, 5416–5429 (2012).
  44. Kitadai, N. & Maruyama, S. Origins of building blocks of life: A review. *Geosci. Front.* **9**, 1117–1153 (2018).
  45. Miller, S. L. A production of amino acids under possible primitive earth conditions. *Science (80-. )*. **117**, 528–529 (1953).
  46. Lazcano, A. & Bada, J. L. The 1953 Stanley L. Miller experiment: fifty years of prebiotic organic chemistry. *Orig. Life Evol. Biosph.* **33**, 235–242 (2003).
  47. Miller, S. L., William Schopf, J. & Lazcano, A. Oparin's 'origin of life': Sixty years later. *J. Mol. Evol.* **44**, 351–353 (1997).
  48. Johnson, A. P. *et al.* The Miller volcanic spark discharge experiment. *Science (80-. )*. **322**, 404 (2008).
  49. Parker, E. T. *et al.* Prebiotic Synthesis of Methionine and Other Sulfur-Containing Organic Compounds on the Primitive Earth: A Contemporary Reassessment Based on an Unpublished 1958 Stanley Miller Experiment. *Orig. Life Evol. Biosph.* **41**, 201–212

- (2011).
50. Parker, E. T. *et al.* Primordial synthesis of amines and amino acids in a 1958 Miller H<sub>2</sub>S-rich spark discharge experiment. *Proc. Natl. Acad. Sci. U. S. A.* **108**, 5526–5531 (2011).
  51. Steinman, G., Smith, A. E. & Silver, J. J. Synthesis of a sulfur-containing amino acid under simulated prebiotic conditions. *Science (80-. )*. **159**, 1108–1109 (1968).
  52. Sagan, C. & Khare, B. N. Long-wavelength ultraviolet photoproduction of amino acids on the primitive earth. *Science (80-. )*. **173**, 417–420 (1971).
  53. Utsumi, Y. & Takahashi, J. I. Synthesis of amino acids from N<sub>2</sub>, H<sub>2</sub>O vapor and CO<sub>2</sub> gas mixture by synchrotron radiation induced photochemical reactions at atmospheric pressure. *Japanese J. Appl. Physics, Part 2 Lett.* **37**, (1998).
  54. Takahashi, J. I. *et al.* Abiotic synthesis of amino acids by x-ray irradiation of simple inorganic gases. *Appl. Phys. Lett.* **74**, 877–879 (1999).
  55. Kobayashi, K., Kaneko, T. & Saito, T. Characterization of complex organic compounds formed in simulated planetary atmospheres by the action of high energy particles. *Adv. Sp. Res.* **24**, 461–464 (1999).
  56. Kobayashi, K., Tsuchiya, M., Oshima, T. & Yanagawa, H. Abiotic synthesis of amino acids and imidazole by proton irradiation of simulated primitive earth atmospheres. *Orig. Life Evol. Biosph.* **20**, 99–109 (1990).
  57. Sephton, M. A. Organic compounds in carbonaceous meteorites. *Nat. Prod. Rep.* **19**, 292–311 (2002).
  58. Snyder, L. E. *et al.* A Rigorous Attempt to Verify Interstellar Glycine. *Astrophys. J.* **619**, 914–930 (2005).
  59. Kuan, Y., Charnley, S. B., Huang, H., Tseng, W. & Kisiel, Z. Interstellar Glycine. *Astrophys. J.* **593**, 848–867 (2003).
  60. Elsila, J. E., Glavin, D. P. & Dworkin, J. P. Cometary glycine detected in samples returned by Stardust. *Meteorit. Planet. Sci.* **44**, 1323–1330 (2009).
  61. Baratta, G. a *et al.* Organics Captured from Comet. *Science (80-. )*. **314**, 1720–1724 (2006).
  62. Altwegg, K. *et al.* Prebiotic chemicals-amino acid and phosphorus in the coma of comet 67P/Churyumov-Gerasimenko. *Sci. Adv.* **2**, 1–6 (2016).

63. Martins, Z. Organic chemistry of carbonaceous meteorites. *Elements* **7**, 35–40 (2011).
64. Pizzarello, S., Huang, Y. & Alexandre, M. R. Molecular asymmetry in extraterrestrial chemistry: Insights from a pristine meteorite. *Proc. Natl. Acad. Sci. U. S. A.* **105**, 3700–3704 (2008).
65. Pizzarello, S. The chemistry of life's origin: A carbonaceous meteorite perspective. *Acc. Chem. Res.* **39**, 231–237 (2006).
66. Strecker, A. Ueber die künstliche Bildung der Milchsäure und einen neuen, dem Glycocoll homologen Körper; *Justus Liebigs Ann. Chem.* **75**, 27–45 (1850).
67. Gromovoy, Taras Yu; Basiuk, Vladimir A.; Chuiko, A. A. Growth of peptide chains on silica in absence of amino acid access from without. *Orig. Life Evol. Biosph.* **21**, 119–128 (1991).
68. Rimola, A., Tosoni, S., Sodupe, M. & Ugliengo, P. Peptide bond formation activated by the interplay of Lewis and Brønsted catalysts. *Chem. Phys. Lett.* **408**, 295–301 (2005).
69. Rimola, A., Sodupe, M., Ugliengo, P., Ifm, C. & Uni, V. Aluminosilicate Surfaces as Promoters for Peptide Bond Formation : An Assessment of Bernal ' s Hypothesis by ab Initio Methods earliest ones , based on the pioneering work of Miller , 5 Miller Along the same line of thought is a suggestion based on the. *Jacs* **129**, 8333–8344 (2007).
70. Napier, J. & Yin, J. Formation of peptides in the dry state. *Peptides* **27**, 607–610 (2006).
71. Kitadai, N., Yokoyama, T. & Nakashima, S. Hydration-dehydration interactions between glycine and anhydrous salts: Implications for a chemical evolution of life. *Geochim. Cosmochim. Acta* **75**, 6285–6299 (2011).
72. Kitadai, N. *et al.* Glycine Polymerization on Oxide Minerals. *Orig Life Evol Biosph* **47**, 123–143 (2017).
73. Kauffman, S. A. Autocatalytic sets of proteins. *J. Theor. Biol.* **119**, 1–24 (1986).
74. Orgel, L. E. The origin of life: A review of facts and speculation. *Nat. Life Class. Contemp. Perspect. from Philos. Sci.* **0004**, 121–128 (1998).
75. Brack, A. From interstellar amino acids to prebiotic catalytic peptides: A review. *Chem. Biodivers.* **4**, 665–679 (2007).
76. Goodwin, J. T., Mehta, A. K. & Lynn, D. G. Digital and analog chemical evolution.

- Acc. Chem. Res.* **45**, 2189–2199 (2012).
77. Cronin, L. & Walker, S. I. Beyond prebiotic chemistry. *Science* (80-. ). **352**, 1174–1175 (2016).
  78. Maury, C. P. J. Amyloid and the origin of life: self-replicating catalytic amyloids as prebiotic informational and protometabolic entities. *Cell. Mol. Life Sci.* **75**, 1499–1507 (2018).
  79. Bowman, J. C., Hud, N. V. & Williams, L. D. The Ribosome Challenge to the RNA World. *J. Mol. Evol.* **80**, 143–161 (2015).
  80. Petrov, A. S. *et al.* History of the ribosome and the origin of translation. *Proc. Natl. Acad. Sci. U. S. A.* **112**, 15396–15401 (2015).
  81. Ghosh, I. & Chmielewski, J. Peptide self-assembly as a model of proteins in the pre-genomic world. 640–644 (2004)
  82. Childers, W. S., Ni, R., Mehta, A. K. & Lynn, D. G. Peptide membranes in chemical evolution §. *Curr. Opin. Chem. Biol.* **13**, 652–659 (2009).
  83. O. Zozulia, † M. A. Dolan† and I. V. Korendovych. Chem Soc Rev Catalytic peptide assemblies. *Chem. Soc. Rev* **47**, 3621–3639 (2018).
  84. Humenik, M. & Smith, A. *Spider Silk : Understanding the Structure – Function Relationship of a Natural Fiber I . Synopsis. Molecular Assembly in Natural and Engineered Systems* vol. 103 (Elsevier Inc., 2011).
  85. Szostak, J., Joyce, G., Chyba, C. & Kiedrowski, V. Lipid-like Self-Assembling Peptides. *Acc. Chem. Res.* **45**, 2142–2150 (2012).
  86. Egel, R. Peptide-dominated membranes preceding the genetic takeover by RNA : latest thinking on a classic controversy. *Probl. Paradig.* 1100–1109 (2009)
  87. Poudyal, R. R., Cakmak, F. P., Keating, C. D. & Bevilacqua, P. C. Physical Principles and Extant Biology Reveal Roles for RNA- Containing Membraneless Compartments in Origins of Life Chemistry. *Biochemistry* **57**, 2509–2519 (2018).
  88. Lambert, J.-F. Adsorption and Polymerization of Amino Acids on Mineral Surfaces: A Review DO9128; No of Pages. *Orig Life Evol Biosph* **38**, 211–242 (2008).
  89. Georgelin, T., Jaber, M., Bazzi, H. & Lambert, J.-F. Formation of Activated Biomolecules by Condensation on Mineral Surfaces-A Comparison of Peptide Bond Formation and Phosphate Condensation. *Orig Life Evol Biosph* **43**, 429–443 (2013).

90. Kitadai, N. Thermodynamic prediction of glycine polymerization as a function of temperature and pH consistent with experimentally obtained results. *J. Mol. Evol.* **78**, 171–187 (2014).
91. Bruce Martin, R. Free energies and equilibria of peptide bond hydrolysis and formation. *Biopolymers* **45**, 351–353 (1998).
92. Schwendinger, G. & Rode, M. Salt-induced conditions. *Inorganica Chim. Acta* **186**, 247–251 (1991).
93. Rode, B. M. Peptides and the origin of life. *Peptides* **20**, 773–786 (1999).
94. Eder, A. H. & Rode, B. M. Influence of alkali- and alkaline-earth-metal cations on the ‘salt-induced peptide formation’ reaction. *J. Chem. Soc. Dalt. Trans.* 1125–1130 (1994)
95. Ei-ichi Imai, Hajime Honda, Kuniyuki Hatori, A. B. and K. M. American association for the advancement of science. *J. Franklin Inst.* **202**, 834 (1926).
96. Lyons, J. R. & Vasavada, A. R. Flash heating on the early earth 1 . Introduction The devastating effects of impact events on the surface environment of the Earth have been often discussed , both for the young Earth ( Maher and Stevenson , 1988 ; Sleep et al . , 1989 ; Oberbeck and Fogl. *Org. Process Res. Dev.* **29**, 123–138 (1999).
97. Blank, J. G., Miller, G. H., Ahrens, M. J. & Winans, R. E. Experimental shock chemistry of aqueous amino acid solutions and the cometary delivery of prebiotic compounds. *Orig. Life Evol. Biosph.* **31**, 15–51 (2001).
98. Yamagata, Y. & Inomata, K. Condensation of glycyglycine to oligoglycines with trimetaphosphate in aqueous solution. II: Catalytic effect of magnesium ion. *Orig. Life Evol. Biosph.* **27**, 339–344 (1997).
99. Basiuk, V. A., Gromovoy, T. Y. & Golovaty, V. G. Mechanisms of amino acid polycondensation on silica and alumina surfaces. *Orig. Life Evol. Biosph.* **20**, 483–498 (1990).
100. Kitadai, N. Dissolved Divalent Metal and ph Effects on Amino Acid Polymerization: A Thermodynamic Evaluation. *Orig. Life Evol. Biosph.* **47**, 13–37 (2017).
101. Barlow, S. M. & Raval, R. Complex organic molecules at metal surfaces: Bonding, organisation and chirality. *Surf. Sci. Rep.* **50**, 201–341 (2003).
102. Bernal, J. D. The physical basis of life. *Proc. Phys. Soc. Sect. B* **62**, 597–618 (1949).



103. Orgel, L. E. Polymerization on the rocks: theoretical introduction. *Orig. Life Evol. Biosph.* **28**, 227–234 (1998).
104. De Duve, C. & Miller, S. L. Two-dimensional life? *Proc. Natl. Acad. Sci. U. S. A.* **88**, 10014–10017 (1991).
105. Hill Jr., A. R., Bohler, C. & Orgel, L. E. Polymerization on the rocks: negatively-charged alpha-amino acids. *Orig Life Evol Biosph* **28**, 235–243 (1998).
106. Gerstner, J. A., Bell, J. A. & Cramer, S. M. Gibbs free energy of adsorption for biomolecules in ion-exchange systems. *Biophys. Chem.* **52**, 97–106 (1994).
107. Marshall-Bowman, K., Ohara, S., Sverjensky, D. A., Hazen, R. M. & Cleaves, H. J. Catalytic peptide hydrolysis by mineral surface: Implications for prebiotic chemistry. *Geochim. Cosmochim. Acta* **74**, 5852–5861 (2010).
108. Lahav, N., White, D. & Chang, S. Peptide formation in the prebiotic era: Thermal condensation of glycine in fluctuating clay environments. *Science (80-. ).* **201**, 67–69 (1978).
109. Lahav, N. & Chang, S. The possible role of solid surface area in condensation reactions during chemical evolution: Reevaluation. *J. Mol. Evol.* **8**, 357–380 (1976).
110. Paecht-Horowitz, M. & Lahav, N. Polymerization of alanine in the presence of a non-swelling montmorillonite. *J. Mol. Evol.* **10**, 73–76 (1977).
111. Vladimir, A., Gromovoy, T. Y. U., Glukhoy, A. M. & Golovaty, V. G. Chemical Transformations of Proteinogenic Silica. *Orig Life Evol Biosph* **21**, 129–144 (1991).
112. Basiuk, V. A. & Gromovoy, T. Y. The “gas–solid-phase” 2,5-dioxopiperazine synthesis. Cyclization of vaporous dipeptides on silica surface. *Collect. Czechoslov. Chem. Commun.* **59**, 461–466 (1994).
113. Bujdák, J. & Rode, B. M. Glycine oligomerization on silica and alumina. *React. Kinet. Catal. Lett.* **62**, 281–286 (1997).
114. Lambert, J. F., Stievano, L., Lopes, I., Gharsallah, M. & Piao, L. The fate of amino acids adsorbed on mineral matter. *Planet. Space Sci.* **57**, 460–467 (2009).
115. Zaia, D. A. M. A review of adsorption of amino acids on minerals: Was it important for origin of life? *Amino Acids* vol. 27 113–118 (2004).
116. Fox, S. W. & Harada, K. The Thermal Copolymerization of Amino Acids Common to Protein. *J. Am. Chem. Soc.* **82**, 3745–3751 (1960).

117. Rodriguez-Garcia, M. *et al.* ARTICLE Formation of oligopeptides in high yield under simple programmable conditions. *Nat. Commun.* **6**, 1–7 (2015).
118. Roddick-Lanzilotta, A. D. & McQuillan, A. J. An in situ infrared spectroscopic study of glutamic acid and of aspartic acid adsorbed on TiO<sub>2</sub>: Implications for the biocompatibility of titanium. *J. Colloid Interface Sci.* **227**, 48–54 (2000).
119. Macklin, J. W. & White, D. H. Infrared spectroscopic studies of the effect of elevated temperature on the association of pyroglutamic acid with clay and other minerals. *Spectrochim. Acta Part A Mol. Spectrosc.* **41**, 851–859 (1985).
120. Meng, M., Stievano, L. & Lambert, J.-F. Adsorption and Thermal Condensation Mechanisms of Amino Acids on Oxide Supports. 1. Glycine on Silica. *Langmuir* **20**, 914–923 (2004).
121. Vinu, A., Hossain, K. Z., Satish Kumar, G. & Ariga, K. Adsorption of L-histidine over mesoporous carbon molecular sieves. *Carbon N. Y.* **44**, 530–536 (2006).
122. El Shafei, G. M. S. & Philip, C. A. Interactions at an alumina-aqueous glycine interface: Characterization of glycine-modified boehmite. *J. Colloid Interface Sci.* **176**, 55–62 (1995).
123. Spanos, N., Klepetsanis, P. G. & Koutsoukos, P. G. Model studies on the interaction of amino acids with biominerals: The effect of L-serine at the hydroxyapatite - Water interface. *J. Colloid Interface Sci.* **236**, 260–265 (2001).
124. Krohn, J. E. & Tsapatsis, M. Amino acid adsorption on zeolite  $\beta$ . *Langmuir* **21**, 8743–8750 (2005).
125. Kalra, S., Pant, C. K., Pathak, H. D. & Mehata, M. S. Studies on the adsorption of peptides of glycine/alanine on montmorillonite clay with or without co-ordinated divalent cations. *Colloids Surfaces A Physicochem. Eng. Asp.* **212**, 43–50 (2003).
126. Tzvetkov, G. *et al.* Bonding and structure of glycine on ordered Al<sub>2</sub>O<sub>3</sub> film surfaces. *Langmuir* **20**, 10551–10559 (2004).
127. Fleming, G. J. & Idriss, H. Probing the reaction pathways of DL-proline on TiO<sub>2</sub> (001) single crystal surfaces. *Langmuir* **20**, 7540–7546 (2004).
128. Qiu, T. Z. & Barteau, M. A. STM study of glycine on TiO<sub>2</sub>(110) single crystal surfaces. *J. Colloid Interface Sci.* **303**, 229–235 (2006).
129. Rimola, A., Costa, D., Sodupe, M., Lambert, O. & Ugliengo, P. Silica Surface Features

- and Their Role in the Adsorption of Biomolecules: Computational Modeling and Experiments. *Chem. Rev.* **113**, 4216–4313 (2013).
130. Croissant, J. G., Butler, K. S., Zink, J. I. & Brinker, C. J. Synthetic amorphous silica nanoparticles: toxicity, biomedical and environmental implications. *Nat. Rev. Mater.* **5**, 886–909 (2020).
  131. Brown, G. E. & Henrich, V. Metal Oxide Surfaces and Their Interactions with Aqueous Solutions and Microbial Organisms. *Chem. Rev.* **99**, 77–174 (1999).
  132. García-Ruiz, J. M., van Zuilen, M. A. & Bach, W. Mineral self-organization on a lifeless planet. *Phys. Life Rev.* **34–35**, 62–80 (2020).
  133. Siever Raymond. The silica cycle in the Precambrian. *Geochim. Cosmochim. Acta* **56**, 3265–3272 (1992).
  134. Hofmann, A. & Harris, C. Silica alteration zones in the Barberton greenstone belt: A window into seafloor processes 3.5-3.3 Ga ago. *Chem. Geol.* **257**, 221–239 (2008).
  135. Marin-Carbonne, J., Chaussidon, M. & Robert, F. Micrometer-scale chemical and isotopic criteria (O and Si) on the origin and history of Precambrian cherts: Implications for paleo-temperature reconstructions. *Geochim. Cosmochim. Acta* **92**, 129–147 (2012).
  136. van den Boorn, S. H. J. M., van Bergen, M. J., Vroon, P. Z., de Vries, S. T. & Nijman, W. Silicon isotope and trace element constraints on the origin of ~3.5 Ga cherts: Implications for Early Archaean marine environments. *Geochim. Cosmochim. Acta* **74**, 1077–1103 (2010).
  137. Robert François & Chaussidon Marc. A palaeotemperature curve for the Precambrian oceans based on silicon isotopes in cherts. *Nature* **443**, 969–972 (2006).
  138. Vallee, A., Humblot, V. & Pradier, C. M. Peptide interactions with metal and oxide surfaces. *Acc. Chem. Res.* **43**, 1297–1306 (2010).
  139. Nawrocki, J. The silanol group and its role in liquid chromatography. *J. Chromatogr. A* **779**, 29–71 (1997).
  140. Hench, L. L., Splinter, R. J., Allen, W. C. & Greenlee, T. K. Bonding mechanisms at the interface of ceramic prosthetic materials. *J. Biomed. Mater. Res.* **5**, 117–141 (1971).
  141. Colilla, M., Manzano, M. & Vallet-Regí, M. *Recent advances in ceramic implants as*

- drug delivery systems for biomedical applications. International Journal of Nanomedicine* vol. 3 (2008).
142. Merget, R. *et al.* Health hazards due to the inhalation of amorphous silica. *Arch. Toxicol.* **75**, 625–634 (2002).
  143. Ne Lopes, I., Piao, L., Stievano, L. & Lambert, J.-F. Adsorption of Amino Acids on Oxide Supports: A Solid-State NMR Study of Glycine Adsorption on Silica and Alumina. *J. Phys. Chem. C* **113**, 18163–18172 (2009).
  144. Bouchoucha, M., Jaber, M., Onfroy, T., Lambert, J.-F.-O. & Xue, B. Glutamic Acid Adsorption and Transformations on Silica. *J. Phys. Chem. C* **115**, 21813–21825 (2011).
  145. Heaney, P. J. Structure and chemistry of the low-pressure silica polymorphs. *Silica* 1–40 (2018) doi:10.1515/9781501509698-006.
  146. Pfeiffer-Laplaud, M., Costa, D., Tielens, F., Gaigeot, M.-P. & Sulpizi, M. Bimodal Acidity at the Amorphous Silica/Water Interface. *J. Phys. Chem. C* **119**, 27354–27362 (2015).
  147. Mathias, J. & Wannemacher, G. Basic characteristics and applications of aerosil. *J. Colloid Interface Sci.* **125**, 61–68 (1988).
  148. Cyran, J. D. *et al.* Molecular hydrophobicity at a macroscopically hydrophilic surface. *Proc. Natl. Acad. Sci. U. S. A.* **116**, 1520–1525 (2019).
  149. Cimas, Á., Tielens, F., Sulpizi, M., Gaigeot, M.-P. & Costa, D. The amorphous silica–liquid water interface studied by *ab initio* molecular dynamics (AIMD): local organization in global disorder. *J. Phys. Condens. Matter* **26**, 244106 (2014).
  150. Pratsinis, E. Flame aerosol synthesis of ceramic powders. *Fuel Energy Abstr.* **39**, 384 (1998).
  151. Ibaseta, N. & Biscans, B. Fractal dimension of fumed silica: Comparison of light scattering and electron microscope methods. *Powder Technol.* **203**, 206–210 (2010).
  152. Zhang, H. *et al.* Processing Pathway Dependence of Amorphous Silica Nanoparticle Toxicity: Colloidal vs Pyrolytic. *Jacs* **134**, 15790–15804 (2012).
  153. Argyo, C., Weiss, V., Bräuchle, C. & Bein, T. Multifunctional mesoporous silica nanoparticles as a universal platform for drug delivery. *Chem. Mater.* **26**, 435–451 (2014).

154. Sun, B., Zhou, G. & Zhang, H. Synthesis, functionalization, and applications of morphology-controllable silica-based nanostructures: A review. *Prog. Solid State Chem.* **44**, 1–19 (2016).
155. Tang, L. & Cheng, J. Nonporous silica nanoparticles for nanomedicine application. *Nano Today* **8**, 290–312 (2013).
156. Mebert, A. M., Baglolle, C. J., Desimone, M. F. & Maysinger, D. Nanoengineered silica: Properties, applications and toxicity. *Food Chem. Toxicol.* **109**, 753–770 (2017).
157. Stober, W., Fink, A. & Ernst Bohn, D. *Controlled Growth of Monodisperse Silica Spheres in the Micron Size Range 1*. *Journal of Colloid and Interface Science* vol. 26 (1968).
158. C. T. Kresge\*, M. E. Leonowicz\*, W. J. Roth\*, J. C. V. & J. S. B. Ordered mesoporous molecular sieves synthesized by a liquid- crystal template mechanism. *Lett. to Nat.* **359**, 710–712 (1992).
159. Hatton, B., Landskron, K., Whitnall, W., Perovic, D. & Ozin, G. A. Past, present, and future of periodic mesoporous organosilicas - The PMOs. *Acc. Chem. Res.* **38**, 305–312 (2005).
160. Guo, C. & Holland, G. P. Alanine Adsorption and Thermal Condensation at the Interface of Fumed Silica Nanoparticles: A Solid-State NMR Investigation. *J. Phys. Chem. C* **119**, 25663–25672 (2015).
161. Guo, C. & Holland, G. P. Investigating lysine adsorption on fumed silica nanoparticles. *J. Phys. Chem. C* **118**, 25792–25801 (2014).
162. Swanson, H. L., Guo, C., Cao, M., Addison, J. B. & Holland, G. P. Probing the binding modes and dynamics of histidine on fumed silica surfaces by solid-state NMR. *Phys. Chem. Chem. Phys.* **22**, 20349–20361 (2020).
163. Rai, A. K., Xu, X., Lin, Z. & Rai, D. K. Conformational search for zwitterionic leucine and hydrated conformers of both the canonical and zwitterionic leucine using the DFT-CPCM model. *Vib. Spectrosc.* **56**, 74–81 (2011).
164. Rimola, A., Tosoni, S., Sodupe, M. & Ugliengo, P. Does Silica Surface Catalyze Peptide Bond Formation? New Insights from First-Principles Calculations. *ChemPhysChem* **7**, 157–163 (2006).
165. Rimola, A., Sodupe, M., Tosoni, S., Civalleri, B. & Ugliengo, P. Interaction of glycine

- with isolated hydroxyl groups at the silica surface: First principles B3LYP periodic simulation. *Langmuir* **22**, 6593–6604 (2006).
166. Rimola, A., Civalleri, B. & Ugliengo, P. Neutral vs zwitterionic glycine forms at the water/silica interface: Structure, energies, and vibrational features from B3LYP periodic simulations. *Langmuir* **24**, 14027–14034 (2008).
  167. Rimola, A., Sodupe, M. & Ugliengo, P. Affinity Scale for the Interaction of Amino Acids with Silica Surfaces. *J. Phys. Chem. C* **113**, 5741–5750 (2009).
  168. Rimola, A. & Ugliengo, P. The role of defective silica surfaces in exogenous delivery of prebiotic compounds: Clues from first principles calculations. *Phys. Chem. Chem. Phys.* **11**, 2497–2506 (2009).
  169. Rimola, A., Sodupe, M. & Ugliengo, P. Amide and peptide bond formation: Interplay between strained ring defects and silanol groups at amorphous silica surfaces. *J. Phys. Chem. C* **120**, 24817–24826 (2016).
  170. Rimola, A., Balucani, N., Ceccarelli, C. & Ugliengo, P. Tracing the Primordial Chemical Life of Glycine: A Review from Quantum Chemical Simulations. (2022) doi:10.3390/ijms23084252.
  171. Lomenech, C., Bery, G., Costa, D., Stievano, L. & Lambert, J. F. Theoretical and Experimental Study of the Adsorption of Neutral Glycine on Silica from the Gas Phase. *ChemPhysChem* **6**, 1061–1070 (2005).
  172. Stievano, L. *et al.* Glycine and lysine adsorption and reactivity on the surface of amorphous silica. *Eur. J. Mineral.* **19**, 321–331 (2007).
  173. Costa, D. *et al.* DFT study of the adsorption of microsolvated glycine on a hydrophilic amorphous silica surface. *Phys. Chem. Chem. Phys.* **10**, 6360–6368 (2008).
  174. Remesal, E. R., Amaya, J., Graciani, J., Márquez, A. M. & Sanz, J. F. Adsorption of prototypical amino acids on silica: Influence of the pre-adsorbed water multilayer. *Surf. Sci.* **646**, 239–246 (2016).
  175. Abadian, H. *et al.* Leucine on Silica: A Combined Experimental and Modeling Study of a System Relevant for Origins of Life, and the Role of Water Coadsorption. *Langmuir* **38**, 8038–8053 (2022).
  176. Lambert, J. F., Jaber, M., Georgelin, T. & Stievano, L. A comparative study of the catalysis of peptide bond formation by oxide surfaces. *Phys. Chem. Chem. Phys.* **15**,

- 13371–13380 (2013).
177. Bouchoucha, M., Jaber, M., Onfroy, T., Lambert, J. F. & Xue, B. Glutamic acid adsorption and transformations on silica. *J. Phys. Chem. C* **115**, 21813–21825 (2011).
  178. Smith, B. *Infrared spectral interpretation: a systematic approach*. (2018).
  179. Elvers, B. Ullmann's encyclopedia of industrial chemistry. in *Ullmann's encyclopedia of industrial chemistry* 363–376 (1991).
  180. Derrick, M. R.; Stulik, D.; Landry, J. M. *Infrared Spectroscopy in Conservation Science*. (1999).
  181. Rodriguez-Saona, L., Ayvaz, H., & Wehling, R. L. Infrared and Raman Spectroscopy. in *In Food analysis* 107–127 (2017).
  182. Lorenz-fonfria, V. A. Infrared Difference Spectroscopy of Proteins : From Bands to Bonds. *Chem. Rev.* **120**, 3466–3576 (2020).
  183. Willard, H H, Merritt, Jr, L L, Dean, J A, and Settle, Jr, F. A. *Instrumental methods of analysis*. (1988).
  184. Harvey, D. Modern analytical chemistry (Vol.1). in *New York:McGraw-Hill* (2000).
  185. Warring, S. L., Beattie, D. A. & McQuillan, A. J. Surficial Siloxane-to-Silanol Interconversion during Room-Temperature Hydration/Dehydration of Amorphous Silica Films Observed by ATR-IR and TIR-Raman Spectroscopy. *Langmuir* **32**, 1568–1576 (2016).
  186. Bumrah, G. S. & Sharma, R. M. Raman spectroscopy – Basic principle, instrumentation and selected applications for the characterization of drugs of abuse. *Egypt. J. Forensic Sci.* **6**, 209–215 (2016).
  187. Mosca, S., Conti, C., Stone, N. & Matousek, P. Spatially offset Raman spectroscopy. *Nat. Rev. Methods Prim.* **1**, 1–16 (2021).
  188. Buscarino, G., Ardizzone, V., Vaccaro, G. & Gelardi, F. M. Sintering process of amorphous SiO<sub>2</sub> nanoparticles investigated by AFM, IR and Raman techniques. *J. Non. Cryst. Solids* **357**, 1866–1870 (2011).
  189. Alessi, A., Agnello, S., Buscarino, G. & Gelardi, F. M. Structural properties of core and surface of silica nanoparticles investigated by Raman spectroscopy. *J. Raman Spectroscopy* **44**, 810–816 (2013).

190. Thommes, M. *et al.* Physisorption of gases, with special reference to the evaluation of surface area and pore size distribution (IUPAC Technical Report). *Pure Appl. Chem.* **87**, 1051–1069 (2015).
191. Fankuchen, I. X-ray diffraction. *Anal. Chem.* **21**, 24–29 (1949).
192. Arrebola-Liébanas, F. J., Romero-González, R. & Garrido Frenich, A. *HRMS: Fundamentals and Basic Concepts. Applications in High Resolution Mass Spectrometry: Food Safety and Pesticide Residue Analysis* (2017). doi:10.1016/B978-0-12-809464-8.00001-4.
193. Lin, L., Lin, H., Zhang, M., Dong, X. & Yin, X. Types, principle, and characteristics of tandem high-resolution mass spectrometry and its applications. *RSC Adv.* **5**, 107623–107636 (2015).
194. Fosgerau, K. & Hoffmann, T. Peptide therapeutics: current status and future directions. *Drug Discov. Today* **20**, 122–128 (2015).
195. Uhlig, T. *et al.* The emergence of peptides in the pharmaceutical business: From exploration to exploitation. *EuPA Open Proteomics* **4**, 58–69 (2014).
196. Pattabiraman, V. R. & Bode, J. W. Rethinking amide bond synthesis. *Nature* **480**, 471–479 (2011).
197. Forsythe, J. G. *et al.* Ester-Mediated Amide Bond Formation Driven by Wet-Dry Cycles: A Possible Path to Polypeptides on the Prebiotic Earth. *Angew. Chemie - Int. Ed.* **54**, 9871–9875 (2015).
198. Campbell, T. D. *et al.* Prebiotic condensation through wet–dry cycling regulated by deliquescence. *Nat. Commun.* **10**, 1–7 (2019).
199. Fabbiani, M. *et al.* Solvent-free synthesis of Ser–His dipeptide from non-activated amino acids and its potential function as organocatalyst. *Res. Chem. Intermed.* **44**, 1797–1810 (2018).
200. McGeoch, M. W., Dikler, S. & McGeoch, J. E. M. Hemolithin: a Meteoritic Protein containing Iron and Lithium. *arXiv* 1–11 (2020).
201. Aponte, J. C. *et al.* Pathways to Meteoritic Glycine and Methylamine. *ACS Earth Sp. Chem.* **1**, 3–13 (2017).
202. Bujdák, J. & Rode, B. M. Silica, alumina, and clay-catalyzed alanine peptide bond formation. *J. Mol. Evol.* **45**, 457–466 (1997).



203. Mian, S. A. *et al.* Investigating the adsorption mechanism of glycine in comparison with catechol on cristobalite surface using density functional theory for bio-adhesive materials †. *RSC Adv.* **6**, 114313–114319 (2016).
204. Chien, C. Y. & Yu, S. S. Ester-mediated peptide formation promoted by deep eutectic solvents: a facile pathway to proto-peptides. *Chem. Commun.* **56**, 11949–11952 (2020).
205. Young, R. P. Infrared spectroscopic studies of adsorption and catalysis. Part 3. Carboxylic acids and their derivatives adsorbed on silica. *Can. J. Chem.* **47**, 2237–2247 (1969).
206. Humbert, B. Estimation of hydroxyl density at the surface of pyrogenic silicas by complementary NMR and raman experiments. *J. Non. Cryst. Solids* **191**, 29–37 (1995).
207. Hadjiivanov, K. I. *et al.* Power of Infrared and Raman Spectroscopies to Characterize Metal-Organic Frameworks and Investigate Their Interaction with Guest Molecules. *Chem. Rev.* **121**, 1286–1424 (2021).
208. Pavan, C. *et al.* Nearly free surface silanols are the critical molecular moieties that initiate the toxicity of silica particles. *Proc. Natl. Acad. Sci. U. S. A.* **117**, 27836–27846 (2020).
209. Ji, Y. *et al.* DFT-Calculated IR Spectrum Amide I, II, and III Band Contributions of N-Methylacetamide Fine Components. *ACS Omega* **5**, 8572–8578 (2020).
210. Cobb, J. S., Zai-Rose, V., Correia, J. J. & Janorkar, A. V. FT-IR Spectroscopic Analysis of the Secondary Structures Present during the Desiccation Induced Aggregation of Elastin-Like Polypeptide on Silica. *ACS Omega* **5**, 8403–8413 (2020).
211. Barth, A. & Zscherp, C. What vibrations tell us about proteins. *Q. Rev. Biophys.* **35**, 369–430 (2002).
212. Sadat, A. & Joye, I. J. applied sciences Peak Fitting Applied to Fourier Transform Infrared and Raman Spectroscopic Analysis of Proteins. *Appl. Sci.* **10**, 5918 (2020).
213. Barth, A. Infrared spectroscopy of proteins. *Biochim. Biophys. Acta - Bioenerg.* **1767**, 1073–1101 (2007).
214. Piers, A. S. & Rochester, C. H. IR Study of the adsorption of 1-aminopropyltrialkoxysilanes on silica at the S\_L interface.pdf. *J. Colloid Interface Sci.* **174**, 97–103 (1995).
215. Lorusso, M., Pepe, A., Ibris, N. & Bochicchio, B. Molecular and supramolecular

- studies on polyglycine and poly-l-proline. *Soft Matter* **7**, 6327–6336 (2011).
216. Bykov, S. & Asher, S. Raman studies of solution polyglycine conformations. *J. Phys. Chem. B* **114**, 6636–6641 (2010).
217. Maury, C. P. J. Origin of life. Primordial genetics: Information transfer in a pre-RNA world based on self-replicating beta-sheet amyloid conformers. *J. Theor. Biol.* **382**, 292–297 (2015).
218. Higgs, P. G. The Effect of Limited Diffusion and Wet-Dry Cycling on Reversible Polymerization Reactions: Implications for Prebiotic Synthesis of Nucleic Acids. *Life* **6**, 24 (2016).
219. Bujdák, J., Le Son, H., Yongyai, Y. & Rode, B. M. The effect of reaction conditions on montmorillonite-catalysed peptide formation. *Catal. Letters* **37**, 267–272 (1996).
220. Zhang, S. Discovery and design of self-assembling peptides. *Interface Focus* **7**, 20170028 (2017).
221. Zozulia, O., Dolan, M. A. & Korendovych, I. V. Catalytic peptide assemblies. *Chem. Soc. Rev* **47**, 3621 (2018).
222. El Samrout, O., Fabbiani, M., Berlier, G., Lambert, J. & Martra, G. Emergence of order in origins-of-life scenarios on minerals surfaces : polyglycine chains on silica. *Langmuir* **38**, 15516–15525 (2022).
223. Swanson, H. L., Guo, C., Cao, M., Addison, J. B. & Holland, G. P. Probing the binding modes and dynamics of histidine on fumed silica surfaces by solid-state NMR †. *Phys. Chem. Chem. Phys* **22**, 20349 (2020).
224. Haris, P. I. Can infrared spectroscopy provide information on protein-protein interactions? *Biochem. Soc. Trans.* **38**, 940–946 (2010).
225. Barth, A. Infrared spectroscopy of proteins. *Biochim. Biophys. Acta - Bioenerg.* **1767**, 1073–1101 (2007).
226. Barth, A. & Zscherp, C. What vibrations tell us about proteins. *Q. Rev. Biophys.* **35**, 369–430 (2002).
227. Lambert, J.-F., Jaber, M., Georgelin, T. & Stievenano, L. A comparative study of the catalysis of peptide bond formation by oxide surfaces. *Phys. Chem. Chem. Phys* **15**, 13371 (2013).
228. Adochitei, A. & Drochioiu, G. Rapid characterization of peptide secondary structure by

- FT-IR spectroscopy. *Rev. Roum. Chim.* **56**, 783–791 (2011).
229. Liu, Y., Cho, R. K., Sakurai, K., Miura, T. & Ozaki, Y. Studies on spectra/structure correlations in near-infrared spectra of proteins and polypeptides. Part I: a marker band for hydrogen bonds. *Appl. Spectrosc.* **48**, 1249–1254 (1994).
230. Sediki, A., Snoek, L. C. & Gaigeot, M. P. N-H<sup>+</sup> vibrational anharmonicities directly revealed from DFT-based molecular dynamics simulations on the Ala7H<sup>+</sup> protonated peptide. *Int. J. Mass Spectrom.* **308**, 281–288 (2011).
231. Taga, K. *et al.* FT-IR spectra of glycine oligomers. *Vib. Spectrosc.* **14**, 143–146 (1997).
232. Suzuki, S., Iwashita, Y., Shimanouchi, T. & Tsuboi, M. Infrared spectra of isotopic polyglycines. *Biopolymers* **4**, 337–350 (1966).
233. Clegg, R. S., Reed, S. M., Hutchison, J. E., January, R. V & Am, C. E. D. J. Self-Assembled Monolayers Stabilized by Three-Dimensional Networks of Hydrogen Bonds. *J. Am. Chem. Soc.* **7863**, 2486–2487 (1998).
234. Liu, C., Ponder, J. W. & Marshall, G. R. Helix stability of oligoglycine, oligoalanine, and oligo- $\beta$ -alanine dodecamers reflected by hydrogen-bond persistence. *Proteins Struct. Funct. Bioinforma.* **82**, 3043–3061 (2014).
235. Krimm, S. & Bandekar, J. Vibrational spectroscopy and conformation of peptides, polypeptides, and proteins. *Adv. Protein Chem.* **38**, 181–364 (1986).
236. Crick, F. H. & Rich, A. Structure of polyglycine II. *Nature* **176**, 780–781 (1955).
237. Athamneh, A. I., Griffin, M., Whaley, M. & Barone, J. R. Conformational changes and molecular mobility in plasticized proteins. *Biomacromolecules* **9**, 3181–3187 (2008).
238. Leonard J. Prins, David N. Reinhoudt, and P. T. The Cooperativity Concept Gulliver constrained by a multitude of weak <sup>a</sup>bonds<sup>o</sup>. Illustration by. *Angew. Chemie - Int. Ed.* **40**, 2382–2426 (2001).
239. Weimann, B. J., Lohrmann, R., Orgel, L. E., Schneider-Bernloehr, H. & Sulston, J. E. Template-directed synthesis with adenosine-5'-phosphorimidazolide. *Science (80-. )*. **161**, 387–388 (1968).
240. Kong, J. & Yu, S. Fourier transform infrared spectroscopic analysis of protein secondary structures. *Acta Biochim. Biophys. Sin. (Shanghai)*. **39**, 549–559 (2007).
241. Karandur, D., Wong, K.-Y. & Pettitt, B. M. Solubility and Aggregation of Gly 5 in Water. *J. Phys. Chem. B* **118**, 9565–9572 (2014).

242. Auton, M. & Bolen, D. W. Additive Transfer Free Energies of the Peptide Backbone Unit That Are Independent of the Model Compound and the Choice of Concentration Scale. *Biochemistry* **43**, 1329–1342 (2004).
243. Schuler, M., Denosiv, L. & Sligar, S. *Lipid-protein interactions : methods and protocols. Methods in Molecular Biology* vol. 974 (2013).
244. Baenziger, J. E. & Methot, N. Fourier transform infrared and hydrogen/deuterium exchange reveal an exchange-resistant core of  $\alpha$ -helical peptide hydrogens in the nicotinic acetylcholine receptor. *J. Biol. Chem.* **270**, 29129–29137 (1995).
245. Sethuraman, A., Vedantham, G., Imoto, T., Przybycien, T. & Belfort, G. Protein Unfolding at Interfaces: Slow Dynamics of-Helix to-Sheet Transition. *Proteins Struct. Funct. Genet.* **56**, 669–678 (2004).
246. Cauvel, A., Brunel, D., Di Renzo, F., Garrone, E. & Fubini, B. Hydrophobic and hydrophilic behavior of micelle-templated mesoporous silica. *Langmuir* **13**, 2773–2778 (1997).
247. Chen, L., He, X., Liu, H., Qian, L. & Kim, S. H. Water Adsorption on Hydrophilic and Hydrophobic Surfaces of Silicon. *J. Phys. Chem. C* **122**, 31 (2018).
248. Fubini, B., Bolis, V., Cavenago, A., Garrone, E. & Ugliengo, P. Structural and Induced Heterogeneity at the Surface of Some SiO<sub>2</sub> Polymorphs from the Enthalpy of Adsorption of Various Molecules. *Langmuir* **9**, 2712–2720 (1993).
249. Morrow, B. A. & Cody, I. A. Infrared studies of reactions on oxide surfaces. 5. Lewis acid sites on dehydroxylated silica. *J. Phys. Chem.* **80**, 1995–1998 (1976).
250. Bunker, B. C. *et al.* Infrared spectra of edge-shared silicate tetrahedra. *Surf. Sci.* **210**, 406–428 (1989).
251. Zhang, M., Vogel, H. J., Fabian, H. & Mantsch, H. H. Isotope-Edited Fourier Transform Infrared Spectroscopy Studies of Calmodulin's Interaction with Its Target Peptides. *Biochemistry* **33**, 10883–10888 (1994).
252. Maekawa, H., Ballano, G., Formaggio, F., Toniolo, C. & Ge, N.-H. C<sup>18</sup>O/<sup>15</sup>N Isotope Dependence of the Amide-I/II 2D IR Cross Peaks for the Fully Extended Peptides. *J. Phys. Chem. C* **118**, 29448–29457 (2014).
253. Brielle, E. S. & Arkin, I. T. Isotope-Edited Amide II Mode: A New Label for Site-Specific Vibrational Spectroscopy. *J. Phys. Chem. Lett.* **12**, 6634–6638 (2021).

254. De La Rica, R. & Matsui, H. Applications of peptide and protein-based materials in bionanotechnology. *Chem. Soc. Rev* **39**, 3499–3509 (2010).
255. Feyzizarnagh, H., Yoon, D.-Y., Goltz, M. & Kim, D.-S. Peptide nanostructures in biomedical technology. *WIREs Nanomed Nanobiotechnol* **8**, 730–743 (2016).
256. Shanker, U., Bhushan, B. & Bhattacharjee, G. Oligomerization of Glycine and Alanine Catalyzed by Iron Oxides: Implications for Prebiotic Chemistry. *Orig Life Evol Biosph* **42**, 31–45 (2012).
257. Bujdák, J. & Rode, B. M. *Alumina catalyzed reactions of amino acids*. *Journal of Thermal Analysis and Calorimetry* vol. 73 (2003).
258. Guo, C. & Holland, G. P. Alanine Adsorption and Thermal Condensation at the Interface of Fumed Silica Nanoparticles: A Solid-State NMR Investigation. *J. Phys. Chem. C* **119**, 25663–25672 (2015).
259. Sakhno, Y. *et al.* One Step up the Ladder of Prebiotic Complexity: Formation of Nonrandom Linear Polypeptides from Binary Systems of Amino Acids on Silica. *Chem. - A Eur. J.* **25**, 1275–1285 (2019).
260. Gh Jeelani, P., Mulay, P., Venkat, R. & Ramalingam, C. Multifaceted Application of Silica Nanoparticles. A Review. *Silicon* **12**, 1337–1354 (2020).
261. Comas-Vives, A. Amorphous SiO<sub>2</sub> surface models: Energetics of the dehydroxylation process, strain, ab initio atomistic thermodynamics and IR spectroscopic signatures. *Phys. Chem. Chem. Phys.* **18**, 7475–7482 (2016).
262. Young, G. J. Interaction of water vapor with silica surfaces. *J. Colloid Sci.* **13**, 67–85 (1958).
263. Mueller, R., Kammler, H. K., Wegner, K. & Pratsinis, S. E. OH Surface Density of SiO<sub>2</sub> and TiO<sub>2</sub> by Thermogravimetric Analysis. *Langmuir* **19**, 160–165 (2003).
264. Ek, S., Root, A., Peussa, M. & Niinistö, L. Determination of the hydroxyl group content in silica by thermogravimetry and a comparison with <sup>1</sup>H MAS NMR results. *Thermochim. Acta* **379**, 201–212 (2001).
265. Zhuravlev, L. T. Concentration of hydroxyl groups on the surface and in the volume of silicas. *Langmuir* **3**, 316–318 (1987).
266. Alessi, A., Agnello, S., Buscarino, G. & Gelardi, F. M. Raman and IR investigation of silica nanoparticles structure. *J. Non. Cryst. Solids* **362**, 20–24 (2013).

267. Hartwig, C. M. & Rahn, L. A. Bound hydroxyl in vitreous silica. *J. Chem. Phys.* **67**, 4260–4261 (1977).
268. Burneau, A., Gallas, J. P., & Legrand, A. E. The surface properties of silicas. in *Vibrational spectroscopies* 147–234 (1998).
269. Hehlen, B. Inter-tetrahedra bond angle of permanently densified silicas extracted from their Raman spectra. *J. Phys. Condens. Matter* **22**, (2010).
270. Uchino, T. *et al.* Microscopic structure of nanometer-sized silica particles. *Phys. Rev. B - Condens. Matter Mater. Phys.* **69**, 1–8 (2004).
271. Plinio Innocenzi. Infrared spectroscopy of sol–gel derived silica-based films: a spectromicrostructure overview. *J. Non. Cryst. Solids* **316**, 309–319 (2003).
272. Gallardo, J., Durán, A., Di Martino, D. & Almeida, R. M. Structure of inorganic and hybrid SiO<sub>2</sub> sol-gel coatings studied by variable incidence infrared spectroscopy. *J. Non. Cryst. Solids* **298**, 219–225 (2002).
273. Galeener, F. L. Band limits and the vibrational spectra of tetrahedral glasses. *Phys. Rev. B* **19**, 4292–4297 (1979).
274. Galeener, F. L., Leadbetter, A. J. & Stringfellow, M. W. Comparison of the neutron, Raman, and infrared vibrational spectra of vitreous SiO<sub>2</sub>, GeO<sub>2</sub>, and BeF<sub>2</sub>. *Phys. Rev. B* **27**, 1052–1078 (1983).
275. El Samrout, O., Berlier, G., Lambert, J. & Martra, G. Polypeptide chain growth mechanisms and secondary structure formation in glycine gas-phase deposition on silica surfaces. *J. Phys. Chem. B* accepted for publication
276. Cheam, T. C. & Krimm, S. Vibrational analysis of crystalline diketopiperazine-I. Raman and i.r. spectra. *Spectrochim. Acta Part A Mol. Spectrosc.* **40**, 481–501 (1984).
277. Fukushima, K., Ideguchi, Y. & Miyazawa, T. The Normal Vibrations of Diketopiperazine and Its N -Deuterated Compound . *Bull. Chem. Soc. Jpn.* **37**, 349–353 (1964).
278. Sakhno, Y. *et al.* One Step up the Ladder of Prebiotic Complexity: Formation of Nonrandom Linear Polypeptides from Binary Systems of Amino Acids on Silica. *Chem. a Eur. J.* **25**, 1275–1285 (2019).
279. Ching, C. B., Hidajat, K. & Uddin, M. S. Evaluation of Equilibrium and Kinetic Parameters of Smaller Molecular Size Amino Acids on KX Zeolite Crystals via Liquid

- Chromatographic Techniques. *Sep. Sci. Technol.* **24**, 581–597 (1989).
280. Takeuchi, M., Bertinetti, L., Martra, G., Coluccia, S. & Anpo, M. States of H<sub>2</sub>O adsorbed on oxides: An investigation by near and mid infrared spectroscopy. *Appl. Catal. A Gen.* **307**, 13–20 (2006).
281. Catalano, F., Alberto, G., Ivanchenko, P., Dovbeshko, G. & Martra, G. Effect of Silica Surface Properties on the Formation of Multilayer or Submonolayer Protein Hard Corona: Albumin Adsorption on Pyrolytic and Colloidal SiO<sub>2</sub> Nanoparticles. *J. Phys. Chem. C* **119**, 45 (2015).

# Appendix 1: Emergence of order in origins-of-life scenarios on mineral surfaces: polyglycine chains on silica

## Supporting information

### Adsorption and reaction of formic acid on the silica surface at 160 °C

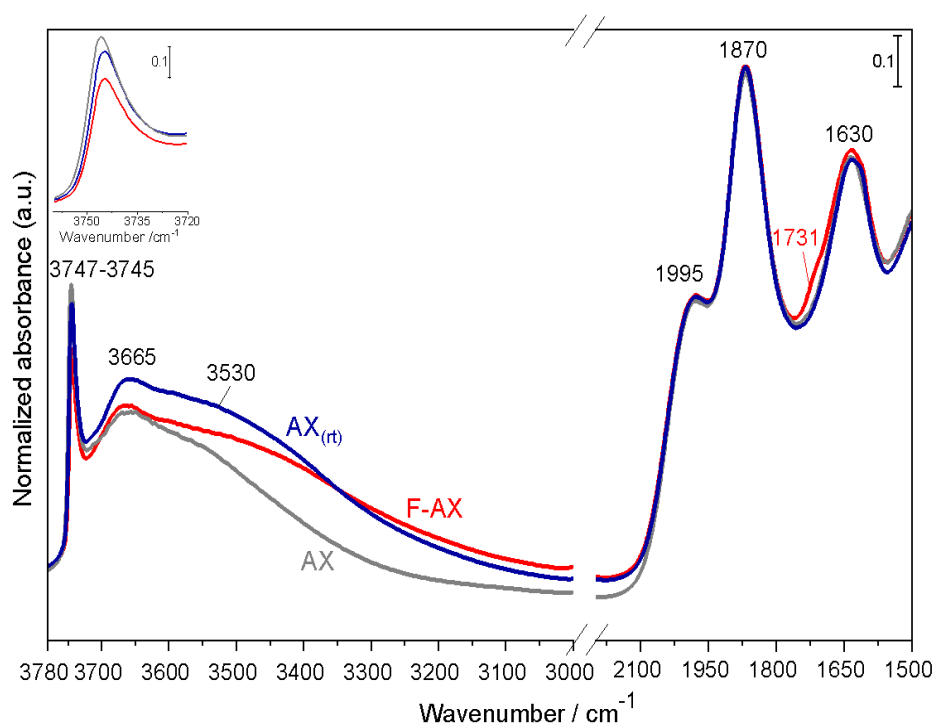


**Figure A1- 0-1:** IR spectra of the three samples: AX<sub>(rt)</sub>, AX, and F-AX just before the adsorption of Gly from the vapor phase. The intensity of the spectra has been normalized with respect to the optical thickness (mg.cm<sup>-2</sup>) of the self-supporting pellets prepared for the measurements using the pattern in the 2100-1800 cm<sup>-1</sup> range.

#### Discussion of Figure A1- 1

IR spectra under controlled atmosphere were collected for the 3 different silica samples (AX<sub>(rt)</sub>, AX, and F-AX) to check their status just before the start of Gly sublimation. The spectra



exhibit a typical pattern with two groups of signals in the range of 3780-3100  $\text{cm}^{-1}$  and 2100-1500  $\text{cm}^{-1}$ .

Based on available literature data<sup>24,281</sup>, the first pattern at high wavenumbers is associated to silanol (Si-OH) stretching  $\nu_{\text{OH}}$  as follows: (i) a narrow peak at 3747  $\text{cm}^{-1}$ , asymmetric on the low frequency side, assigned to isolated silanols separated by more than 6 Å, not involved in any intersilanol interaction, (ii) a band in the 3700-3600  $\text{cm}^{-1}$  range with a maximum at 3665  $\text{cm}^{-1}$  associated to silanols interacting via weak H-bonding (including internal Si-OH not accessible to heavy water), (iii) a broad asymmetric feature from 3600  $\text{cm}^{-1}$  down to 3000  $\text{cm}^{-1}$  with a maximum at 3530  $\text{cm}^{-1}$  assigned to H-bonding silanols located at a distance of 2.5-2.8 Å apart, and which establish mutual strong H-bonded interactions.

A higher dehydration level is reached when the outgassing is performed at 160 °C versus rt. More H-bonding silanol and intraglobular Si-OH are condensed (a certain depletion in the broad band starting from 3700  $\text{cm}^{-1}$ ) resulting in the formation of more isolated silanols (an increase in the intensity of the narrow band at 3747  $\text{cm}^{-1}$ ).

The second pattern at low wavenumbers is due to combinations and overtones of symmetric and anti-symmetric bulk modes:  $\nu_{\text{sym}} + \nu_{\text{as}}$  (1995  $\text{cm}^{-1}$ ),  $\nu_{\text{sym}} + \nu_{\text{as}}$  (1870  $\text{cm}^{-1}$ ) and  $2 \nu_{\text{sym}}$  (1630  $\text{cm}^{-1}$ ). Because they are only due to bulk silica, they were used to normalize the different samples.<sup>24</sup>

The IR profile recorded for the F-AX sample after the three runs of pre-treatment in FA shows the persistence of a band at 1731  $\text{cm}^{-1}$ . This could indicate to the presence of chemisorbed species on the surface since such species would resist prolonged outgassing. This band was more clearly evidenced by subtracting the spectrum of bare silica, as shown in Figure III-2.

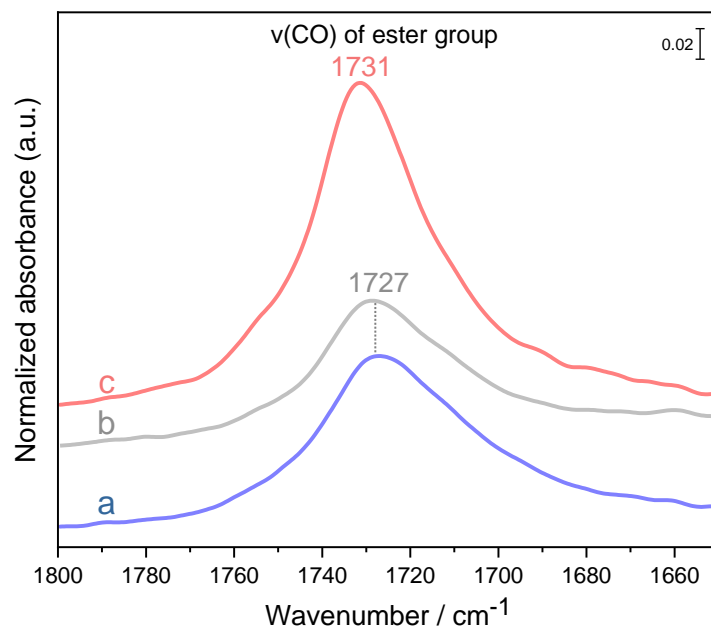


**Figure A1- 0-2:**IR spectra of F-AX sample after the (a) 1<sup>st</sup>, (b) 2<sup>nd</sup> and (c) 3<sup>rd</sup> run of pretreatment in FA where the sample, in each run, was contacted with FA and heated at 160 °C for 2 h, then outgassed at bt. The spectrum of bare SiO<sub>2</sub> obtained after outgassing at 160 °C and subsequent isotopic H/D exchange (by admission of 20 mbar D<sub>2</sub>O vapor followed by outgassing at bt) was subtracted as a baseline.

### Discussion of Figure A1- 2

IR spectroscopy measurements performed at the end of each run showed the formation of a significant band at around 1727-1731 cm<sup>-1</sup>, a characteristic band of the presence of ester species on the surface,<sup>205</sup> which increased in intensity after each step.

### Gly deposition and polymerization on silica surfaces in CVD conditions

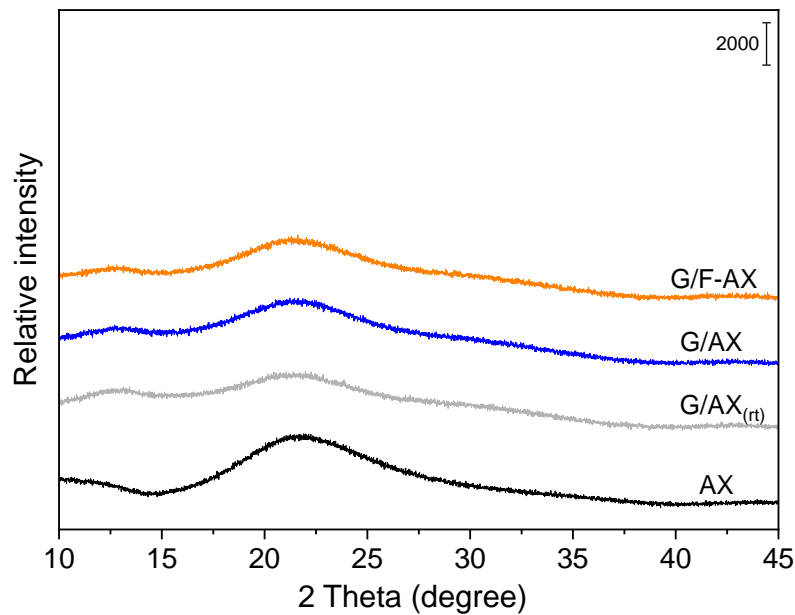


**Figure A1- 0-3:** XRD patterns for: AX, bare amorphous silica; G/AX<sub>(rt)</sub>, glycine adsorbed on silica outgassed at rt under vacuum; G/AX, glycine adsorbed on silica outgassed at 160 °C under vacuum; G/F-AX, glycine adsorbed on silica pre-treated with formic acid at 160 °C under vacuum.

### Discussion for Figure A1- 3

The XRD patterns of the samples only show the broad background of the amorphous silica support without additional peaks. This confirms the absence of crystalline glycine after deposition by CVD method for 20 h.

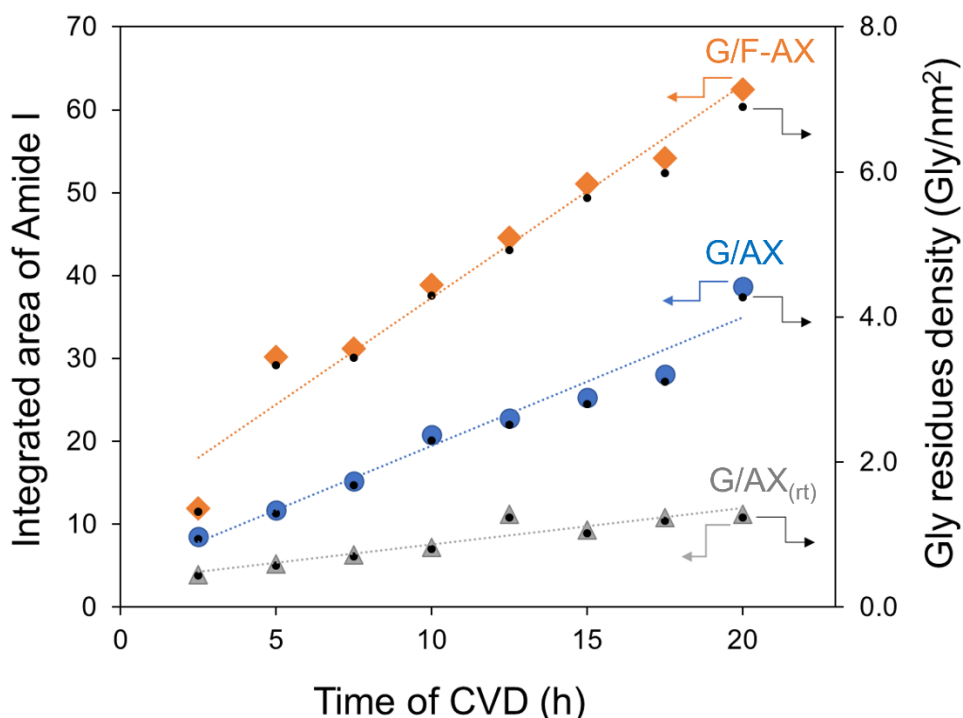


**Figure A1- 0-4:** Evolution of the amide I band intensity and Gly residues density (estimated based on TGA measurements) as function of time during Gly deposition by CVD over: G/AX<sub>(rt)</sub>, G/AX and G/F-AX samples.

#### Discussion of Figure A1- 4

Analysis of the integrated area (proportional to the concentration) of amide I versus time (h) allows to deduce that the Gly polymerization was much more efficient on G/F-AX sample compared to the other samples: higher values of the amide I integrated area were reached in shorter time on G/F-AX. The corresponding Gly residues density for the 3 samples at different CVD time is estimated based on the amount of peptide loading measured on the washed pellet by TGA that implies the amount of peptide loading to be 3.25% by weight after 20 h CVD. This corresponds to 6.9 Gly residues/ nm<sup>2</sup>.

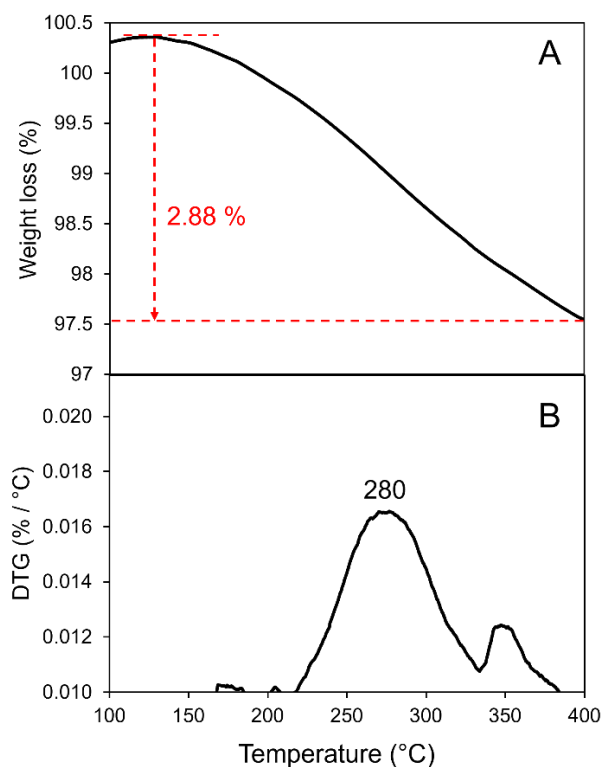


**Figure A1- 0-5:** A) TGA and B) DTG profiles of the sample G/F-AX after washing with liquid water at the end of 20 h CVD reaction

### Discussion of Figure A1- 5

The DTG profile recorded for the sample G/F-AX after washing with liquid water at the end of the 20 h CVD reaction shows a major event at around 280 °C. This corresponds to the burning off or destruction of the organic materials remaining on the surface. The weight loss between 130 and 400 °C represents 2.88 % by weight for this sample. When subtracting the weight loss of the corresponding blank silica (0.40 %), the actual peptide loading is estimated to be around 2.48 % by weight on G/F-AX after washing. This value corresponds to around 5.2 Gly residues/nm<sup>2</sup>. If washing with liquid water only allows solubilization of ca. 24% of the formed peptides (as stated in the main text, Figure 6) then before washing the peptide weight loading could be concluded to be 6.9 Gly residues/nm<sup>2</sup> after 20 h CVD.

## Self-assembly and secondary structures of poly-Gly

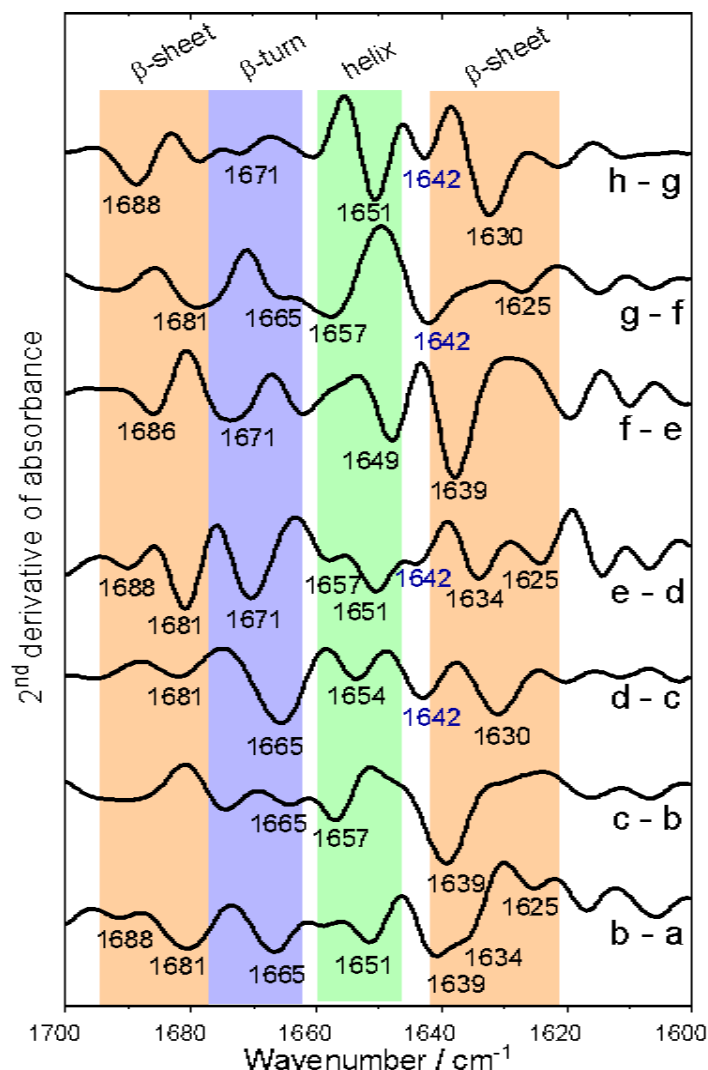


**Figure A1-0-6:** Second derivative in the amide I region of the double difference IR spectra of the intermediate CVD steps from 2.5 h (a) to 20 h (h) on G/F-AX, obtained by subtracting each step from the previous one.

### Discussion for Figure A1- 6

As discussed for Figure 5 in the main text, poly-Gly chains of large-scale elements are formed on the surface. The minima of the second derivative of the double difference spectra represent an additional evidence for the formation of peptides containing  $\beta$ -turn (1665, 1671 cm<sup>-1</sup>),  $\beta$ -sheet (1625, 1630, 1634, 1639, 1681, 1686, 1688 cm<sup>-1</sup>), and helical (1649, 1651, 1657 cm<sup>-1</sup>) conformations<sup>213</sup> starting from 5 h till 20 h CVD on G/F-AX. Some non-ordered

chains are also formed as indicated by the minima at around  $1642\text{ cm}^{-1}$  for the IR spectra at some intermediate CVD steps.

### Effect of hydration/dehydration cycles on grafted poly-Gly

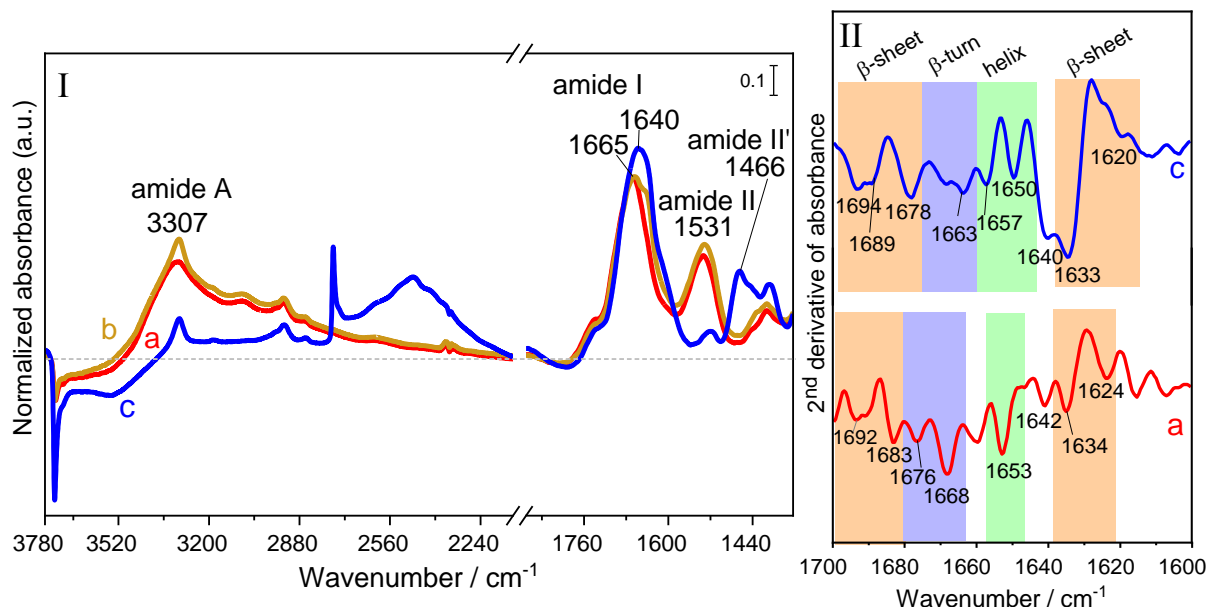


**Figure A1- 0-7:** Panel (I): IR spectra of G/AX sample submitted to successive treatments: (a) directly after Gly sublimation for 20 h, (b) after subsequent contact with water v.p.(20 mbar) and outgassing for 30 min at bt, and (c) after H/D exchange and then outgassing of D<sub>2</sub>O for 30 min at bt.

The corresponding spectrum of the material obtained before the start of CVD process is subtracted as a baseline. Panel (II) shows the second derivative of the IR spectra a, and c.

### Discussion of Figure A1- 7

The general trends observed on G/AX (Figure A1- 7, Panel I) upon water vapor admission are similar to the ones reported for G/F-AX sample (Figure III-7 of Chapter III, Panel I). The second derivative of the spectra obtained after outgassing at bt following the 20 h CVD (Figure A1- 7, Panel II, curve a) indicates, in coherence with the outcomes reported by Martra at al.<sup>25</sup>, that self-assembled structures containing both  $\beta$ -sheet ( $1692, 1683, 1634, 1624\text{ cm}^{-1}$ ) and helical ( $1653\text{ cm}^{-1}$ ) conformations are formed on G/AX sample at the end of the reaction. Some non-ordered structures are also formed on the surface ( $1642\text{ cm}^{-1}$ ).

However, the second derivative of the spectrum obtained after D<sub>2</sub>O exchange (Figure A1- 7, Panel II, curve c) revealed, interestingly, that the remaining oligomers were then almost similar to the one obtained on G/F-AX sample directly after CVD (Figure 6 of the main text, Panel II,

curve a'): more  $\beta$ -sheet (1694, 1689, 1678, 1633 and 1620  $\text{cm}^{-1}$ ) and helical (1657, 1650  $\text{cm}^{-1}$ ) structures are present while a certain amount was still in random coil (1640  $\text{cm}^{-1}$ )<sup>210</sup>. Thus, the peptides that resist D-exchange because they are strongly H-bonded resemble those that predominate in the sample with a higher density of adsorbed Poly-Gly.



## Appendix 2: Polypeptide chain growth mechanisms and secondary structure formation in glycine gas-phase deposition on silica surfaces

### Supporting information

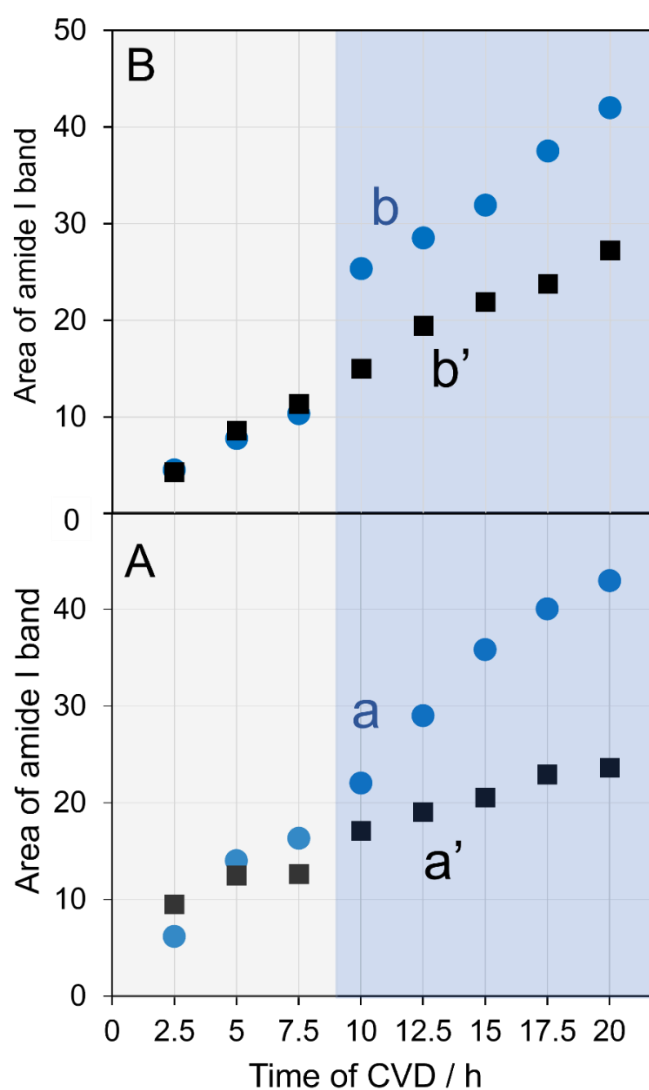


**Figure A2- 1:** Evolution of the integrated area of amide I as function of time during Gly deposition by CVD before (light grey shadow) and after (blue shadow) the HF cycles on the two samples: a) G<sub>TFHF</sub>/AX<sub>it</sub> and b) G<sub>TFHF</sub>/AX<sub>160</sub>. Both a') G<sub>TF</sub>/AX<sub>it</sub> and b') G<sub>TF</sub>/AX<sub>160</sub>, not subjected to any intermediate HF cycles, were prepared and presented for the sake of comparison.

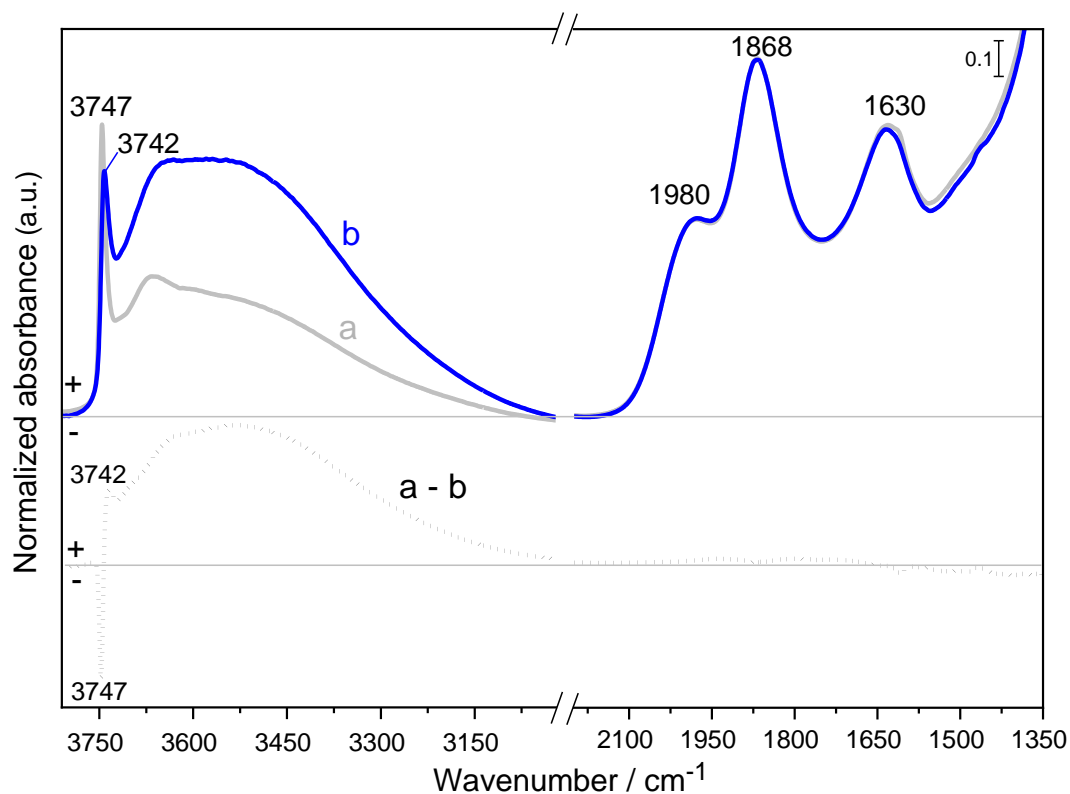


**Figure A2- 2:** IR spectra of the two bare silica samples before any Gly deposition: (a)  $AX_{rt}$ , bare silica outgassed at rt and (b)  $AX_{WD}$ , bare silica subjected to wetting/drying cycles then outgassed at rt. The difference of these IR spectra (b-a) shows the effect of the surface washing on the silanol groups.

The intensity of the spectra has been normalized with respect to the optical thickness ( $\text{mg}\cdot\text{cm}^{-2}$ ) of the self-supporting pellets prepared for the measurements using the pattern in the 2100-1800  $\text{cm}^{-1}$  range.

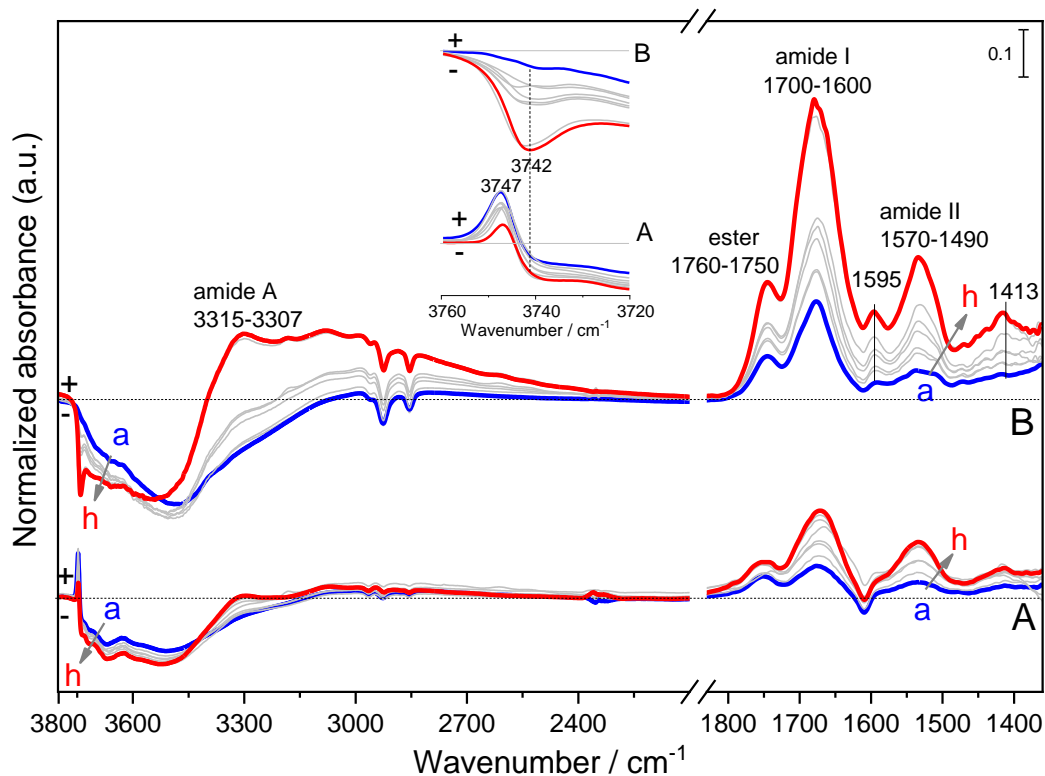


**Figure A2- 3:** IR difference spectra after Gly CVD at 160 °C from 2.5 h (a) to 20 h (h) on the two samples: A)  $G_{TF}/AX_{rt}$ , Gly deposition on silica outgassed at rt and B)  $G_{TF}/AX_{WD}$ , Gly deposition on silica subjected to wetting/drying cycles then outgassed at rt. The gray curves show intermediate sublimation steps of 2.5 h. The spectrum of the silica support before the start of CVD ( $AX_{rt}$  or  $AX_{WD}$ , respectively) has been subtracted as a baseline.

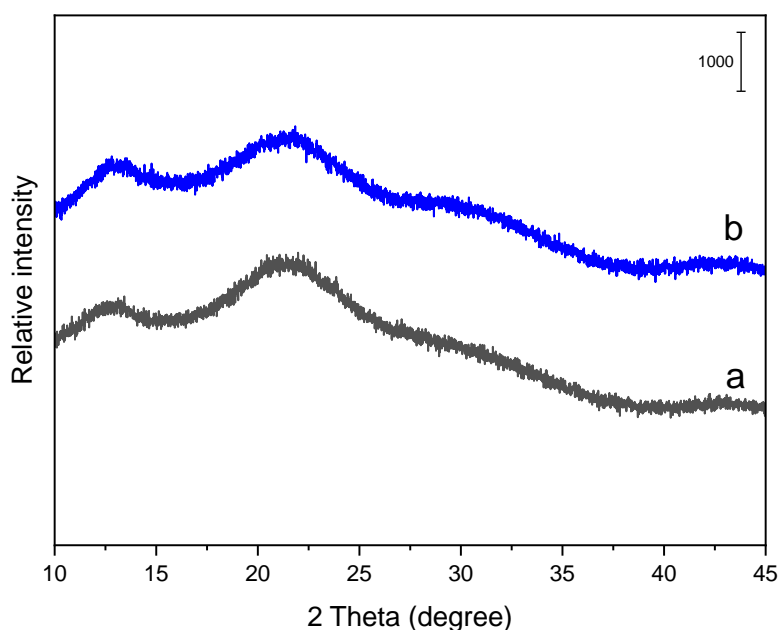


**Figure A2- 4:** XRD patterns for  $G_{TF}/AX_{WD}$  after (a)  $^{12}C$ -Gly deposited on  $AX_{WD}$  for 20 h by CVD then subjected to wetting/drying cycles and outgassed, and (b) after  $^{15}N$ -Gly deposited on the same sample as a subsequent set by CVD for 15 h.

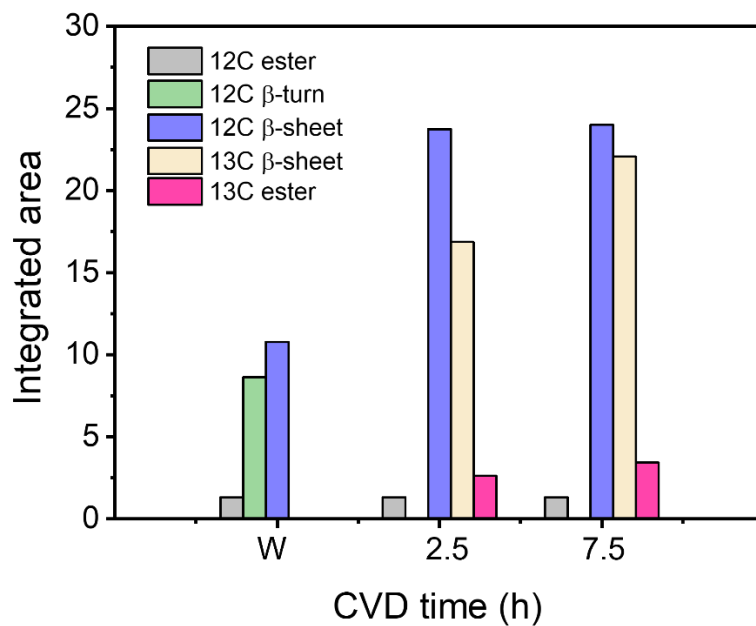


**Figure A2- 5:** Evolution of the integrated area of the different types of secondary structures and ester as a function of time during  $^{13}\text{C}$ -Gly deposition for 7.5 h on  $G_{\text{TFHF}}/AX_{\text{WD}}$  already subjected to 20 h CVD of  $^{12}\text{C}$ -Gly then subjected to WD cycles. The different integrated areas are obtained as a result of a peak fitting done on the ester and amide I bands of the IR spectral data.

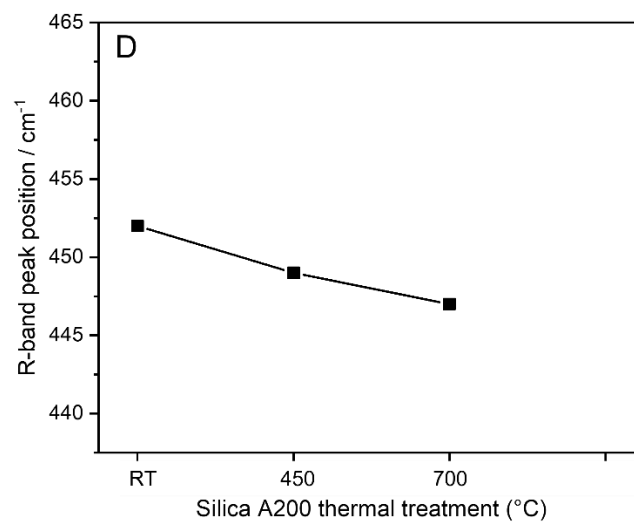
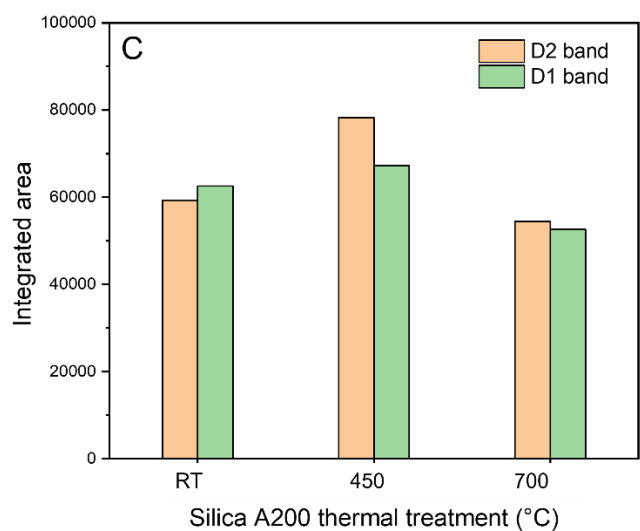
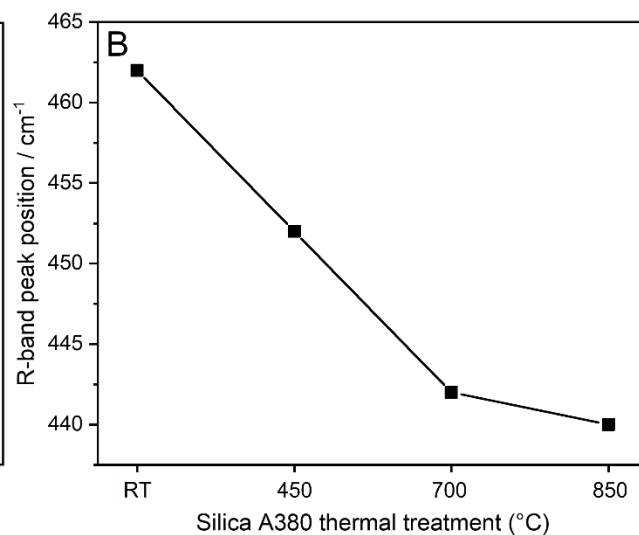
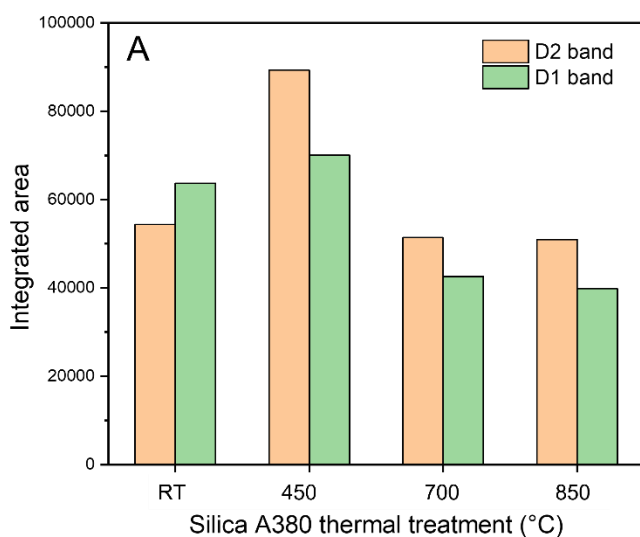
# Appendix 3: Cyclic or linear? Parameters determining the outcome of glycine polymerization in silica surface prebiotic scenarios

## Supporting information

Gly deposited on silica from the vapor phase

Silica supports

Raman spectroscopy



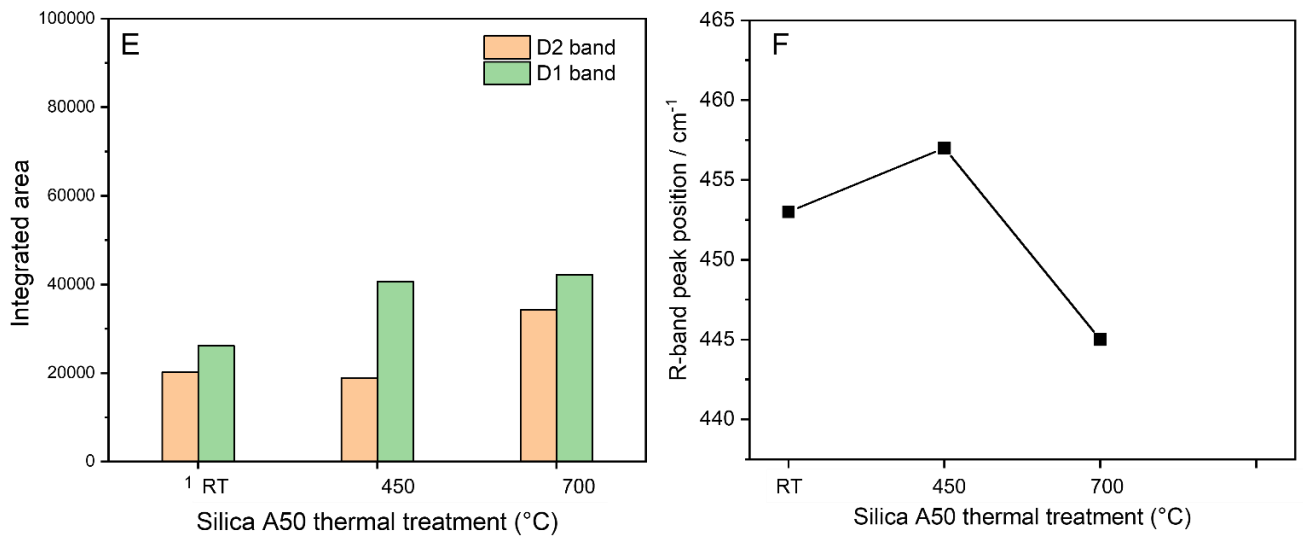


**Figure A3- 1:** A) D1 and D2 integrated areas as function of the thermal treatments; B) peak position of the R-band obtained by fitting normalized Raman spectra, for silica A380; C) and D) same data, for silica A200; E) and F) same data, for silica A50

**IR measurements by transmission on KBr pellets**

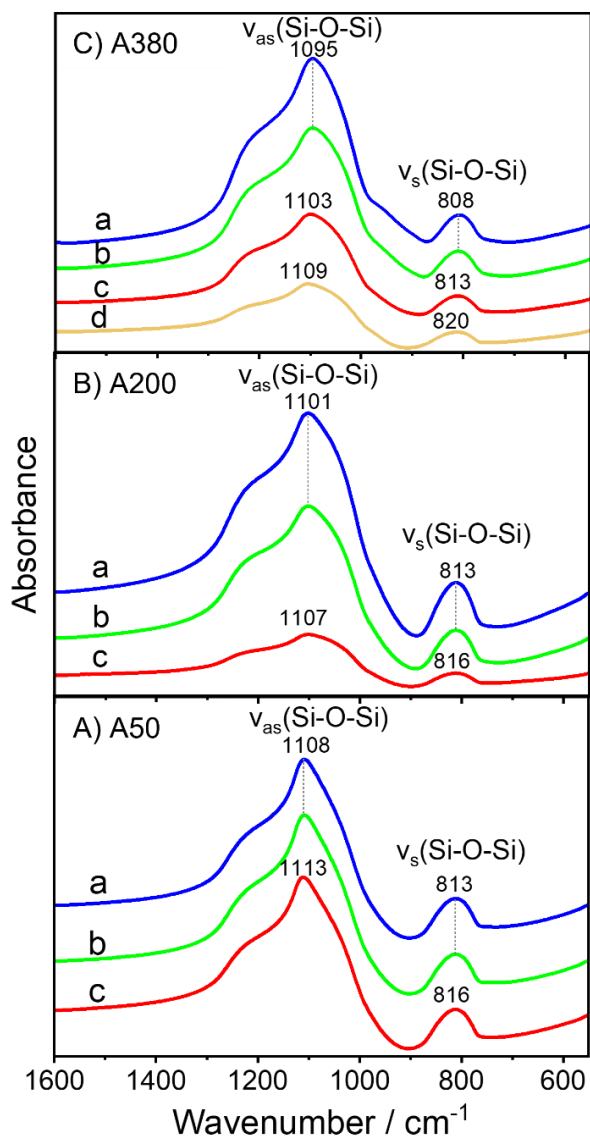


**Figure A3- 2:** FTIR spectra recorded in the transmission mode on KBr pellets for A) A50, B) A200, and C) A380 silica samples; pre-treated each at different temperatures: (a) rt, (b) 450, (c) 700, and (d) 850 °C for 2.5 h.

## Gly reactivity on silica

### XRD analysis

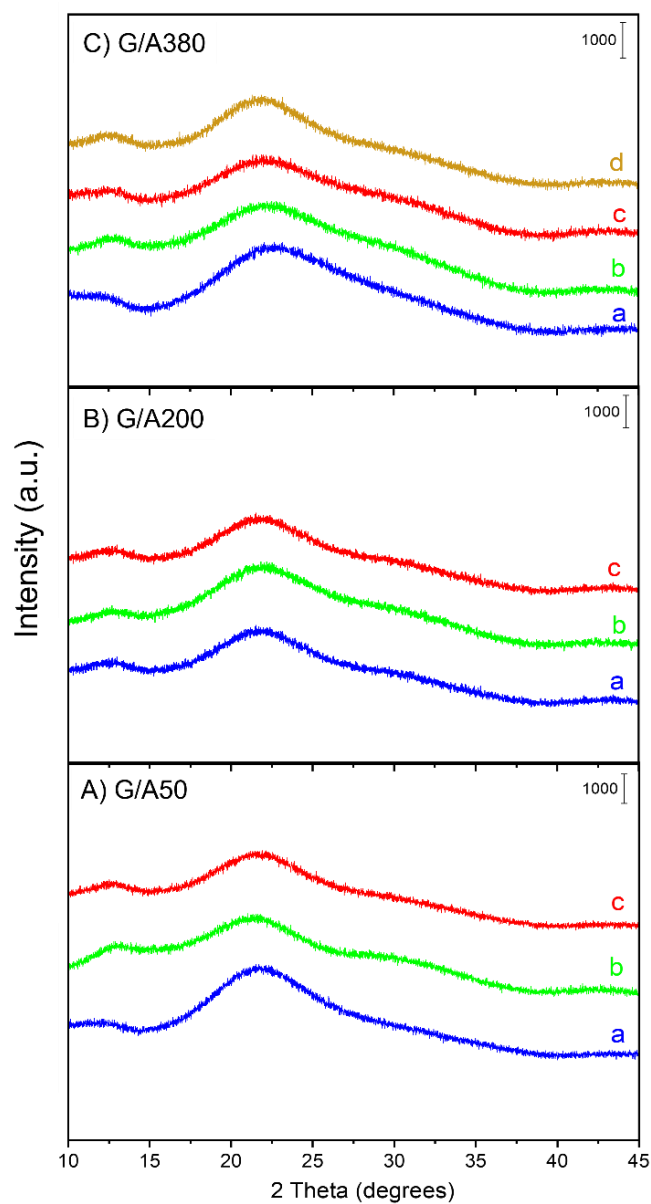


**Figure A3- 3:** XRD profiles measured after Gly sublimation for 20 h by CVD at 160 °C under argon flow on silica: (A) G/A50, (B) G/A200, and (C) G/A380; which supports were pre-treated each at different temperatures: (a) room temperature (rt), (b) 450, (c) 700, and (d) 850 °C for 2.5 h.



## FTIR spectroscopic studies

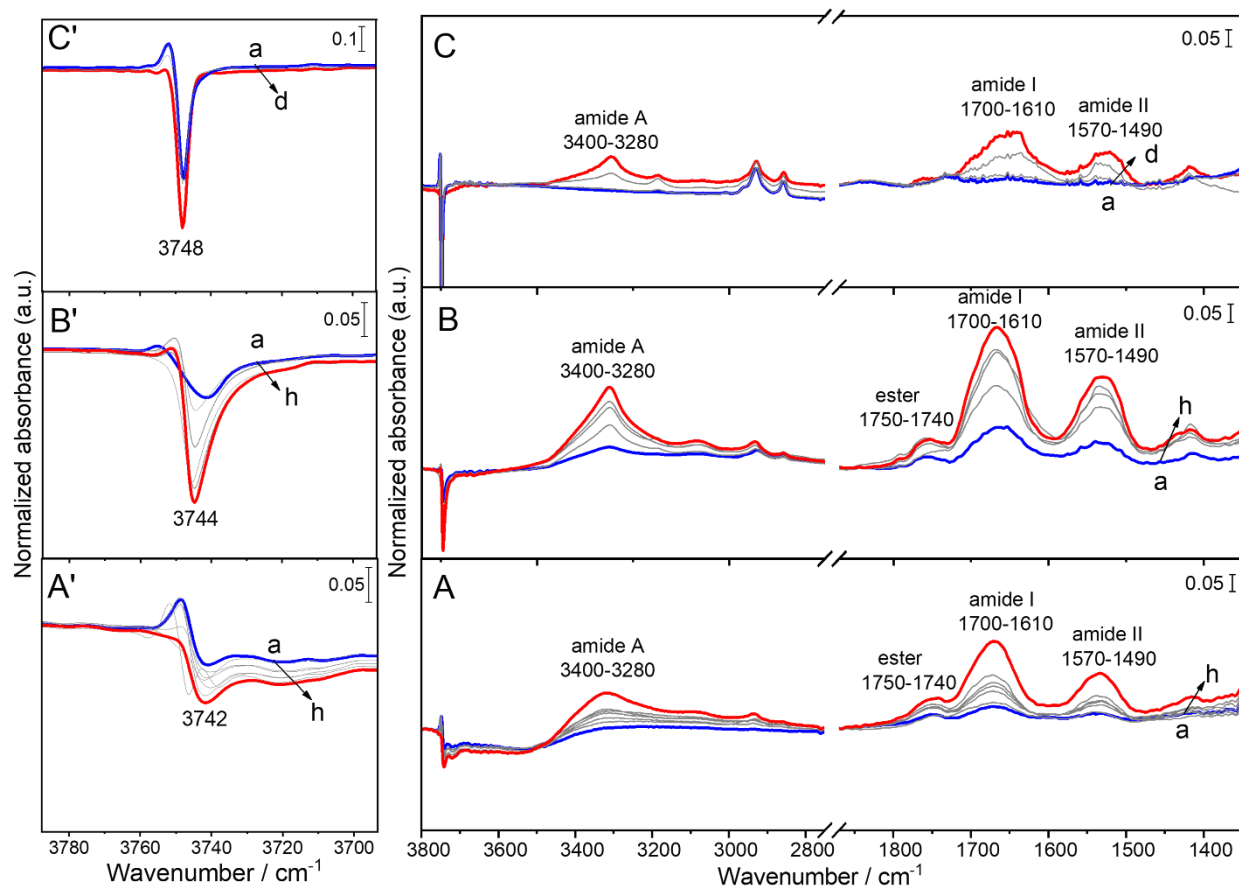


**Figure A3- 4:** IR difference spectra resulting from Gly sublimation by CVD at 160 °C under vacuum on A50 silica surfaces pre-treated each at different temperatures: (A) room temperature (rt), (B) 450, and (C) 700 for 2.5 h; measured from 2.5 h (a) to 20 h (h) (gray curves show intermediate sublimation steps of 2.5 h) on the three samples. The corresponding spectra of the materials obtained before the start of CVD process are subtracted as baselines. In panels A', B' and C', the intensities are enhanced for the sake of clarity.

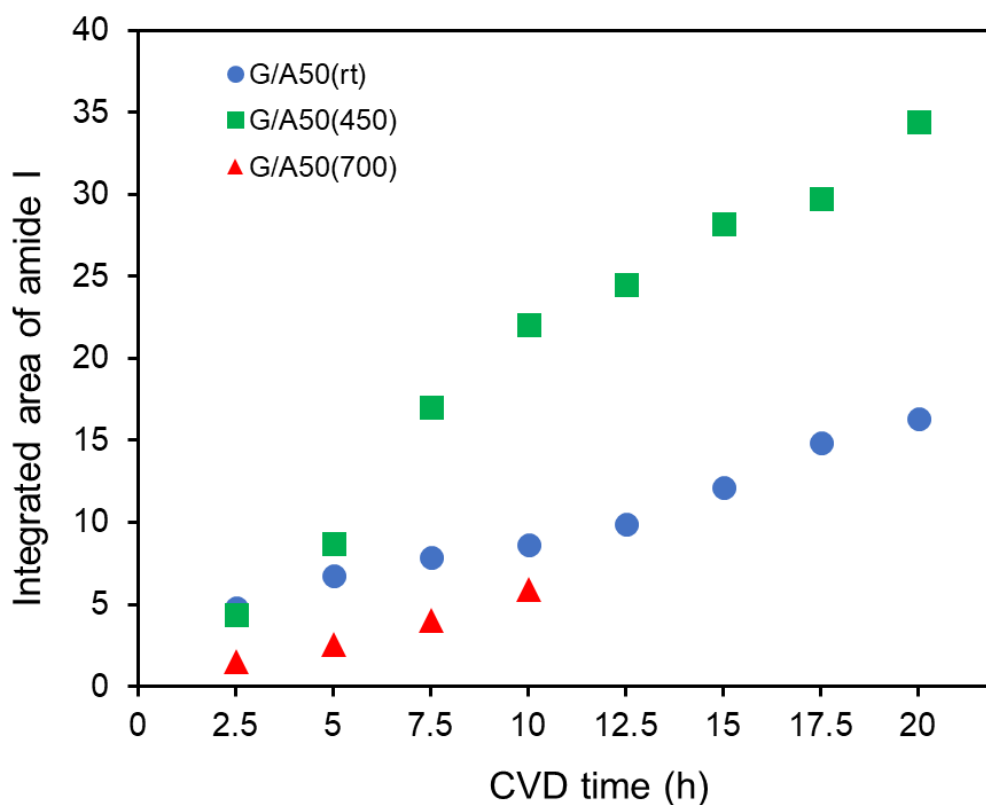


**Figure A3- 5:** Integrated areas of amide I bands as a function of CVD time (h) for G/A50 samples prepared by in-situ CVD. Each support was pre-treated at different temperatures: room temperature (rt), 450, and 700 °C for 2.5 h.

### Gly deposited on silica from the liquid phase

weight loading (%)	Gly/nm <sup>2</sup>					
	0.5	1	2	3	4	5
A50	0.85	1.71	3.41	5.12	6.83	8.53
A200		0.41	0.81	1.22	1.63	2.04
A380		0.21	0.41	0.62	0.83	1.04

**Table A3- 1:** Table presenting the number of Gly per nm<sup>2</sup> silica for different samples G<sub>x</sub>/A50, G<sub>x</sub>/A200, and G<sub>x</sub>/A380. The theoretical values of monolayer (ML) coverage of Gly would represent 4.5 weight % on A50, 18.0 weight % on A200, and 34.8 weight % on A380.

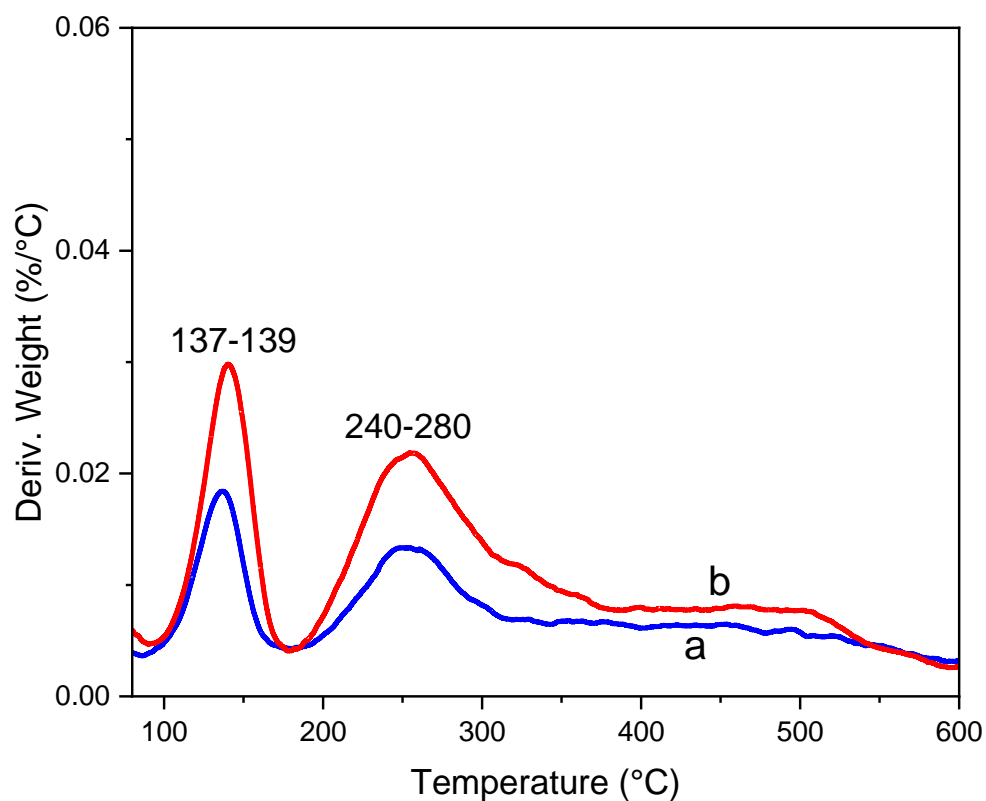


**Figure A3- 6:** Thermograms (DTG) of samples after Gly deposition by incipient wetness impregnation before any thermal activation: (a) G<sub>2%</sub>/A380 and (b) G<sub>3%</sub>/A380.

Gly/silica sample	Weight loss for DTG peaks (%)		Total adsorbed amount of Gly (%)
	peak 1	peak 2	
G <sub>2%</sub> /A380	0.65 (137)	1.44 (255)	2.09
G <sub>3%</sub> /A380	1.14 (139)	1.88 (255)	3.02

**Table A3- 2:** Table presenting the total adsorbed amount of Gly (%) on G<sub>2%</sub>/A380 and G<sub>3%</sub>/A380 calculated from the integration of DTG peaks of Figure S4 for the unactivated samples.

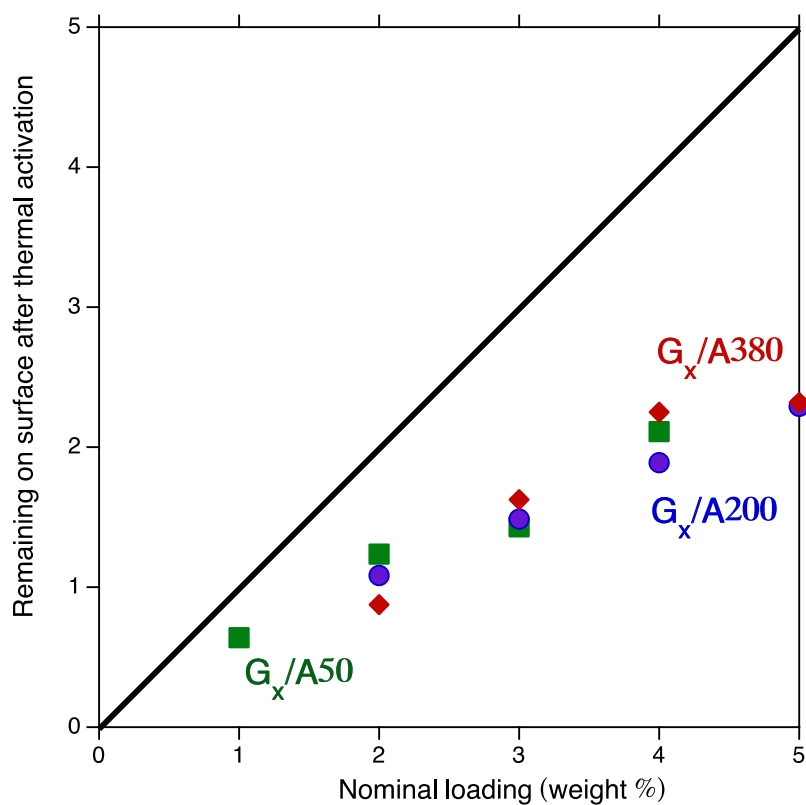


**Figure A3- 7:** Amounts of organic matter remaining in the samples after thermal activation, as a function of the nominal amount of Gly deposited. In order to correct for the water lost upon thermal condensation, the amounts measured by DTG have been multiplied by a factor  $Mm(Gly)/(Mm(Gly)-18)$ .

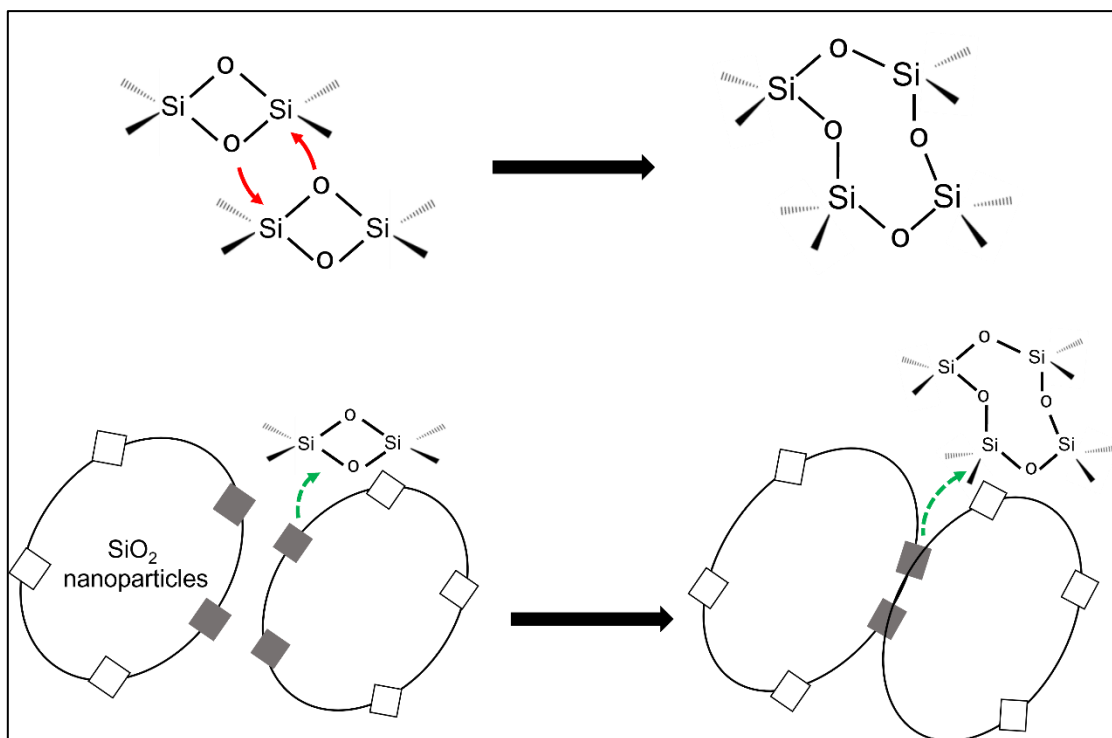


**Figure A3- 8:** Scheme representing the formation of neck between adjacent particles leading to larger rings at the molecular level.

## List of figures

<b>Figure I-1:</b> Schematic representation of a conventional pathway for amide bond formation using coupling reagents where A* represents an activating agent and R <sub>1</sub> and R <sub>2</sub> are organic moieties. <sup>1</sup> .....	11
<b>Figure I-2:</b> Examples of drugs involving an amide bond linkage. <sup>28</sup> .....	15
<b>Figure I-3:</b> a) Schematic drawing of the spark-discharge apparatus used in the Miller-Urey experiments; b) schematic representation of the Strecker reaction mechanism for abiotic synthesis of amino acids (and hydroxy acids). <sup>44</sup> .....	16
<b>Figure I-4:</b> Schematic representation showing the central role of peptides in molecular interactions and functions in extant life. Similar interactions could have occurred between prebiotic peptides and other molecules. <sup>40</sup> .....	18
<b>Figure I-5:</b> Scheme representing the condensation reaction of peptide bond formation between two amino acids .....	20
<b>Figure I-6:</b> Timeline of the early Earth, showing key steps for the evolution of life, from initial sterile conditions during high meteorite bombardment in the early Hadean to the rise of atmospheric oxygen during the Neoproterozoic (G.O.E., Great Oxidation Event). <sup>132</sup> .....	24
<b>Figure I-7:</b> Schematic representations of the framework and surface chemistry of amorphous and crystalline silica. <sup>130</sup> .....	28
<b>Figure I-8:</b> Timeline of the development of the synthesis of amorphous nanoparticles. <sup>130</sup> ....	29
<b>Figure I-9:</b> Schematic representation of different synthesis routes for amorphous silica: a) flame pyrolysis, b) sol-gel synthesis, <sup>130</sup> and c) soft template synthesis. <sup>159</sup> .....	31
<b>Figure II-1:</b> Diagram representative of the principle of FTIR instrument. ....	39
<b>Figure II-2:</b> Schematic representation of total internal reflection in ATR-IR system. <sup>183</sup> .....	42
<b>Figure II-3:</b> Schematic representation of the Raman Spectroscopy scattering <sup>186</sup> .....	44
<b>Figure II-4:</b> Schematic representation for X-ray Diffraction (XRD).....	48
<b>Figure II-5:</b> Schematic representation of the structure and the signal converter manner for Orbitrap mass analyzer. <sup>193</sup> .....	50
<b>Figure II-6:</b> Gly adsorption from vapor phase using the vacuum cell on silica surface. <sup>25</sup> .....	53
<b>Figure II-7:</b> Gly adsorption from vapor phase using the U-shaped cell on silica surface. ....	54
<b>Figure III-1:</b> IR spectra of F-AX for the first run: (a) after treatment in FA vapor (48 mbar) at 160 °C for 2 h; (a - e) after outgassing overnight at bt until invariance of spectra; (f) after contact with water vapor (20 mbar) for 30 min followed by outgassing at bt; (g) after outgassing at 160 °C for 2 h. The spectrum of bare SiO <sub>2</sub> after outgassing at 160 °C for 2 h (AX) is subtracted as a baseline. In panels B, B' and B'', the intensities are enhanced for the sake of clarity. ....	65
<b>Figure III-2:</b> IR difference spectra resulting from Gly sublimation by CVD at 160 °C measured from 2.5 h (a) to 20 h (h) (gray curves show intermediate sublimation steps of 2.5 h) on the two samples: G/AX and G/F-AX. The corresponding spectra of the materials obtained before the start of CVD process are subtracted as baselines. ....	68

<b>Figure III-3:</b> HR-MS spectra of the solutions resulting from washing (with pure water) of the samples produced by adsorbing Gly from the vapor phase onto the three samples: G/AX <sub>(rt)</sub> , G/AX, and .....	70
<b>Figure III-4:</b> Enlarged sections in the 3760 - 3700 cm <sup>-1</sup> range of IR spectra measured on: F-AX, G/AX, and G/F-AX. ....	71
<b>Figure III-5:</b> Enlarged sections of IR spectra during Gly sublimation by CVD at 160 °C for 20 h (in 2.5 hr steps, from 2.5 h (a) to 20 h (h) sublimation) on G/F-AX: .....	74
<b>Figure III-6:</b> Suggested scheme for (A) β-turn, (B) ligation and β-sheet structures formation. ....	76
<b>Figure III-7:</b> Panel (I): IR spectra of G/F-AX submitted to successive treatments: (a) directly after Gly sublimation for 20 h, (b) after subsequent contact with water vapor (20 mbar) and outgassing for 30 min at bt, (c) after H/D exchange and then outgassing of D <sub>2</sub> O for 30 min at bt and (d) after sample washing with ultrapure water followed by H/D exchange (then bt outgassing). ....	79
<b>Figure IV-1:</b> IR difference spectra resulting from Gly sublimation at 160 °C by CVD carried out from 2.5 h (a) to 20 h (h) on the two samples: A) G <sub>TF</sub> /AX <sub>160</sub> , Gly adsorbed on silica pre-treated at 160°C, and B) G <sub>TFHF</sub> /AX <sub>160</sub> , Gly adsorbed on silica pre-treated at 160 °C and subjected to intermediate HF cycles during CVD.....	93
<b>Figure IV-2:</b> Evolution of (a) and (b) the absolute intensities of the different types of secondary structures and (a') and (b') integrated area of ester groups as a function of time during Gly deposition by CVD during the different cycles on the two samples: A) G <sub>TF</sub> /AX <sub>160</sub> and B) G <sub>TFHF</sub> /AX <sub>160</sub> .....	96
<b>Figure IV-3:</b> Suggested scheme for the polymerization of peptides on amorphous silica during Gly CVD with intermediate HF cycles.....	98
<b>Figure IV-4:</b> Panel (I) represents the IR difference spectra obtained (a and b) directly after Gly sublimation on silica for 20 h; (A and B) after subsequent H/D exchange and then outgassing of D <sub>2</sub> O at bt until invariance of spectra, on the two samples: G <sub>TF</sub> /AX <sub>160</sub> and G <sub>TFHF</sub> /AX <sub>160</sub> respectively. For G <sub>TFHF</sub> /AX <sub>160</sub> , spectra obtained after a first washing with liquid water at rt (B') and a second washing with liquid water while heating at 70 °C (B'') on G <sub>TFHF</sub> /AX <sub>160</sub> are also displayed. ....	99
<b>Figure IV-5:</b> Evolution of the integrated area of the different types of secondary structures at the end of the HF cycles (time 0) and during subsequent D <sub>2</sub> O adsorption/desorption (time > 0) on the two samples: G <sub>TF</sub> /AX <sub>160</sub> (A), and G <sub>TFHF</sub> /AX <sub>160</sub> (B), and after washing of the latter with liquid water at rt (B') and at 70 °C (B'').....	102
<b>Figure IV-6:</b> IR difference spectra on G <sub>TFHF</sub> /AX <sub>WD</sub> resulting from Gly sublimation at 160 °C by CVD with TF cycles measured from 2.5 h (a) to 20 h (h); (i) after D <sub>2</sub> O adsorption/desorption cycles at bt until spectral invariance; (j) after wetting/drying cycles with liquid water and outgassing at rt; (k) after subsequent D <sub>2</sub> O adsorption/desorption cycles at bt; a second set of <sup>15</sup> N-Gly sublimation at 160 °C with TF cycles, by CVD measured from 2.5 h (l) to 15 h (q); (r) after D <sub>2</sub> O adsorption/desorption at bt until spectral invariance. ....	106
<b>Figure V-1:</b> Raman spectra recorded for A) A50, B) A200, and C) A380 silica samples; pre-treated each at different temperatures: (a) rt, (b) 450, (c) 700, and (d) 850 °C for 2.5 h. The spectra are normalized at 800 cm <sup>-1</sup> , a band characteristic of the silica network. ....	122

<b>Figure V-2:</b> ATR-IR spectra for A) A50, B) A200, and C) A380 silica samples, pre-treated at different temperatures: (a) rt, (b) 450, (c) 700, and (d) 850 °C for 2.5 h. ....	125
<b>Figure V-3:</b> Transmission IR difference spectra measured on self-supporting pellets resulting from Gly deposition by CVD under argon flow for 20 h at 160 °C for the following samples: (A) G/A50, (B) G/A200, and (C) G/A380; in each panel, supports were pre-treated at different temperatures: (a) room temperature (rt), (b) 450, (c) 700, and (d) 850 °C for 2.5 h. ....	128
<b>Figure V-4:</b> Derivative thermograms (DTG) of samples obtained after Gly sublimation for 20 h by CVD at 160 °C under argon flow on silica: (A) G/A50, (B) G/A200, and (C) G/A380; which supports were pre-treated each at different temperatures: (a) rt, (b) 450, and (c) 700 °C for 2.5 hrs .....	131
<b>Figure V-5:</b> XRD profiles measured after Gly deposition by incipient wetness impregnation followed by activation for 30 min at 160 °C under argon flow on silica: (A) G <sub>x</sub> /A50, (B) G <sub>x</sub> /A200, and (C) G <sub>x</sub> /A380; where x refers to different Gly monomers loadings: (a) 0.5, (b) 1, (c) 2, (d) 3, (e) 4, or (f) 5 wt%.....	134
<b>Figure V-6:</b> Transmission IR difference spectra measured on self-supporting pellets after Gly deposition by incipient wetness impregnation followed by activation for 30 min at 160 °C under argon flow on silica: (A) G <sub>x</sub> /A50, (B) G <sub>x</sub> /A200, and (C) G <sub>x</sub> /A380; where x refers to different Gly monomers loading: (a) 0.5, (b) 1, (c) 2, (d) 3, (e) 4, or (f) 5 wt%.....	136
<b>Figure V-7:</b> Thermograms (DTG) of samples after Gly deposition by incipient wetness impregnation followed by activation for 30 min at 160 °C under argon flow on silica: (A) G <sub>x</sub> /A50, (B) G <sub>x</sub> /A200, and (C) G <sub>x</sub> /A380; where x refers to different Gly monomers loading: (a) 1, (b) 2, (c) 3, (d) 4, or (e) 5 wt%.....	140



## List of tables

<b>Table II-1:</b> Table showing the comparison between DTGS and MCT detectors for FTIR spectroscopy. ....	39
<b>Table V-1:</b> Specific Surface Area ( $SSA_{BET}$ ) of silica samples (A50, A200, and A380) in the pristine form and after calcination in air at 450, 700 and 850 °C. ....	120
<b>Table V-2:</b> Number of silanol (OH) groups / $nm^2$ for silica samples (A50, A200, and A380) in the pristine form and after calcination in air at 450 and 700 °C, calculated using thermogravimetric analysis. ....	121
<b>Table V-3:</b> Main results obtained from the characterization techniques (FTIR, and TGA) for all the G/SiO <sub>2</sub> samples prepared by Gly deposition from the gas phase. XRD showed the absence of crystalline phases in all samples. ....	133

## Journal Publications

1. El Samrout, O.; Fabbiani M.; Berlier G.; Lambert J.F.; Martra G., Emergence of order in origins-of-life scenarios on minerals surfaces: polyglycine chains on silica, published in *Langmuir*, 2022. Cited as *Langmuir* 2022, 38, 50, 15516–15525
2. El Samrout, O.; Berlier G.; Lambert J.F.; Martra G., Polypeptide chain growth mechanisms and secondary structure formation in glycine gas-phase deposition on silica surfaces, published in the *Journal of Physical Chemistry B*, 2023. Cited as *J. Phys. Chem. B* 2023, 127, 3, 673–684
3. El Samrout, O.; Mezzetti, A.; Berlier G.; Lambert J.F.; Cyclic or linear? Parameters determining the outcome of glycine polymerization in silica surface prebiotic scenarios, published in *Chemistry-a European Journal*, 2023. Cited as <https://doi.org/10.1002/chem.202204010>
4. Fatehbasharzard, P., Ivanchenko P., El Samrout O., Martra G., Morales J., “Study of relevant properties of metallic and non-metallic materials in biomedical applications”, submitted to the publishing house of Taylor & Francis eBooks on June 23, 2022, accepted with minor modifications. Corresponding author: Ola El Samrout.

## Résumé :

La réaction de polymérisation des acides aminés sur les surfaces d'oxydes est l'objet d'un intérêt significatif dans divers domaines allant de la biotechnologie et de la chimie prébiotique aux théories de l'origine de la vie. Cependant, malgré le grand nombre d'études qui ont abordé cette réaction, celle-ci n'est toujours pas bien comprise. Cette thèse de doctorat est consacrée à l'étude de la réaction de polymérisation de la glycine sur la surface de la silice amorphe en se concentrant principalement sur son mécanisme, sa cinétique, l'effet de l'exposition à l'eau à différentes étapes de la réaction sur l'efficacité de la réaction et le type de produit obtenu par différentes méthodes de dépôt de monomères, le comportement des biomolécules obtenues dans différentes conditions environnementales, etc. Les différentes surfaces de silice et les systèmes Gly/silice préparés par dépôt de monomères à partir de la phase gazeuse ou de la phase liquide ont été analysés en combinant différentes techniques de caractérisation, principalement la spectroscopie IR in-situ, la spectroscopie Raman, la diffraction des rayons X, l'analyse thermogravimétrique, la spectrométrie de masse et la physisorption de N<sub>2</sub>. Les résultats révèlent que les monomères Gly se lient à la surface de la silice de manière covalente par la formation de groupes esters qui constituent, avec les groupes silanols presque libres (NFS), des sites de surface cruciaux pour l'activation des monomères. Une fois activés, des conformations de coudes  $\beta$  se forment qui s'allongent ensuite en structures secondaires plus complexes principalement constituées de feuillet  $\beta$  de haute résistance à l'hydrolyse. De plus, la formation de peptides par condensation thermique de Gly en phase gazeuse dans des environnements fluctuants de silice (cycles de fluctuations de température et d'humidité) s'est avérée être un cadre géochimique favorable pour la réaction de polymérisation. Les étapes de déshydratation favorisent thermodynamiquement la réaction de condensation tandis que les cycles d'hydratation entraînent l'hydrolyse de certaines chaînes, la réorganisation des oligomères en surface et le rétablissement des sites d'ancrage NFS. De tels cycles humidification-séchage entraînent la formation d'une grande quantité de peptides avec un niveau élevé de structuration mettant en évidence le concept d'une croissance de peptides utilisant comme « patrons » des structures de feuillet  $\beta$ . Enfin, le résultat de la polymérisation de la glycine à la surface de silices de différentes surfaces et densités de silanol a montré une dépendance à divers paramètres, principalement la densité globale de silanols et l'état dans lequel les monomères sont adsorbés à la surface (zwitterions ou formes canoniques). La complexité de la chimie de surface de la glycine dans la réaction de polymérisation étudiée dans ce travail met en évidence l'intérêt d'une approche de science des surfaces pour évaluer les scénarios prébiotiques géochimiques.

**Mots clés :** dimère cyclique, esters, adsorption en phase gazeuse, glycine, peptides linéaires, adsorption en phase liquide, polymérisation, auto-assemblage, silanols, siloxanes, silice, eau.

## Abstract:

The polymerization reaction of amino acids on oxide surfaces has attracted significant interest in various fields ranging from biotechnology, prebiotic chemistry, and origin of life theories. However, despite the big number of studies tackling this reaction, it is still poorly understood. This PhD thesis is devoted to study the polymerization reaction of Glycine on amorphous silica focusing mainly on its mechanism, kinetics, the effect of water exposure at different stages of the reaction on the efficiency of the reaction and the type of product obtained upon different method of monomers deposition, the behavior of the biomolecules obtained under different environmental conditions, etc. The different silica surfaces and Gly/silica systems prepared by monomers deposition from gas or liquid phases were analyzed by combining different characterization techniques, mainly in-situ IR spectroscopy, Raman spectroscopy, X-ray diffraction, thermogravimetric analysis, Mass Spectrometry, and N<sub>2</sub> physisorption. The results reveal that Gly monomers bind to the silica surface covalently through the formation of ester groups which are, together with the nearly-free silanol (NFS) groups, crucial surface sites for monomers activation. Once activated,  $\beta$ -turns conformations are formed which then elongate into more complex secondary structures of mainly  $\beta$ -sheet with high resistance to hydrolysis. Moreover, peptides formation through thermal condensation of gas-phase Gly in fluctuating silica environments with both temperature

and humidity fluctuations cycles proved to be a favorable geochemical setting for the polymerization reaction. The dehydration steps thermodynamically drive the condensation reaction while the hydration cycles result in the hydrolysis of some chains, the reorganization of the oligomers on the surface, and the re-establishment of the NFS anchoring sites. Such wetting-drying cycles result in the formation of high amount of peptides with a high level of structuring, suggesting templated peptides growth on  $\beta$ -sheet structures. Finally, the outcome of the polymerization of glycine mediated by the surface of silica samples of different surface areas and silanol densities showed a dependency to various parameters, mainly the global silanol density and the state of monomers (zwitterionic or neutral) when adsorbed on the surface. The complexity of glycine surface chemistry in the polymerization reaction investigated in this work highlights the interest of a surface science approach to evaluate geochemical prebiotic scenarios.

**Keywords:** cyclic dimer, esters, chemical vapor deposition, glycine, linear peptides, incipient wetness impregnation, polymerization, self-assembly, silanols, siloxanes, silica, water